Flavour tagging with baryons and a study of two body Λ_b decays with the LHCb experiment

James William Storey

of
King's College

A dissertation submitted to the University of Cambridge
for the degree of Doctor of Philosophy

Abstract

The LHCb experiment will perform precision measurements of $\mathcal{CP}$-violation and search for rare B decays at the Large Hadron Collider (LHC), which is due to begin operation in 2008. The LHCb Ring Imaging Cherenkov (RICH) system provides the particle identification crucial for these studies. The Multi-Anode photomultiplier tube (MaPMT) is a candidate photon detector for the LHCb RICH system. Performance studies of the MaPMT in a charged particle beam at CERN demonstrate that the pulse shape of the BeetleMA readout ASIC does not return to zero after 125ns, which will lead to ghost pixel hits and the possible drift of the pedestal outside the dynamic range of the amplifier.

Measurement of key $\mathcal{CP}$ asymmetries at LHCb requires that the flavour of the B-meson at creation is known. Flavour tagging using protons is shown to have potentially useful tagging performance, but the implementation is found to be challenging. A correlation between b-quark and Λ flavour is observed for a Λ produced in the same fragmentation process as a $\mathrm{B_s^0}$ meson, analogous to a same-side kaon tag. A small, but non-negligible, tagging performance is attained.

$\mathcal{CP}$-violation asymmetries are expected in the b-flavoured baryon decays $\Lambda_\mathrm{b} \to \mathrm{p}\,\pi$ and $\Lambda_\mathrm{b} \to \mathrm{p\,K}$. Studies of the reconstruction and selection of these decay channels with Monte Carlo simulated data suggest an annual event yield of $\sim$2k $\Lambda_\mathrm{b} \to \mathrm{p}\,\pi$ and $\sim$3k $\Lambda_\mathrm{b} \to \mathrm{p\,K}$ events. The R-parity violating Minimal Supersymmetric Standard Model is expected to suppress the $\mathcal{CP}$ asymmetry of $\Lambda_\mathrm{b} \to \mathrm{p}\,\pi$ decays and enhance the branching fraction. Evidence for $\mathcal{CP}$-violation consistent with the Standard Model is expected to require an integrated luminosity of more than 1.5 fb^{-1}, while evidence for $\mathcal{CP}$-violation consistent with R-parity-violation in the Minimal Supersymmetric Standard Model will require $50 - 250$ fb^{-1}; which in the latter case will only be achievable with an upgraded luminosity "Super"-LHCb detector.

Declaration

This dissertation is the result of my own work, except where explicit reference is made to the work of others, and has not been submitted for another qualification to this or any other university. This dissertation does not exceed the word limit for the respective Degree Committee.

James Storey

Acknowledgements

During the research and writing of this thesis I benefited from the help and advice of many people from both the Cambridge HEP group and at CERN. To mention a few to whom I am particularly indebted :

My supervisor Val Gibson, for guidance, support and extreme patience throughout my PhD.

Steve Wotton, for supervising the hardware aspects, general guidance and organising the HEP curry nights.

Karl Harrison, Chris Jones and Cristina Lazzeroni for their highly professional help and advice on all aspects of this thesis.

Andy Buckley, for providing the LaTeX template for this thesis and instilling his enthusiasm for linux in my first year.

Franz Muheim, Stephan Eisenhardt, Alex Howard, Andrew Pickford and Richard Plackett for their help during the MaPMT testbeams.

Marta Calvi and Olivier Leroy for guidance on the flavour tagging work.

Patrick Koppenburg and Patrick Robbe for help with the LHCb software.

I would like to thank all members of the Cambridge HEP group for the friendly environment that has made the last few years so enjoyable.

Finally, I would like to thank my parents without whom's support I would never have made it this far.

Preface

A symmetry arises when a physical system is invariant under a particular transformation. This feature of nature is expressed by Noether's theorem which states that there is a one-to-one correspondence between a symmetry and a conservation law. For instance, the invariance of the laws of physics under translation and rotation leads to the conservation of linear and angular momentum. In particle physics the concept of symmetry plays a central role. The Standard Model of particle physics is a relativistic quantum field theory that provides a complete description of the fundamental particles; the interactions of which arise from the requirement that the Standard Model is invariant under local gauge transformations [1, 2, 3].

Two types of symmetries can be distinguished; continuous and discrete. Rotations in space and translations in time are examples of continuous symmetries, while a mirror reflection is an example of a discrete symmetry. The parity operation, $\mathcal{P}$, under which all spatial coordinate signs are reversed, was thought to be a discrete symmetry of the weak interaction. However, in 1957 it was found that weak interactions did not conserve parity in the radioactive decay of cobalt-60 [4]. Following this discovery it was thought that the weak interaction was symmetric under the combined operation of $\mathcal{P}$ and charge conjugation, $\mathcal{C}$, where $\mathcal{C}$ transforms a particle into it's anti-particle. In 1964, however, $\mathcal{CP}$ violation was observed in the kaon decays [5] and has since been established in the decay of B-mesons [6, 7].

The accommodation of $\mathcal{CP}$ violation in the Standard Model naturally arises from the complex couplings between the quarks, which is represented by the so-called Cabbibo-Kobayashi-Maskawa (CKM) matrix [8]. All $\mathcal{CP}$ violation measurements are, so far, consistent with the Standard Model expectations. Nevertheless, measuring the parameters that describe $\mathcal{CP}$-violation in the Standard Model by different methods enables discrepancies to be identified, which could indicate the presence of new physics. In fact,

evidence already exists from Cosmology for a beyond Standard Model description of $\mathcal{CP}$ violation. Assuming that the universe began with equal amounts of matter and anti-matter, the observed matter dominated universe can be generated through a process called Baryogenesis which requires $\mathcal{CP}$ to be violated [9]. However, the level of Standard Model $\mathcal{CP}$-violation is insufficient to explain the observed cosmological baryon asymmetry $\mathcal{O}(10^{-10})$, and requires additional beyond Standard Model sources of $\mathcal{CP}$-violation [10].

The Large Hadron Collider Beauty experiment, LHCb, is a dedicated detector for B-physics measurements at the Large Hadron Collider (LHC). LHCb will use the unprecedented numbers of B_d^0, B^+, B_s^0 and Λ_b hadrons produced at the LHC to overconstrain the Standard Model description of $\mathcal{CP}$-violation and search for new physics through the presence of rare decays.

To motivate the research presented in this thesis, Chapter 1 presents a discussion of the theoretical motivation for B-physics studies and is followed in Chapter 2 by a description of the experimental apparatus which has been designed to make these physics measurements.

This thesis describes three different aspects of the LHCb experiment:

- The ability to identify the particle type of a reconstructed track with high efficiency and purity is critical to the physics performance at LHCb. Hadron identification will be provided by Ring Imaging Cherenkov (RICH) detectors, the photon detectors of which are a crucial component of the system. The RICH system is described in Chapter 3. Chapter 4 will present a measurement of the pulse shape from a candidate photon detector techology, the Multi-Anode photomultiplier, in a CERN charged particle beam. In the course of this measurement, an analytic function is developed for the number of electrons at the end of a photomultiplier tube which includes photoelectric conversion on the first dynode.

- The measurement of key $\mathcal{CP}$-violation rate asymmetries require that the flavour of the B-meson at production is known. Methods to determine this flavour, known as flavour-tagging, typically use the charge of kaons or leptons from the companion b-hadron to infer the flavour of the signal B-meson. Since LHCb is able to readily identify protons with the RICH system, the potential to use protons for flavour tagging purposes is investigated. This is the subject of Chapter 5.

- While most $\mathcal{CP}$-violation studies at LHCb will be based on the study of B-mesons,

LHCb will also have access to copious numbers of Λ_b's. Direct $\mathcal{CP}$ violation is expected in the b-flavoured baryon decays $\Lambda_b \to p\,\pi$ and $\Lambda_b \to p\,K$ decays. The former decays are of particular interest since the R-parity violating Minimal Supersymmetric Standard Model predicts that the $\mathcal{CP}$-violation asymmetry will be suppressed and the branching fractions enhanced relative to the Standard Model predictions [11, 12]. Methods to reconstruct and select $\Lambda_b \to p\,\pi/K$ decays are discussed in Chapter 6 and the sensitivity to the physics parameters are presented in Chapter 7.

Contents

Chapter 1

$\mathcal{CP}$-violation in B decays

This chapter presents the formalism for $\mathcal{CP}$-violation and mixing in, first, a model independent manner and then describes how the Standard Model can accommodate $\mathcal{CP}$-violation; a process which is intrinsically linked to the mechanism of mass generation, the mass hierarchy and the number of fermion generations. The final part of the chapter motivates the study of $\mathcal{CP}$-violation with b-baryons; the properties of $\Lambda_b \to p\,\pi$ decays are of particular interest since, compared to the Standard Model, significantly different branching fractions and $\mathcal{CP}$ asymmetries are predicted in the case of R-parity-violation in the Minimal Supersymmetric Standard Model.

1.1 Model-Independent Description of Mixing and $\mathcal{CP}$-violation

The b-hadrons produced at the LHC are formed from the hadronisation of quarks with definite flavour. The corresponding flavour eigenstates are :

$$\begin{array}{llll} B_d^0 = (\overline{b}d), & B_s^0 = (\overline{b}s), & B^+ = (\overline{b}u), & \Lambda_b = (bud) \\ \overline{B}_d^0 = (b\overline{d}), & \overline{B}_s^0 = (b\overline{s}), & B^- = (b\overline{u}), & \overline{\Lambda}_b = (\overline{b}\overline{u}\overline{d}), \end{array} \tag{1.1}$$

where the upper and lower lines refers to the particle and anti-particle flavour eigenstates respectively. Since flavour is not conserved in the weak interaction it is possible for a neutral B-meson to oscillate into the corresponding charge conjugate state. This section will present the formalism for neutral B-meson oscillations, and demonstrates that there

exist three different mechanisms by which $\mathcal{CP}$ can be violated in neutral B-meson decays and one mechanism for $\mathcal{CP}$-violation in the decay of charged and baryonic b-hadron decays.

1.1.1 Neutral meson mixing

The following section develops the quantum mechanical formalism for the time evolution of a generic neutral-meson state, X^0, and its anti-state $\overline{\mathrm{X}}^0$.

At the time of creation, $t = 0$, the particle and anti-particle are stable under the strong and electromagnetic interactions, as both are flavour conserving processes. However, at time $t > 0$, due to the presence of the weak interaction the particles may oscillate to the flavour conjugate state or decay into final states $|f_i\rangle$. The system can be represented by a general state $|\psi(t)\rangle$, which is a linear superposition of the initial and final states;

$$|\psi(t)\rangle = a(t)|\mathrm{X}^0\rangle + b(t)|\overline{\mathrm{X}}^0\rangle + \sum_i c_i(t)|f_i\rangle, \tag{1.2}$$

where $a(t)$, $b(t)$ and $c_i(t)$ are coeffiencts which describe the amplitude for observing a state $|\mathrm{X}^0\rangle$, $|\overline{\mathrm{X}}^0\rangle$ and $|f_i\rangle$ at time t respectively. The time evolution of $|\psi(t)\rangle$ is governed by the Schrödinger equation,

$$i\frac{\partial}{\partial t}|\psi(t)\rangle = \mathbf{H}_{\mathrm{tot}}|\psi(t)\rangle, \quad \mathbf{H}_{\mathrm{tot}} = \mathbf{H}_{\mathrm{s}} + \mathbf{H}_{\mathrm{em}} + \mathbf{H}_{\mathrm{w}}, \tag{1.3}$$

where the total Hamiltonian, $\mathbf{H}_{\mathrm{tot}}$, is the sum of the strong, electromagnetic and weak contributions. The total Hamiltonian is assumed to be Hermitian, whereby transition probabilities are conserved and the coefficients satisfy,

$$|a(t)|^2 + |b(t)|^2 + \sum_i |c_i(t)|^2 = 1. \tag{1.4}$$

In order to solve equation 1.3 a number of assumptions are applied to simplify the calculation [13, 14],

- at time $t = 0$: $|a(0)|^2 + |b(0)|^2 = 1$, $\forall i : c_i(0) = 0$,
- for the purposes of studying mixing the values of $a(t)$ and $b(t)$ need to be calculated, but not $c_i(t)$,

- the values of t of interest are much longer than the typical strong interaction timescale.

These assumptions are known as the Wigner-Weisskopf approximation [14]. Under this approximation equation 1.3 reduces to an effective time-dependent Schrödinger equation

$$i\frac{\partial}{\partial t}\begin{pmatrix} a(t) \\ b(t) \end{pmatrix} = \mathbf{H}_{\text{eff}}\begin{pmatrix} a(t) \\ b(t) \end{pmatrix} \equiv \left(\mathbf{M} - \frac{i}{2}\mathbf{\Gamma}\right)\begin{pmatrix} a(t) \\ b(t) \end{pmatrix}, \tag{1.5}$$

where $\mathbf{H}_{\text{eff}}$ is the effective Hamiltonian and $\mathbf{M}$ and $\mathbf{\Gamma}$ are the so-called mass and decay matrices respectively [15]. The effective Schrödinger equation has two-state solutions of the form

$$|\psi(t)\rangle = a(t)|\mathrm{X}^0\rangle + b(t)|\overline{\mathrm{X}}^0\rangle. \tag{1.6}$$

As a consequence of the Wigner-Weisskopf, approximation the effective Hamiltonian is not Hermitian. However, both the mass and decay matrices are Hermitian. Assuming $\mathcal{CPT}$ invariance,

$$\left\langle \mathrm{X}^0 \left| \mathbf{H}_{\text{eff}} \right| \mathrm{X}^0 \right\rangle = \left\langle \overline{\mathrm{X}}^0 \left| \mathbf{H}_{\text{eff}} \right| \overline{\mathrm{X}}^0 \right\rangle, \tag{1.7}$$

such that $H_{11} = H_{22} = H$, $M_{11} = M_{22} = M$ and $\Gamma_{11} = \Gamma_{22} = \Gamma$ [16]. Combined with the fact that the off-diagonal terms of Hermitian matrices form a self-conjugate pair, the effective Hamiltonian can be expressed as

$$\mathbf{H}_{\text{eff}} = \begin{pmatrix} H & H_{12} \\ H_{21} & H \end{pmatrix} = \mathbf{M} - \frac{i}{2}\mathbf{\Gamma} = \begin{pmatrix} M & M_{12} \\ M_{12}^* & M \end{pmatrix} - \frac{i}{2}\begin{pmatrix} \Gamma & \Gamma_{12} \\ \Gamma_{12}^* & \Gamma \end{pmatrix}. \tag{1.8}$$

The eigenvalues of the effective Hamiltonian, $\lambda_{1,2}$, are obtained by solving the characteristic equation

$$|\mathbf{H}_{\text{eff}} - \lambda_{1,2}\mathbf{I}| = 0, \tag{1.9}$$

where $\mathbf{I}$ is the unit matrix. The solutions are

$$\lambda_{1,2} = H \pm \sqrt{H_{21}H_{12}} \tag{1.10a}$$

$$= M - \frac{i}{2}\Gamma \pm \sqrt{\left(M_{12} - \frac{i}{2}\Gamma_{12}\right)\left(M^*_{12} - \frac{i}{2}\Gamma^*_{12}\right)} \tag{1.10b}$$

$$= M_{1,2} - \frac{i}{2}\Gamma_{1,2} \tag{1.10c}$$

where

$$M_{1,2} = M \pm \mathsf{Re}\left(\sqrt{H_{21}H_{12}}\right), \quad \Gamma_{1,2} = \Gamma \mp 2\mathsf{Im}\left(\sqrt{H_{21}H_{12}}\right) \tag{1.11}$$

are physically interpreted as the mass and decay widths of the two eigenstates. The difference in mass and width are defined to be,

$$\Delta M = M_1 - M_2, \quad \Delta\Gamma = \Gamma_1 - \Gamma_2. \tag{1.12}$$

The eigenstates of the effective Hamiltonian, $|\mathrm{X}_1\rangle$ and $|\mathrm{X}_2\rangle$, can be written as a linear combination of the particle and anti-particle flavour eigenstates,

$$|\mathrm{X}_1\rangle = p|\mathrm{X}^0\rangle + q|\overline{\mathrm{X}}^0\rangle \tag{1.13a}$$

$$|\mathrm{X}_2\rangle = p|\mathrm{X}^0\rangle - q|\overline{\mathrm{X}}^0\rangle, \tag{1.13b}$$

where the admixture constants p and q are complex numbers with the normalisation condition $|p|^2 + |q|^2 = 1$. The eigenvector equation,

$$(\mathbf{H} - \lambda_{1,2}\mathbf{I}) \begin{pmatrix} p \\ \pm q \end{pmatrix} = 0, \tag{1.14}$$

constrains the relationship between q and p,

$$\frac{q}{p} = \sqrt{\frac{h_{21}}{h_{12}}} = \sqrt{\frac{M^*_{12} - \frac{i}{2}\Gamma^*_{12}}{M_{12} - \frac{i}{2}\Gamma_{12}}}. \tag{1.15}$$

The time evolution of the effective Hamiltonian states, $|\mathrm{X}_1\rangle$ and $|\mathrm{X}_2\rangle$, is given by

$$|\mathrm{X}_1(t)\rangle = |\mathrm{X}_1(0)\rangle e^{-i\lambda_1 t} = |\mathrm{X}_1(0)\rangle e^{-i\left(M_1 - \frac{i}{2}\Gamma_1\right)t} \tag{1.16a}$$

$$|\mathrm{X}_2(t)\rangle = |\mathrm{X}_2(0)\rangle e^{-i\lambda_2 t} = |\mathrm{X}_2(0)\rangle e^{-i\left(M_2 - \frac{i}{2}\Gamma_2\right)t}, \tag{1.16b}$$

Re-arranging the energy eigenstates of equation 1.13 in terms of the flavour eigenstates

$$|\mathrm{X}^0(t)\rangle = \frac{1}{2p}\left(|\mathrm{X}_1(t)\rangle + |\mathrm{X}_2(t)\rangle\right) \tag{1.17a}$$

$$|\overline{\mathrm{X}}^0(t)\rangle = \frac{1}{2q}\left(|\mathrm{X}_1(t)\rangle - |\mathrm{X}_2(t)\rangle\right) \tag{1.17b}$$

and substituting equation 1.16, yields

$$|\mathrm{X}^0(t)\rangle = g_+(t)|\mathrm{X}^0(0)\rangle + \frac{q}{p}g_-(t)|\overline{\mathrm{X}}^0(0)\rangle \tag{1.18a}$$

$$|\overline{\mathrm{X}}^0(t)\rangle = g_+(t)|\overline{\mathrm{X}}^0(0)\rangle + \frac{p}{q}g_-(t)|\mathrm{X}^0(0)\rangle \tag{1.18b}$$

where

$$g_\pm(t) = \frac{1}{2}\left[e^{-i(M_1-\frac{i}{2}\Gamma_1)t} \pm e^{-i(M_2-\frac{i}{2}\Gamma_2)t}\right]. \tag{1.18c}$$

Therefore a flavour eigenstate created at time $t = 0$ is, at a later time, a mixture of both flavour eigenstates. It follows from equation 1.18a that the probabilities of obtaining an $|\mathrm{X}^0\rangle$ and $|\overline{\mathrm{X}}^0\rangle$ state with a measurement at time t from an initially pure $|\mathrm{X}^0\rangle$ state are

$$P(\mathrm{X}^0 \to \mathrm{X}^0 : t) = \left|\left\langle \mathrm{X}^0 \,\middle|\, \mathrm{X}^0(t)\right\rangle\right|^2 = |g_+|^2 \tag{1.19a}$$

$$P(\mathrm{X}^0 \to \overline{\mathrm{X}}^0 : t) = \left|\left\langle \overline{\mathrm{X}}^0 \,\middle|\, \mathrm{X}^0(t)\right\rangle\right|^2 = \left|\frac{q}{p}g_-\right|^2 \tag{1.19b}$$

where

$$|g_\pm|^2 = \frac{1}{4}\left[e^{-\Gamma_1 t} + e^{-\Gamma_2 t} \pm 2e^{-\overline{\Gamma}t}\cos(\Delta M t)\right] \tag{1.19c}$$

and

$$\overline{\Gamma} = \frac{\Gamma_1 + \Gamma_2}{2}. \tag{1.19d}$$

The last term in equation 1.19c describes the nature of the oscillations between the $|\mathrm{X}^0\rangle$ and $|\overline{\mathrm{X}}^0\rangle$ states. The so-called oscillation parameter,

$$x = \frac{\Delta M}{\overline{\Gamma}}, \tag{1.20}$$

characterises the magnitude of the oscillations. Since x is defined as the ratio of the oscillation and decay rates, a larger value of x corresponds to a greater probability of

oscillation before decay. This behaviour is illustrated in Figure 1.1 where the probabilities for obtaining an $|\mathrm{X}^0\rangle$ and an $|\overline{\mathrm{X}}^0\rangle$ are shown as a function of time. In constructing the figure it is assumed that $|q/p| = 1$, which is shown later to be an assumption that is equivalent to assuming $\mathcal{CP}$ conservation.

The mixing parameters chosen in the sub-figures of Figure 1.1 correspond to K^0- $\overline{\mathrm{K}}^0$ mixing, B^0_d- $\overline{\mathrm{B}}^0_\mathrm{d}$ mixing and B^0_s- $\overline{\mathrm{B}}^0_\mathrm{s}$ mixing. In the case of the neutral kaon mixing the difference in mass between the physical eigenstates, K^0_S and K^0_L, is very small ($|\Delta M_k| = (3.483 \pm 0.006) \times 10^{-15}$ GeV/c^2) [17]. However, the K^0_L and K^0_S have very different decay widths on account of the dominant $\mathrm{K}^0_\mathrm{S} \to \pi\,\pi$ decay and thus overall $\Gamma_S > \Gamma_L$ and $x \approx 1$. In the neutral B-meson system the vast majority of final states are common to both B^0 and $\overline{\mathrm{B}}^0$ decays, and hence the decay widths of the physical eigenstates are approximately the same ($\Gamma_L \approx \Gamma_H$). Unlike the kaon system, the difference between the eigenstate masses is large,

$$\Delta M_d = (3.337 \pm 0.033) \times 10^{-10}\ \text{MeV}, \quad \Delta M_s > 94.8 \times 10^{-10}\ \text{MeV (95\% cl)} \tag{1.21}$$

The oscillation parameters are $x_d = 0.776 \pm 0.008$ and $x_s = 25.5 \pm 0.6$ [17]; the corresponding oscillation behaviours are shown in Figures 1.1(b) and 1.1(c) respectively.

1.1.2 $\mathcal{CP}$-violation Mechanisms

The time dependent amplitudes for neutral mesons X^0 and $\overline{\mathrm{X}}^0$ to decay into the same final state f are

$$A(\mathrm{X}^0(t) \to f) = \left\langle f \,\middle|\, H_\text{eff} \,\middle|\, \mathrm{X}^0(t) \right\rangle = g_+(t)A_f + \frac{q}{p} g_-(t)\overline{A}_f \tag{1.22a}$$

$$A(\overline{\mathrm{X}}^0(t) \to f) = \left\langle f \,\middle|\, H_\text{eff} \,\middle|\, \overline{\mathrm{X}}^0(t) \right\rangle = g_+(t)\overline{A}_f + \frac{p}{q} g_-(t)A_f, \tag{1.22b}$$

where $g_\pm$ are given by equation 1.18c and the instantaneous decay amplitudes from X^0 and $\overline{\mathrm{X}}^0$ to final state f are

$$A_f \equiv A(\mathrm{X}^0 \to f) = \left\langle f \,\middle|\, H_\text{eff} \,\middle|\, \mathrm{X}^0 \right\rangle, \quad \overline{A}_f \equiv A(\overline{\mathrm{X}}^0 \to f) = \left\langle f \,\middle|\, H_\text{eff} \,\middle|\, \overline{\mathrm{X}}^0 \right\rangle. \tag{1.23}$$

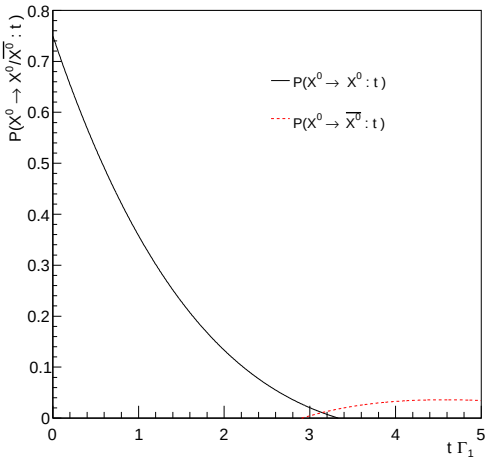

(a) $\Gamma_1 > \Gamma_2, x = 1$

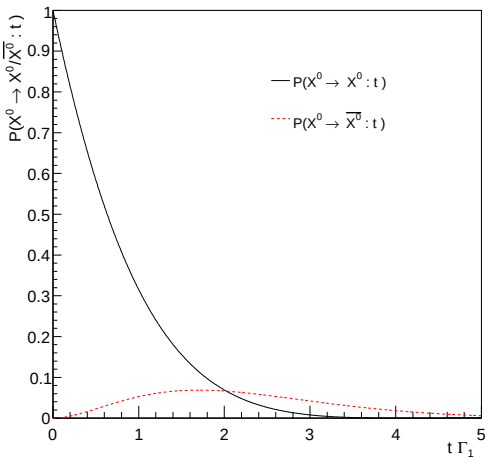

(b) $\Gamma_1 = \Gamma_2, x = 0.776$

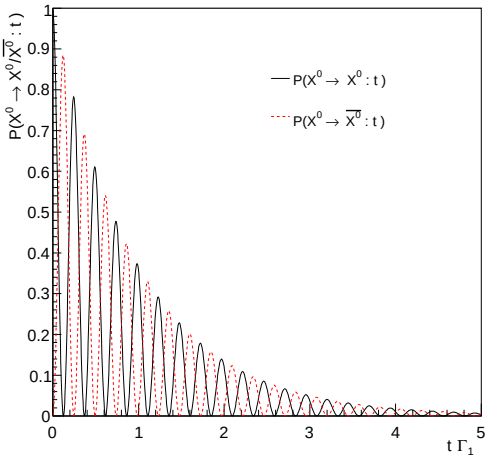

(c) $\Gamma_1 = \Gamma_2, x = 25.5$

Figure 1.1: Probability for finding a $|\mathrm{X}^0\rangle$ (solid line) and a $|\overline{\mathrm{X}}^0\rangle$ (dashed line) with a measurement at time $\Gamma_1 t$ from an initially pure $|\mathrm{X}^0\rangle$ state. The mixing parameters correspond approximately to (a) K^0- $\overline{\mathrm{K}}^0$ mixing, (b) B^0_d- $\overline{\mathrm{B}}^0_\mathrm{d}$ mixing and (c) B^0_s- $\overline{\mathrm{B}}^0_\mathrm{s}$ mixing.

The corresponding decay rates are

$$\begin{aligned}\Gamma_f(t) &\equiv \Gamma(\mathrm{X}^0(t) \to f) \qquad (1.24a)\\ &= |A_f|^2 \left\{ |g_+(t)|^2 + \left(\frac{q}{p}\frac{\overline{A}_f}{A_f}\right)^2 |g_-(t)|^2 + 2\mathsf{Re}\left[\frac{q}{p}\frac{\overline{A}_f}{A_f} g_+^*(t) g_-(t)\right]\right\},\\ \overline{\Gamma}_f(t) &\equiv \Gamma(\overline{\mathrm{X}}^0(t) \to f) \qquad (1.24b)\\ &= |A_f|^2 \left\{ \left|\frac{\overline{A}_f}{A_f}\right|^2 |g_+(t)|^2 + \left(\frac{p}{q}\right)^2 |g_-(t)|^2 + 2\left(\frac{p}{q}\right)^2 \mathsf{Re}\left[\left(\frac{q}{p}\frac{\overline{A}_f}{A_f}\right)^* g_+^*(t) g_-(t)\right]\right\}.\end{aligned}$$

The following sections will seek to demonstrate that violation of $\mathcal{CP}$ invariance in the decay of mesons leads to

1. $\left|\frac{p}{q}\right| \neq 1 \quad \Leftrightarrow \quad \mathcal{CP}$-violation in the mixing,
2. $\left|\overline{A}_f\right| \neq |A_f| \quad \Leftrightarrow \quad \mathcal{CP}$-violation in the decay, and
3. $\mathsf{Im}\left\{\frac{q}{p}\frac{\overline{A}_f}{A_f}\right\} \neq 0, \left|\frac{q}{p}\frac{\overline{A}_f}{A_f}\right| = 1 \quad \Leftrightarrow \quad \not{\mathcal{CP}}$ in the interference between decay and mixing,

which, when compared with equation 1.24a and 1.24b, will result in a difference between the decay rates of Γ_f and $\overline{\Gamma}_f(t)$. Hence, measurement of a decay rate asymmetry provides clear evidence for $\mathcal{CP}$-violation in the decay of mesons.

1.1.3 $\mathcal{CP}$-violation in meson mixing

Recalling from equation 1.8 that the effective Hamiltonian is a function of the mass and decay matrices and using second-order perturbation theory, it can be shown that the two matrices are given by sums over intermediate states $|n\rangle$ [16, 13];

$$M_{ij} = m_{\mathrm{X}}\delta_{ij} + \langle i \,|\, \mathrm{H_W} \,|\, j\rangle + \sum_n \mathcal{P}\left(\frac{\langle i \,|\, \mathrm{H_W} \,|\, n\rangle \langle n \,|\, \mathrm{H_W} \,|\, j\rangle}{m_{\mathrm{X}^0} - E_n}\right), \qquad (1.25)$$

$$\Gamma_{ij} = 2\pi \sum_n \delta(m_{\mathrm{X}} - E_n) \langle i \,|\, \mathrm{H_W} \,|\, n\rangle \langle n \,|\, \mathrm{H_W} \,|\, j\rangle \qquad (1.26)$$

where $\mathrm{H_W}$ is the weak Hamiltonian, $i, j = 1, 2$ correspond to X^0 and $\overline{\mathrm{X}}^0$ respectively and $\mathcal{P}$ is the Cauchy's projection value.[1]. The Kronecker delta distribution $\delta(m_X - E)$ in Γ_{ij} ensures energy conservation and therefore X^0 and $\overline{\mathrm{X}}^0$ may decay only to physical

[1] Defined as $\mathcal{P}\left(\int_a^b f(x)dx\right) = \lim_{\epsilon\to 0^+}\left[\int_a^{c-\epsilon} f(x)dx + \int_{c+\epsilon}^b f(x)dx\right]$

on-mass-shell states. No such condition appears in equation 1.25, such that the states are virtual (off-mass-shell) and the sum must be taken over all possible intermediate states. The density of states, ρ_n, is defined as

$$\rho_n = \sum_n \delta(m_{\mathrm{X}} - E_n), \tag{1.27}$$

whereby equation 1.26 can be expressed as,

$$\Gamma_{ij} = \sum_n \rho_n \langle i \,|\, \mathrm{H_W} \,|\, n \rangle \langle n \,|\, \mathrm{H_W} \,|\, j \rangle . \tag{1.28}$$

The conditions on the matrix elements M and Γ for CP-invariance can be derived by considering the effect of $\mathcal{CP}$ transformations in equations 1.25 and 1.26.

The $\mathcal{CP}$ transformation interchanges X^0 and $\overline{\mathrm{X}}^0$,

$$\mathcal{CP}|\mathrm{X}^0\rangle = e^{i\xi}|\overline{\mathrm{X}}^0\rangle, \quad \mathcal{CP}|\overline{\mathrm{X}}^0\rangle = e^{-i\xi}|\mathrm{X}^0\rangle, \tag{1.29}$$

where ξ is an arbitrary phase. Consider the matrix element Γ_{21},

$$\Gamma_{21} = \rho_n \left\langle \overline{\mathrm{X}}^0 \,\middle|\, \mathrm{H_W} \,\middle|\, n \right\rangle \left\langle n \,\middle|\, \mathrm{H_W} \,\middle|\, \mathrm{X}^0 \right\rangle . \tag{1.30}$$

If $\mathrm{H_W}$ is invariant under $\mathcal{CP}$, $\mathrm{H_W} = \mathcal{CP}^{-1}\,\mathrm{H_W}\,\mathcal{CP}$, whereby

$$\begin{aligned} \Gamma_{21} &= \rho_n \left\langle \overline{\mathrm{X}}^0 \,\middle|\, \mathcal{CP}^\dagger\,\mathrm{H_W}\,\mathcal{CP} \,\middle|\, n \right\rangle \left\langle n \,\middle|\, \mathcal{CP}^\dagger\,\mathrm{H_W}\,\mathcal{CP} \,\middle|\, \mathrm{X}^0 \right\rangle \\ &= \rho_n \left\langle \mathrm{X}^0 \,\middle|\, \mathrm{H_W} \,\middle|\, n \right\rangle \left\langle n \,\middle|\, \mathrm{H_W} \,\middle|\, \overline{\mathrm{X}}^0 \right\rangle e^{2i\xi} \\ &= \Gamma_{12} e^{2i\xi} \end{aligned} \tag{1.31}$$

Following a similar procedure it can be shown that [13]

$$M_{21} = M_{12} e^{2i\xi} \tag{1.32}$$

and, using the fact that both M and Γ are Hermitian,

$$M_{12}^* = M_{12} e^{2i\xi} \quad \text{and} \quad \Gamma_{12}^* = \Gamma_{12} e^{2i\xi}. \tag{1.33}$$

Substituting equations 1.33 into equation 1.15, leads to the following condition for $\mathcal{CP}$

invariance in the mixing of neutral mesons:

$$\left|\frac{q}{p}\right| = 1 \iff \mathrm{H}_{\mathrm{W}}^{\mathcal{CP}} = \mathrm{H}_{\mathrm{W}}. \tag{1.34}$$

If this condition holds, the physical (mass) eigenstates of equation 1.13 can be expressed as [2]

$$|X_1\rangle = \frac{1}{\sqrt{2}}\left(|\mathrm{X}^0\rangle + |\overline{\mathrm{X}}^0\rangle\right), \tag{1.35a}$$

$$|X_2\rangle = \frac{1}{\sqrt{2}}\left(|\mathrm{X}^0\rangle - |\overline{\mathrm{X}}^0\rangle\right). \tag{1.35b}$$

In which case the physical eigenstates are also eigenstates of $\mathcal{CP}$. Violation of the condition stated in equation 1.34 is called $\mathcal{CP}$ violation in the mixing, as it physically corresponds to a difference in the mixing rates between $\mathrm{X}^0 \to \overline{\mathrm{X}}^0$ and $\overline{\mathrm{X}}^0 \to \mathrm{X}^0$.

$\mathcal{CP}$-violation in the mixing has been measured in the K^0 semi-leptonic decay asymmetry [17],

$$\mathcal{A}_{\mathrm{sl}}^{\mathrm{K}^0} = \frac{\Gamma(\mathrm{K}_{\mathrm{L}}^0 \to \pi^- \ell^+ \nu) - \Gamma(\mathrm{K}_{\mathrm{L}}^0 \to \pi^+ \ell^- \nu)}{\Gamma(\mathrm{K}_{\mathrm{L}}^0 \to \pi^- \ell^+ \nu) + \Gamma(\mathrm{K}_{\mathrm{L}}^0 \to \pi^+ \ell^- \nu)} = 0.332 \pm 0.006. \tag{1.36}$$

A semi-leptonic decay asymmetry can also be measured in neutral B-meson decays,

$$\mathcal{A}_{\mathrm{sl}}^{\mathrm{B}^0} = \frac{\Gamma(\overline{\mathrm{B}}^0 \to \ell^- \nu X) - \Gamma(\mathrm{B}^0 \to \ell^+ \nu X)}{\Gamma(\overline{\mathrm{B}}^0 \to \ell^- \nu X) + \Gamma(\mathrm{B}^0 \to \ell^+ \nu X)} = \frac{1 - |q/p|^4}{1 + |q/p|^4}, \tag{1.37}$$

but as yet the experimental error in this measurement is an order of magnitude larger than the theoretical prediction of $\mathcal{A}_{\mathrm{sl}}^{\mathrm{B}_{\mathrm{d}}^0} = -(5.5 \pm 1.3) \times 10^{-4}$ [18]. The predicted asymmetry is orders of magnitude smaller than that measured in the kaon system. This can be attributed to the fact that $\mathcal{A}_{\mathrm{sl}} \lesssim \Delta\Gamma_{\mathrm{B}^0}/\Delta m_{\mathrm{B}^0}$ and since $\Delta\Gamma$ is $\mathcal{O}(10^{-3})$ for $\mathrm{B}_{\mathrm{d}}^0$ and $\mathcal{O}(10^{-5})$ for $\mathrm{B}_{\mathrm{s}}^0$, and thereby to the expectation that indirect $\mathcal{CP}$-violation in B-mesons will be a very small effect [19, 20].

[2] where the arbitrary phase is taken to be zero.

1.1.4 $\mathcal{CP}$-violation in the decay

The time dependent decay amplitudes representing $\mathrm{X}^0 \to f$ and $\overline{\mathrm{X}}^0 \to \bar{f}$, A_f and $\overline{A}_{\bar{f}}$, are defined as

$$A_f = \left\langle f \left| H_{\text{eff}} \right| \mathrm{X}^0 \right\rangle, \quad \text{and} \quad \overline{A}_{\bar{f}} = \left\langle \bar{f} \left| H_{\text{eff}} \right| \overline{\mathrm{X}}^0 \right\rangle \tag{1.38}$$

where f and $\bar{f}$ are the final states of the X^0 and $\overline{\mathrm{X}}^0$ decays respectively. The effect of $\mathcal{CP}$ transformations on the final states $|f\rangle$ and $|\bar{f}\rangle$ are

$$\mathcal{CP}|f\rangle = e^{i\xi_f}|\bar{f}\rangle, \quad \text{and} \quad \mathcal{CP}|\bar{f}\rangle = e^{-i\xi_f}|f\rangle, \tag{1.39}$$

where ξ_f is an arbitrarily defined phase. If H_{eff} is invariant under $\mathcal{CP}$ transformations,

$$H_{\text{eff}} = \mathcal{CP}^{-1} H_{\text{eff}} \mathcal{CP}, \tag{1.40}$$

which leads to the following relationship between $\overline{A}_{\bar{f}}$ and A_f,

$$\begin{aligned} \overline{A}_{\bar{f}} &= \left\langle \bar{f} \left| \mathcal{CP}^\dagger H_{\text{eff}} \mathcal{CP} \right| \overline{\mathrm{X}}^0 \right\rangle \\ &= e^{i(\xi_f - \xi)} \left\langle f \left| H_{\text{eff}} \right| \mathrm{X}^0 \right\rangle \\ &= e^{i(\xi_f - \xi)} A_f. \end{aligned} \tag{1.41a}$$

Following the same procedure it can be shown that the decay amplitudes for $\mathrm{X}^0 \to \bar{f}$ and $\overline{\mathrm{X}}^0 \to \bar{f}$, $A_{\bar{f}}$ and $\overline{A}_f$, are related by the condition,

$$A_{\bar{f}} = e^{i(\xi_f + \xi)} \overline{A}_f. \tag{1.41b}$$

It follows from equations 1.41a and 1.41b that if $\mathcal{CP}$ is invariant in the decay of neutral mesons :

$$\left.\begin{aligned} |A_f| &= |\overline{A}_{\bar{f}}|, \\ |A_{\bar{f}}| &= |\overline{A}_f|. \end{aligned}\right\} \quad \Longleftrightarrow \quad H_{\text{eff}} = \mathcal{CP}^{-1} H_{\text{eff}} \mathcal{CP} \tag{1.42}$$

Violation of this condition is called $\mathcal{CP}$-violation in the decay and is often referred to as *direct* $\mathcal{CP}$-violation. This is an additional requirement for $\mathcal{CP}$ invariance in the decay of neutral mesons in addition to that stated in equation 1.34. However, unlike $\mathcal{CP}$-violation in the mixing, the argument presented can be equally applied to charged mesons and b-baryons. The case of direct $\mathcal{CP}$-violation in the decay $\Lambda_{\mathrm{b}} \to \mathrm{p}\,\pi/\mathrm{K}$ is explained in

detail in section 1.4.

In order to incorporate this model independent description of $\mathcal{CP}$-violation into the Standard Model (see section 1.2), it is useful to write the decay amplitude of each contribution to A_f and $\overline{A}_{\bar{f}}$ in terms of its magnitude A_i and two phases terms, $e^{i\phi}$ and $e^{i\delta}$. If several amplitudes contribute to A_f and $\overline{A}_{\bar{f}}$, then

$$A_f = \sum_i A_i e^{i(\delta_i+\phi_i)} \quad \text{and} \quad \overline{A}_{\bar{f}} = \sum_i A_i e^{i(\delta_i-\phi_i)}. \tag{1.43}$$

A complex parameter in a Lagrangian will appear in complex conjugate form in $\mathcal{CP}$-conjugate amplitude. As the phase ϕ appears with opposite sign in A_f and $\overline{A}_{\bar{f}}$ it therefore derives from a complex parameter. In the Standard Model these phases only occur in the CKM matrix of the quark mixing model and hence ϕ is called the *weak phase*. The δ phase has the same sign in A_f and $\overline{A}_{\bar{f}}$ and can thus arise from a real Lagragain, and originates from the final state interactions which are dominated by strong interactions and is thus termed the *strong phase*.

If a meson or baryon can decay by at least two different decay mechanisms with different weak and strong phases, then the interference between the amplitudes results in

$$\left|\frac{\overline{A}_{\bar{f}}}{A_f}\right| = \left|\frac{\sum_j A_j e^{i(\delta_j+\phi_j)}}{\sum_i A_i e^{i(\delta_i-\phi_i)}}\right| \neq 1 \tag{1.44}$$

and corresponds to $\mathcal{CP}$ violation in the decay. A measurement of the asymmetry

$$\mathcal{A}_{\pm} = \frac{\Gamma(\mathrm{X}^+ \to f^+) - \Gamma(\mathrm{X}^- \to f^-)}{\Gamma(\mathrm{X}^+ \to f^+) + \Gamma(\mathrm{X}^- \to f^-)} = \frac{1 - |\overline{A}_{f^-}/A_{f^+}|^2}{1 + |\overline{A}_{f^-}/A_{f^+}|^2} \tag{1.45}$$

in charged B-mesons and Λ_b decays is entirely due to $\mathcal{CP}$-violation in the decay. However, extraction of the weak phase from such a measurement requires theoretical calculation of the magnitude and strong phase of each amplitude. This is technically difficult as it involves long distance strong interaction physics. Direct $\mathcal{CP}$-violation has been observed in the neutral kaon system and in the B-system via $\mathrm{B}^0_\mathrm{d} \to \mathrm{K}\,\pi$ decays

$$\mathcal{A}_{\mathrm{B}^0_\mathrm{d}\to\mathrm{K}\,\pi} = \frac{\Gamma(\mathrm{B}^0_\mathrm{d} \to \mathrm{K}^+\,\pi^-) - \Gamma(\overline{\mathrm{B}}^0_\mathrm{d} \to \mathrm{K}^-\,\pi^+)}{\Gamma(\mathrm{B}^0_\mathrm{d} \to \mathrm{K}^+\,\pi^-) + \Gamma(\overline{\mathrm{B}}^0_\mathrm{d} \to \mathrm{K}^-\,\pi^+)} \tag{1.46}$$

$$= -0.107 \pm 0.020 \tag{1.47}$$

which was first measured in 2004 by the *BABAR* and Belle collaborations [17, 21, 22] .

1.1.5 Mixing induced $\mathcal{CP}$-violation

A third condition for $\mathcal{CP}$ invariance in the decay of neutral B-mesons can be derived from a combination of the conditions for $\mathcal{CP}$ invariance in the mixing and decay.

If $\mathcal{CP}$ is conserved in the mixing, then from equations 1.15 and 1.33 it follows that

$$\frac{q^2}{p^2} = e^{2i\xi} \quad \Longleftrightarrow \quad \mathrm{H}_{\mathrm{W}}^{\mathcal{CP}} = \mathrm{H}_{\mathrm{W}}. \tag{1.48}$$

If $\mathcal{CP}$ is conserved in the decay amplitudes, combining equations 1.41a and 1.41b

$$A_f A_{\bar{f}} = e^{2i\xi}\overline{A}_{\bar{f}}\overline{A}_f \quad \Longleftrightarrow \quad H_{\mathrm{eff}}^{\mathcal{CP}} = H_{\mathrm{eff}}. \tag{1.49}$$

Combining equations 1.48 and 1.49 leads to an additional condition for $\mathcal{CP}$ conservation,

$$\mathsf{arg}\left(\frac{p^2}{q^2}A_f\overline{A}_f^* A_{\bar{f}}\overline{A}_{\bar{f}}^*\right) = 0 \quad \Longleftrightarrow \quad H_{\mathrm{eff}}^{\mathcal{CP}} = H_{\mathrm{eff}}. \tag{1.50}$$

If $\mathcal{CP}$ is conserved, the complex parameter,

$$\lambda_f \equiv \frac{q}{p}\frac{\overline{A}_f}{A_f}, \tag{1.51}$$

satisfies the condition

$$\lambda_f = \frac{1}{\lambda_{\bar{f}}} \quad \Longleftrightarrow \quad H_{\mathrm{eff}}^{\mathcal{CP}} = H_{\mathrm{eff}} \tag{1.52}$$

where the moduli are equal because of equations 1.34 and 1.42 and the phases are equal on account of equation 1.50. If $\mathcal{CP}$ is neither violated directly nor indirectly, then

$$|\lambda_f| = \frac{1}{|\lambda_{\bar{f}}|}. \tag{1.53}$$

However, $\mathcal{CP}$ violation may still be present if

$$\mathsf{arg}(\lambda_f) + \mathsf{arg}(\lambda_{\bar{f}}) \neq 0. \tag{1.54}$$

Since this condition arises from the interference of the mixing and decay amplitude

phases, it is called $\mathcal{CP}$-violation in the *interference between the mixing and decay amplitudes*.

Experimentally it is interesting to measure the asymmetry of neutral B-meson decays to $\mathcal{CP}$ eigenstates, since it is possible to extract the weak phases of such decays in a theoretically clean manner. For the case of decay to $\mathcal{CP}$ eigenstates ($f = \bar{f}$), it follows from equation 1.54 that

$$\mathsf{Im}\lambda_f \neq 0 \tag{1.55}$$

if there is $\mathcal{CP}$ violation in the interference between the mixing and decay amplitudes. To calculate the observed asymmetry, it is useful to first re-express the time time-dependent decay rates $\Gamma_f(t)$ and $\overline{\Gamma}_f(t)$, given by equations 1.24a and 1.24b, as

$$\Gamma_f(t) = \frac{|A_f|^2}{2} e^{-\overline{\Gamma}t} \left[I_+(t) + I_-(t)\right] \tag{1.56}$$

$$\overline{\Gamma}_f(t) = \frac{|\overline{A}_f|^2}{2|\lambda_f|^2} e^{-\overline{\Gamma}t} \left[I_+(t) - I_-(t)\right], \tag{1.57}$$

where the interference terms, $I \pm (t)$ are

$$I_+(t) = (1 + |\lambda_f|^2)\cosh\left(\frac{\Delta\Gamma t}{2}\right) - 2\mathsf{Re}(\lambda_f)\sinh\left(\frac{\Delta\Gamma t}{2}\right), \tag{1.58}$$

$$I_-(t) = (1 - |\lambda_f|^2)\cos(\Delta M t) + 2\mathsf{Im}(\lambda_f)\sin(\Delta M t). \tag{1.59}$$

The time dependent $\mathcal{CP}$ asymmetry $\mathcal{A}_{\mathcal{CP}}(t)$ can be expressed in terms of λ_f as,

$$\begin{aligned}\mathcal{A}_{\mathcal{CP}}(t) &= \frac{\Gamma_f - \overline{\Gamma}_f}{\Gamma_f + \overline{\Gamma}_f} \\ &= \frac{(1 - |\lambda_f|^2\cos(\Delta M t) + 2\ \mathsf{Im}(\lambda_f)\sin(\Delta M t)}{(1 + |\lambda_f|^2)\cosh(\frac{\Delta\Gamma t}{2}) + 2\ \mathsf{Re}(\lambda_f)\sinh(\frac{\Delta\Gamma t}{2})}.\end{aligned} \tag{1.60}$$

Alternatively, $\mathcal{A}_{\mathcal{CP}}$ can be expressed in terms of the direct $\mathcal{CP}$ violating contribution, $\mathcal{A}^{\mathrm{dir}}_{\mathcal{CP}}$, and that corresponding to $\mathcal{CP}$ violation in the interference between the mixing and decay amplitudes, $\mathcal{A}^{\mathrm{mix}}_{\mathcal{CP}}$,

$$\mathcal{A}_{\mathcal{CP}}(t) = \mathcal{A}^{\mathrm{dir}}_{\mathcal{CP}}\cos(\Delta M t) + \mathcal{A}^{\mathrm{mix}}_{\mathcal{CP}}\sin(\Delta M t). \tag{1.61}$$

In the B-mesons system $\Delta\Gamma$ is small, such that

$$\mathcal{A}_{\mathcal{CP}}^{\text{dir}} = \frac{1-|\lambda_f|^2}{1+|\lambda_f|^2} \quad \text{and} \quad \mathcal{A}_{\mathcal{CP}}^{\text{mix}} = \frac{2\,\mathsf{Im}(\lambda_f)}{1+|\lambda_f|^2}. \tag{1.62}$$

In the specific case of decay to $\mathcal{CP}$ eigenstates, $|\lambda_f| = 1$ and the decay is dominated by a single weak phase. In this case,

$$\begin{aligned} \mathcal{A}_{\mathcal{CP}}(t) &= \mathcal{A}_{\mathcal{CP}}^{\text{mix}} \sin(\Delta M t) \\ &= \mathsf{Im}(\lambda_f) \sin(\Delta M t), \end{aligned} \tag{1.63}$$

where $\mathsf{Im}(\lambda_f)$ is the phase difference between the mixing phase and the phase of the decay amplitude, and can be interpreted in terms of purely electroweak parameters. $\mathcal{CP}$-violation in the interference of the mixing and decay amplitudes has been observed in the K^0 decays, where it is found to have approximately the same magnitude as $\mathcal{CP}$-violation in the mixing [23]. In the B-system $\mathcal{CP}$-violation in the interference was first measured in $\mathrm{B}^0_{\mathrm{d}} \to \mathrm{J}/\psi\,\mathrm{K}^0_{\mathrm{S}}$ decays in 2001 by the *BABAR* and Belle collaborations [24, 25].

1.2 $\mathcal{CP}$-violation and Mixing in the Standard Model

This section will describe the source of $\mathcal{CP}$-violation in the Standard Model, which is found to be intrinsically connected to many of the unanswered questions; such as the origin of mass, the number of fermion generations and the mass hierarchy of the fermions.

1.2.1 Flavour Physics in the Standard Model

The interactions of the Standard Model arise from the requirement that the theory is invariant under local gauge transformations. Since an explicit mass term will violate this symmetry, the gauge bosons and fermions are implicitly massless. Before Spontaneous Symmetry Breaking (SSB) of the electroweak group, the Lagrangians that describe the Standard Model interactions are all invariant under $\mathcal{CP}$ transformations. However, after SSB the fermions and gauge bosons aquire a mass term through their coupling to the scalar Higgs field and it is these couplings that are the only source of $\mathcal{CP}$-violation in the Standard Model.

The interaction between the quarks and the scalar Higgs field in the Standard Model

before SSB of the electroweak group are given by the Yukawa Lagrangian,

$$-\mathcal{L}_{\text{Yukawa}} = Y^d_{ij}\overline{Q^I_{Li}}\phi d^I_{Rj} + Y^u_{ij}\overline{Q^I_{Li}}\tilde{\phi}u^I_{Rj} + \text{h.c.}, \tag{1.64}$$

where i,j are the generation labels, Q^I_{Li} represents the SU(2)$_L$ quark doublet and ϕ represents the Higgs doublet (ϕ^+, ϕ^0). Y^u_{ij} and Y^d_{ij} are arbitrary *complex* matrices [19, 26]. The mass terms arise from the scalar Higgs field acquiring a vacuum expectation value, $\mathsf{Re}(\phi^+) \rightarrow \frac{1}{\sqrt{2}}(v + H^0)$, which spontaneously breaks the gauge invariance and produces the mass terms

$$-\mathcal{L}_M = (M_d)_{ij}\overline{d^I_{Li}}d^I_{Rj} + (M_u)_{ij}\overline{u^I_{Li}}u^I_{Rj} + \text{h.c.} \tag{1.65}$$

where the mass matrices are given by

$$(M_d)_{ij} = \frac{v}{\sqrt{2}}(Y^d)_{ij}, \quad \text{and} \quad (M_u)_{ij} = \frac{v}{\sqrt{2}}(Y^u)_{ij}. \tag{1.66}$$

It is apparent from equation 1.65 that in the flavour eigenbasis there are couplings between generations. The physical particles are therefore defined as those states which diagonalise the mass matrix and as such are not superpositions of different Yukawa couplings. Any complex matrix can be diagonalised by two *unitary* matrices, such that

$$M_d^{\text{diag}} = V_{dL}M_dV^\dagger_{dR}, \quad M_u^{\text{diag}} = V_{uL}M_dV^\dagger_{uR} \tag{1.67}$$

where,

$$M_d^{\text{diag}} = \text{diag}(m_d, m_s, m_b, \dots), \quad M_u^{\text{diag}} = \text{diag}(m_u, m_c, m_t, \dots).$$

The mass eigenstates u_i and d_i are therefore defined as linear combinations of the corresponding weak (flavour) eigenstates u^I_i and d^I_i,

$$u_{Li} = (V_{uL})_{ij}u^I_{Lj}, \quad u_{Ri} = (V_{uR})_{ij}u^I_{Rj} \tag{1.68}$$

$$d_{Li} = (V_{dL})_{ij}d^I_{Lj}, \quad d_{Ri} = (V_{dR})_{ij}d^I_{Rj}. \tag{1.69}$$

Interaction of quarks with the charged SU(2)$_L$ gauge bosons $W^\pm$, referred to as charged current interactions, are in the flavour eigenbasis

$$-\mathcal{L}_{\text{CC}} = \frac{g}{\sqrt{2}}\overline{u^I_{Li}}\gamma^\mu d^I_{Lj}W^+_\mu + \text{h.c.} \tag{1.70}$$

which transforms to,

$$-\mathcal{L}_{\rm CC} = \frac{g}{\sqrt{2}}\overline{u_{Li}}\gamma^{\mu}\underbrace{(V_{uL}V_{dL}^{\dagger})_{ij}}_{\mathbf{V}_{\rm CKM}}d_{Lj}W_{\mu}^{+} + \text{h.c.} \tag{1.71}$$

in the mass eigenbasis. For three generations the mixing matrix $\mathbf{V}_{\rm CKM} = V_{uL}V_{dL}^{\dagger}$ is called the Cabibbo-Kobayashi-Maskawa (CKM) matrix and can be written explicitly as

$$\mathbf{V}_{\rm CKM} = \begin{pmatrix} V_{\rm ud} & V_{\rm us} & V_{\rm ub} \\ V_{\rm cd} & V_{\rm cs} & V_{\rm cb} \\ V_{\rm td} & V_{\rm ts} & V_{\rm tb} \end{pmatrix} \tag{1.72}$$

where V_{ij} is the matrix element that couples the ith up-type quark with the jth down-type quark [8]. Following from the fact that $\mathbf{V}_{\rm CKM}$ has off-diagonal terms, the $\mathrm{W}^{\pm}$ gauge bosons couple to quarks of different generations. This is the only source of *flavour changing* interactions in the Standard Model. In contrast, for the neutral Z^0 gauge boson, the mass matrices equivalent to equation 1.66 have no off-diagonal terms and hence there are no *flavour changing neutral currents*. The Standard Model does not predict the strength of these couplings, but it does require that $\mathbf{V}_{\rm CKM}$ is unitary;

$$\mathbf{V}_{\rm CKM}\mathbf{V}_{\rm CKM}{}^{\dagger} = 1, \tag{1.73}$$

since both V_{uL} and V_{dL} are unitary matrices. A general unitary matrix is characterised by $n \times n$ free parameters : $n(n-1)/2$ moduli and $n(n+1)/2$ phases. However, since redefining the phase differences between the quark fields has no effect on the diagonal mass matrix, $(2n-1)$ phase differences can be freely chosen, leaving $(n-1)(n-2)/2$ physically meaningful phases. The three dimensional CKM matrix therefore has 4 independent parameters; three are taken as mixing angles between generations and one is a complex phase. It is this complex phase that is a feature of the Standard Model that enables $\mathcal{CP}$-violation to be incorporated. This derives from the fact that $\mathcal{CP}$ invariance of the charged current Lagrangian, $(\mathcal{CP})\mathcal{L}_{\rm CC}\mathcal{CP}^{-1} = \mathcal{L}_{\rm CC}$, requires that $V_{ij} = V_{ij}^{*}$. The single complex phase enables this condition to be violated. However, violation of this condition alone is not sufficient for $\mathcal{CP}$-violation. If two quarks of the same charge also have the same mass, field re-definitions can be used to rotate away the one complex phase. Therefore $\mathcal{CP}$-violation requires that

$$(m_t^2 - m_c^2)(m_t^2 - m_u^2)(m_c^2 - m_u^2)(m_b^2 - m_s^2)(m_b^2 - m_d^2)(m_s^2 - m_d^2) \neq 0. \tag{1.74}$$

Furthermore, the phase could be removed if any one of the three mixing angles is 0 or $\pi/2$ and $\mathcal{CP}$-violation would not occur if the phase were either 0 or π. These conditions are encapsulated in the Jarlskog parameter, $J_{\mathcal{CP}}$,

$$\mathsf{Im}[V_{ij}V_{kl}V_{il}^{*}V_{kj}^{*}] = J_{\mathcal{CP}} \sum_{m,n=1}^{3} \epsilon_{ikm}\epsilon_{jln}, \tag{1.75}$$

which is required to be non-zero for any choice of $i, j, k, l = 1, 2, 3$ for $\mathcal{CP}$-violation to occur in the Standard model [27]. The angle and phase conditions expressed in the Jarlskog parameter can be combined with the mass condition stated in equation 1.74 into a single requirement for $\mathcal{CP}$-violation in the Standard Model,

$$\mathsf{Im}(\det[M_d M_d^{\dagger}, M_u M_u]) \neq 0 \quad \Leftrightarrow \quad \mathcal{CP} - \text{violation} \tag{1.76}$$

where the mass matrices M_d and M_u are given by equation 1.66. It is interesting to note that $\mathcal{CP}$-violation in the Standard Model would not occur if there were only two fermion generations; the only free parameter in this case is a single mixing angle. Furthermore, $\mathcal{CP}$-violation would not occur if there were not a hierarchy in the quark masses. However, neither the number of fermion generations nor the hierarchy of masses is explained in the Standard Model. Hence, the origin of $\mathcal{CP}$-violation in the Standard Model is intrinsically linked to many of the open questions in particle physics.

1.2.2 Parametrisation of the CKM matrix

It is useful to parameterise the CKM matrix in terms of the four independent parameters, which are fundamental parameters of the Standard Model, as this facilitates the formulation of a framework in which to experimentally look for violations of unitarity in the three generation theory. The standard parametrisation is formulated in terms of the three angles θ_{12}, θ_{13}, and θ_{23}, and the complex phase δ_{KM}:

$$\mathbf{V}_{\mathrm{CKM}} = \begin{pmatrix} c_{12}c_{13} & s_{12}c_{13} & s_{13}e^{-i\delta_{\mathrm{KM}}} \\ -s_{12}c_{23} - c_{12}s_{23}s_{13}e^{i\delta_{\mathrm{KM}}} & c_{12}c_{23} - s_{12}s_{23}s_{13}e^{i\delta_{\mathrm{KM}}} & s_{23}c_{13} \\ s_{12}s_{23} - c_{12}c_{23}s_{13}e^{i\delta_{\mathrm{KM}}} & -c_{12}s_{23} - s_{12}c_{23}s_{13}e^{i\delta_{\mathrm{KM}}} & c_{23}c_{13} \end{pmatrix} \tag{1.77}$$

where $c_{ij} \equiv \cos(\theta_{ij})$ and $s_{ij} \equiv \sin(\theta_{ij})$. Experimentally it is found that the magnitude of the CKM matrix elements follow a clear structure. In terms of $\lambda \equiv \sin(\theta_{12}) = 0.22$[3], the CKM matrix elements are of order ,

$$|\mathbf{V}_{\rm CKM}| \sim \begin{pmatrix} 1 & \lambda & \lambda^3 \\ \lambda & 1 & \lambda^2 \\ \lambda^3 & \lambda^2 & 1 \end{pmatrix}. \tag{1.78}$$

This motivated the parameterisation of the CKM matrix in terms of a power series of the parameter λ,

$$\mathbf{V}_{\rm CKM} = \begin{pmatrix} 1-\frac{1}{2}\lambda^2 & \lambda & A\lambda^3(\rho - i\eta) \\ -\lambda & 1-\frac{1}{2}\lambda^2 & A\lambda^2 \\ A\lambda^3(1-\rho-i\eta) & -A\lambda^2 & 1 \end{pmatrix} + \mathcal{O}(\lambda^4) \tag{1.79}$$

where the expansion parameters are,

$$A \equiv \frac{s_{23}}{s_{12}^2}, \quad \rho \equiv \frac{s_{13}\cos\delta}{s_{12}s_{23}} \quad \text{and} \quad \eta \equiv \frac{s_{13}\sin\delta}{s_{12}s_{23}} \tag{1.80}$$

This is known as the Wolfenstein parameterisation [28]. The parameterisation makes explicit the smallness of Standard Model $\mathcal{CP}$-violation, since the matrix only acquires an imaginary component at 3rd order in λ. In the LHC era, the experimental accuracy will be such that higher-order terms in the Wolfenstein expansion are required, in particular for the study of the $\mathrm{B_s^0}$-$\overline{\mathrm{B}}_\mathrm{s}^0$ mixing phase. Continuing the expansion to $\mathcal{O}(\lambda^5)$,

$$\mathbf{V}_{\rm CKM} = \begin{pmatrix} 1-\frac{1}{2}\lambda^2+\frac{1}{8}\lambda^4 & \lambda & A\lambda^3(\rho-i\eta) \\ -\lambda + A^2\lambda^5(\frac{1}{2}-\rho-i\eta) & 1-\frac{1}{2}\lambda^2+\frac{1}{8}\lambda^4(1-4A^2) & A\lambda^2 \\ A\lambda^3(1-\tilde{\rho}-i\tilde{\eta}) & -A\lambda^2 + A\lambda^4(\frac{1}{2}-\rho-i\eta) & 1+\frac{1}{2}A^2\lambda^4 \end{pmatrix} + \mathcal{O}(\lambda^6), \tag{1.81}$$

where $\tilde{\rho} = \rho(1-\lambda^2/2)$ and $\tilde{\eta} = \eta(1-\lambda^2/2)$. In terms of the standard and Wolfenstein parameterisations, the Jarlskog parameter (equation 1.75) can be expressed as,

$$J_{\mathcal{CP}} = s_{12}s_{13}s_{23}c_{12}c_{23}c_{13}\sin\delta_{\rm KM} = \lambda^6 A^2 \eta = \mathcal{O}(10^{-5}), \tag{1.82}$$

[3]Note the λ in the Wolfenstein parametrisation is not the same as the λ used earlier to parameterise $\mathcal{CP}$-violation in the interference of the mixing and decay amplitudes.

which shows explicitly that $\mathcal{CP}$-violation requires the mixing angles not to be 0 or $\pi/2$ and $\delta_{\rm KM}$ not to be equal to 0 or π. The fact that $J_{\mathcal{CP}}$ is so small means that $\mathcal{CP}$-violation is only a small effect in the Standard Model. However, the smallness of $\mathcal{CP}$-violation effects in the Standard Model is not because $\mathcal{CP}$-violation is an approximate symmetry of the Standard Model, but is a negligible effect on account of the smallness of flavour violation in the Standard Model. This will be discussed further in section 1.3.

1.2.3 The unitarity triangles

The Standard Model requirement that the CKM matrix is unitary can be expressed as a set of six normalisation conditions and the following six orthogonality conditions :

$$\begin{aligned}
V_{\rm ud}V_{\rm ub}^* &+ V_{\rm cd}V_{\rm cb}^* + V_{\rm td}V_{\rm tb}^* = 0, && (db)\\
V_{\rm us}V_{\rm ub}^* &+ V_{\rm cs}V_{\rm cb}^* + V_{\rm ts}V_{\rm tb}^* = 0, && (sb)\\
V_{\rm ud}V_{\rm us}^* &+ V_{\rm cd}V_{\rm cs}^* + V_{\rm td}V_{\rm ts}^* = 0, && (ds)\\
V_{\rm ud}V_{\rm td}^* &+ V_{\rm us}V_{\rm ts}^* + V_{\rm ub}V_{\rm tb}^* = 0, && (ut)\\
V_{\rm cd}V_{\rm td}^* &+ V_{\rm cs}V_{\rm ts}^* + V_{\rm cb}V_{\rm tb}^* = 0, && (ct)\\
V_{\rm ud}V_{\rm cd}^* &+ V_{\rm us}V_{\rm cs}^* + V_{\rm ub}V_{\rm cb}^* = 0. && (uc)
\end{aligned} \tag{1.83}$$

Since each orthogonality condition requires the sum of three complex numbers to be zero, each can be represented geometrically as a triangle in the complex plane. These are known as *unitarity triangles* and are illustrated in Figure 1.2. Each triangle has an area $J_{\mathcal{CP}}/2$, whereby the area of a triangle in the complex plane is a measure of $\mathcal{CP}$-violation in the Standard Model. As is seen in Figure 1.2, many of the triangles have particularly unequal sides. For example, the (ds) triangle, which is associated to the $\rm K^0$ system, has two long sides with little relative phase difference and therefore exhibits only small $\mathcal{CP}$ violating effects. However, decays related to the short side, which corresponds to low branching fractions, are expected to exhibit significant $\mathcal{CP}$-violation since this side has a large relative phase compared to the other sides. In contrast the triangles (db) and (ut), which are both related to observables in the decay of neutral B-mesons, have sides of the same length up to $\mathcal{O}(\lambda^3)$ in the Wolfenstein parameterisation and, as such, motivates the search for $\mathcal{CP}$-violation in the b-sector. Since the (db) triangle is the primary focus of the $\mathcal{CP}$-violation measurements it is often referred to as *the* unitary triangle.

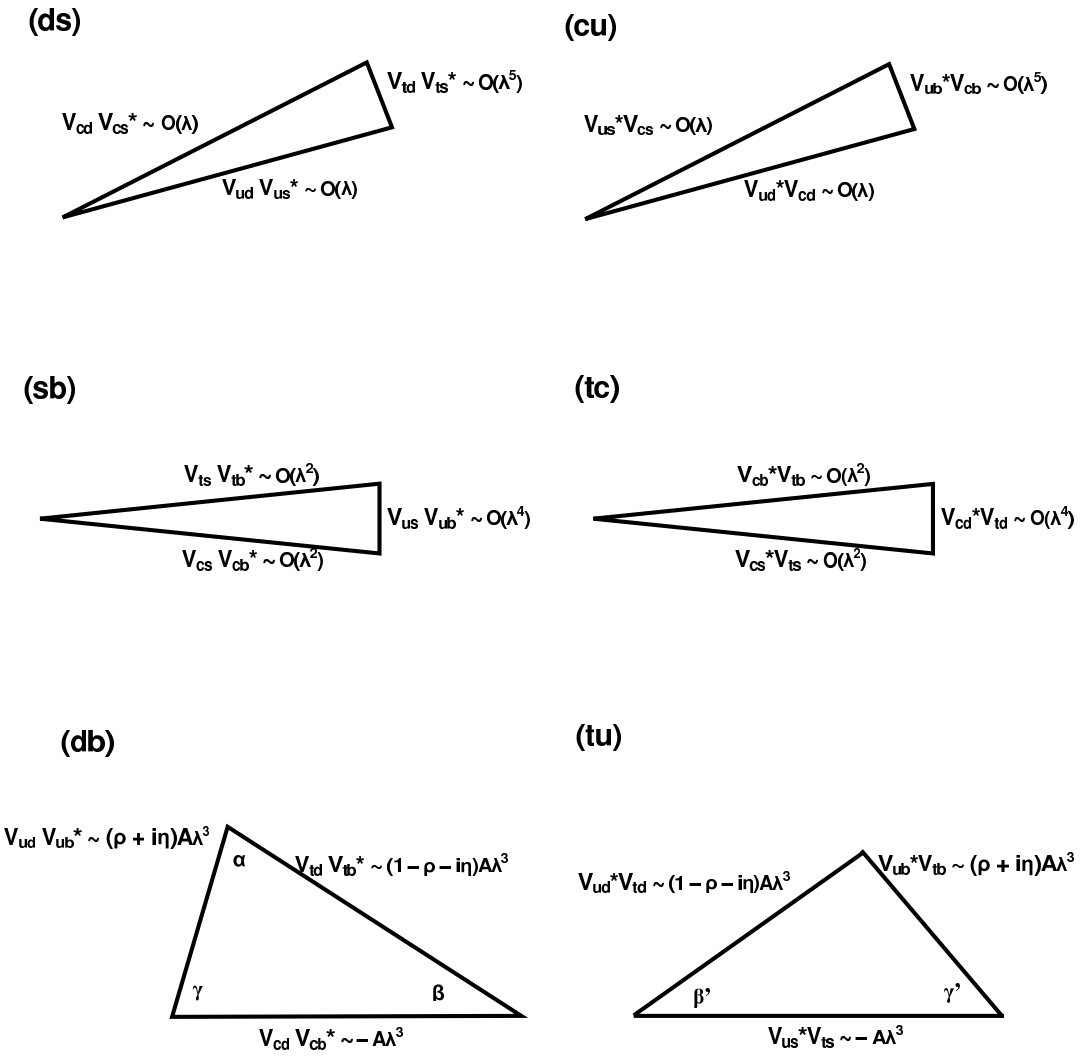

Figure 1.2: The six CKM unitarity triangles, labelled as in equation 1.83, showing the relative sizes of the triangles in terms of the leading order Wolfenstein parameterisation.

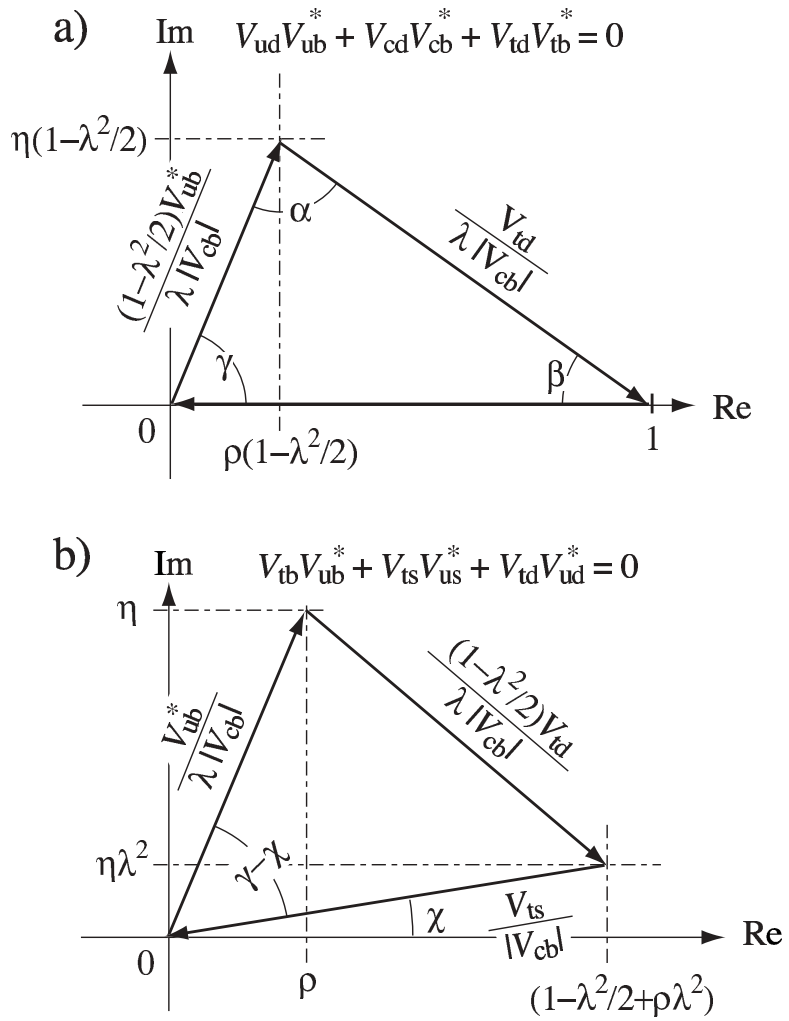

Figure 1.3: The two unitarity triangles corresponding to a) (db) and b) (ut) in equation 1.83. The phase convention is chosen such that the baseline of the (db) triangle, $V_{cd}\,V_{cb}^*$, is real and all lengths are normalised so that $|V_{cd}V_{cb}^*| = 1$.

Both the (db) and (ut) triangles are shown in Figure 1.3, with the phase convention chosen such that $V_{\rm cd}\,V_{\rm cb}^*$ is aligned along the real axis and all lengths are normalised to $|V_{cd}V_{cb}{}^*|$. The inner angles of the (db) unitarity triangle are defined as α, β and γ;

$$\alpha \equiv \arg\left[-\frac{V_{\rm td}V_{\rm tb}^*}{V_{\rm ud}V_{\rm ub}^*}\right], \quad \beta \equiv \arg\left[-\frac{V_{\rm cd}V_{\rm cb}^*}{V_{\rm td}V_{\rm tb}^*}\right], \quad \gamma \equiv \arg\left[-\frac{V_{\rm ud}V_{\rm ub}^*}{V_{\rm cd}V_{\rm cb}^*}\right]. \tag{1.84}$$

At $\mathcal{O}(\lambda^3)$ in the Wolfenstein parameterisation only $V_{\rm ub}$ and $V_{\rm td}$ are complex. However, at $\mathcal{O}(\lambda^5)$ a phase is introduced into $V_{\rm ts}$ such that the angles β and γ and the angles β' and γ' in the (ut) triangle,

$$\beta' \equiv \arg\left(-\frac{V_{\rm ts}V_{\rm us}^*}{V_{\rm td}V_{\rm ud}^*}\right), \quad \gamma' = \arg\left(-\frac{V_{\rm tb}V_{\rm ub}^*}{V_{\rm ts}V_{\rm us}^*}\right), \tag{1.85}$$

are related by $\beta' = \beta + \chi$ and $\gamma' = \gamma - \chi$. That there are only 3 complex CKM matrix elements (neglecting the order λ^5 correction to $V_{\rm cd}$), implies that

$$\arg V_{\rm td} = -\beta, \quad \arg V_{\rm ub} = -\gamma, \quad \arg V_{\rm ts} = \chi + \pi \tag{1.86}$$

and that all other CKM matrix elements are real. Therefore the complex argument of the CKM matrix is given by,

$$\arg(\mathbf{V}_{\rm CKM}) = \begin{pmatrix} 0 & 0 & -\gamma \\ 0 & 0 & 0 \\ -\beta & \chi+\pi & 0 \end{pmatrix}. \tag{1.87}$$

Comparing this matrix of arguments with the $\mathcal{O}(\lambda^5)$ Wolftenstein parameterisation given in equation 1.81 enables the angles to be identified with the Wolfenstein parameters,

$$\beta = \arctan\left(\frac{\tilde{\eta}}{1-\tilde{\rho}}\right), \gamma = \arctan\left(\frac{\eta}{\rho}\right), \tag{1.88a}$$

and

$$\chi = \arctan\left(\frac{\lambda^2\eta}{1+\lambda^2(\rho-\frac{1}{2})}\right) \simeq \lambda^2\eta. \tag{1.88b}$$

One aim of LHCb is to make many independent measurements of the unitarity triangle angles, which are related to physical quantities, thereby overconstraining the triangle in order to check for violations of the consequences of unitarity in the three generation

Standard Model. The experimental methods to make these independent measurements are the subject of section 1.3

1.2.4 Weak decays of b-hadrons in the Standard Model

The decay of b-hadrons can be broadly classified as leptonic, semi-leptonic and non-leptonic; which for mesons are characteristed by the transitions $B^- \to \ell^- \overline{\nu}_\ell$, $b \to c\ell^- \overline{\nu}_\ell$ and $b \to q_1 \overline{q}_2 q_d$ respectively (where $\ell \in \{e, \mu, \tau\}$, $q_1 \overline{q}_2 \in \{u, d, s, c\}$ and $q_d \in \{d, s\}$). Since non-leptonic decays directly involve the CKM transitions at the quark level, such decay modes offer many opportunities for $\mathcal{CP}$-violation studies. Non-leptonic decay modes are the primary focus of the LHCb experiment and consequently the remainder of the discussion will be based on this decay class.

Most non-leptonic decay channels have contributions from both tree and penguin diagrams, examples of which are shown in Figure 1.4. Tree diagrams are quark level Feynman diagrams in which the W-boson responsible for the b-quark flavour change decays directly to a final state quark anti-quark pair. Tree diagrams are further categorised as spectator, exchange and annihilation diagrams. The spectator diagram shows the light quark of the initial mesons is disconnected in the weak decay diagram; in the exchange diagram the W-boson is exchanged between the two initial quarks, whilst in the annihilation diagrams the quarks of the initial meson annihilate to form the W-boson. The subdivision of trees into these three classes has no effect on $\mathcal{CP}$-violation studies since all three carry the same weak phase.

Penguin diagrams are loop diagrams in which the W-boson reconnects to the quark line from which it was emitted and the quark anti-quark pair are formed from the decay of the neutral boson emitted in the quark part of the penguin loop. Penguin diagrams are classified by the type of boson emitted from the loop : the boson in a gluonic (QCD) penguin is a gluon and the boson in a electroweak penguin is a neutral electroweak gauge boson. Furthermore, the penguin diagrams are classified by the identity of the quark in the loop. This is important for $\mathcal{CP}$-violation studies since diagrams with different intermediate particles have different weak and strong phases.

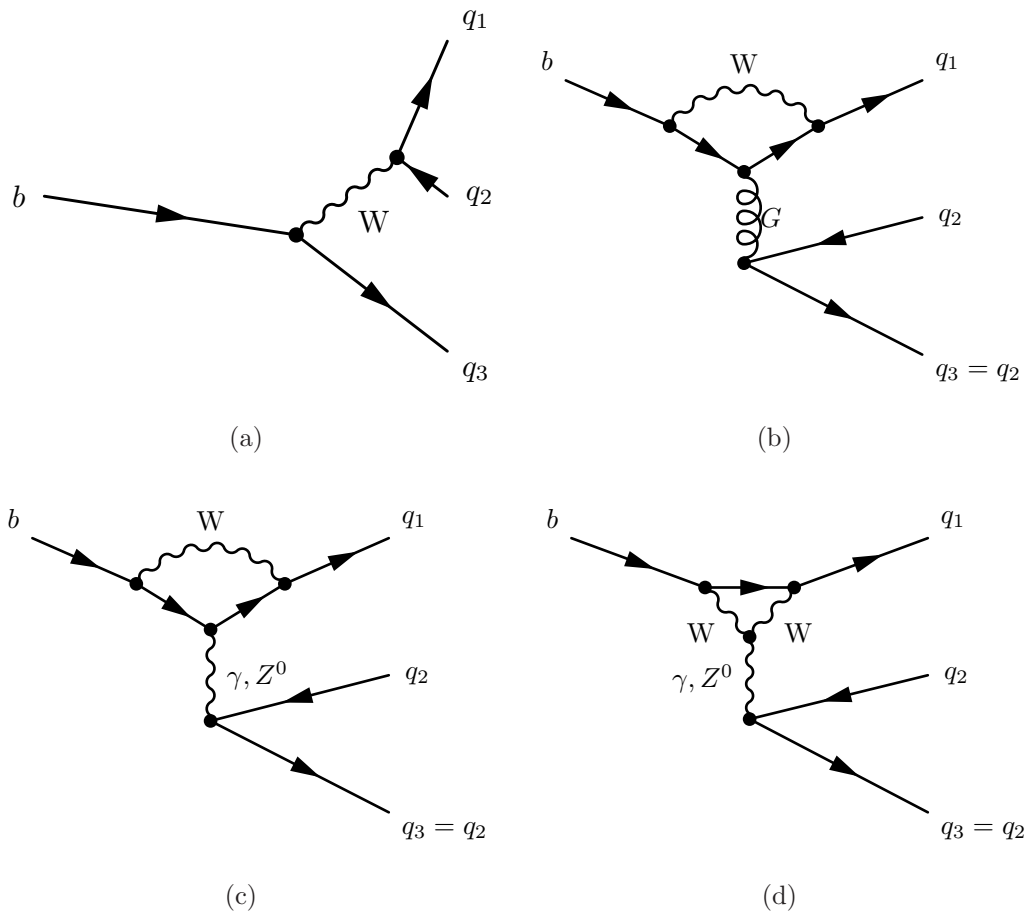

Figure 1.4: Standard Model B decay topologies. a) is an example of a first-order (tree-level) decay, b) is a gluonic (QCD) penguin diagram and c), d) are examples of electroweak penguins.

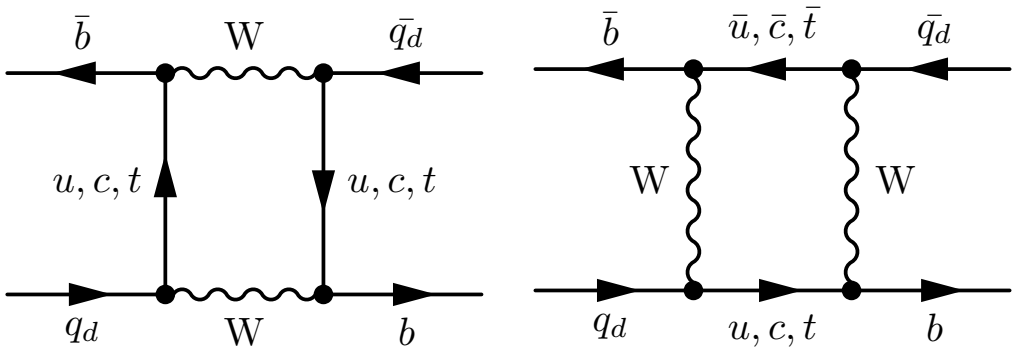

Figure 1.5: The leading order Feynman box diagrams for B-$\overline{\text{B}}$ mixing. The label q_d refers to the the down-type quark that partners the bottom quark to form the neutral meson.

1.2.5 B-$\overline{\text{B}}$ mixing in the Standard Model

In the Standard Model, the transition of a neutral B-meson to the corresponding conjugate particle is the result of weak charged current interactions. At lowest order such interactions are described by box diagrams consisting of two W gauge bosons and two up-type quarks, examples of which are illustrated in Figure 1.5. Such transitions are mediated by CKM factors of the form $V_{\text{ib}}^* V_{\text{iq}} V_{\text{jb}}^* V_{\text{jq}}$ where the label q refers to the down-type quark partner of the bottom quark and i, j are up-type quarks. The box diagrams are dominated by contributions from the internal top quark propagation [13].

Calculation of the box diagram amplitudes yields the following prediction for the ratio of the off-diagonal elements of the decay and mass matrices [17],

$$\left|\frac{\Gamma_{12}}{M_{12}}\right| \approx \frac{3\pi}{2}\frac{m_{\text{b}}^2}{m_{\text{W}}^2}\frac{1}{S_0(m_{\text{t}}^2/m_{\text{W}}^2)} \approx 5 \times 10^{-3}, \tag{1.89}$$

where m_{W} is the W boson mass, m_{b} the bottom quark mass, m_{t} the top quark mass and the function $S_0(x_t)$ is well approximated by [29],

$$S_0(x_t) = 2.40 \times \left(\frac{m_t}{167\ \text{GeV}}\right)^{1.52}. \tag{1.90}$$

It follows from equation 1.11 that the mass and decay rate differences are given by

$$\Delta M = 2\,\mathsf{Re}\sqrt{(M_{12} - \frac{\Gamma_{12}}{2})(M_{12}^* - \frac{\Gamma_{12}^*}{2})} \tag{1.91a}$$

and

$$\Delta\Gamma = -4\,\mathsf{Im}\sqrt{(M_{12} - \frac{\Gamma_{12}}{2})(M_{12}^* - \frac{\Gamma_{12}^*}{2})}. \tag{1.91b}$$

Which can be simplified using the approximation $|\Gamma_{12}| \ll |M_{12}|$,

$$\Delta M = M_H - M_L = 2|M_{12}| > 0 \quad \text{and} \quad \Delta\Gamma = \Gamma_L - \Gamma_H = 2|\Gamma_{12}|. \tag{1.92}$$

where the mass eigenstates M_1 and M_2 are re-labelled M_H ("heavy") and M_L ("light") respectively, and ΔM is positive by definition. Using the current measured values of the mass and lifetime differences [17],

$$\begin{aligned} \Delta M_{\mathrm{B_d^0}} &= 0.507 \pm 0.005\ \mathrm{ps}^{-1}, \quad \tau_{\mathrm{B_d^0}} = 1.530 \pm 0.009\ \mathrm{ps}, \\ \Delta M_{\mathrm{B_s^0}} &= 17.77 \pm 0.12\ \mathrm{ps}^{-1}, \quad \tau_{\mathrm{B_s^0}} = 1.437 \pm 0.031\ \mathrm{ps} \end{aligned} \tag{1.93}$$

it follows that

$$\frac{\Delta\Gamma_{\mathrm{B_d^0}}}{\overline{\Gamma}_{\mathrm{B_d^0}}} \approx 0.4\%, \quad \text{and} \quad \frac{\Delta\Gamma_{\mathrm{B_s^0}}}{\overline{\Gamma}_{\mathrm{B_s^0}}} \approx 13\%. \tag{1.94}$$

Therefore the Standard Model predicts that the difference between the mass eigenstate decay rates for $\mathrm{B_d^0}$ mesons are small, while it may be sizeable for $\mathrm{B_s^0}$ mesons. The current experimental measurements are consistent with the Standard Model prediction [30],

$$\frac{\Delta\Gamma_{\mathrm{B_d^0}}}{\overline{\Gamma}_{\mathrm{B_d^0}}} = 0.9 \pm 3.7\% \quad \text{and} \quad \frac{\Delta\Gamma_{\mathrm{B_s^0}}}{\overline{\Gamma}_{\mathrm{B_s^0}}} = 12.1 \pm 9.0\%. \tag{1.95}$$

The result of equation 1.89 also has implications for the expected magnitude of $\mathcal{CP}$-violation in the mixing. Expanding equation 1.15,

$$\left|\frac{q}{p}\right|^2 = 1 + \left|\frac{\Gamma_{12}}{M_{12}}\right| \sin(\phi_m - \phi_\Gamma) + \mathcal{O}\left(\left|\frac{\Gamma_{12}}{M_{12}}\right|^2\right), \tag{1.96}$$

it therefore follows from equation 1.89 that $|q/p| \approx 1$ and therefore Standard Model $\mathcal{CP}$-

violation in the mixing is predicted to be very small in the b-sector.

1.3 Measuring $\mathcal{CP}$-violation

The magnitude of seven of the nine CKM elements can be measured directly from the weak decay of the relevant quarks, whilst the remaining two elements, $|V_{\rm td}|$ and $|V_{\rm ts}|$, are accessed through loop diagrams such as the QCD and electroweak penguins shown in Figure 1.4, or, the box diagrams shown in Figure 1.5. Assuming only three generations, the 95% confidence intervals for the magnitude of the CKM elements are [17]

$$|\mathbf{V}_{\rm CKM}| = \begin{pmatrix} 0.97338 - 0.97432 & 0.22514 - 0.22916 & 0.003525 - 0.003946 \\ 0.22502 - 0.22905 & 0.97252 - 0.97346 & 0.04036 - 0.04285 \\ 0.00767 - 0.00938 & 0.03973 - 0.04217 & 0.999075 - 0.999179 \end{pmatrix}$$

and the corresponding 95% confidence interval for the sines of the mixing angles are

$$s_{12} = 0.22514 - 0.22917, \quad s_{13} = 0.003524 - 0.003946, \quad s_{23} = 0.04037 - 0.04285.$$

The Wolfenstein parameters λ and A are well determined from measurements of the CKM matrix elements. The experimental focus of the B-factories and the B-physics programmes at CDF and the LHC are primarily focused on probing the ρ - η plane. Comparing the constraints of the many independent measurements in the ρ - η plane provides a framework to check for inconsistencies in the Standard Model; if two regions do not overlap this would be evidence for beyond the Standard Model physics.

Prior to the B-factory results, constraints in the ρ - η plane were inferred from three "classical" experiments :

- The determination of $|V_{\rm ub}|$ and $|V_{\rm cb}|$ from B-decays containing $\mathrm{b} \to \mathrm{u}\,\ell^-\,\overline{\nu}_\ell$ and $\mathrm{b} \to \mathrm{c}\,\ell^-\,\overline{\nu}_\ell$ transitions, constrains

$$R_b = \sqrt{\rho^2 + \eta^2} \tag{1.97}$$

  which corresponds to circles centred on (ρ, η)=(0,0).

- The mass difference between the $\mathrm{B}^0_{\rm d}$ mass eigenstates is dominated by box diagrams

with terms proportional to $|V_{\rm td}V_{\rm td}|^2$, leading to the constraint

$$R_t = \sqrt{(1-\rho)^2+\eta^2} \tag{1.98}$$

which corresponds to circles centred on (ρ,η)=(1,0), the lower bound of which is further constrained by the mass difference in the $\rm B_s^0$-$\overline{\rm B}_s^0$ system.

- Constraints on the parameter $\epsilon_{\rm K}$, which characterises indirect $\mathcal{CP}$-violation in the kaon system, leads to a bounds corresponding to a hyperbola in the ρ - η plane.

In 2001 the *BABAR* and Belle collaborations made the first non-zero measurement of $\sin(2\beta)$, thus confirming the existence of $\mathcal{CP}$-violation in the B-meson system [24, 25]. Later, in 2006, the CDF collaboration made the first observation of $\rm B_s^0$-$\overline{\rm B}_s^0$ oscillations [31]. The current constraints in the (ρ,η) plane, including measurements from the B-factories and the Tevatron experiments, are shown in Figure 1.6. Note that the $\sin(2\beta)$ measurement overlaps perfectly with the "classical" constraints; this represents a significant success of the Standard Model CKM mechanism of $\mathcal{CP}$-violation.

There remains, however, large uncertainties in many constraints, particularly γ and α. LHCb aims to further constrain these bounds by exploiting the unprecedented number of b-hadrons, of all types, that will be produced at the LHC. The following sections will detail examples of methods to extract measurements in the (ρ,η) plane from the experimental observables at LHCb.

1.3.1 Direct measurement of β

The angle β appears in the CKM matrix element $V_{\rm td} = |V_{\rm td}|e^{-i\beta}$, as shown by equation 1.87. Two instances of this CKM element appear in the box diagrams for $\rm B_d^0$-$\overline{\rm B}_d^0$ mixing, the form of which are shown in Figure 1.5. All up-type quarks contribute to the internal quarks lines, but the amplitude is proportional to the quark mass and therefore the top quark contributions dominate.

As discussed previously in section 1.2.5, in the b-sector $|p| \approx |q|$ such that,

$$\frac{q}{p} = e^{i\phi_{\rm mix}^{\rm d}} \tag{1.99}$$

where $\phi_{\rm mix}^{\rm d}$ is the mixing phase. As the box diagram for $\rm B_d^0$-$\overline{\rm B}_d^0$ mixing consists of two

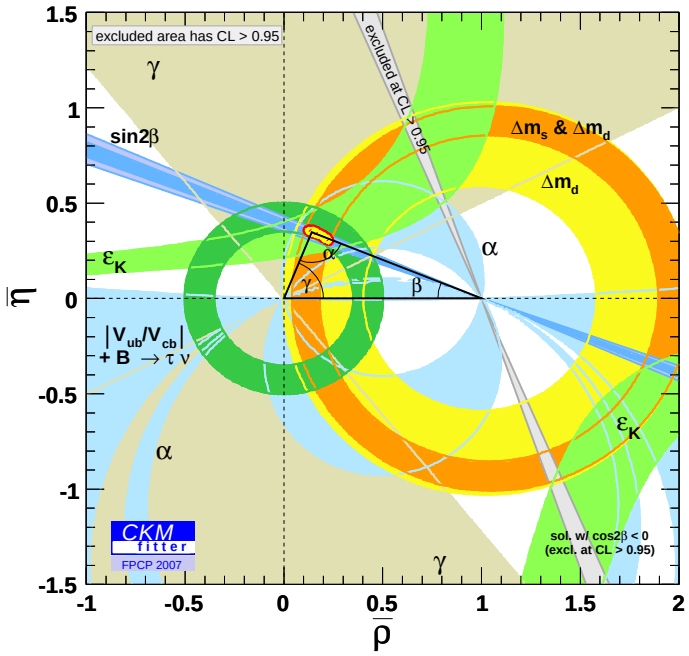

Figure 1.6: CKM fitter group global indirect fits to the CKM parameters as of 2007 [32].

V_{td} vertices each with a phase $-\beta$, it follows that

$$\frac{q}{p} = e^{-i2\beta}. \tag{1.100}$$

The decay $\mathrm{B}^0_{\mathrm{d}} \to \mathrm{J}/\psi\,\mathrm{K}^0_{\mathrm{S}}$ provides a means of measuring the angle β in a manner that is both theoretically and experimentally clean. The tree and penguin contributions to the decay have CKM elements with mostly zero phases; the only exception is the non-zero phase arising from the b $\to$ u transition in the penguin contributions. However, this transition can be neglected as it is doubly Cabbibo suppressed relative to the other contributions.

The mixing phase enters as the phase difference between the two decay paths illustrated in Figure 1.7; one path leads to the direct decay to the final state, while the other oscillates to the conjugate state before decaying to the same final state. Therefore the parameter λ defined in equation 1.51 is given by,

$$\lambda = \frac{q}{p}\frac{\overline{A}_f}{A_f} = -1.e^{-i2\beta}, \tag{1.101}$$

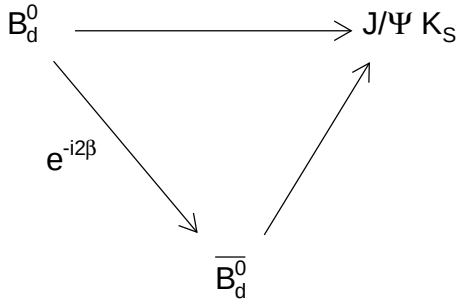

Figure 1.7: Illustation of the phase difference between the two interfering decay paths for $B^0_d \to J/\psi\, K^0_S$ decays.

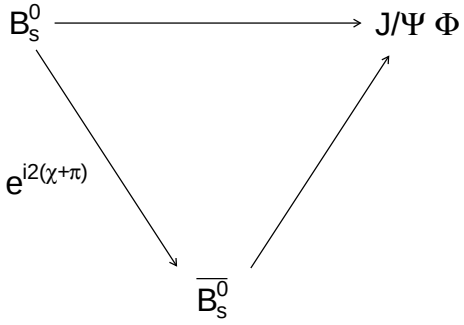

Figure 1.8: Illustration of the phase difference between the two interfering decays paths for $B^0_s \to J/\psi\, \phi$ decays.

where the minus sign is required because J/ψ a $\mathcal{CP}$ odd state. It follows from equation 1.63 that the time dependent asymmetry is,

$$\mathcal{A}_{\mathcal{CP}} = \frac{\Gamma(B^0_d \to J/\psi\, K^0_S : t) - \overline{\Gamma}(\overline{B}^0_d \to J/\psi\, K^0_S : t)}{\Gamma(B^0_d \to J/\psi\, K^0_S : t) + \overline{\Gamma}(\overline{B}^0_d \to J/\psi\, K^0_S : t)} = \sin(2\beta)\sin(\Delta M_{B^0_d} t) \qquad (1.102)$$

where $\Delta M_{B^0_d}$ is the mass difference between the two B^0_d mass eigenstates.

The extraction of $\sin(2\beta)$ in such a clean manner is made possible by the fact that the decay is dominated by a single weak phase. In which case both the magnitude A and the strong phase δ cancel in the ratio of the decay amplitudes in equation 1.51. However, this is an un-typical case; usually, there are additional penguin contributions which carry weak phases different to that of the tree-level contribution and thus complicate the extraction of the physically interesting phase. From an experimental viewpoint it is particularly convenient to study decays to $\mathcal{CP}$ eigenstates since no distinction is required between λ_f and $\lambda_{\bar{f}}$.

One possible method to search for physics beyond the Standard Model is to compare $\mathcal{CP}$ phases extracted from tree level processes with those which are measured from decay modes with significant penguin contributions. In the latter case new physics contributions could enter in the loop diagrams. For example, a difference between the angle β extracted from the tree-level process $B^0_d \to J/\psi\, K^0_S$, compared to the penguin process $B^0_d \to \phi\, K^0_S$, would be evidence for beyond Standard Model physics. In fact, current measurements indicate a difference between these two measurements of $\Delta(\sin 2\beta) \approx 0.15$, a 2.6σ effect [30].

1.3.2 Direct measurement of the B_s^0 mixing phase

In the Standard Model the B_s^0 mixing phase, $\phi_s = -2\chi = -2\lambda^2\eta$, is expected to be very small; $\phi_s = (-0.037 \pm 0.002)$ radians from fits to the unitarity triangles [33]. However, the presense of new physics contributions in the box diagram could introduce additional contributions to the phase.

The B_s^0 mixing angle can be cleanly extracted from $B_s^0 \to J/\psi\,\phi$ decays in a similar manner to the extraction of the B_d^0-$\overline{B}_d^0$ mixing angle ϕ_{mix}^d from $B_d^0 \to J/\psi\,K_S^0$ decays. Figure 1.8 illustrates how the phase difference $\phi_{mix}^s = -2\chi$ arises from the interference of the two $B_s^0 \to J/\psi\,\phi$ decay paths. As discussed in section 1.2.5, in the B_s^0 system $\Delta\Gamma$ cannot be neglected and therefore the complete expression for the time-dependent asymmetry, equation 1.60, is required. A precision on ϕ_s of ~ 0.023 radians is expected for 2 fb^{-1} [34]. Combining this result with the expected sensitivity from the pure $\mathcal{CP}$ eigenstate decay modes ($B_s^0 \to D_s^+\,D_s^-$, $J/\psi\;\eta$ and $\eta_c\;\phi$), leads to a combined sensitivity of ~ 0.021 radians for 2 fb^{-1} and 0.01 radians with 10 fb^{-1} [34].

1.3.3 Measurement of γ

The angle γ is the least well measured of the unitary triangle angles. LHCb aims to establish the Standard Model benchmark for γ using many complimentary tree-level B decays. Comparison of measurements from tree-level processes with those involving penguin contributions may reveal the presense of new physics though additional contributions in the loop diagrams.

One possible method to measure γ is expected to come from the decay of B_s^0 and $\overline{B}_s^0$ mesons to the same final state, $D_s^- K^+$, or the corresponding charge conjugate state $D_s^+ K^-$. The decay mode is dominated by the tree-level contribution and no significant penguin contributions are expected. $\mathcal{CP}$-violation arises from the interference of the two decay paths illustrated in Figure 1.9, which results in an overall phase difference of $-(\gamma + 2\chi)$. Since the final states are not $\mathcal{CP}$-eigenstates it is necessary to measure the time dependent asymmetries A_f and $\overline{A}_{\bar{f}}$, as defined in section 1.1.5. Combined with a measurement of ϕ_s from $B_s^0 \to J/\psi\,\phi$ decays, a sensitivity of $\sigma(\gamma) = 13^\circ$ is expected with 2 fb^{-1} of data [35].

A second approach is to measure γ directly from the interference between the $\overline{b} \to \overline{c}\,W^+$ and $\overline{b} \to \overline{u}\,W^+$ decay amplitudes. This interference can be observed by measur-

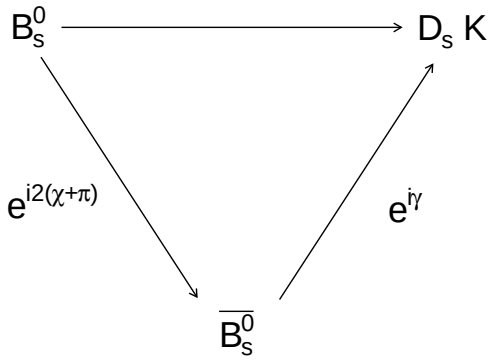

Figure 1.9: Illustration of the phase difference between the two interfering decay paths for $B_s^0 \to D_s^{\pm} K^{\mp}$ decays.

ing the time-dependent decay rates for $B_d^0 \to D^0 K^{*0}$, $B_d^0 \to \overline{D}^0 K^{*0}$ and $B_d^0 \to D^0{}_{\mathcal{CP}+} K^{*0}$, where $D^0{}_{\mathcal{CP}+} = (D^0 + \overline{D}^0)/\sqrt{2}$. For 2 fb^{-1} of data a sensitivity of $\sigma(\gamma) = 7 - 10^\circ$ is expected [36]. The equivalent measurement in the B^+ system, uses the decay rates of $B^+ \to D^0 K^-$, $B^+ \to \overline{D}^0 K^-$ and $B^+ \to D^0{}_{\mathcal{CP}+} K^-$ to extract γ with a precision of $\sigma(\gamma) = 5 - 15^\circ$ with 2 fb^{-1} of data [37].

Combining all the measurements, a $2 - 3^\circ$ precision on γ is expected with 10 fb^{-1} of data [38]. The measurements discussed thus far are tree-level processes which set a benchmark for new physics studies. Other decay modes that can be used for extracting γ include contributions from penguin diagrams. For example, a measurement of γ from $B_d^0 \to \pi\,\pi$ and $B_s^0 \to K^+ K^-$ is sensitive to new physics since significant penguin contributions are present. A precision on γ of $\sigma(\gamma) = \sim 10^\circ$ for 2 fb^{-1} of data is expected [39].

1.4 $\mathcal{CP}$-violation in Λ_b Decays

$\mathcal{CP}$-violation has yet to be observed with b-flavoured baryons, although, large $\mathcal{CP}$-violation effects are predicted for many b-flavoured baryons [40]. LHCb is well suited to observe $\mathcal{CP}$-violation in this sector as the number of Λ_b baryons available for study will be unprecedented; approximately 10% of all b-hadrons produced will be in the form of Λ_b s. Furthermore, from the experimental viewpoint $\mathcal{CP}$-violation studies with baryons have a number of advantages compared to studies with mesons, since neither flavour tagging studies nor time dependent measurements are required. This section describes

the expected Standard Model $\mathcal{CP}$-violation in two charmless Λ_b decays; $\Lambda_b \to p\,\pi$ and $\Lambda_b \to p\,K$. The former mode is of particular interest since the Standard Model level of $\mathcal{CP}$-violation is modified in the Minimal Supersymmetric Standard Model (MSSM) with R-parity violation [12].

1.4.1 Standard Model $\mathcal{CP}$-violation

In both $\Lambda_b \to p\,\pi$ and $\Lambda_b \to p\,K$ decays, direct $\mathcal{CP}$-violation arises from the interference of decay amplitudes with different weak and strong phases. The weak phase differences arise from the superposition of the the tree-level and penguin contributions, while the strong phases arise from final state interactions. The tree-level and penguin contributions are illustrated in Figure 1.10. The non-zero weak phases, and thus $\mathcal{CP}$-violating terms, derive from V_{ub} in the tree-level contribution and V_{td} in the penguin contributions.

The decay amplitudes are calculated using effective Hamiltonians, which are themselves expressed using the Operator Product Expansion (OPE), which separates the QCD and electroweak effects. The amplitude for the $\Lambda_b \to p\,\pi$ decay is given by [41],

$$\begin{aligned} A &= \langle p\ \pi \,|\, H_{\text{eff}} \,|\, \Lambda_b \rangle \\ &= \frac{G_F}{\sqrt{2}} \left[V_{ub} V_{ud}^* \sum_{i=1}^{i=2} c_i(\mu) \,\langle p\pi \,|\, Q_i \,|\, \Lambda_b \rangle\,(\mu) - V_{tb} V_{td}^* \sum_{i=3}^{i=10} c_i(\mu)\,\langle p\pi \,|\, Q_i \,|\, \Lambda_b \rangle\,(\mu) \right] \end{aligned}$$

where μ is the appropriate renormalisation scale, $\mathcal{O}(m_b)$, and G_F is the Fermi coupling constant. The purpose of the expansion is to separate the short and long range contributions to the amplitude; the short distance physics corresponds to the electroweak scale effects and are absorbed into the Fermi constant, while the long range physics is governed by the hadronic matrix operators, Q_i, and the Wilson coefficients, c_i. The hadronic matrix operators $Q_{1,2}$ represent the tree level QCD and electroweak processes, $Q_{3,6}$ the QCD penguins and $Q_{7,10}$ the electroweak penguins. The hadronic matrix elements are technically difficult to calculate since they contain all the hadronisation physics and the results are typically plagued by large hadronic uncertainties.

The branching ratio and $\mathcal{CP}$ asymmetry have been calculated from the procedure outlined above to be [41, 12],

$$\mathcal{B}(\Lambda_b \to p\,\pi) = 0.9 \times 10^{-6}, \quad \text{and} \quad \mathcal{A}_{\mathcal{CP}}(\Lambda_b \to p\,\pi) = 8.3\% \tag{1.103}$$

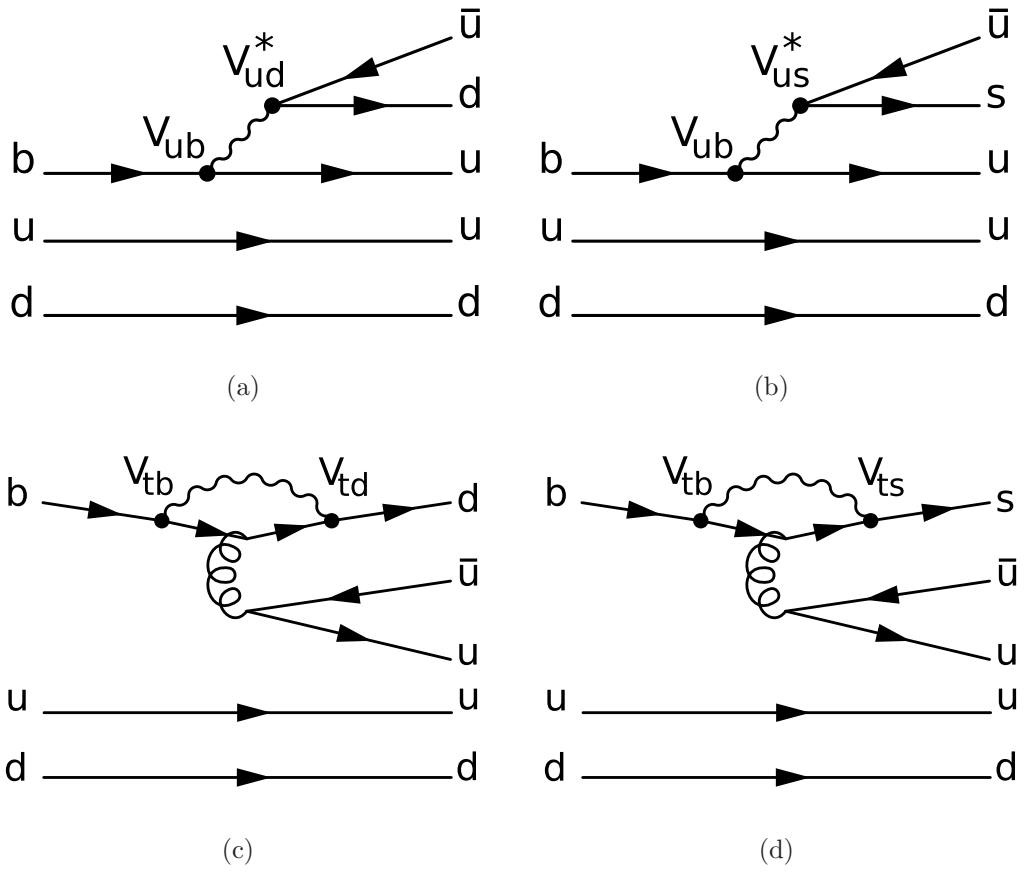

Figure 1.10: Tree-level (top row) and QCD penguin (bottom row) contributions to the $\Lambda_b \to p\,\pi$, (a) and (c), and $\Lambda_b \to p\,K$, (b) and (d), decays.

where the $\mathcal{CP}$ asymmetry, $\mathcal{A}_{\mathcal{CP}}$, is defined as

$$\mathcal{A}_{\mathcal{CP}}(\Lambda_b \to p\,\pi) = \frac{\Gamma(\Lambda_b \to p\,\pi^-) - \Gamma(\overline{\Lambda}_b \to \overline{p}\,\pi^+)}{\Gamma(\Lambda_b \to p\,\pi^-) + \Gamma(\overline{\Lambda}_b \to \overline{p}\,\pi^+)}. \tag{1.104}$$

For $\Lambda_b \to p\,K$ decays the branching ratio is calculated to be $\mathcal{B}(\Lambda_b \to p\,K) = 1.54 \times 10^{-6}$. However, the expected $\mathcal{CP}$ asymmetry has yet to be calculated in the manner described above, although the upper asymmetry bound, assuming optimal circumstances, has been calculated to be $\mathcal{A}_{\mathcal{CP}} < 66\%$ [40].

1.4.2 Effect of R-parity violation on $\mathcal{CP}$-violation

In supersymmetric theories, R-parity is a discrete symmetry under which all Standard Model particles are even ($R_{\rm p} = +1$) while their corresponding superpartner is odd ($R_{\rm p} = -1$) [11]. Conservation of R-parity has a number of important consequences for suspersymmetric theories [11]:

- It guarantees that the new spin-0 squarks and sleptons cannot be directly exchanged between ordinary quarks and leptons.
- It requires that the new R-odd sparticles can only be pair produced and that the decay of an odd sparticle can only lead to another sparticle or an odd number of sparticles.
- It ensures the stability of the "Lightest Supersymmetric Particle", such as a neutralino, which is a leading candidate for non-baryonic dark matter.

Conservation of R-parity is closely linked to the conservation of the baryon (B) and lepton (L) number in supersymmetric theories, as is made explicit by the following R-parity definition,

$$R\text{-parity} = (-1)^{2S}(-1)^{3B+L} \tag{1.105}$$

where S is the spin of the (s)particle. This is always equal to unity for all known particles, while is negative unity for the corresponding superpartners. Note from the form of equation 1.105 that R-parity may be conserved even if both the baryon and lepton numbers are violated, provided that the difference, B - L, remains the same.

In the Standard Model it is not possible to construct gauge invariant interactions that violate baryon or lepton numbers. However, this is not the case with supersymmetric extensions of the Standard Model and only the conservation of R-parity prevents such interactions. As such, the conservation of R-parity, or lack of, has important phenomenological consequences for supersymmetric models.

If R-parity is not conserved then it is possible for coupling between scalar squark and slepton fields and the fermionic lepton and quark fields. For example, the following Yukawa-like coupling between a scalar slepton field and two fermionic fields would be

forbidden if R-parity is conserved,

$$\begin{aligned}\mathcal{L} = -\lambda^{'}_{ijk}(\widetilde{\nu}_{iL}\overline{\mathrm{d}}_{kR}\mathrm{d}_{jL} + \widetilde{\mathrm{d}}_{jL}\overline{\mathrm{d}}_{kR}\nu_{iL} + \widetilde{\mathrm{d}}^{*}_{kR}\overline{\nu}^{c}_{iR}\mathrm{d}_{jL} \\ -\widetilde{\ell}_{iL}\mathrm{d}_{kR}\mathrm{u}_{jL} - \widetilde{\mathrm{u}}_{jL}\overline{\mathrm{d}}_{kR}\ell_{iL} - \widetilde{\mathrm{d}}^{*}_{kR}\overline{\ell}^{c}_{iR}\mathrm{u}_{jL})\end{aligned} \tag{1.106}$$

where $\lambda^{'}_{ijk}$ is a Yukawa-like coupling. The R and L chirality indices identify fields corresponding to the superpartners of the right and left handed fermion fields respectively, the superscript * the complex conjugate of a scalar field, and the superscript c the charge conjugate of a spinor. The interaction is illustrated in Figure 1.11, along with two other R-parity violating interactions.

Assuming R-parity is violated yields the effective Hamiltonian

$$H^{\not R}_{\mathrm{eff}} = \sum_{n,p,q}^{3} \frac{\lambda^{'}_{npi}\lambda^{'*}_{nql}}{M_{\widetilde{\ell}_n}} V_{kq}V^{*}_{jp}(\overline{\mathrm{d}}_i P_L \mathrm{u}_j)(\overline{\mathrm{u}}_k P_R \mathrm{d}_l) \tag{1.107}$$

where $P_{L,R} = (1 \mp \gamma_5)/2$ and for the decay $\Lambda_{\mathrm{b}} \to \mathrm{p}\,\pi$ it follows that $i = 1, j = 1, k = 1$ and $l = 3$. The interaction corresponding to Figure 1.11(a) is not included as it does not contribute to non-leptonic decays. Furthermore, only lepton violation is assumed and thus the interaction corresponding to Figure 1.11(c) is not considered.

Incorporating the above R-parity-violating effective Hamiltonian and following the procedure outlined in the section 1.4.1, the effect of R-parity violation on the expected branching ratio and $\mathcal{CP}$ asymmetry, has been calculated to be [12]

$$\mathcal{B}(\Lambda_{\mathrm{b}} \to \mathrm{p}\,\pi) < 1.6 \times 10^{-4}, \quad \text{and} \quad \mathcal{A}_{\mathcal{CP}}(\Lambda_{\mathrm{b}} \to \mathrm{p}\,\pi) \simeq 0.3\%. \tag{1.108}$$

The effect of R-parity violation can significantly modify the Standard Model result for the expected branching ratio and $\mathcal{CP}$ asymmetry in the decay $\Lambda_{\mathrm{b}} \to \mathrm{p}\,\pi$, as given in equation 1.103. In summary, the study of the branching ratio and $\mathcal{CP}$ asymmetry in $\Lambda_{\mathrm{b}} \to \mathrm{p}\,\pi$ decays is sensitive to new physics in R-parity violating supersymmetry scenarios.

The reconstruction and selection of both $\Lambda_{\mathrm{b}} \to \mathrm{p}\,\pi$ and $\Lambda_{\mathrm{b}} \to \mathrm{p\,K}$ decays is the subject of Chapter 6 and the sensitivity of LHCb to the predicted Standard Model and R-parity violating branching fractions and $\mathcal{CP}$ asymmetries are presented in Chapter 7.

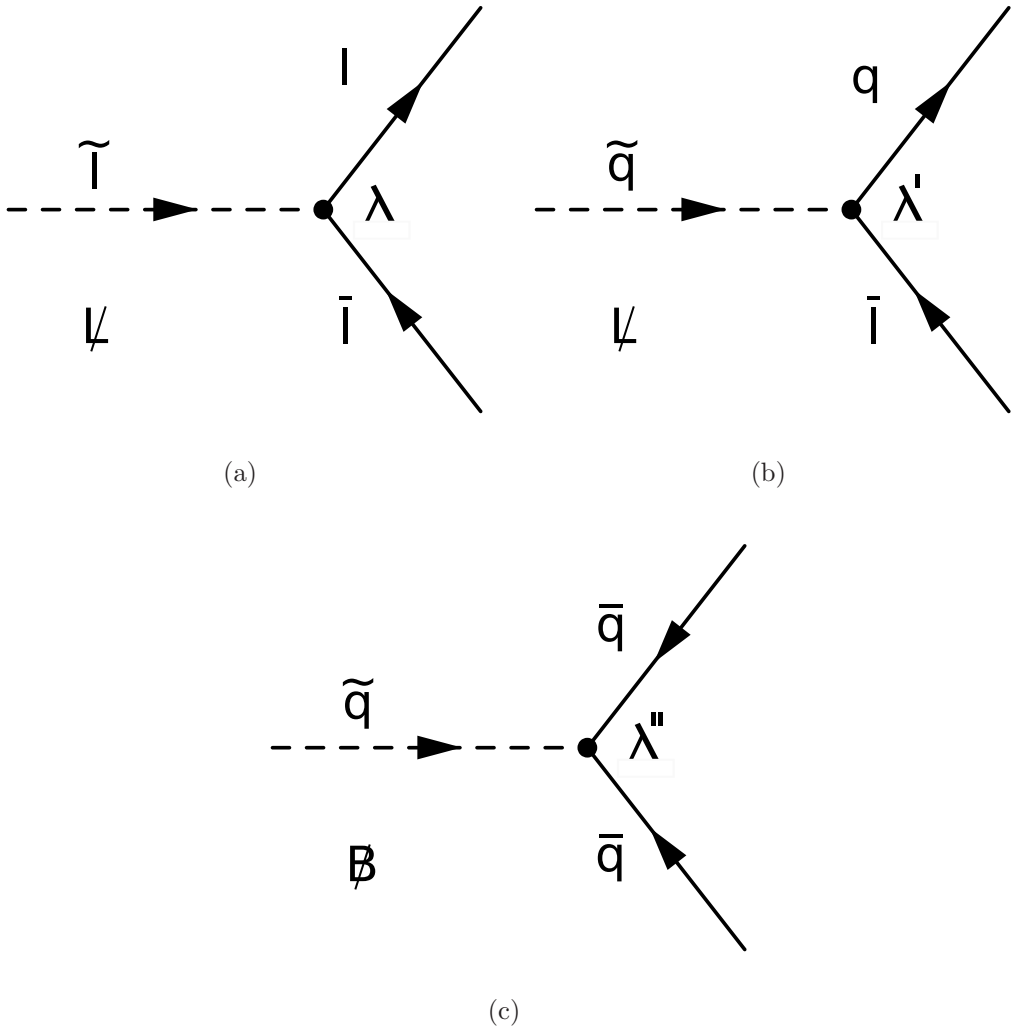

Figure 1.11: Tree diagrams of R-parity-violating interactions between scalar and fermionic fields. The squarks and sleptons are labelled $\widetilde{q}$ and $\widetilde{\ell}$, and the quarks and leptons q and ℓ. λ, $\lambda^{'}$ and $\lambda^{''}$ are the corresponding Yukawa-like couplings. The arrows indicate the flow of the lepton and baryon numbers respectively. Interactions (a) and (b) violate lepton number, and (c) violates baryon number [11].

Chapter 2

The LHCb Experiment

LHCb is a dedicated b-physics experiment that will operate at the CERN Large Hadron Collider (LHC), which will provide access to an unprecedented number of b-hadron statistics. This chapter begins with an overview of the LHC and b-hadron production and then details the design aims and implementation of the LHCb detector. Finally, the Monte-Carlo simulation and reconstruction software, which form the basis for the studies presented in this thesis, is presented.

2.1 The Large Hadron Collider

The Large Hadron Collider (LHC) will collide protons at center-of-mass energy of 14 TeV at a design luminosity of $\sim 10^{34}$ cm^{-2}s^{-1} [42]. The LHC is under construction at the European Organisation for Nuclear Research (CERN) and is due to begin high energy collisions in May 2008. There are four principal experiments:

- ATLAS and CMS are general purpose detectors designed to discover the Higgs boson and to search for evidence of beyond the Standard Model physics, such as Supersymmetry (SUSY).
- LHCb will perform high precision B-physics measurements, utilising the unprecedented number of B-hadrons that are expected to be produced at the LHC.
- ALICE will study the physics of matter at extreme energy densities, where the formation of a quark-gluon plasma matter phase is expected, using dedicated LHC runs that will collide heavy ions.

The LHC will be located in the 27km tunnel that was used for the Large Electron Positron (LEP) collider. The location of the experiments around the LHC ring and the series of accelerators that are required to inject 450 GeV protons into the LHC are shown in Figure 2.1. Although an electron-positron collider provides for a much cleaner environment to study high energy collisions than a hadron collider, the collision energy that can be attained is limited by synchrotron radiation losses. For a charged particle in a circular accelerator of radius ρ, the power loss due to synchrotron radiation is given by:

$$\frac{dE}{dt} \propto \frac{E^4 q^2}{m^4 \rho^2} \tag{2.1}$$

where E, q and m are the particle energy, charge and mass respectively. At LEP the power loss due to synchrotron radiation was approximately 10 MW. Considering that the radius, ρ, is fixed it follows from equation 2.1 that to increase the LEP energy to the 1 TeV scale would result in a prohibitive 100 GW power loss. However, given that the synchrotron losses are inversely proportional to the fourth power of the mass, acceptable energy losses are attainable by colliding protons.

The Lorentz force required to contain 7 TeV protons in the 2.8 km radial ring, for which $\sim 2/3$ of the length is used for dipole magnets, requires a 8.3 T dipole field. This is accomplished by means of 1,232 Niobium-Titanium alloy superconducing magnets, which are operated at 1.9 K using superfluid helium. Both proton beams are guided in the same dipole magnet, a unique field design providing opposite field directions in each pipe. The resulting field gradient is the maximum achievable for such a design and this provides the ultimate limit on the LHC energy [43].

Notwithstanding the technical challenge of creating and containing 7 TeV protons, the design luminosity of $\sim 10^{34}\ \mathrm{cm}^{-2}\mathrm{s}^{-1}$ is unprecedented, being a factor 100 greater than the Tevatron luminosity [44]. To attain this luminosity, the number of proton bunches per beam, n_b, will be $\sim 2,800$, each consisting of $N_p \sim 10^{11}$ protons. The bunch crossing frequency is 40 MHz, corresponding to a 25 ns spacing between consecutive bunches, which dictates the readout frequency for the front-end electronics of the experiments. As a result of the filling procedure there are some gaps between bunches; the average bunch crossing frequency, υ_{bx}, at the LHCb interaction point is expected to be $\sim$30MHz. The luminosity is given by the expression:

$$\mathcal{L} = \frac{n_b N_p^2 \upsilon_{bx}}{A} \tag{2.2}$$

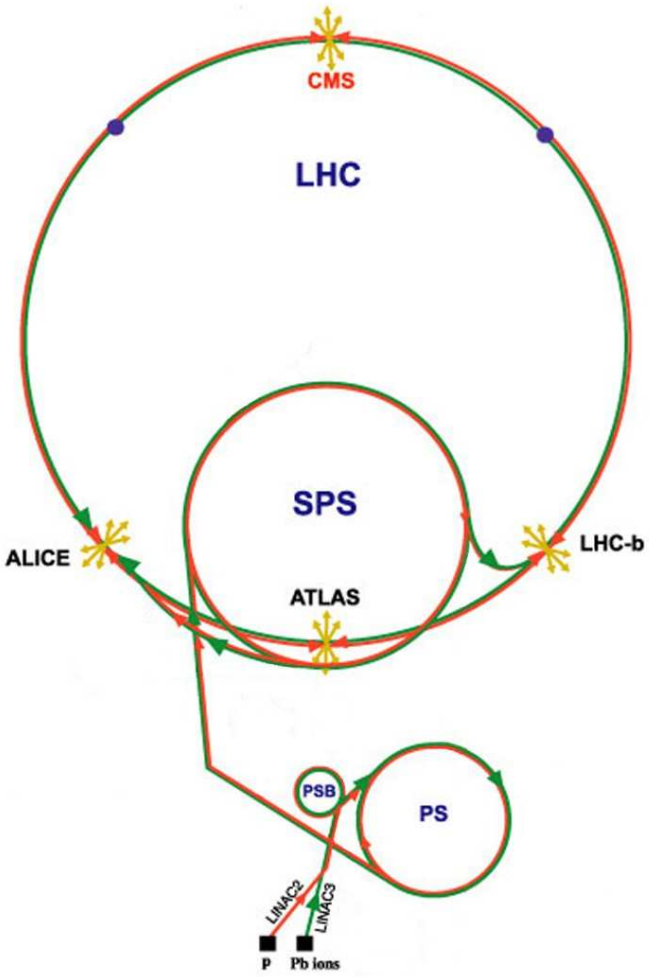

Figure 2.1: The LHC accelerator chain for protons (red line) and ions (green line). The Proton Synchrotron Booster (PSB) accelerates 50 MeV protons from the LINAC up to 1 GeV. Protons from the PSB pass into the Proton Synchrotron (PS) where they are accelerated to 26 GeV before entering the Super Proton Synchrotron (SPS). The SPS accelerates protons to the 450 GeV LHC injection energy.

where A is the effective area of the beam at collision and depends on the compactness of the beam (emittance), the ability of the magnets to focus the beam at the interaction point (betatron function) and the crossing angle of the two beams.

The number of inelastic pp collisions in a given time period, N_{pp}^{inel}, is determined by the integrated luminosity and the inelastic pp cross section, σ_{pp}^{inel} :

$$N_{pp}^{inel} = \sigma_{pp}^{inel} \int \mathcal{L} dt \tag{2.3}$$

From extrapolation of SPS and Tevatron data, the inelastic cross section, σ_{pp}^{inel}, at $\sqrt{s} = 14$ TeV is estimated to be 80 mb [45]. The mean number of inelastic pp collisions per bunch crossing is given by:

$$\langle N_{pp}^{inel} \rangle = \frac{\mathcal{L}\sigma_{pp}^{inel}}{\upsilon_{bx}} \tag{2.4}$$

which for the LHC design luminosity equates to ~ 25 inelastic pp collisions per bunch crossing. The luminosity for LHCb is, however, made deliberately smaller and is discussed further in section 2.3.2 .

2.2 Bottom Production at the LHC

In proton-proton collisions heavy flavour quark-antiquark pairs, such as $b\overline{b}$, are created when a parton from each of the protons interact with a large momentum transfer, a so-called hard scatter, which leads to the production of heavy quark-antiquark pairs via the strong interaction [46]. The QCD leading order Feynman diagrams for $b\overline{b}$ creation mechanisms are illustrated in Figure 2.2. Although the perturbative QCD cross-section for heavy flavour production has been calculated to next-to-leading order accuracy, $\mathcal{O}(\alpha_s^3)$, large uncertainties remain in the calculation of the bottom production cross section at the LHC, with an expectation between 175 and 950 μb. The uncertainty is principally attributed to unknown higher order effects, but uncertainties also arise from the parameters that enter the perturbative QCD calculation, such as the strong coupling constant and the parton density functions. Uncertainties in the bottom production ratio are not expected to effect $\mathcal{CP}$ asymmetry measurements, as such measurements are based on the ratio of rates. They are likely, however, to be a significant consideration for absolute branching ratio measurements [47]. For the purposes of comparing the performance of

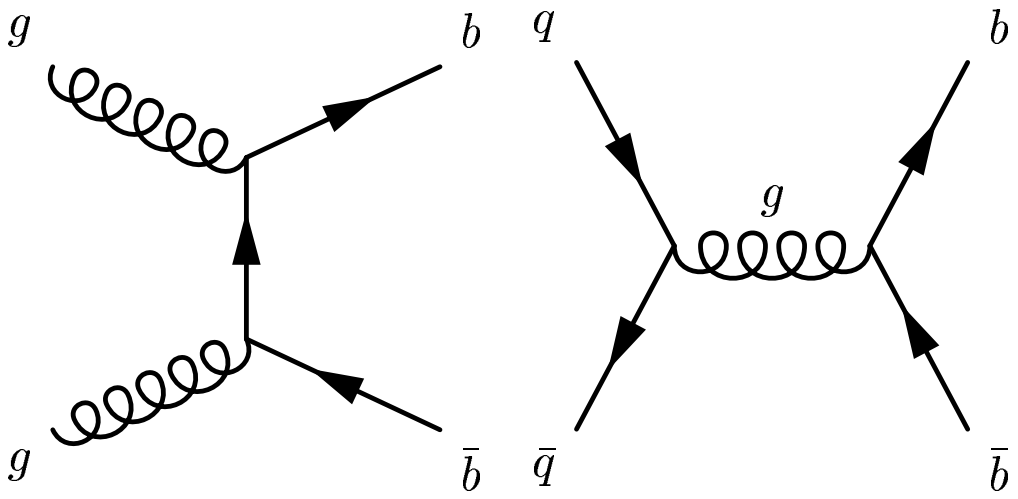

(a) Gluon fusion. (b) Quark-antiquark annihilation.

Figure 2.2: Leading order, $\mathcal{O}(\alpha_s^2)$, heavy flavour production mechanisms in pp collisions.

ATLAS/CMS and LHCb, the bottom production cross section is assumed to be 500 μb. Heavy flavour production is discussed further in section 2.4.1 in the context of Monte-Carlo event generation.

At the LHC energies, the parton distribution functions of the proton are such that it is highly likely that the partons that interact to form the $b\overline{b}$ pair will have very different momenta [47]. In the laboratory frame the $b\overline{b}$ pair must be produced back-to-back in the plane transverse to the beam. As a result, the $b\overline{b}$ pair are boosted with respect to the laboratory frame and are predominantly produced in the same forward or backward cone relative to the beam axis. This correlation is evident in Figure 2.3, which shows the simulated polar angle[1] of the b and $\overline{b}$ produced at the LHC energy.

The dominant CKM matrix element, V_{tb}, for the weak decay of B-hadrons is kinematically forbidden due to the large top quark mass (172.5 ± 2.7 GeV/c^2 [17]). As such, the weak decays of B-hadrons proceed via the suppressed V_{cb} and V_{ub} transitions, resulting in a relatively long proper lifetime of $\sim\mathcal{O}(1\text{ps})$. Combined with the Lorentz boost, this results in a typical decay length of $\sim\mathcal{O}(1\text{cm})$, a signature that can be readily used to identify a B-hadron decay.

[1] The polar angle is defined as the angle between the particle track and the beam line in the particle center-of-mass frame.

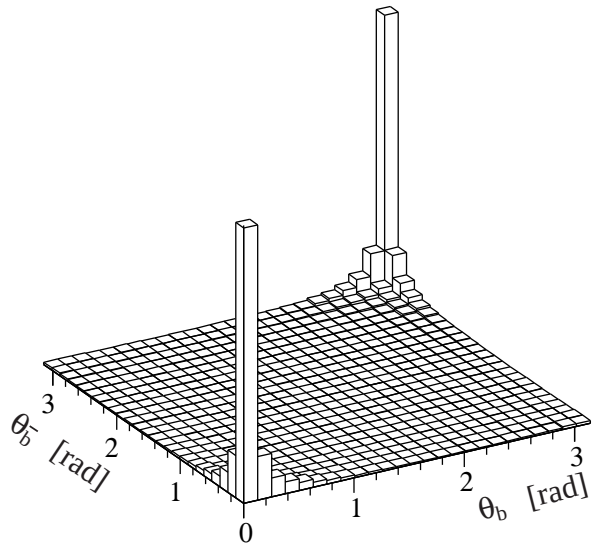

Figure 2.3: Polar angle correlations of the b and $\overline{\text{b}}$ produced in pp collisions at $\sqrt{s} = 14$ TeV, as calculated by the PYTHIA event generator [48]. Figure from the Technical Proposal [45].

2.3 The LHCb Experiment

The LHCb apparatus is designed to exploit the copious number of b-hadrons that will be produced at the LHC to make precision measurements of $\mathcal{CP}$-violation in the B-sector and to search for rare B decays. Specific requirements of the detector are :

- Excellent proper time resolution to measure, for example, the fast B_s^0 oscillation and the corresponding $\mathcal{CP}$ asymmetries. The vertexing resolution must also be able to accurately identify secondary vertices, which are characteristic of a B-hadron decay.
- Particle identification over the momentum range 1 - 100 GeV/c is required to separate b-hadron decay modes that are topologically and kinematically similar. In addition, a clean sample of kaons is vital for flavour tagging (see Chapter 5).
- A precise mass resolution is required to remove the significant combinatorial background that results from the high multiplicity LHC environment. This requires that tracks are reconstructed with sufficient momentum resolution.
- The trigger system must identify the few tens of Hz of interesting physics events from the 40MHz collision rate.

- In order to measure many $\mathcal{CP}$ asymmetries, the flavour of the reconstructed B-meson at creation must be known. Typically, the flavour of the B-meson is inferred from the accompanying b-hadron, a procedure known as "opposite-side tagging" (see section 5.1), which requires that both b-hadrons are in the detector acceptance.

2.3.1 Detector overview

LHCb re-uses the experimental cavern formerly occupied by the DELPHI experiment at LHC interaction point 8 (IP8); this constrains the detector length to $\sim$20m. A schematic of the LHCb detector is shown in Figure 2.4. A right-handed coordinate system is defined with the origin at the nominal interaction point, the z-axis along the beam direction, x towards the center of the accelerator ring and y vertically upwards. The detector only covers the region forward of the interaction point. In terms of the polar angle, θ, with respect to the z axis, the acceptance is 10 - 300 mrad in the horizontal plane and 10 - 250 mrad in the vertical plane. Equivalently, this corresponds to a range in pseudorapidity of $1.9 < \eta < 4.9$, where $\eta = -\ln(\tan(\theta/2))$.

The choice of a forward only detector geometry is motivated by the kinematics of the LHC b-hadron production. Since both b-hadrons are produced preferentially in the same direction of the beam line, the statistical loss of covering only the region forward of the interaction point is a factor 2. Further advantages of a forward only compared to a central design are:

- All the available cavern space can be utilised to attain the highest possible pseudorapidity acceptance. In contrast, the ATLAS detector has a central coverage and covers the pseudorapidity range $|\eta| < 2.5$ [51].
- The forward geometry allows the vertex detector to be positioned closer to the interaction point than is possible with a central coverage detector, thereby improving the vertex resolution.
- The open design of the forward geometry simplifies the mechanical design and enables access for maintenance and future upgrades.

The detector is organised into five main subdetector areas (see Figure 2.4):

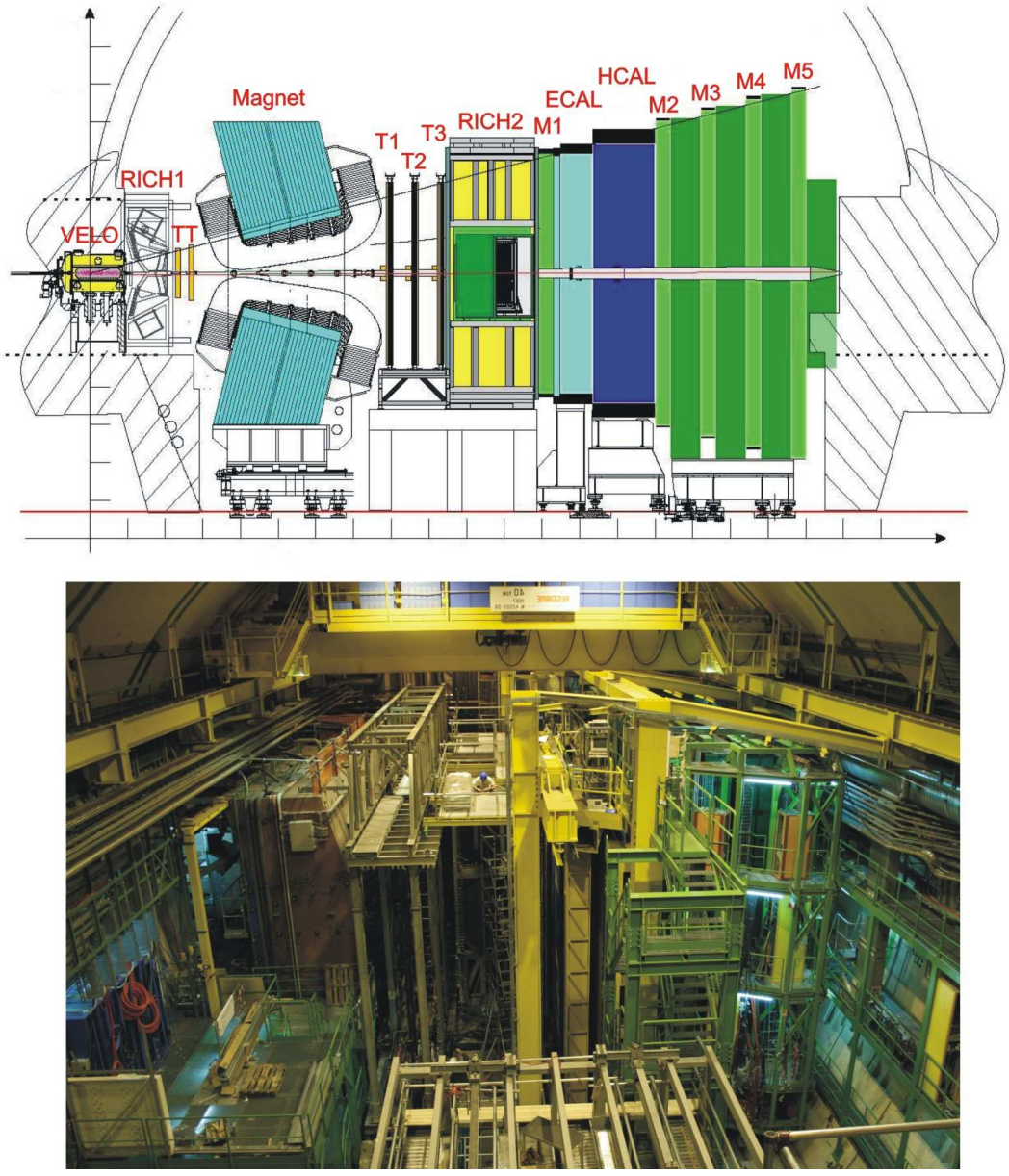

Figure 2.4: Side view (y-z plane) schematic of the LHCb detector (top) and view in the IP8 cavern taken in December 2006 (bottom). Refer to text for details of the labelled subdetectors. Figures taken from [49] and [50].

- A silicon microstrip vertex detector (VELO) : used for tracking and the reconstruction of primary and secondary vertices and the identification of events with multiple proton-proton interactions.
- A spectrometer and downstream tracking system consisting of a 2T warm dipole magnet, an outer tracker (OT), an inner tracker (IT) and a trigger tracker (TT) used for trigger purposes.
- Ring imaging Cherenkov detectors (RICH1, RICH2) to provide hadron particle identification.
- Electromagnetic and hadronic calorimeters (ECAL, HCAL) used to measure the position and energy of all particles except muons.
- Muon detectors (M1, M2, M3, M4, M5) for muon identification.

The subdetectors and LHC environment are discussed in more detail in the following sections.

2.3.2 Interaction point

At the nominal LHC design luminosity there are on average ~ 25 inelastic proton-proton interactions. The presence of multiple interactions severely complicates the identification of an individual B-hadron origin and decay vertex and the tagging of the initial B-hadron flavour, both of which are vital for time dependent decay rate asymmetry measurements. Events with multiple interactions, referred to as pile-up events, are identified by a subsystem of the vertex detector (see section 2.3.3) and vetoed by the trigger system. In order to optimise the number of single proton-proton interaction events the luminosity at the interaction point is reduced by defocussing the beam. The number of pp collisions in a bunch crossing follows a Poisson distribution with a mean given by equation 2.4. Figure 2.5 shows the number of interactions per bunch crossing as a function of luminosity at the interaction point. The number of single proton-proton collisions is maximised at a luminosity of $4 \times 10^{32}\text{cm}^{-2}\text{s}^{-1}$, two orders of magnitude less than the LHC design luminosity. LHCb has chosen to operate at a nominal luminosity of $2 \times 10^{32}\text{cm}^{-2}\text{s}^{-1}$, which results in a small reduction in the number of single particle interactions, but reduces by half the number of multiple particle interactions. At this luminosity the expected annual (10^7s) yield of single interaction $b\bar{b}$ events is 10^{12}, assuming a $b\bar{b}$ cross section of 500μb.

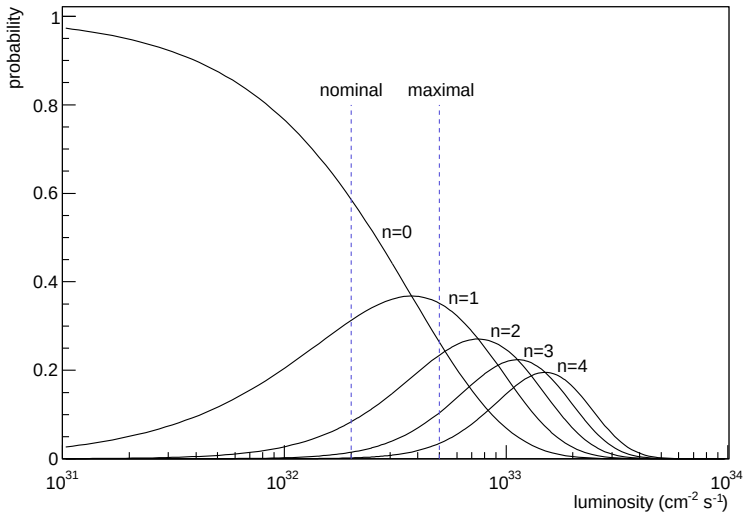

Figure 2.5: Probability of n=0,1,2,3,4 inelastic pp interactions as a function of LHC luminosity, assuming an inelastic pp cross section of 80mb. The dashed lines illustrate the nominal LHCb operating luminosity and the maximum design luminosity.

2.3.3 Vertex locator and pile-up system

The VErtex LOcator (VELO) is the principal LHCb tracking system immediately surrounding the interaction point and one of its main functions is the reconstruction of B-hadron primary and secondary decay vertices [52]. The reconstruction resolution is designed to achieve a proper time resolution sufficient for time-dependent asymmetry measurements, particularly in the rapidly oscillating B_s^0 system. Vertex positions are also an important input into the high level trigger; the $\mathcal{O}(1\text{ mm})$ displacement between two vertices being highly characteristic of an event with a B-hadron decay.

The VELO detector consists of planes of silicon microstrip detectors located perpendicular to the beam. The detector design aims to minimise the impact parameter[2] resolution whilst keeping the material budget to a minimum.

For optimum tracking performance the sensors need to be as close as possible to the interaction region. Although the LHC beam cross-section will be less than 100μm , the radial extent of the LHC beam halo dictates that the minimum radius at which it is safe to operate is 5 mm. During LHC injection periods this distance increases to 3 cm.

[2]The distance of closest approach between a reconstructed track and the primary vertex is called the *impact parameter*.

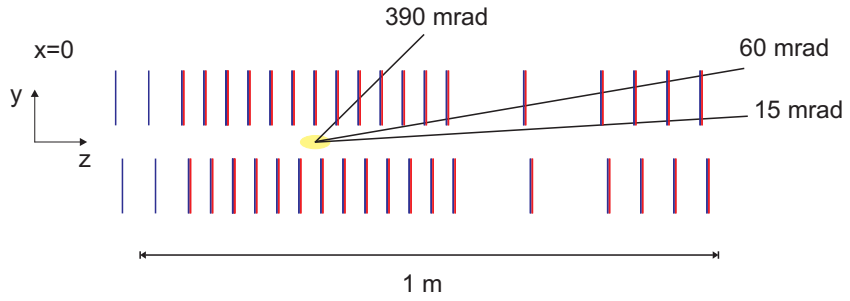

Figure 2.6: Layout of the VELO detector silicon tracking stations in the non-bending y-z plane. The ϕ and r-sensors are indicated by the blue and red lines respectively and the interaction region by the shaded yellow area. Note that the detector positions are such that tracks at the minimum and maximum LHCb acceptance, 15 and 390 mrad, respectively, traverse at least three detector planes.

In order to accommodate both regimes, each detector plane is formed from pairs of semi-circular sensors which can be mechanically retracted in the vertical direction - a so called "Roman pot" design. Each sensor has a minimum radius of 8mm and an azimuthal coverage of 182°, giving a small overlap between the two halves for alignment purposes. Each semi-circular silicon plane is made up of two 220μm thick silicon microstrip sensors bonded back-to-back; one disc has semi-annular strips to measure the radial distance from the beam axis and the other has radial strips to measure the azimuthal angle. The former is referred to as a r-sensor and the latter a ϕ-sensor. A schematic of the detector layout is shown in Figure 2.6.

The silicon sensors are a n^+-on-n design; the segmented strips being n^+ implants on a lightly n-doped silicon bulk, with a p-doped back plane. Under a reverse bias an electric field emanates from the back plane to the front n^+ strip implants. A particle passing through the silicon creates an electron-hole pair, the charge of which drifts to the segmented n^+ strips. The charge is routed out from the sensor via a second metal layer to the analogue front end readout chip, called the "Beetle" [53], where the analogue signals are buffered for the duration of the L0 trigger decision (see section 2.3.8). A more complex and costly n^+-on-n design was chosen over the conventional p-on-n design, where the segmented strips are p-doped, since its performance is expected to be less susceptible to damage from the extreme radiation environment (up to 1.3×10^{14} 1MeV neutron equivalents/cm^2/year) in which the sensors must operate [54]. The n^+-on-n design sensors are expected to survive for an integrated luminosity of 6-8 fb^{-1} with no performance degradation [55].

The strip layout of the two sensor variants is illustrated in Figure 2.7. The layout is

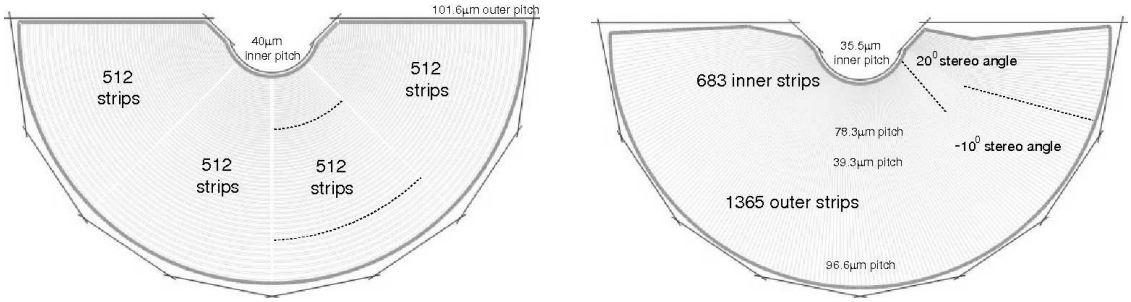

(a) r-measuring sensor (b) ϕ-measuring sensor

Figure 2.7: Layout of the VELO silicon microstrip sensors [49]. The location of some strips is indicated by a dashed line for illustration.

chosen to provide the best resolution for those hits closest to the interaction point and a low uniform occupancy of $\sim$1% across the sensor. The r-sensor has four 45° sections in ϕ, each consisting of 512 concentric circular strips. The strip pitch is 40μm at the inner 8mm radius and increases to 100μm at the outer 42mm radius. The ϕ-sensor is divided into an inner and outer region of 683 and 1365 radial strips respectively, with a strip pitch that varies from 36μm at the innermost regions to 100μm at the outer radii. The r-ϕ geometry is particularly well suited for the trigger system, since high impact parameter tracks can be easily identified using just the r-sensors alone, whereby saving valuable computational time.

The VELO primary vacuum vessel forms, along with the LHCb beam pipe, part of the LHC vacuum [56]. The silicon sensors and readout electronics are separated from the LHC vacuum by a 300μm thick aluminium alloy "RF" foil. The foil protects the LHC vacuum from mechanical failures of the VELO detector and protects the sensors from the RF currents induced by the beam. The foil has a corrugated design to minimise the material traversed by particles and to dissipate the induced RF currents. The VELO vacuum vessel and the main VELO components are shown in Figure 2.8 and a photograph of the assembled detector sensors is shown in Figure 2.9.

From Monte Carlo simulations the primary vertex resolution is expected to be $\sim$42μm in the direction of the beam and $\sim$10μm in the plane perpendicular to the beam. The precision on decay lengths ranges from 220μm to 375μm . This precision leads to a typical proper time resolution of 40fs in a typical B- meson decay channel [52].

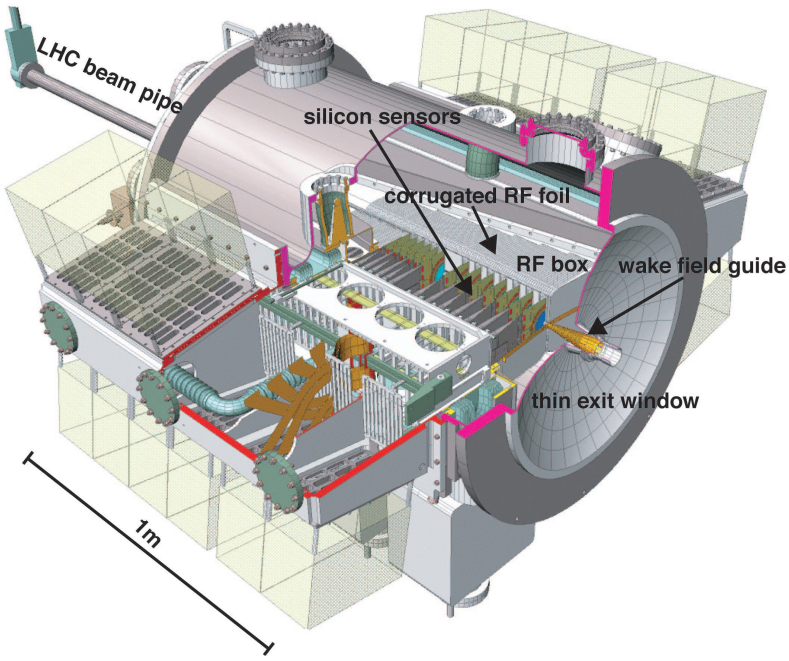

Figure 2.8: The VELO detector [49]. The main components are the silicon sensors, the RF foil, the RF box which comprises the secondary detector vacuum and the cylindrical outer body containing the primary detector vacuum.

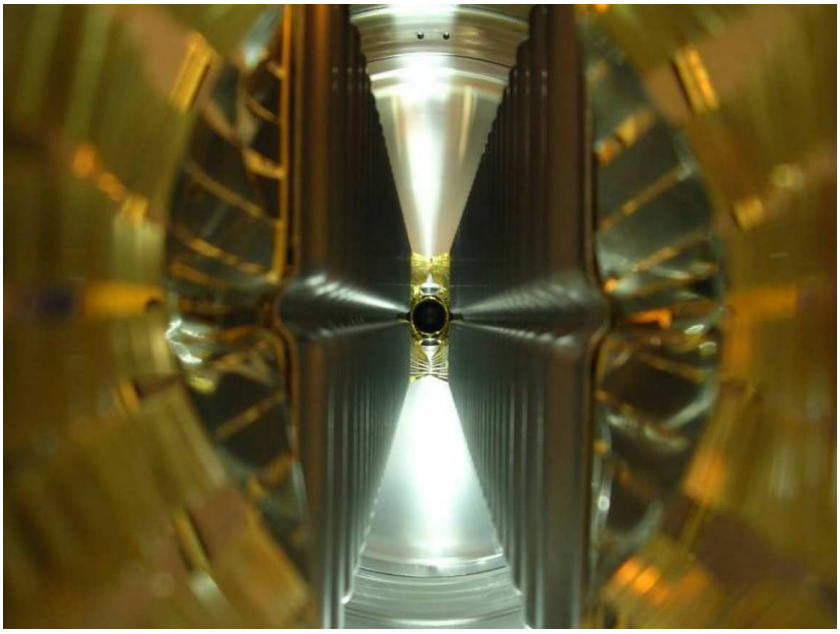

Figure 2.9: The LHCb VELO detector sensors after mounting in the RF box, as viewed along the beam axis looking towards the thin exit window [50].

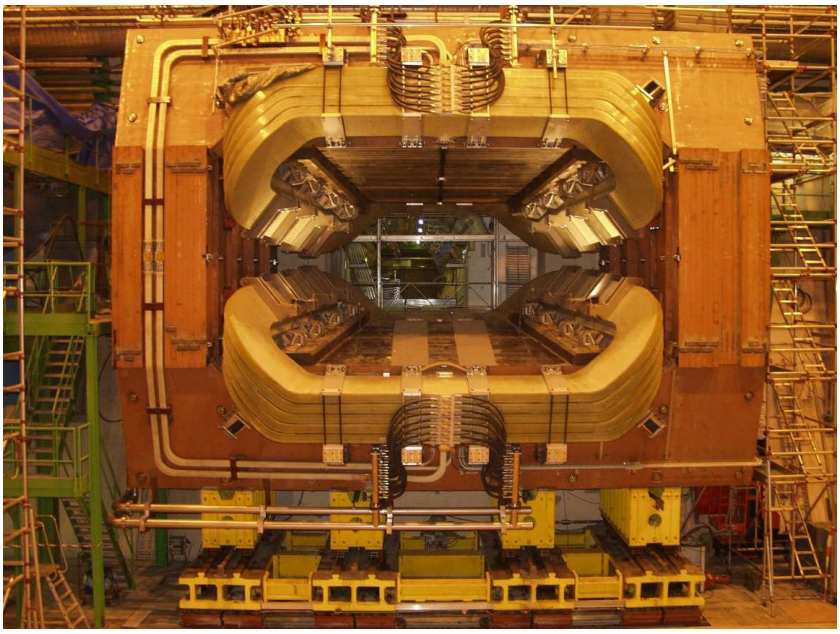

Figure 2.10: The LHCb dipole magnet, as viewed from downstream of the interaction point [50].

The VELO detector system also includes a pile-up veto counter, which consists of two dedicated r-type sensors upstream of the interaction point. The information from these detectors is used in the L0 trigger to reject events with multiple proton-proton interactions. Simulations have shown that 80% of multiple interactions can be rejected, whilst retaining 95% of single event interactions [45].

2.3.4 Tracking stations and dipole magnet

The momentum of a charged particle is inferred from the curvature of the particle's trajectory in a dipolar magnetic field. Measurement of the particle trajectory, referred to as a *track*, is provided by the VELO and four tracking stations; labelled TT, T1, T2 and T3 in Figure 2.4. The precision attained on a momentum measurement is important as it directly effects the mass resolution of the reconstructed B-hadrons. The momentum resolution is a function of the tracking resolution and the integrated magnetic field, but it can also be limited by multiple scattering in the detector materials [58]. The design of the tracking system is therefore a compromise between having numerous tracking stations to maximise the tracking precision and introducing so much material that the tracking measurement is limited by multiple scattering.

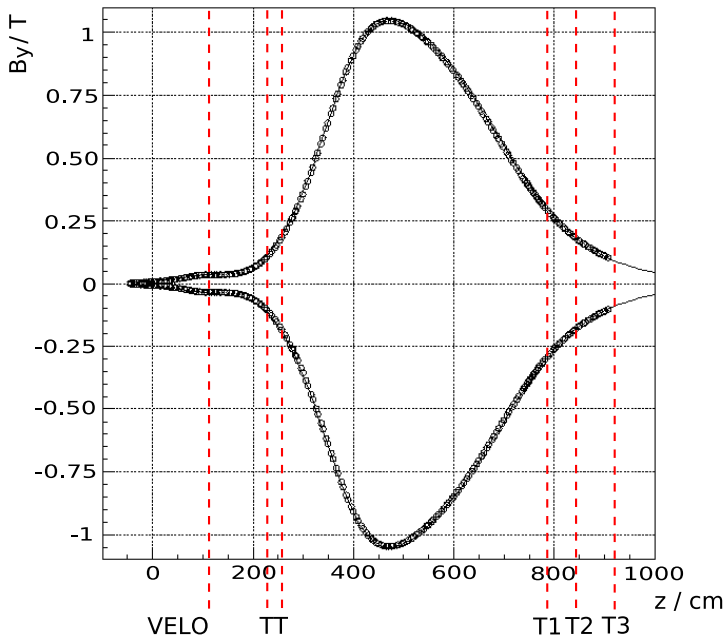

Figure 2.11: The measured on axis field ($x = 0, y = 0$) of the LHCb dipole magnet [57]. The positions of the tracking system detectors relative to the beam axis are indicated.

Aside from momentum measurement, the tracking system is also important for interpreting the data in the other sub-detectors. For example, tracks are used to reconstruct Cherenkov rings in the RICH detector and also provide the link between measurements in the VELO and energy clusters in the calorimeters and muon planes.

The LHCb dipole magnet is located between the TT and T1 tracking stations and provides a integrated field of 4Tm, with a peak field of 1.1T. A photograph of the magnet is shown in Figure 2.10. The main component of the field is orientated along the vertical y-axis; the measured field is shown in Figure 2.11 as a function of the z-axis. The magnet is made up of 15 layers of 15 turns of 50 mm square aluminium, with each coil carrying 5.8 kA. A warm magnet was chosen in favour of superconducting techology since it allows for rapid field ramping, to facilitate switching of the field polarity between LHC fills, to help control systematics arising from left-right detector asymmetries.

The first tracking station downstream of the interaction point, called the Trigger Tracker (TT), is located between RICH1 and *before* the entrance to the dipole magnet. As can be seen in Figure 2.11, there is a low integrated field of $\sim$0.15 Tm between the VELO and TT stations. The presence of this field enables a determination of a track transverse momentum with 10-40 % accuracy using information from only the VELO and

TT detectors. This is a valuable input into the high level trigger system, since a full track reconstruction and momentum measurement requires considerably more processing time. In addition to its use in the trigger, the TT station also serves to measure the momentum of low momentum tracks that are swept outside the detector acceptance by the dipole magnet. Finally, the TT enables the reconstruction of the decay products of long-lived particles that decay beyond the VELO acceptance, for example the reconstruction of K^0_S and Λ decays. The latter is described in detail in Chapter 5.

The Trigger Tracker is made up of 4 planes of p^+-on-n type silicon microstrip detectors, each covering an area 140 cm in x and 120 cm in y with a 200 μm strip pitch. Since the bending plane is in the x-z plane, the strips are aligned relative to the vertical y axis at 0°,-5°,+5°and 0°; the stereo angles[3] enabling a full 3D track reconstruction. The two inclined planes are separated by 30 cm to improve the angular resolution.

Tracking stations, T1, T2 and T3, are located between the magnet and RICH2. In order to maintain low occupancy across the detector and minimise cost, each tracking station is composed of two detector technologies :

- In the region close to the beam-pipe, where particle fluxes are highest, high resolution silicon microstrip sensors are used. This sub-detector is called the Inner Tracker (IT).
- The region further out from the beam-pipe, where particle densities are lower, employs a coarser straw-tube drift chamber detector. This subdetector is named the Outer Tracker (OT).

For high pattern recognition efficiency the boundary between the Inner and Outer Tracker is chosen such that the occupancy in any one readout channel is less than 10% [59]. The inner tracker uses the same silicon microstrip sensors as those used in the Trigger Tracker. Each IT station consists of 4 planes with the strips arranged in the same 0°, -5°, +5°, 0° manner as the TT station. The detector covers a cross-shaped area approximately 120 cm in x and 40 cm in y, the shape of which is designed to match the particle density profile.

Each OT station is made up of 4 planes of straw tubes, with the straw tubes orientated in the same manner as the other tracking stations. Each straw tube consists of a 25 μm gold wire anode surrounded by a 5 mm diameter carbon-doped Kapton tube

[3]The stereo angle in this context is defined as the angle between the strip's direction and the y-axis.

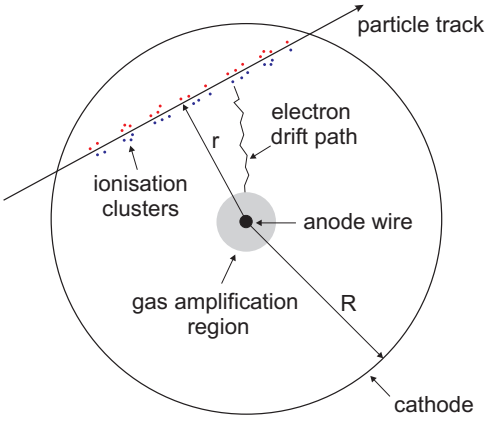

Figure 2.12: Basic operating principals of a straw tube drift chamber.

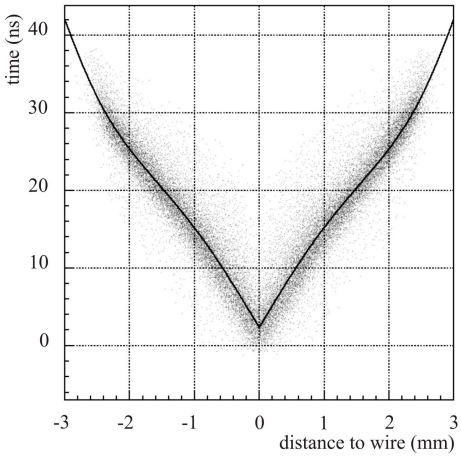

Figure 2.13: Relation between the drift time and the anode distance for a prototype straw tube. Figure taken from [60].

acting as the cathode. The tube is filled with a gas mixture consisting of 75% Argon, 15% CF_4 and 10% CO_2. A charged particle traversing the straw tube ionises this gas and the liberated electrons drift towards the anode due to the presence of an electric field resulting from the 1500 V applied to the anode. At 50-100 μm from the anode wire, the electric field strength is sufficient for an electron avalanche to be initiated, thereby amplifying the signal. An illustration of the basic principles of the straw tube operation is given in Figure 2.12. The time period between the signal traversing the detector and a signal on the anode is dominated by the drift time of the electrons. This can be exploited to determine the distance of the particle track relative to the anode. Figure 2.13 shows the relation between drift time and distance from a test of a prototype LHCb straw tube in a 10 GeV/c pion testbeam; a spatial resolution better than 200 μm is expected. The gas mixture and tube diameter have been chosen such that the drift time is less than 50 ns, which is the length of two bunch crossing intervals, thus there is always a possibility that an event accepted by the trigger will contain hits from the previous as well as the current bunch crossing.

The expected performance of the tracking system is the subject of section 2.4.

2.3.5 RICH system

The Ring Imaging Cherenkov (RICH) detectors provide information which, when combined with the momentum measurement from track curvature, can be used for charged particle identification. The ability to separate the π and K tracks is particularly important for the efficient and clean reconstruction of the decay modes of $\mathcal{CP}$ asymmetries which have identical decay topologies. The RICH system is described further in Chapter 3.

2.3.6 Calorimeters

The aim of the calorimeter system is to identify hadrons, electrons and photons and to measure their energies and positions [61]. This information is used by the Level-0 trigger to identify particles with high transverse energy, which are indicative of B-hadron decays. The calorimeter also provides the only measurement of neutral particles, the energy resolution of the calorimeter is therefore an important factor in the reconstructed mass resolution of B-hadron decays containing a π^0 or prompt photon.

Sampling calorimeters, of the type used at LHCb, consist of alternating layers of absorber and detector material. The absorber layer is made from a material chosen to develop the electromagnetic or hadronic shower. The detector layer is made from a scintillating material. The energy of a particle is inferred from the sum of scintillating light produced by the shower. An accurate energy measurement therefore requires that the shower is completely contained within the calorimeter.

The calorimeter system is located downstream of RICH2, between the first and the second Muon stations. Going from up to downstream, the system consists of four components :

- The **Scintillating Pad Detector (SPD)** is located before the calorimeters and consists of a single 15 mm-thick plane of scintillator tiles. The SPD identifies charged particles through ionisation of the scintillator material, enabling electrons and photons to be distinguished.
- The **Pre-Shower (PS)** is made up of a 12 mm-thick lead wall located after the SPD, corresponding to 2.5 X_0[4], followed by a single 15 mm-thick scintillator plane.

[4]The radiation length, X_0, of a material is defined as the distance over which the electron energy is

The PS is designed to separate electrons from the large charged pion background by exploiting the fact that an electron will shower in the lead wall, whereas only a small fraction of charged pions will interact.

- The **Electromagnetic Calorimeter (ECAL)** is a sampling calorimeter for the detection of electrons, positrons and photons and is made up of 70 alternating layers of 2 mm lead absorber followed by 4 mm of scintillator, corresponding to a depth of 25 X_0.

- The **Hadronic Calorimeter (HCAL)** is a sampling calorimeter for the detection of hadrons and consists of alternating layers of iron and scintillator planes. The overall depth of 5.6 λ_I, where λ_I is the nuclear interaction legnth[5], is a compromise between detector performance, space requirements along the beam axis and financial cost [61].

The calorimeter layers are segmented in the plane transverse to the beam into units called cells. The granularity of the PS, ECAL and HCAL calorimeter cells are designed to match the particle flux density and is two orders of magnitude larger for the cells closest to the beam pipe. A fine cell granularity is important for π^0 reconstruction, since this requires that the two showers from the π^0 decay are identified separately. In the innermost region of the ECAL the cell size is chosen to match the Molière radius, such that the majority of the shower energy is contained within a quartet of cells. In all 4 detectors, the scintillation light is collected by wave-length shifting fibres and read out by 64 anode multianode photomultiplier tubes in the case of the SPD/PS and single anode photo-multipliers in the case of the ECAL and HCAL. Figure 2.14 illustrates the ECAL and HCAL tile arrangements and the connection of the wavelength shifting fibres to the scintillators.

The energy resolution of the highest granularity ECAL modules has been measured in electron and muon beams to be $\sigma(E)/E = (8.2 \pm 0.4)\%/\sqrt{E} \oplus (0.87 \pm 0.07)\%$, where the first term describes the statistical fluctuations in the shower, the second accounts for detector systematic uncertainties and the two terms are added in quadrature[62]. With this energy resolution π^0 decays can be reconstructed with a $\sim$10 MeV/c^2 mass resolution [49]. The HCAL energy resolution has been measured to be $\sigma(E)/E = 67\%/\sqrt{E} \oplus 9\%$ [62].

reduced by $1/e$ due to Bremsstrahlung radiation only.

[5]The nuclear interaction length is defined as the average distance a hadron has to travel before an inelastic nuclear interaction occurs.

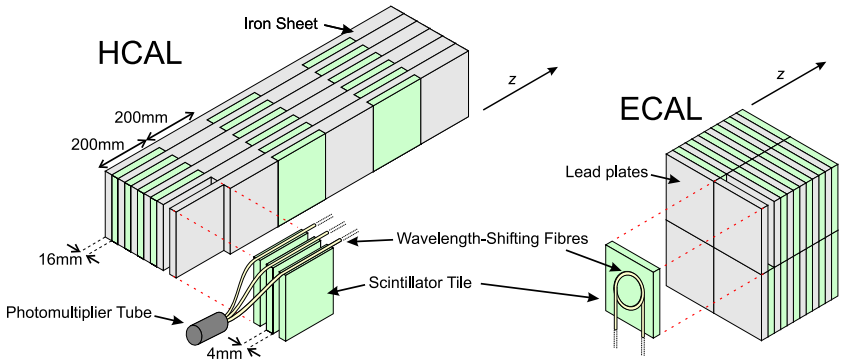

Figure 2.14: The ECAL and HCAL scintillator tile arrangement.

2.3.7 Muon system

Muon detection is important for both the first level trigger, which searches for high p_{T} muons, and the offline reconstruction of the many benchmark $\mathcal{CP}$-violating channels that have muons in their final state. Muons from semi-leptonic B-meson decays are also used to identify the flavour of the companion b-hadron.

The muon system is made up of 5 detector planes, labelled M1 - M5 in Figure 2.4, and three iron filter plates [63, 64, 65]. One station, M1, is positioned before the calorimeters, whilst the four stations, M2 - M5, are located downstream of the HCAL and are interspersed with 800 mm-thick iron plates to filter out the hadronic background. The total absorption length, including the calorimeters, is 20 λ_I, and consequently only muons with an energy in excess of approximately 6 GeV will reach the furthest M5 station. Stations M1-M3 have a high spatial resolution along the bending x-axis and are optimised for muon track reconstruction for the p_{T} calculation, while stations M4-M5 are primarily intended for muon identification.

The muon detectors are primarily made of MultiWire Proportional Chambers (MWPC) and consist of a 5 mm gas filled potential gap with a series of anode wires aligned in the centre. A schematic of a MWPC cross-section is depicted in Figure 2.15. A muon traversing the gap produces $\sim$50 electrons, which are attracted towards the anode wires by a 3 kV potential applied to each anode wire. Close to the wire the signal will undergo gas amplification, in the same manner as the straw drift tube described in section 2.3.4.

The inner region of the M1 station employs Gas Electron Multiplier (GEM) detectors [66] and is subject to a very high $\sim$460 kHz/cm^2 particle flux, which over a 10-year period is expected to lead to a degradation in the MWPC performance. The triple-

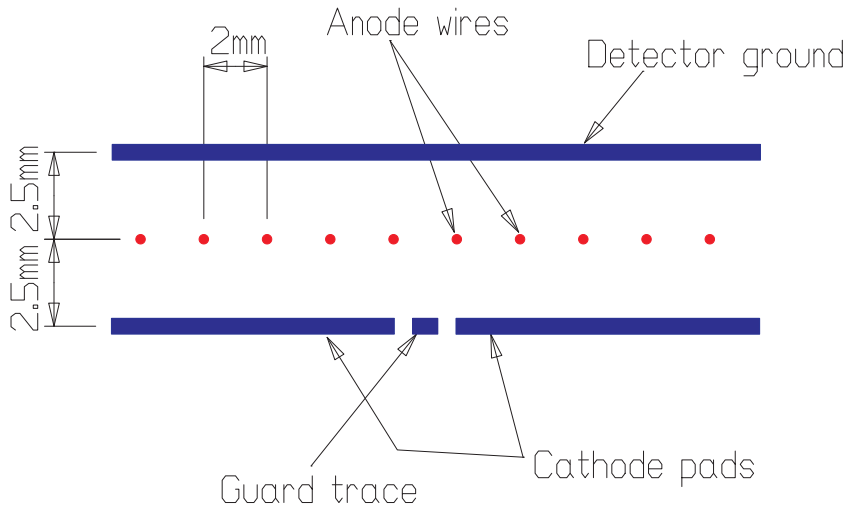

Figure 2.15: Schematic cross-section of a MWPC detector.

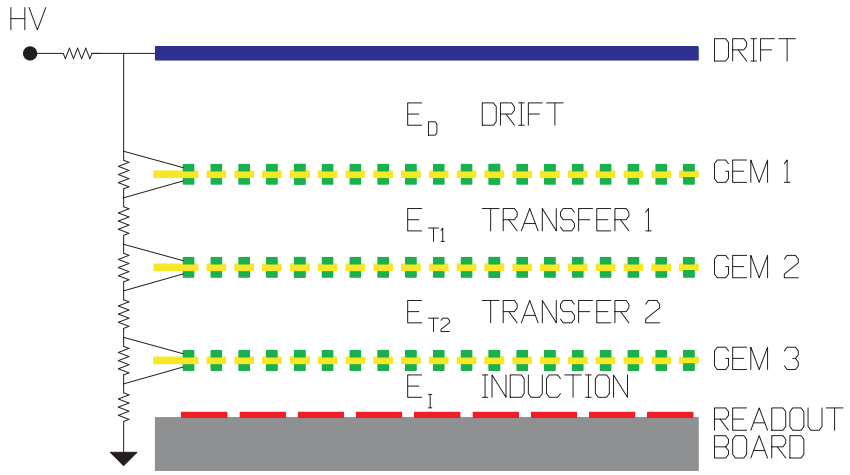

Figure 2.16: Schematic cross-section of a triple-GEM detector.

GEM detector used in the muon system consists of a gas volume and three layers of thin copper-clad kapton foils sandwiched between anode and cathode planes. The kapton foils are chemically pierced with a high density of 70 μm diameter holes. The ionisation electrons formed by a charged particle traversing the gap between the cathode and the first foil are accelerated by electric fields through the 3 foils. At the entrance of each hole the electric field strength is of order 100 kV/cm and causes gas amplification of the electrons of order a few thousand [65]. After the last foil, the charge is collected on lateral and transverse cathode strips. A schematic of the triple-GEM detector is shown in Figure 2.16.

The muon detection efficiency in LHCb exceeds 95%, since the muon identification in the L0-triggers requires a hit in all 5 detectors, and the time resolution must be less than 25 ns so as to unambiguously associate a muon with a particular bunch crossing. The necessary detection efficiency is addressed by using 4 consecutive detector units at each muon station, with the exception of M1, and taking the OR-ed result. To limit the material before the ECAL, the M1 station uses only two consecutive detector units. The required time resolution is obtained by optimising the argon, CO_2 and CF_4 gas mixture in the MWPC and GEM detectors.

2.3.8 Trigger and data acquisition

At the nominal LHCb operating luminosity, $\mathcal{L} = 2 \times 10^{32}$ cm^{-2}s^{-1}, the inelastic pp collision rate is 12 MHz, of which 9 MHz will be single pp interactions and 3 MHz multiple interactions. Assuming a $b\overline{b}$ cross section of 500μb, the probability of $b\overline{b}$ production from a pp interaction is $\sim 1/160$, which leads to a mean $b\overline{b}$ production rate of order 100 kHz. Taking into account the small fraction of $b\overline{b}$ final state particles that will be in the detector geometrical acceptance, the hadronisation fractions to B-mesons and b-baryons, and the inherently small branching ratio of the phenomologically interesting channels, events which are of interest occur at a rate of only tens of events per second.

The task of the trigger system is to extract the interesting events from the background, reducing the 40 MHz bunch crossing rate down to a 2 kHz rate that can be stored on tape for further offline analysis. To limit the required sub-detector readout buffer size, the trigger system is split into two levels; the Level-0 trigger (L0) and the High Level Trigger (HLT). The input, output and reduction rates for each level are given in Table 2.1 and a schematic of the trigger structure is shown in Figure 2.17.

The L0 trigger operates at the LHC 40 MHz bunch crossing frequency and is required to have an average acceptance of ~ 1 MHz [67, 68] . Since the L0 front-end readout can only buffer 160 consecutive events, the L0 trigger decision must be made within a 4 μs time window. In such a short time period it is impractical to process all the available sub-detector data, in particular there is insufficient time for vertex and track reconstruction and the RICH particle identification. However, the calorimeters and muon system are well suited to approximate measurements of transverse energy and momentum respectively. Since b-hadrons typically decay to low mass daughters with

	L0	HLT	Offline
Input rate	40 MHz	1 MHz	2 kHz
Output rate	1 MHz	2 kHz	-
Sub-detectors used	VELO, ECAL, HCAL, Muon	All	All
Location	On detector	Counting room	GRID

Table 2.1: Characteristics of the trigger and offline data bandwidths.

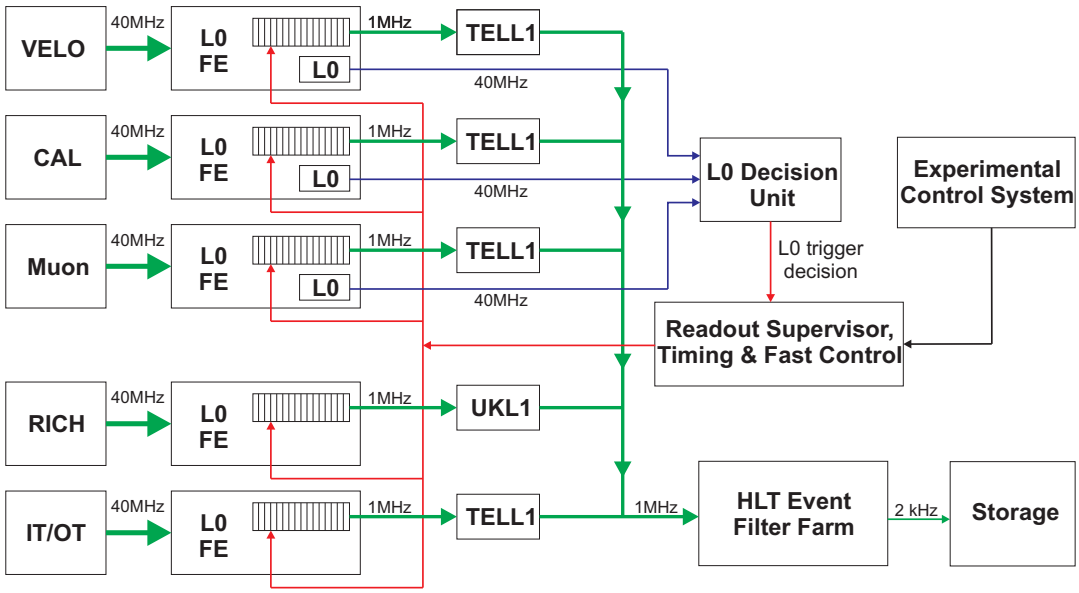

Figure 2.17: Schematic of the trigger and front-end readout electronics organisation. After each bunch crossing (40 MHz), the sub-detector data is buffered on the L0 front-end electronics (L0 FE) for the duration of the 4μs L0 trigger latency. Information from the pile-up counters (VELO), calorimeters (CAL) and muon system are used by the L0 Decision Unit to formulate a L0 trigger decision. The L0 decision is propagated to the front-end electronics by the Timing and Fast Control system (TFC). Sub-detector data for events accepted by the L0 trigger is multiplexed and zero-suppressed by the TELL1/UKL1 boards and sent to the High Level Trigger event filter farm. Events that pass the HLT selection are sent for storage for further offline analysis.

high momentum; high p_{T} electrons, muons and hadrons can be used as an effective trigger. The complete L0-trigger conditions, which are used for the studies in Chapters 5 and 6 of this thesis, are as follows

- **Calorimeter trigger** : An event is accepted if the energy in a cluster, E_{T}, satisfies the condition E_{T} >2.6 GeV for electrons, E_{T} >2.3 GeV for photons and E_{T} >3.5 GeV for hadrons. In addition, the event is not accepted if the total energy deposited in the calorimeters is less than 5 GeV. Finally, events are vetoed if the SPD multiplicity is greater than 280.
- **Muon trigger** : An event is accepted if a muon is identified with transverse momentum p_{T} >1.3 GeV, or if the sum of the largest p_{T} muons exceeds 1.5 GeV. In the latter case all other veto conditions are ignored.
- **Pile-up counter** : All events with multiple pp interactions are vetoed.

The algorithms to construct these measurements are implemented in fast, on-detector, custom electronics. The results from the 3 sub-detectors are processed by the "L0 Decision Unit" which relays the L0 trigger decision to the front-end electronics via the Readout Supervisor (RS) and Trigger and Fast Control (TFC) system. The sub-detector data of accepted events are multiplexed and zero-suppressed by dedicated electronics boards (TELL1/UKL1) and sent directly to the High Level Trigger (HLT) event filter farm over multiple gigabit ethernet links at an average rate of $\sim$1 MHz. A schematic of the data acquisition system in the context of the trigger structure is shown in Figure 2.17.

The HLT is tasked with reducing the 1 MHz input rate down to the 2 kHz storage rate. The HLT is implemented in software, with the full algorithm running on each node of a 1800 CPU farm. The input rate and farm size dictate that on average only 1.8 ms is available to process each input event. All sub-detector data is available to the HLT algorithm, but given the limited processing time available the algorithm is designed to reject the majority of events using only part of the available data.

The HLT is organised on a confirmation concept; each L0-trigger line is addressed by a dedicated HLT algorithm, which is called an *alley*. If the event passes the conditions of at least one of the alleys, it is processed by the so-called inclusive and exclusive selection algorithms. A flow diagram of the various HLT trigger sequences is shown in Figure 2.18.

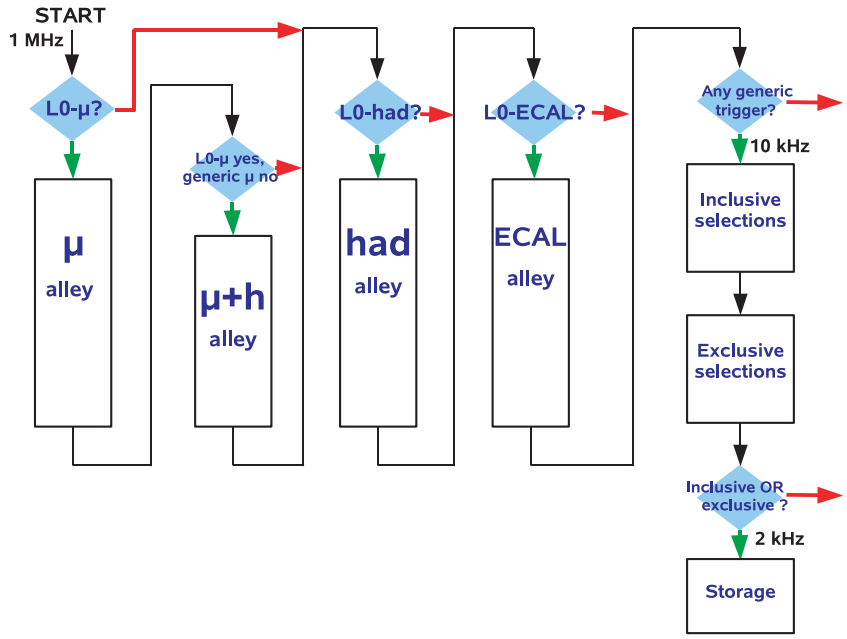

Figure 2.18: Flow diagram of the High Level Trigger (HLT). An event is processed through a particular HLT alley if the event was accepted by the corresponding L0 trigger line. If an event passes the conditions of one or more alleys it is processed by the inclusive and exclusive algorithms. An event passing either algorithm will be stored for further offline analysis [69].

Each alley follows the same structure and is designed to improve the momentum resolution of the L0-trigger in a series of increasingly time consuming steps and add impact parameter information. First, the VELO r-sensors are used to reconstruct so-called 2D tracks, which are used for a rapid reconstruction of the approximate primary vertex position. The muon alley associates muons with the 2D VELO tracks, which are then combined with VELO ϕ-sensors to form full 3D tracks; this improves the muon momentum resolution, σ_p/p, from 20% to 5%. In the other alleys, 2D tracks with significant impact parameter are combined with ϕ-sensor measurements to form 3D tracks. A full reconstruction using the T1-T3 stations is too time consuming since no estimate of the track momentum is available; instead, 3D tracks are combined with hits in the TT. Using the magnet fringe fields the momentum of these so called VELO-TT tracks can be measured with an accuracy of 20-40%. At this point, the so-called *pre-trigger* applies transverse momentum and impact parameter selection criteria, which reduces the event rate to 30 kHz. The VELO-TT tracks of events that pass the pre-trigger are fully reconstructed using the T1-T3 sub-detectors to obtain a σ_p/p precision of 1%. A final set of topological and transverse momentum selection criteria are applied to produce a final combined alley output rate of 10 kHz [70].

The final stage of the HLT is the exclusive and inclusive triggers which reduces the data rate from 10 kHz to the 2 kHz storage rate. As the input rate is low there is now sufficient time to combine the remaining 2D tracks with the T1-T3 tracking stations. This allows for the first time the use of invariant mass selection criteria. Furthermore, the RICH particle ID can be incorporated via a fast ring-track matching algorithm. The 2 kHz HLT output bandwidth is divided between the following four data streams :

- **Exclusive b-hadrons ($\sim$ 200 Hz) :** The core physics stream. The decays of interest are selected using what are essentially the final-offline selection with loose selection criteria.
- **Inclusive $\mathbf{b \to \mu X}$ ($\sim$ 900 Hz) :** Samples of b-hadrons are selected by the presence of a high p_{T} and high impact parameter muon. The sample is not biased to any signal channel and as such can be used to study the trigger and flavour tagging systematics. The stream can also be used for the study of b-hadron decays not considered in the exclusive selections.
- **Dimuon ($\sim$ 600 Hz) :** J/ψ decays can be reconstructed from two muons without applying geometrical selection criteria. As such, the sample can be used to study the detector proper time resolution.

- **D* ($\sim$300 Hz) :** The decay chain $D^*(2010)^+ \to D^0(K^-\pi^+)\,\pi^+$ can be cleanly selected without the use of RICH particle identification information. This is due to the clear kinematic signature of the decay, which derives from the small mass difference between the $D^*(2010)^+$ and D^0 ($m_{D^*(2010)^+} - m_{D^0} = 144.5$ MeV/c^2) compared to the pion mass (139.5 MeV/c^2) [17]. These decays can therefore be used for an unbiased calibration of the particle identification performance for pions and kaons.

Prior to November 2005, the trigger system was structured into 3 trigger levels, with an additional so-called Level-1 (L1) software trigger between the L0-trigger and HLT. Events passed by the L0-trigger were intended to be buffered on the TELL1/UKL1 boards to await the L1 trigger result. Events passing the L1 trigger would be sent to the HLT at the L1 accept rate of approximately 40 kHz. This avoided the need to send all sub-detector data to the HLT event filter farm at 1MHz, which was considered at the time to exceed the limit of available network switching technology. However, the advent of switching technology with capacities greater than terabits per second has facilitated the possibility to send the full detector data to the HLT farm at the L0 1 MHz acceptance rate. This approach has been adopted since it enables the data acquisition system to be simplified and enables the trigger system access to the full detector data after L0. It should be noted that the studies presented in Chapters 5 and 6 are based on the 3-level trigger system. However, no degradation in performance is expected, as to first order the same Level-1 algorithm will be run on the HLT. To the contrary, improvements are expected as the trigger algorithms evolve to use the sub-detector data that was previously unavailable at the Level-1 trigger level.

The performance of the trigger system in the context of $\Lambda_b \to p\,\pi/K$ decays is the subject of Chapter 6.

2.4 Detector Simulation and Event Reconstruction

A detailed simulation of the LHCb detector's response to pp interactions at $\sqrt{s} = 14$ TeV is crucial for the development of reconstruction, trigger, flavour tagging and signal selection algorithms. Furthermore, the simulation enables the expected signal yields to be determined, from which sensitivities to B-physics parameters can be estimated. The detector simulation also plays a pivotal role in the development of the detector design. For example, the detector simulation demonstrated that the amount of material present

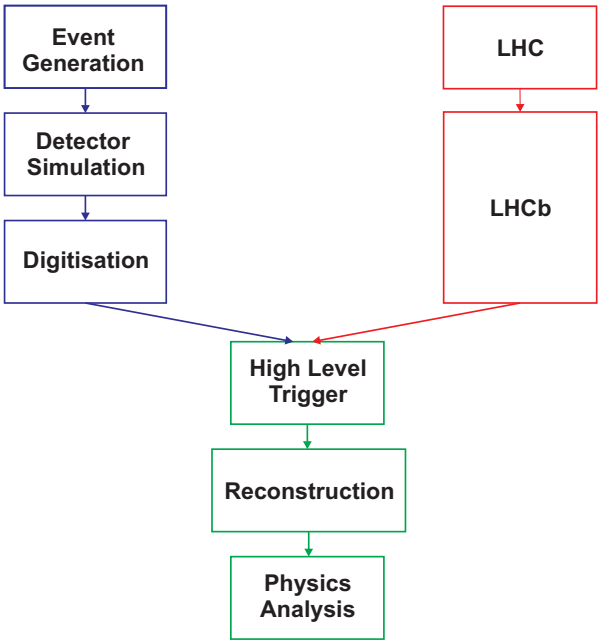

Figure 2.19: The LHCb simulation and reconstruction software organisation.

was inhibiting particle detection, leading to a redesign of the detector and a reduction in the material budget [49].

A schematic of the LHCb Monte-Carlo simulation and reconstruction software is shown in Figure 2.19. First, a Monte-Carlo event generator simulates the pp collision and generates the particles that are to be propagated through the detector. The interaction of the generated particles with the detector material is then simulated. The response of the sub-detectors to this interaction is simulated in a so-called digitisation step. Events that pass the high level trigger[6], previously discussed in Section 2.3.8, are subject to the full track reconstruction and particle identification algorithms. The results of the reconstruction are used in the final offline analysis stage to extract the interesting physics signals. The HLT reconstruction and analysis software that has been developed on simulated data has been designed so that it can be applied seamlessly to the real data when it becomes available.

The LHCb software is implemented in the object-orientated GAUDI framework, which provides the core administrative tools such as data persistency and run-time configuration, with external packages providing the Monte-Carlo event generation and detector simulation [71].

[6]The response of the Level-0 trigger electronics is part of the digitisation stage.

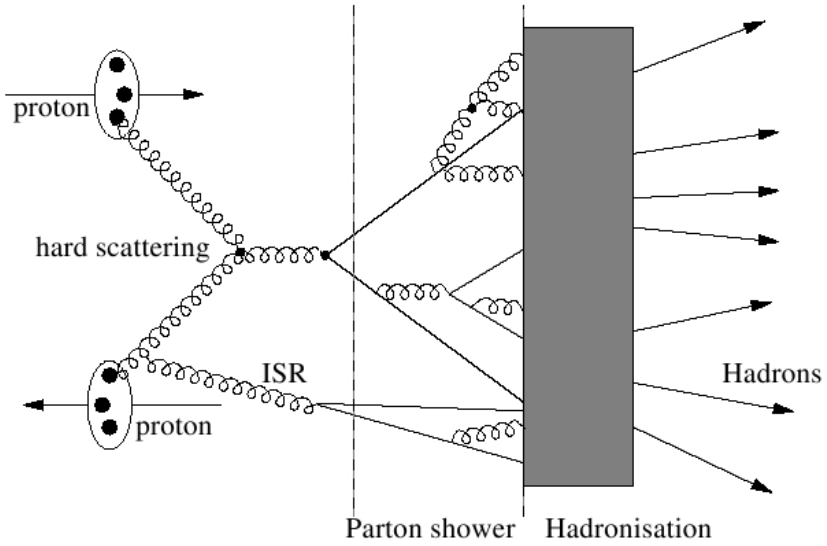

Figure 2.20: Schematic of the PYTHIA simulation of a proton-proton collision illustrating the processes used to generate stable hadrons from a parton-parton hard scatter [74].

2.4.1 Event generation and detector simulation

The simulation of the pp collision at a $\sqrt{s} = 14$ TeV center of mass energy is performed by the PYTHIA Monte-Carlo event generator [72]. A schematic of the processes used by PYTHIA to simulate the parton-parton hard scatter are shown in Figure 2.20. The hard interaction is calculated with leading order QCD perturbation theory, while the higher order processes are approximated by the parton shower model. Since the generated quarks and gluons are coloured they must first fragment to colourless hadrons before they can escape the interaction region, which in PYTHIA is modelled by the Lund fragmentation model [73]. Finally, unstable hadrons are decayed until only stable particles are left. The process of fragmentation and decay is often referred to as hadronisation.

The subject of $b\bar{b}$ production from pp collisions has been previously discussed in Section 2.2. Listed hereafter are the *categories* of $b\bar{b}$ production in PYTHIA [75, 76] :

- **Pair creation** ($\sim 16\%$) : At leading order the heavy quark flavours are produced in quark-antiquark annihilation ($q\bar{q} \to b\bar{b}$) and gluon fusion ($gg \to b\bar{b}$) processes, with the dominant contribution coming from gluon fusion. The Feynman diagrams for both processes are shown in Figure 2.2.

- **Flavour excitation** ($\sim 57\%$) : A virtual b quark in one of the protons is put

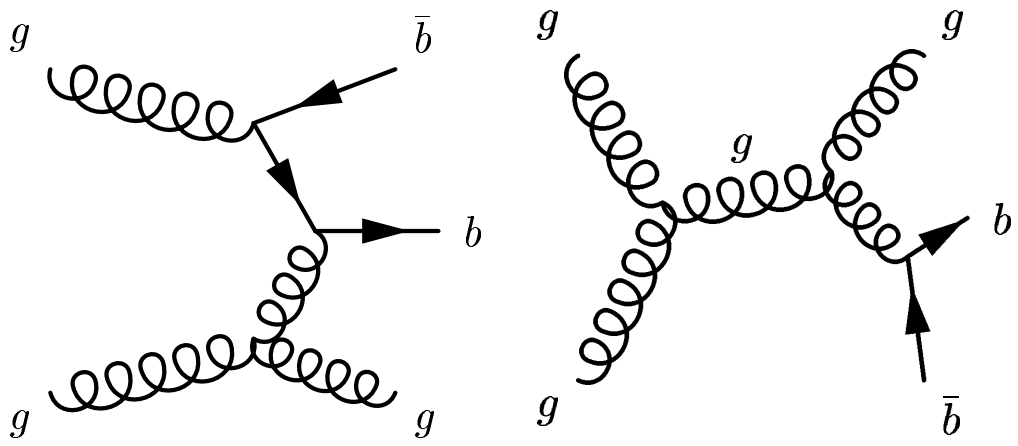

(a) Flavour excitation. (b) Gluon splitting.

Figure 2.21: Next-to-leading order contributions to the $b\bar{b}$ production.

on-mass shell by scattering with a parton in the other proton. Since the b quark is a sea-quark, there must therefore be a $\bar{b}$ quark from a prior $gg \to b\bar{b}$. A next-to-leading order Feynman diagram for flavour excitation is depicted in Figure 2.21(a).

- **Gluon splitting** ($\sim 27\%$) : The heavy flavour is not created in the hard scattering, but is produced when a $g \to b\bar{b}$ branching occurs in the parton shower. An example of a next-to-leading order Feynman diagram with a $b\bar{b}$ pair produced in the final cascade is shown in Figure 2.21(b).

Indicated in parenthesis are the relative contributions of each catergory to the PYTHIA $b\bar{b}$ production cross section, for which at least one b-hadron is in the LHCb acceptance. It should be noted that, although the $b\bar{b}$ cross section arising from pair creation processes is well known from leading order QCD perturbation theory, the true production contributions from the higher order processes are subject to large uncertainties (see Section 2.2). Simulations with PYTHIA indicate, however, that the higher order processes make a significant contribution to the $b\bar{b}$ production cross section. Since each production process leads to different final state kinematics, uncertainties in the higher order contributions may lead to discrepancies between the real and simulated data [46].

The final stage of event generation is the decay of the outgoing hadrons produced by PYTHIA. This phase is handled by the EVTGEN generator, which was developed by the *BABAR* collaboration for the specific purpose of simulating the physics of b-hadron

decays [77].

The generated events are divided into three categories, the nomenclature of which will be useful for the studies that follow this chapter:

- **Minimum bias events** : All hadrons generated by PYTHIA are decayed with EVTGEN. The generated data sample is equivalent to operating the real detector with a randomly applied trigger.
- **Inclusive $b\overline{b}$ events** : At least one b-hadron must be inside the 400mrad LHCb acceptance. The b-hadrons are decayed with EVTGEN.
- **Signal events** : The b-hadron flavour of interest is forced by EVTGEN to decay to the channel of interest. The EVTGEN generator takes care of the physics processes relevant to b-hadron decays, such as the mixing of neutral B-mesons, angular correlations and time-dependent CP asymmetries. To avoid processing unreconstructable events, the signal b-hadron is required to be inside the detector acceptance.

After the Monte-Carlo event generation, the interaction of the generated particles with the detector is simulated with the GEANT 4 toolkit [78]. The physical processes modelled by the simulation include the highly non-uniform magnetic field effect, the interaction with the detector and external material and the decay of long-lived particles such as K^0_S and Λ. The output of the simulation are so-called *hits*, which are points where the particles have interacted with sensitive areas of the sub-detectors.

The final stage of the simulation, called digitisation, applies the response of the sub-detectors to the GEANT hits. The response includes the effects of electronics noise, cross-talk and spill-over from the previous bunch crossings. The digitised output of each sub-detector is written in a format that is identical to that which will be generated by the real detector and as such marks the end of the simulation process.

The C++ GAUDI algorithms for the generation and detector simulation phases are grouped togther into the GAUSS application and the alogrithms for the digitisation phase form the BOOLE application [79, 80].

2.4.2 Reconstruction and analysis

The aim of the reconstruction and analysis stage is to extract from the real data the signal decay of interest as efficiently as possible and in a manner which minimises the effects of the finite detector resolution. The algorithms are developed using the Monte-Carlo data, which enables the performance to be continually assessed.

Reconstruction begins with track reconstruction, which is performed in two stages. The first stage is called pattern recognition and seeks to assign clusters of hits in the tracking stations to a common track, while the second stage, called track fitting, aims to accurately determine the track parameters and associated errors. The reconstructed tracks are categorised depending on their trajectory and origin in the detector. They are shown schematically in Figure 2.22 and described hereafter :

- **Long tracks** traverse the full tracking system. They have the most accurate momentum measurement and are thus the most useful for physics studies.
- **Upstream tracks** are low momentum tracks that originate in the VELO and traverse the TT, but are swept out of the detector acceptance by the magnet and are consequently reconstructed with poor momentum resolution.
- **Downstream tracks** originate outside of the VELO and traverse only the TT and T stations. They are principally used for the reconstruction of long-lived particles such as the K^0_S and Λ.
- **VELO tracks** only traverse the VELO. They are used for the primary vertex reconstruction.
- **T tracks** typically arise from secondary interactions and traverse only the T stations. They are used by the RICH2 ring fitting algorithm.

Figure 2.23 shows the tracking performance for long tracks in terms of the track reconstruction efficiency and the corresponding rate of finding so-called ghost tracks that are not associated with a simulated particle. For tracks with momentum greater than 10 GeV/c the track finding efficiency is 94%. The average ghost rate for tracks from a b-hadron decay, for which typically $p_T > 0.5$ GeV/c, is approximately 3%. The performance deteriorates for low momentum particles on account of the multiple scattering angle being inversely-proportional to the particle momentum. The momentum

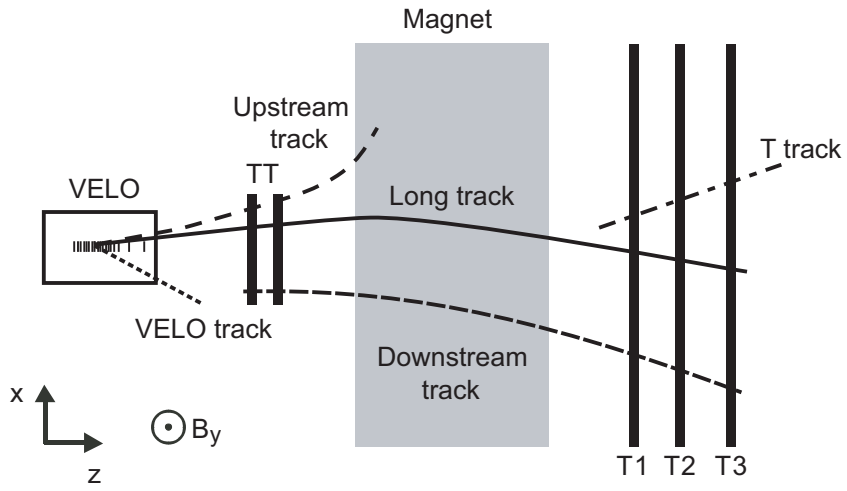

Figure 2.22: Schematic illustation (not to scale) of the five track reconstruction categories.

and impact parameter resolutions, which are measures of track fitting performance, are shown in Figure 2.24. The momentum resolution of tracks from b-hadron decays is typically $\sigma_p/p = 0.35 - 0.40\%$. The impact parameter resolution exhibits a linear dependence on the inverse of the transverse momentum and can be parameterised as $14\mu\text{m} \pm 35\mu\text{m}/p_\text{T}$ where p_T is in GeV/c.

The long, upstream and VELO track types, which are all measured in the VELO, are used to reconstruct the primary vertex. The vertex is reconstructed with a 98% efficiency, with a resolution of 41.7μm along the beam axis and 7.9μm in the plane transverse to the beam [49]. The reconstructed tracks are also used to reconstruct the secondary vertices corresponding to the b-hadron decays.

The final phase of the reconstruction process is to determine the particle PID likelihoods for each track by matching the tracks to RICH rings, calorimeter clusters and muon candidates. The particle identification performance is presented in Chapter 3.

The output of the reconstruction phase is in the form of a Data Storage Tape (DST) file containing the reconstructed tracks, vertices and PID objects. The DST files of signal and inclusive $b\overline{b}$ events are input into the offline algorithms. The C++ GAUDI algorithms for the reconstruction phase are grouped into the BRUNEL application [81], which can process either real data or the digitised output of the detector simulation.

The aim of the offline selection is to maintain high selection efficiency for the signal channel of interest whilst rejecting the huge combinatorial and channel specific back-

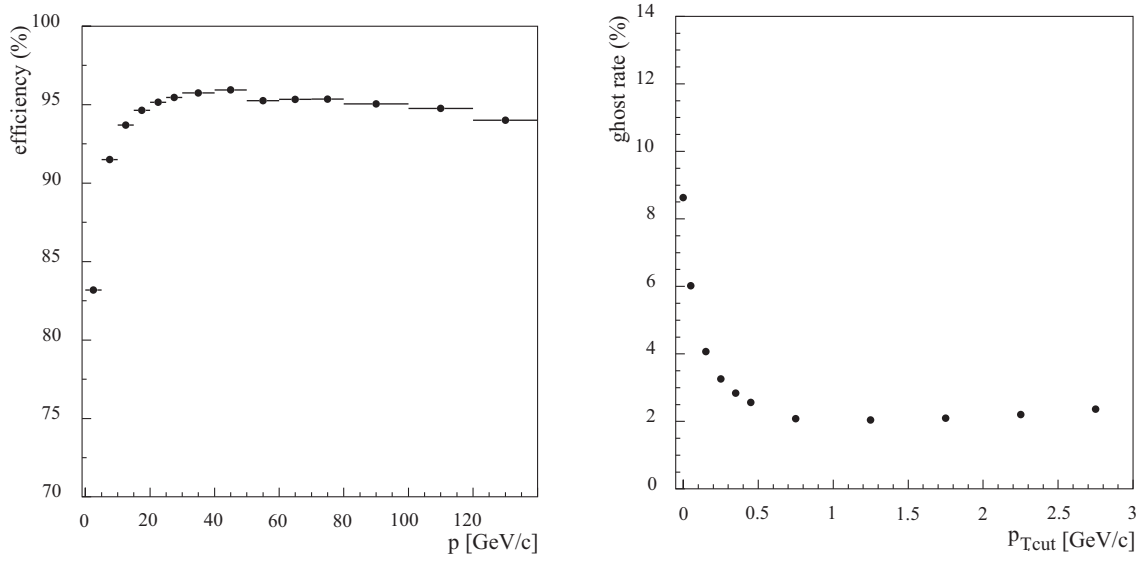

(a) (b)

Figure 2.23: Long track reconstruction performance : (a) efficiency as a function of momentum and (b) ghost rate for tracks with reconstructed transverse momentum greater than $p_{T,cut}$. Obtained from the study of a sample of $B^0_d \to J/\psi\, K^0_S$ decays. Figure taken from [49].

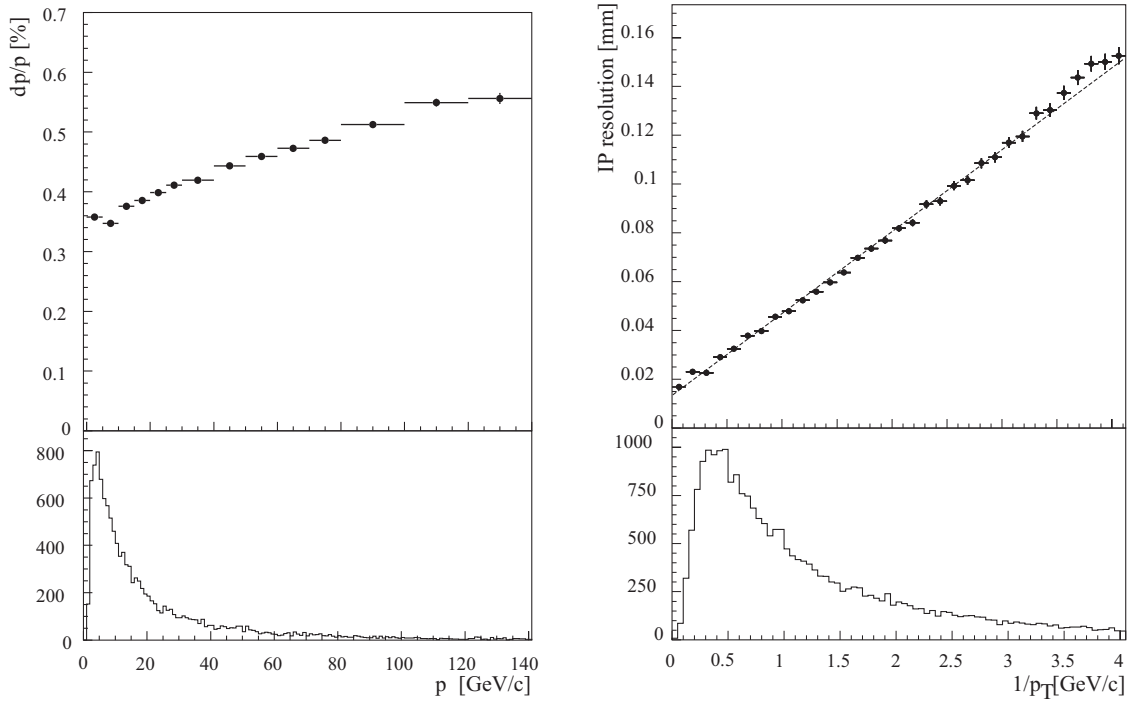

(a) (b)

Figure 2.24: (a) Momentum resolution as a function of track momentum and (b) Impact resolution as a function of $1/p_{\mathrm{T}}$. For comparison the corresponding momentum and transverse-momentum spectra of the b-hadron decay products are shown in the lower plots. Obtained from the study of a sample of $\mathrm{B}^0_{\mathrm{d}} \to \mathrm{J}/\psi\, \mathrm{K}^0_{\mathrm{S}}$ decays. Figure taken from [49].

grounds. The process begins by assigning particle identities to the tracks and then a series of kinematic, geometric, topological and invariant mass selection criteria are applied until the complete signal decay chain is selected. Crucial to the development of the selection criteria is the so-called Monte-Carlo truth information, which enables the selection efficiency and purity to be evaluated. The Monte-Carlo truth information is obtained from "associator" algorithms, which associate a particle to the Monte-Carlo particle by following a series of links that are stored at each step of the simulation and reconstruction process [82]. The C++ GAUDI algorithmns for physics analysis are grouped into a application called DAVINCI [83].

The offline selection process is described in detail in Chapter 6 for the case of the $\Lambda_b \to p\,\pi/K$ selection.

Chapter 3

The RICH System

The Ring Imaging Cherenkov (RICH) detector system provides particle identification information that is crucial for the B-physics studies at LHCb. This chapter motivates the design of the RICH system and details the two photon detector technologies that were evaluated for use in the RICH detectors. The chapter concludes with an overview of the RICH particle identification algorithms and simulated performance.

3.1 Requirement for Hadron Identification

Hadron identification is a crucial requirement for the precise measurement of $\mathcal{CP}$ asymmetries at LHCb. Many of the decay modes of interest are subject to topologically similar backgrounds; the RICH system provides an ability to distinguish between pions, kaons and protons, which significantly improves the efficiency and purity with which the decays of physics interest can be selected.

For example, the analysis of the signal decay modes $B^0_d \to \pi\,\pi$ and $B^0_s \to K^+\,K^-$ which can be used to extract the CKM angle γ must be identified from the numerous topologically identical two-body charmless b-hadron decays : $B^0_d \to K\,\pi$, $B^0_s \to K^+\,\pi^-$, $\Lambda_b \to p\,K$ and $\Lambda_b \to p\,\pi$. The benefit of the RICH system for this purpose is illustrated in Figure 3.1. In Figure 3.1(a) no RICH information is used and all the tracks are assumed to be pions; in this case the signal decay modes are overwhelmed by the other two-body final-states. However, in Figure 3.1(b) only tracks that are identified as pions by the RICH system are used and in Figure 3.1(c) only tracks identified as kaons. In both cases the background channels are suppressed considerably.

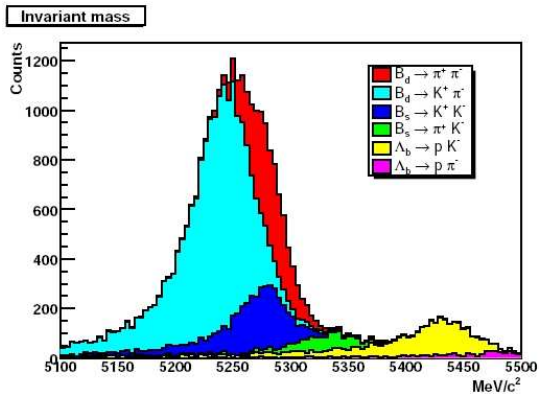

(a) no RICH PID information

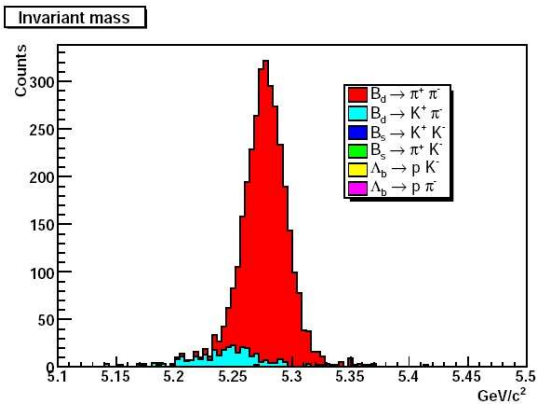

(b) both tracks identified as pions

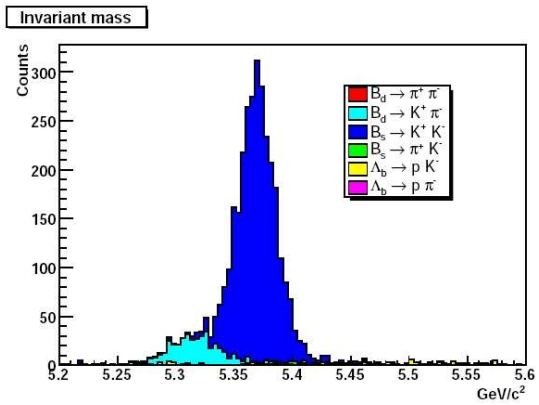

(c) both tracks identified as kaons

Figure 3.1: Reconstructed invariant mass of two body charmless B-hadron decays both without (a) and with, (b) and (c), RICH particle identification information. For (a) the invariant mass is calculated assuimg the $\pi^+ \pi^-$ hypothesis [84].

Furthermore, the identification of kaons using the RICH system is a crucial part of strategies to determine the b-quark flavour of neutral B-mesons at the point of creation, a process referred to as flavour tagging. The subject of flavour tagging is discussed further in Chapter 5, including a study of the potential to use the protons identified with the RICH system for flavour tagging.

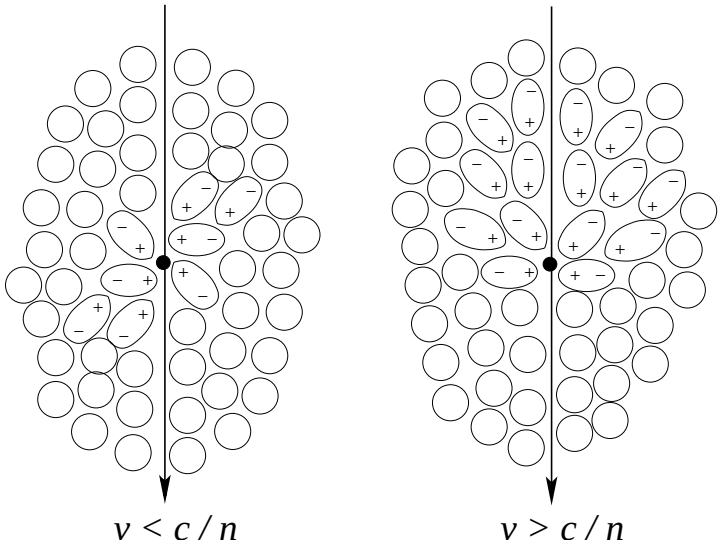

Figure 3.2: Arrangement of dipoles induced by a charged particle that traverses a dielectric of refractive index n at a velocity a) $v < c/n$ and b) $v > c/n$.

3.2 Cherenkov Radiation

The electric field of a charged particle traversing a dielectric medium of refractive index n will cause the electrons of the atoms of the medium to be displaced and the atoms to become polarised. Photons are emitted as the electrons of the dielectric return to equilibrium. If the velocity of the particle v is less than the speed of light in the dielectric, c/n, the arrangement of the induced dipoles is symmetric and the emitted photons destructively interfere and no radiation is detected. However, if the particle velocity is superluminal, i.e. $v > c/n$, the induced dipoles are not symmetric and consequently the photons constructively interfere and photons are emitted, which is known as Cherenkov radiation [85]. The induced dipole arrangements for the subluminal and superluminal cases are illustrated in Figure 3.2.

The Huygens construction of the emitted Cherenkov radiation is illustrated in Figure 3.3, from which it follows that the angle, θ_c, at which light is emitted relative to the particle's trajectory is

$$\cos(\theta_c) = \frac{1}{n\beta} = \frac{1}{n}\sqrt{1 + \left(\frac{m}{p}\right)^2}, \tag{3.1}$$

where β is the particle's velocity, expressed as fraction of c, m is the particle mass and p the particle momentum. The angle θ_c is often referred to as the Cherenkov angle. From

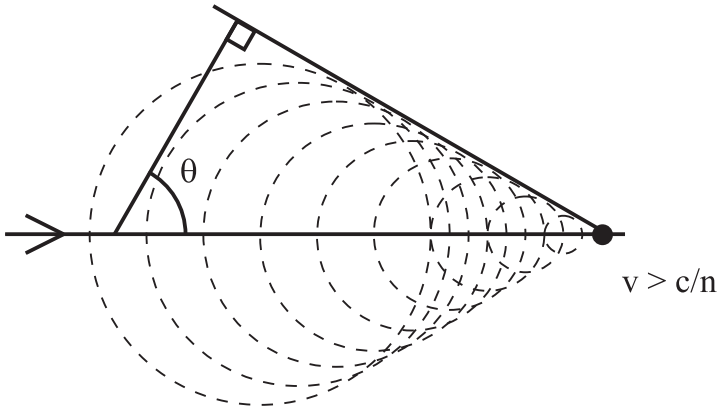

Figure 3.3: Huygens construction for Cherenkov radiation of a superluminal charged particle, which results in a coherent front at an angle θ_c relative to the particle's trajectory.

equation 3.1 it follows that a the mass of a particle, and thus it's identity, can be derived from a measurement of the Cherenkov angle and the particle's momentum.

The intensity and spectrum of photons produced by the Cherenkov effect is governed by the Frank-Tamm relation [86],

$$\frac{dN}{dE} = \left(\frac{\alpha}{\hbar c}\right) Z^2 L \sin^2 \theta_c, \tag{3.2}$$

where dN is the number of photons generated with energy between between E and $E + dE$, α is the fine structure constant, Z the particle charge and L the distance traversed through the radiator. For a particle with Z=1 and velocity $\beta \approx 1$, it follows that

$$\frac{dN}{dE} = (370 \text{ cm}^{-1}\text{eV}^{-1}) L \sin^2 \theta_c \tag{3.3}$$

For a particle with energy above 1 GeV only a negligible fraction of its energy is radiated as photons [85]. The Cherenkov mechanism is therefore a non-destructive process and as such an ideal tool for particle measurement. The weak light yield does, however, impose stringent requirements on the photon detector sensitivity.

3.3 RICH Detectors

Ring Imaging Cherenkov (RICH) detectors are designed to measure the Cherenkov angle of a charged particle. In a RICH detector the Cherenkov light is produced in a medium, called a radiator, and the emitted light cone is focused by a mirror onto a plane of position sensitive photon detectors. This results in a circle with a radius that is independent of the emission point along the particle track. The Cherenkov angle can then be calculated from the radius of the circle and knowledge of the detector optics.

3.3.1 Momentum coverage

The momentum range over which a RICH detector can operate follows from equation 3.1 where the minimum momentum required for the emission of Cherenkov light is

$$p_{\text{min}} = \frac{m}{\sqrt{n^2 - 1}}. \tag{3.4}$$

The implication being that for a given radiator there exists a band of momentum over which pions will emit Cherenkov light, but no light will be emitted from the heavier kaons. Thus, the emission or not of light in a certain momentum band can be used to distinguish between particles; this is the principle behind a threshold Cherenkov detector. This effect is evident in Figure 3.4 which shows the Cherenkov angle of pions and kaons as a function of momentum for 3 different radiators. For example, Cherenkov light is emitted in the aerogel for pions with $p > 1$ GeV/c, but only for kaons with $p > 2$ GeV/c. Reasonable, although not continuous, separation between pions and kaons can be achieved in this manner for particles with momentum between approximately $1 - 10$ GeV/c. However, separation of pions and kaons with momentum greater than approximately 10 GeV/c necessitates reconstruction of the Cherenkov angle.

It is evident from Figure 3.4 that the difference between the Cherenkov angles of the pion and koan decreases for larger momentum. Assuming that the emitted Cherenkov angle is small, a valid assumption for LHCb, it can be shown from equation 3.1 that the maximum momentum p_{max} for which two particles of mass m_1 and m_2 can be separated is [87],

$$p_{\text{max}} = \sqrt{\frac{1}{2}\frac{1}{\sigma_{\theta_c}\sqrt{n^2 - 1}}\frac{\Delta(m^2)}{n_\sigma}} \tag{3.5}$$

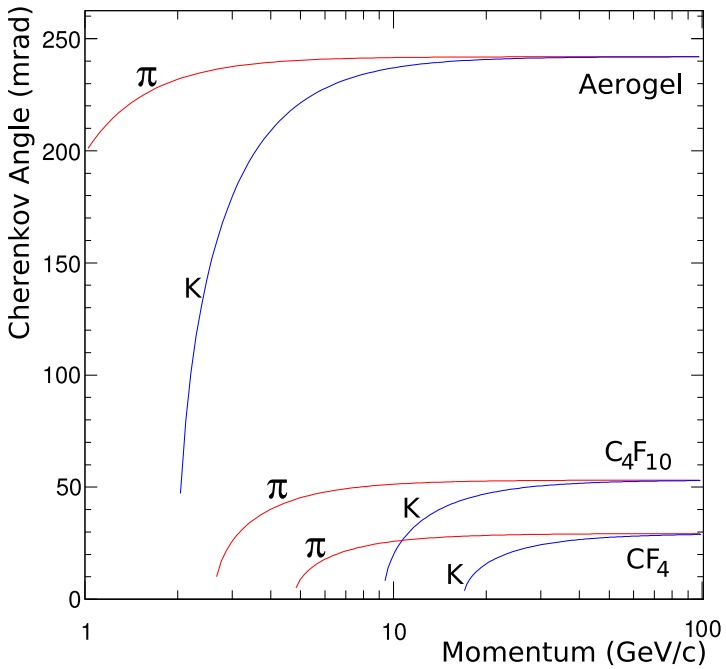

Figure 3.4: Angle of emitted Cherenkov light as a function of momentum for aerogel, C_4F_{10} and CF_4 radiators, calculated from equation 3.1. The refractive indices of the three radiators are given in Table 3.1

where σ_{θ_c} is the uncertainty on the reconstructed Cherenkov angle, the mass difference $\Delta(m^2) = m_2^2 - m_1^2$ and n_σ the number of σ_{θ_c} between the two Cherenkov angles. Therefore, the maximum momentum for which pions and kaons can be separated is a function of the Cherenkov angle resolution and the radiator refractive index.

3.3.2 Cherenkov angle resolution

The resolution of a reconstructed Cherenkov angle, θ_c in equation 3.5, is determined by the following contributions

- **Emission point error**: If the spherical mirrors are inclined relative to the track axis, as is required in the LHCb design, the point at which a Cherenkov photon hits the detector plane will depend on the point along the particle track from which emission occurred. Since it is not possible to determine this position, the point of emission is assumed to be at the mid-point of the track's path through the radiator, which results in an uncertainty in the reconstructed Cherenkov angle.
- **Pixel size**: The photon detectors have a finite granularity, which limits the posi-

tion resolution on the detector plane and therefore the Cherenkov angle resolution.

- **Chromatic dispersion**: The radiator refractive index depends on the energy of the emitted photon. Since the photon energy is not measured, this leads to an uncertainty in the value of the refractive index used to calculate the Cherenkov angle.
- **Track error**: Calculation of θ_c requires that the track position is known. Tracks are reconstructed with a finite resolution and this results in another source of uncertainty in the reconstructed Cherenkov angle.

The Cherenkov angle resolution also depends on the number of detected photoelectrons. Although the tracking uncertainty is independent of the number of detected photoelectrons, the contributions to the Cherenkov uncertainty from the other three sources listed above scale as $1/\sqrt{N_{pe}}$, where N_{pe} is the number of detected photoelectrons. The number of detected photoelectrons depends on the length of the radiator, L, and is also a function of the following parameters:

- **Transmission efficiency T(E)**: is the probability that a Cherenkov photon will reach the photon detector plane. It incorporates the transmission probability through the radiator medium and the mirror reflectivities.
- **Geometric efficiency ϵ_A**: is the probability that a photon incident on the photon detector plane hits an active area of a photon detector.
- **Quantum efficiency Q(E)**: is the probability that a photoelectron is produced from a photon incident on the photocathode.
- **Photoelectron detection efficiency ϵ_D**: is the efficiency with which a photoelectron is detected.

Using equation 3.3 and the above definitions, the number of detected photons, N_{pe}, is given by

$$N_{pe} = L\epsilon_A \int n_0(E) sin^2\theta_c(E) dE \tag{3.6}$$

where,

$$n_0(E) = (370 \text{ cm}^{-1}\text{eV}^{-1})\, T(E)Q(E)\epsilon_D$$

and L is the length of the radiator. Optimising the Cherenkov angle resolution requires a careful balance between all these factors. For example, the emission point uncertainty is proportional to the radiator length, but reducing the radiator length leads to a reduction in the photon yield. Another example is the choice of photocathode; increasing the range of wavelength sensitivity leads to a larger photoelectron yield, but exacerbates the problem of chromatic dispersion.

3.3.3 The LHCb RICH detectors

From simulations of the momentum distribution of decay channels of interest, it can be demonstrated that LHCb requires a pion-kaon separation over the momentum range $1 - 100$ GeV/c. As shown by equations 3.4 and 3.5, the lower and upper momentum bounds for the separation of two particles is a function of the radiator refractive index and the Cherenkov angle resolution. In order to cover the required momentum range, LHCb uses three radiators of different refractive index distributed between two independent detectors [84]. The first detector, called RICH1, is located immediately downstream of the VELO and uses silica aerogel and C_4F_{10} radiators to detect particles with momentum between ~ 2 and 70 GeV/c. The second larger detector, RICH2, is located between the trigger tracker stations and the calorimeters, and uses a CF_4 radiator to identify the higher, $\sim 20 - 100$ GeV/c, momenta particles. The location of the two detectors is designed to match the polar distribution of the particles; low momenta particles are swept out of the detector acceptance and thus RICH1 is located upstream of the magnet, while higher momenta particles have polar angles closer to the beam axis. The resulting polar angle and momentum coverage for the two detectors compared to the simulated decay of $B_d^0 \to \pi^+ \pi^-$ events is shown in Figure 3.5.

In order to increase the momentum coverage towards higher momenta, equation 3.5 shows that a lower refractive index and smaller Cherenkov angle resolution is required. This is achieved in RICH2 by the use of a lower refractive index radiator and by making the detector considerably larger than RICH1. The larger size improves the Cherenkov angle resolution compared to RICH1; the longer radiator yields more photons and the focal lengths of the optics are increased, which generates a larger image on the photon detector plane and reduces the effects of pixelisation error. Simulations of the various contributions to the Cherenkov angle resolution are listed in Table 3.1.

The optical layout of both detectors is illustrated in Figure 3.6. The Cherenkov

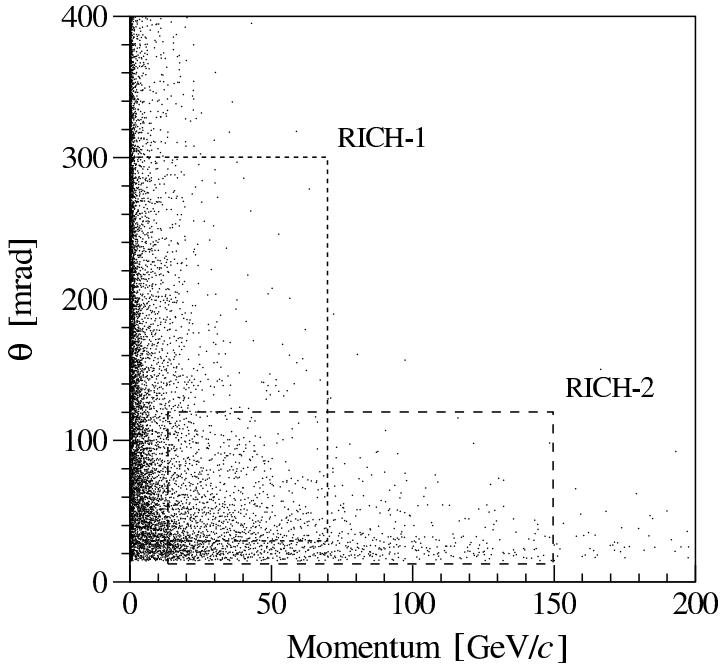

Figure 3.5: Momentum versus polar angle distribution in simulated $B^0_d \to \pi^+\pi^-$ events. The polar acceptance and momentum coverage of the two detectors is indicated by the two boxes [45].

Radiator	Aerogel	C_4F_{10}	CF_4
n	1.03	1.0014	1.0005
L (cm)	5	85	167
$\theta_C^{\max}$ (mrad)	242	53	32
$p_{\text{thresh}}(\pi)$ (GeV/c)	0.6	2.6	4.4
$p_{\text{thresh}}(\text{K})$ (GeV/c)	2.0	9.3	15.6
$\sigma_{\theta_c}^{\text{emission}}$ (mrad)	0.29	0.69	0.31
$\sigma_{\theta_c}^{\text{pixel}}$ (mrad)	0.62	0.62	0.18
$\sigma_{\theta_c}^{\text{chromatic}}$ (mrad)	1.61	0.81	0.42
$\sigma_{\theta_c}^{\text{track}}$ (mrad)	0.52	0.40	0.20
$\sigma_{\theta_c}^{\text{total}}$ (mrad)	1.9	1.3	0.7
N_{pe}	6.8	30.3	23.2

Table 3.1: Physical characteristics of the three radiator materials and the simulated emission, pixel, chromatic and track contributions to the total Cherenkov angle resolution per photoelectron and the number of photoelectrons detected in the ring [49].

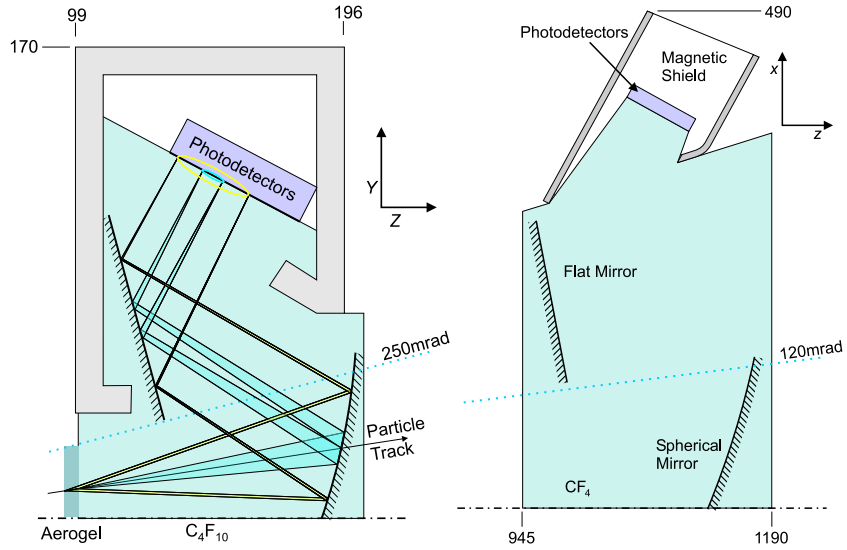

Figure 3.6: Cross-section of the RICH1 (left) and RICH2 (right) detectors, showing the relative positions of the spherical mirrors, flat mirrors and the photodetectors [84].

Figure 3.7: The LHCb RICH2 detector during installation at IP8 [50]. The green box on the left of the photograph is the magnetic shield which contains the photodetectors.

light cone is focused by spherical mirrors and the use of flat mirrors allows the photon detectors to be located outside of the detector acceptance. The RICH1 spherical mirrors are constructed from a composite carbon material which is chosen for its low contribution to the material budget. The flat mirrors are located outside the detector acceptance which allows them to be constructed from a glass substrate with an aluminum coating. Since RICH2 is located after the tracking stations the material budget of the mirrors is less critical, facilitating the use of glass based mirrors. The mirror alignment must be better than 0.1 mrad, which will be achieved with a laser-based alignment system [88]. A photograph of the RICH2 detector during installation is shown in Figure 3.7.

3.4 Photon Detectors and Readout

In light of the discussion concerning the expected light yield from Cherenkov radiation and the contributions to the reconstructed Cherenkov angle resolution, the response of the LHCb RICH photon detectors and readout electronics must fulfil the following requirements:

- **Single photon sensitivity**: Since Cherenkov radiation is such a weak light source, as shown by equation 3.3, it is important that the detector is sensitive to individual hits.
- **A high quantum efficiency**: As is shown by equation 3.6, the number of detected photo-electrons is proportional to the quantum efficiency. Furthermore, the photo-cathode must be sensitive to a sufficiently broad range of photon energies.
- **A high signal to noise ratio**: Background hits degrade the performance of the off-line ring-finding algorithms.
- **40 MHz readout rate**: The photon detectors must be capable of efficiently sampling the photon-induced signals at a repetition rate of 40MHz.

In terms of the environment in which the photon detector must operate, important factors to consider are:

- **Radiation tolerance**: The photon detectors and on-detector electronics must be tolerant to radiation doses up to 3 kRad/yr.

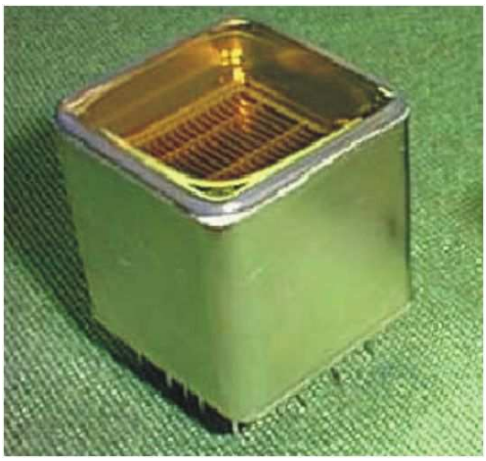

Figure 3.8: A Hamamatsu 12-dynode 64 anode MaPMT [91].

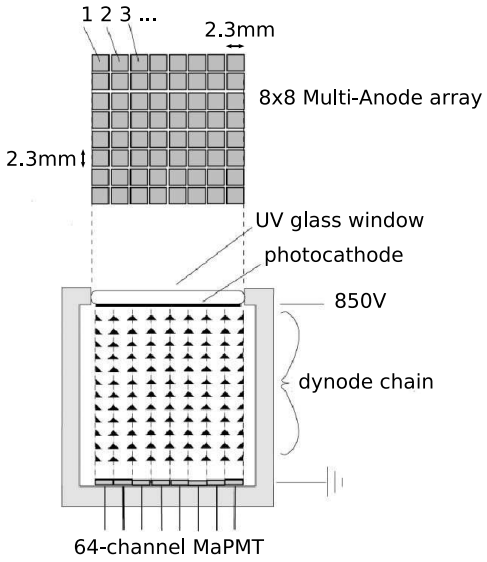

Figure 3.9: Schematic of the dynode chain in a Hamamatsu MaPMT.

- **Magnetic field tolerance**: Must be insensitive to magnetic fringe fields of order 20-30 Gauss.

Two photon detector technologies have been considered for the LHCb RICH detectors; the Hamamatsu Multi-anode Photo Multiplier Tube (MaPMT) and the Pixel Hybrid Photon Detector (HPD) developed at CERN in collaboration with industry [89, 90].

3.4.1 The Hamamatsu Multi-anode Photomultiplier Tube

The Hamamatsu M64 family of multi-anode photomultiplier tubes (MaPMTs) consist of an 8x8 array of square anodes, each with its own dynode chain and encapsulated in a single vacuum tube. Each of the 64 channels operates in much the same manner as a conventional photomultiplier tube. Photons enter via a 0.8mm thick UV glass window and excite photoelectrons from a bialkali photocathode deposited on the inner surface of the window. The photoelectron is accelerated and focused electrostatically onto the first dynode of one of the 64 independent dynode chains. After the first dynode are a series of dynodes with progressively increasing voltage. Each dynode is coated with a secondary emitter material, BeO or Mg-O-Cs, which yields 2-5 electrons for every incident electron with energy over 100 eV. In this manner an electron cascade is initiated, leading to an

amplification of $\mathcal{O}(10^6)$ for a 800 V potential, with a 5 ns pulse length. Each of the 64 anodes has an active area of 2×2 mm^2, with a 0.3 mm dead zone between the pixels. Since there is a dead area surrouding the photocathodes, a set of quartz lenses are used to focus the incident photons onto the active area of the MaPMTs.

The performance of a 3×3 array of 12-dynode MaPMTs has been tested in a CERN charged particle beam with a prototype RICH detector and found to meet the RICH photon detector requirements for Cherenkov angle resolution and magnetic field tolerance [87]. However, the electronic readout of the MaPMT used an ASIC (Application-Specific Integrated Circuit) that is not designed to meet the LHCb trigger and readout requirements. The particular Analogue Pipeline Voltage (APVm) ASIC used is unable to readout the analogue MaPMT signals at the 1MHz Level-0 trigger rate and it is not possible to trigger on consecutive bunch crossings [92].

The MaPMT front-end readout must have a peaking time and sampling frequency compatible with the 40 MHz bunch crossing frequency and the readout speed must match the 1 MHz Level-0 accept rate. The pipeline buffer must store events for the 4 μs Level-0 trigger latency. The VELO and IT sub-detectors have the same requirements and a custom 128 channel pipelined ASIC has been developed for their use [93, 53]. The so-called *Beetle* chip was also adopted for use in the MaPMT readout. However, the dynamic range of the standard *Beetle* is incompatible with output of the 12-dynode MaPMT. Hence, a modified version of the chip was developed with a front-end amplifier customised for the 12-dynode amplifier; the modified chip is called the *BeetleMA*. The performance of a 12-dynode MaPMT readout with a *BeetleMA* ASIC in a CERN charged particle beam is the subject of Chapter 4.

In 2002 Hamamatsu produced a 8-dynode version of the M64 MaPMT family. The 8-dynode version provides a gain of 50,000 electrons for a 800 V potential, which is compatible with the dynamic range of the standard *Beetle* input amplifier. The performance of the 8-dynode MaPMT with the standard *Beetle* 1.2 chip is discussed in section 4.5.

3.4.2 The Pixel Hybrid Photon Detector (HPD)

The pixel HPD was developed at CERN in collaboration with DEP [1] [90]. A photograph of the HPD and schematic of the operating principals are shown in Figures 3.10 and 3.11 respectively. A photon enters through a spherically-curved quartz window and may

[1] Delft Electronic Products, Netherlands

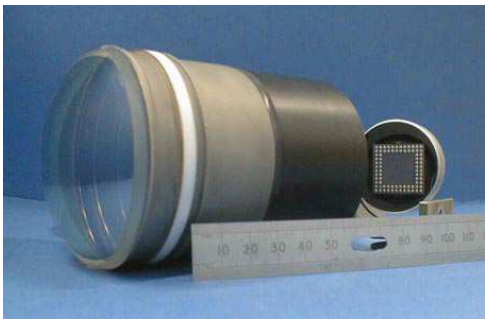

Figure 3.10: A prototype HPD detector. The pin grid array (PGA) for the readout of the Si sensor is shown reflected in the mirror [84].

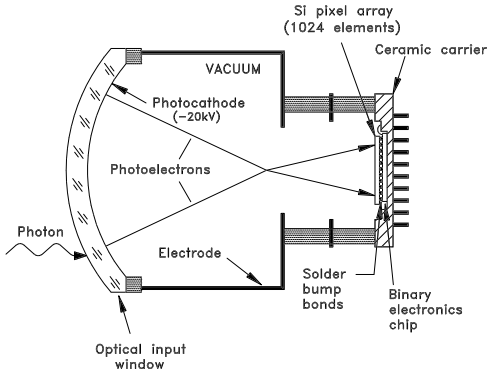

Figure 3.11: Schematic illustrating the HPD operating principals [84].

eject a photoelectron at a multi-alkali photocathode deposited on the inner surface of the window. Photoelectrons are accelerated towards the anode by a 20kV potential. Two further electrodes focus the electrons electrostatically onto the pixelated anode assembly, with a demagnification factor of approximately 5.4 from cathode to anode. The anode assembly consists of a 300 μm thick array of 32×256 reverse biased p-n junctions, bump bonded to a custom binary readout chip [94]. The anode assembly is encapsulated within the vacuum assembly. The readout chip converts the charge deposited in the silicon into a binary signal which is readout at the 40MHz LHC bunch crossing rate.

A discussion of the final choice of technology for the LHCb RICH photodetectors is presented in Chapted 4.

3.5 Pattern Recognition and Simulated Particle Identification Performance

In the RICH system, the particle identity of reconstructed tracks is determined from both "global" and "local" pattern recognition algorithms. In the "global" approach, for each track the number and position of expected Cherenkov photons on the photo-detector plane is calculated for a particular particle hypothesis; the final particle assignments correspond to the combination of all track particle hypothesis that maximises a log-likelihood function based on the observed photon detector yields. Whilst in the "local"

approach the following log-likelihood is maximised for each track *independently*,

$$\ln\mathcal{L}(\theta_{\mathcal{H}}) = \sum_i \ln\left(1 + \frac{1}{\sqrt{2\pi}\sigma_\theta} e^{-\frac{\theta_i - \theta_{\mathcal{H}}}{2\sigma_\theta^2}}\right) \tag{3.7}$$

where θ_i is the reconstructed emission angle of hit i, $\theta_{\mathcal{H}}$ the expected emission angle assuming a particle hypothesis $\mathcal{H} \in e, \mu, \pi, \mathrm{K}, \mathrm{p}$ and σ_θ is the Cherenkov angle resolution. The local approach is computationally faster than the global algorithm but the local algorithm is subject to the background from other tracks, which are correctly accounted for in the global approach. A typical strategy is to use the fast local algorithm to seed the global algorithm. An example fit to simulated Cherenkov hits in the RICH1 and RICH2 detectors with the pattern recognition algorithms is shown in Figure 3.12.

The particle type of reconstructed tracks is identified using information from the RICH, calorimeter and muon systems. A global likelihood hypothesis for each particle type is formed by combining the particle likelihood hypothesis of each sub-detector as follows:

$$\begin{aligned}
\mathcal{L}(h) &= \mathcal{L}^{\mathrm{RICH}}(h)\mathcal{L}^{\mathrm{CALO}}(\text{non } e)\mathcal{L}^{\mathrm{MUON}}(\text{non } \mu) \\
\mathcal{L}(\mu) &= \mathcal{L}^{\mathrm{RICH}}(\mu)\mathcal{L}^{\mathrm{CALO}}(\text{non } e)\mathcal{L}^{\mathrm{MUON}}(\mu) \\
\mathcal{L}(e) &= \mathcal{L}^{\mathrm{RICH}}(e)\mathcal{L}^{\mathrm{CALO}}(e)\mathcal{L}^{\mathrm{MUON}}(\text{non } \mu)
\end{aligned}$$

where h represents a hadron, μ a muon and e an electron. The absolute likelihood value is not useful as the scale will be different for each event. The true particle type is identified by making cuts on the differences between particle likelihoods. For this purpose a delta-log likelihood (DLL) function is defined as,

$$\mathrm{DLL} = \Delta\ln\mathcal{L}_{AB} = \ln\mathcal{L}(A) - \ln\mathcal{L}(B) = \ln\left(\frac{\mathcal{L}(A)}{\mathcal{L}(B)}\right) \tag{3.8}$$

where A and B are two different particle hypothesis. The performance of the RICH PID can be measured by the difference in likelihood between particle hypothesis as a function of momentum. Figure 3.13 shows the significance of π-K separation $\Delta\sigma$,

$$\Delta\sigma = \sqrt{2|\Delta\ln\mathcal{L}_{\pi\mathrm{K}}|} \tag{3.9}$$

between the pion and kaon hypothesis for true pions. There is a clear separation of at least 3σ over the required momentum range [84]. The particle identification performance in the context of selecting protons for flavour tagging is described in Chapter 5 and for

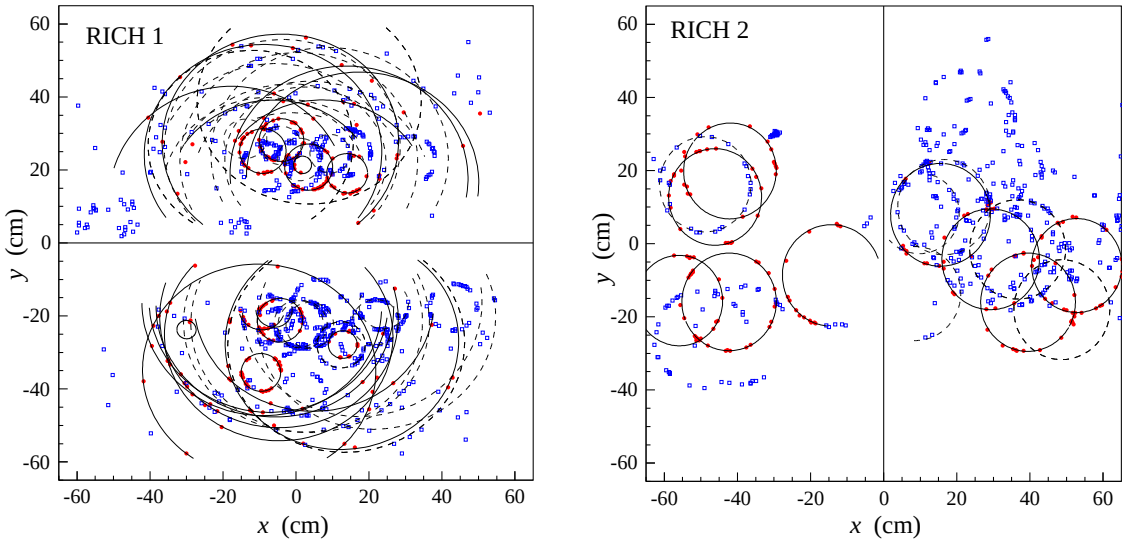

(a) RICH 1

(b) RICH 2

Figure 3.12: Photon detector hits and reconstructed Cherenkov rings (black lines) from the simulation of $B^0_d \to \pi^+\pi^-$ events. The Cherenkov hits associated to a track by the pattern recognition algorithms are indicated by red dots. The blue dots are caused by backgrounds such as secondary particles, electronic and detector noise, or are associated with tracks not reconstructed by the tracking algorithms. The smaller radii rings in RICH1 are due to the C_4F_{10} radiator, whilst the larger rings originate from the aerogel [49].

the purpose of reconstructing charmless two-body decays of the Λ_b baryon in Chapter 6.

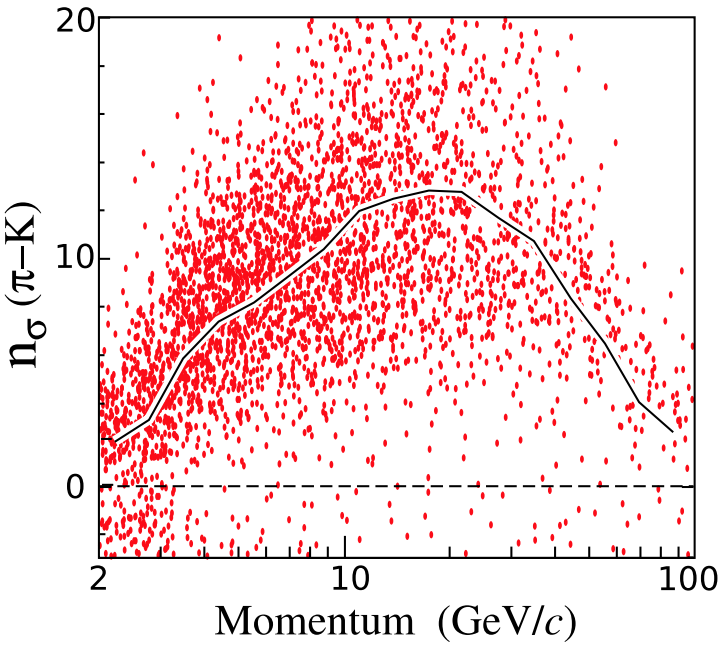

Figure 3.13: π-K separation in units of σ as a function of momentum for true pions, from the simulation of $B^0_d \to \pi^+ \pi^-$ events [49].

Chapter 4

Characterisation of the BeetleMA Pulse Shape in a Charged Particle Beam

This chapter presents the measurement of the readout pulse shape from a BeetleMA ASIC coupled to a 12-dynode Multi-anode photomultiplier (MaPMT), mounted in a prototype RICH vessel in a CERN charged particle beam. Knowledge of the pulse shape is important since the spill-over of signal from a previous bunch-crossing will lead to ghost pixel hits and the possible drift of the pedestal outside the dynamic range of the amplifier. In order to extract the pulse shape, an analytic function is developed that describes the number of expected electrons at the end of a dynode chain which includes photoelectric conversion on the first dynode and is adapted to extract the time-dependency of the BeetleMA output. The chapter concludes with a discussion of the final photon detector choice.

The performance of 12-dynode MaPMTs has been previously measured in a CERN charged particle beam and the device was found to be a viable photon-detector for the LHCb RICH detectors [92]. However, readout of the MaPMT in a manner compatible with the LHCb trigger and electronic requirements has yet to be established. This section presents a study of a 3×2 array of 12-dynode MaPMTs with a BeetleMA readout (v1.2/MA0). Specifically, the time evolution of the BeetleMA output, referred to as the pulse shape, is extracted from fits to ADC spectra of known time range. Measurement of the pulse shape is important since if the signal return to zero time is too long it will not be possible to trigger on consecutive events.

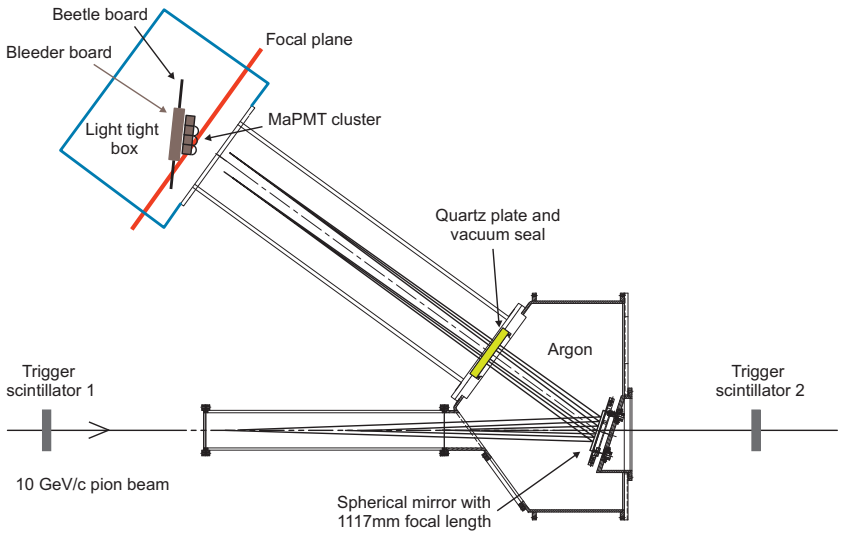

Figure 4.1: Schematic of the 12-dynode MaPMT testbeam setup. Cherenkov light generated by the incoming beam is focused by the spherical mirror through a quartz window onto the plane of MaPMTs. The two scintillators are used for the data acquisition trigger.

4.1 Testbeam setup

Measurement of the 12-dynode MaPMT / BeetleMA pulse shape was conducted in parallel with performance tests of a 8-dynode MaPMT with unmodified Beetle 1.2 readout. The experimental setup and data-acquisition was common to both; the results of 8-dynode tests are discussed in section 4.5. The tests were conducted with a prototype RICH vessel at the T9 PS beam facility at CERN. The asynchronous beam was made up of 10 GeV pions with $\sim 5\%$ electron contamination, the latter being vetoed by a threshold Cherenkov counter. The experimental setup is shown in Figure 4.1. The prototype RICH detector consists of a 1m long tube of 90 cm diameter and is filled with either argon or CF_4 radiator gas. The Cherenkov light generated by the pions as they traverse the length of the tube is focused by a spherical mirror through a quartz window into a light tight box containing the array of MaPMTs and readout electronics. The mirror was mounted on micrometer screws, which allowed for the fine adjustments needed to align the Cherenkov ring on the plane of photon detectors.

A close packed 3×2 array of 12-dynode MaPMTs were mounted on a bleeder board[1], which supplied the high voltage to the MaPMTs, the mechanical support and the interface to the readout electronics. The BeetleMA readout chips were mounted on a

[1] developed by the Cambridge HEP group.

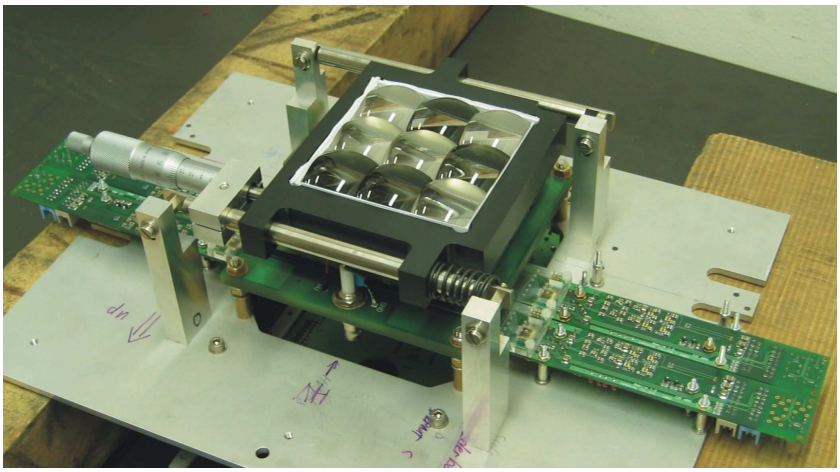

Figure 4.2: The 3×2 array of 12-dynode MaPMTs complete with lenses and four beetle board readouts.

so-called *Beetle board*, which connected to a pair of MaPMTs via the rear of the bleeder board, and provided the interface to the data acquisition system. Figure 4.2 shows a photo of the MaPMT, bleeder board, lens and beetle board assembly, prior to mounting inside the light tight box.

4.1.1 Trigger timing and data acquisition

The data acquisition (DAQ) system is shown schematically in Figure 4.3. The BeetleMA ASICs continuously sample the MaPMT outputs every 25 ns, storing the samples in a 4 μs (160×25 ns) analogue pipeline. Event readout is triggered by the coincidence between two scintillators mounted along the beam axis. This causes the SEQSI[2] programmable control module to generate a low voltage differential signal (LVDS), which is transmitted to the BeetleMA chip via the Beetle board.

To ensure that the peak of the MaPMT signal is sampled, the trigger timing is optimised by scanning the signal output from light generated by LEDs positioned at the beam entrance as a function of a trigger delay introduced between the scintillator coincidence and the SEQSI. In addition, the Beetle chip contains a latency setting which enables adjustments in units of 25 ns. The latency value corresponds to the number of 25 ns clock periods between the signal entering the analogue pipeline and the trigger decision.

[2]Rutherford Appleton Laboratory, Oxford.

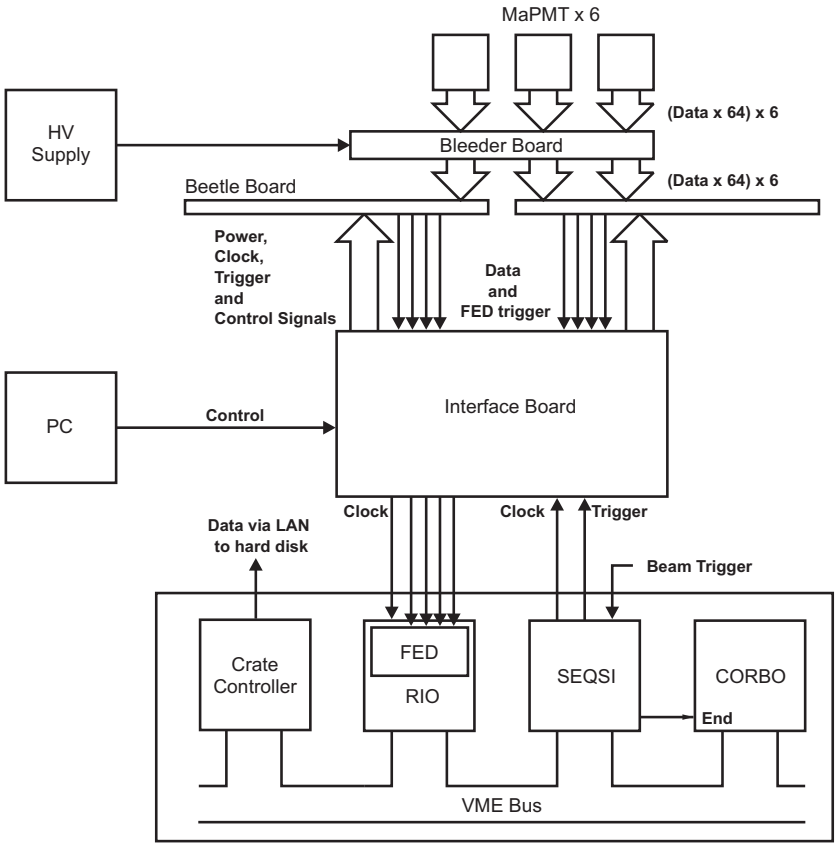

Figure 4.3: Schematic of the MaPMT electronic readout and data acquisition system.

Since the pion beam is asynchronous, the point sampled on the MaPMT output will vary in time by up to 25 ns between events. However, the time of the trigger relative to the 40 MHz sampling clock is digitised with a time-to-digital convertor (TDC), such that the relative time of any one sample point compared to another is known. This feature is exploited in section 4.3 to measure the MaPMT / BeetleMA pulse shape.

Differential analogue signals are transmitted from the Beetle boards to Flash ADCs (FADCs), which are embedded in the so-called Front-End Digitizer (FED)[3] card. The FED is a PCI Mezzanine Card (PMC) which is mounted inside a VME based mother-board and processor unit, called the RIO [4] in Figure 4.3. The analogue inputs to the FED are continuously digitised by the 9-bit FADCs at a 40MHz sampling rate. The FED and BeetleMA sampling clocks were both operated from a 40MHz clock generated by the SEQSI; this was done to preserve the phase relationship between the sample points and trigger signals. On receipt of a trigger from the SEQSI, the delay of which also required optimisation, the sampled FADC data was stored in memory. After readout from the BeetleMA is complete, the SEQSI notifies the CORBO[5] module which generates a VME interupt signal. In response to this interupt the data from the FED memory is transmitted for offline storage via the crate controller.

4.1.2 Method to extract the BeetleMA pulse shape

The time evolution of the analogue signal generated by the MaPMT / BeetleMA can be extracted from knowledge of the TDC value, Beetle latency setting and the ADC spectra.

Since the beam is asynchronous the time between the 40 MHz sampling clock and the trigger signal results in a flat 25 ns wide TDC distribution; this means that a single event samples a point on the pulse shape with a random 25 ns distribution. By taking multiple samples the pulse shape is fully sampled over a 25 ns width. Furthermore, the Beetle latency setting allows for 25 ns unit increments between the trigger and sample time. Thus, by combining the TDC and Beetle latency settings, the pulse shape can be measured with 1 ns resolution. To extract the pulse amplitude corresponding to a particular time interval, a fit is made to the ADC spectrum of events which fall within that time interval. The development of a function suitable for this purpose is the subject

[3]Rutherford Appleton Laboratory, Oxford.
[4]RIO, CES Model No.8061.
[5]CORBO, CES RCB8047.

of the next section.

4.2 Describing PMT spectra

In order to extract the MaPMT / BeetleMA pulse height, a fit must be made to the ADC spectrum. A function that describes the ADC spectra of MaPMTs was developed for the 1998 testbeam from an exact analytic expression for the probability of measuring k_n electrons at the end of a photomultiplier dynode chain [95]. The derivation is based on the assumption that the number of photoelectrons per event, as well as the number of secondary electrons caused by a single primary electron incident on a dynode, can be described by Poisson distributions. The exact expression is a function of

- the mean number of photoelectrons, λ_1, incident on the first dynode, and
- the gain of the n MaPMT dynodes, $g_1 \cdots g_n$.

The probability to find k_n electrons at the end of a chain of n dynodes is determined from a numerical algorithm that requires k_n^3 operations, which is prohibitive for a MaPMT with a typical $\mathcal{O}(10^6)$ gain. Therefore, for an MaPMT with n dynodes, only the exact distribution up to m dynodes is calculated and then scaled by the gain of the remaining dynodes

$$g_{\text{left}} = g_{m+1} g_{m+2} \cdots g_n. \tag{4.1}$$

The approximated probability for k_n electrons at the end of a chain of $n-1$ dynodes, is given by

$$P_{\sim}(k_n) = \sum_{j=0}^{j=\infty} \frac{1}{\sqrt{2\pi}\sqrt{j}\sigma_0} e^{-\frac{(j g_{\text{left}} - k_n)^2}{(\sqrt{2j}\sigma_0)^2}} P(j) \tag{4.2}$$

where

$$\sigma_0 = (g_{m+1} g_{m+2} + \cdots + g_n) \left(\frac{1}{g_{m+1}} + \frac{1}{g_{m+1} g_{m+2}} + \cdots + \frac{1}{g_{m+1} \cdots g_n} \right)^{\frac{1}{2}}$$

and $P(j)$ is the exact probability of j electrons after m dynodes. In turns out that it is sufficient to only calculate the sum for values of $j.g_{\text{left}}$ that are a few $\sigma_{\text{scale}} = \sqrt{j}\sigma_0$ around k_n [95].

4.2.1 Modelling the photoelectric conversion at the first dynode

The semi-transparency of the photocathode allows for photoelectric conversion on the first dynode [96]. However, this effect is not included in the expression for PMT spectra described by equation 4.2. The following details the modification of equation 4.2 to include this effect.

The number of photoelectrons produced by photoelectric conversion on the first dynode is assumed to follow a Poisson distribution with a mean γ_1. Thereafter, it is assumed that the behaviour is modelled by equation 4.2. Therefore, the probability of k_n photoelectrons at the end of the dynode chain due to photoelectric conversion on the first dynode, $P^{\mathrm{DC}}_{\sim}(k_n)$, is given by

$$P^{\mathrm{DC}}_{\sim}(k_n) = \sum_{h=0}^{h=\infty} \frac{1}{\sqrt{2\pi}\sqrt{h}\sigma_0} e^{-\frac{(hg_{\mathrm{left}}-k_n)^2}{(\sqrt{2h}\sigma_0)^2}} P^{\mathrm{DC}}(h), \tag{4.3}$$

where $P^{\mathrm{DC}}(h)$ is the exact probability of h photoelectrons after $m-1$ dynodes due to photoelectric conversion on the first dynode. The total probability of k_n electrons at the end of the dynode chain $P^{t}_{\sim}(k_n)$, including both photoelectric conversion at the photocathode and the first dynode, is therefore a convolution of $P_{\sim}(k_n)$ and $P^{\mathrm{DC}}_{\sim}(k_n)$,

$$P^{t}_{\sim}(k_n) = P^{PC}_{\sim}(k_n) * P^{DC}_{\sim}(k_n), \tag{4.4}$$

where $P_{\sim}(k_n)$ is labelled $P^{PC}_{\sim}(k_n)$ to emphasise that this probability derives from photoelectric conversion on the photocathode. The resulting analytic expression is given in Appendix A.1.

4.2.2 Fitting the ADC spectra

In practice, the number of electrons at the end of the last MaPMT dynode is not measured. Rather, the electrical signal from the MaPMT is input into the Beetle 1.2 / MA0 front-end chip, from which the signal is transmitted to off-detector electronics for digitisation into integer ADC units. It is from the sprectra of ADC counts grouped by TDC value and the Beetle latency setting that the Beetle 1.2 / MA0 pulse height must be extracted. Therefore, the function in 4.4 must be extended to relate electrons at the end of the dynode chain, k_n, to the measured ADC value, k_{adc}.

First, electronic noise is accounted for by convolving the probability function with a Gaussian of width σ. The probability of measuring k_n electrons, including the effects of electronic noise, is given by

$$F(k_n) = \frac{1}{\sqrt{2\pi}\sigma} e^{-\frac{k_{adc}^2}{2\sigma^2}} * P_{\sim}^{t}(k_n). \tag{4.5}$$

Evaluation of this convolution is given in Appendix A.2. It is useful to split $F(k_n)$ into the signal and pedestal contributions, $F^S(k_n)$ and $F^P(k_n)$ respectively,

$$F(k_n) = F^S(k_n) + F^P(k_n). \tag{4.6}$$

To translate the pedestal to ADC units, the electrons at the end of the dynode chain, k_n, are scaled by a time constant factor, c, and translated by a pedestal offset p_0. The signal is converted to ADC units by scaling the electrons, k_n, by a *time dependent* conversion factor, c_{eff}, and translating by the same pedestal offset p_0. The time dependent conversion factor, c_{eff}, accounts for the time evolution of the signal from the Beetle 1.2/MA0. Therefore, the Beetle 1.2/MA0 pulse shape can be extracted from fits of c_{eff} to ADC sprectra of known time interval (i.e. known Time-Digital-Convertor (TDC) values and Beetle latency settings).

If the ADC counts are considered a continuous variable, the probability of measuring k_{adc} counts is given by

$$F_{\text{cont}}(k_{adc}, t) = F^S((k_{adc} - p_0)/c_{eff}(t)) + F^P((k_{adc} - p_0)/c). \tag{4.7}$$

Since the readout electronics measure only integer ADC units, the function for fitting the measured ADC spectra is

$$F(k_{adc}, t) = \int_{k_{adc}-0.5}^{k_{adc}+0.5} F_{\text{cont}}(k'_{adc}, t) dk'_{adc}. \tag{4.8}$$

The free parameters of this function are listed in Table 4.1. Only the gain of the first dynode is a free parameter; the gains of the others dynodes are calculated from

$$g \propto V^{\alpha}, \tag{4.9}$$

where V is the potential difference over which the electrons are accelerated and, for the MaPMTs tested, $\alpha = 0.75$ [87]. The proportionality constant is calculated from the 1st

Parameter	Description
λ_1	photoelectrons incident on 1st dynode
g_1	gain of 1st dynode
p_0	pedestal mean
σ_0	pedestal width
c	time constant electron to ADC conversion factor
c_{eff}	time dependent electron to ADC conversion factor
γ_1	photoelectrons from photoelectric conversion on the 1st dynode

Table 4.1: The 7 free parameters in the function to describe photomultiplier ADC spectra.

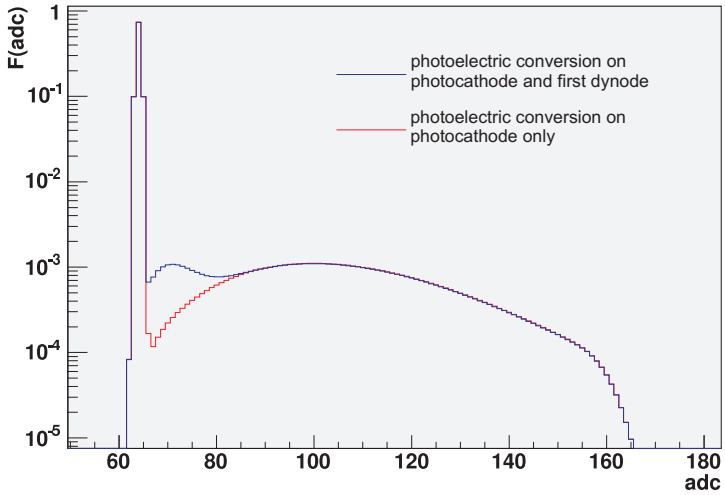

Figure 4.4: Modelling ADC spectra with photoelectric conversion on the first dynode (blue line) and not including this effect (red line). The parameters used in the simulated spectra are : $\lambda_1 = 0.06$ p.e's / event, $g_1 = 5.5$, $p_0 = 64$, $\sigma_0 = 0.4$, $c = 1 \times 10^{-4}$, $c_{eff} = 1.$ and $\gamma_1 = 0.01$ p.e's / event. A description of the parameters is given in Table 4.1.

dynode gain.

The effect on the ADC spectrum from including photelectric conversion on the first dynode is shown in Figure 4.4. It is shown in the next section that the function developed in this section models well the measured ADC spectra.

4.3 MaPMT / Beetle 1.2 MA0 pulse shape

The following steps are taken to reconstruct the pulse shape from the testbeam data.

1. The data are prepared by identifying and removing the effects of cross-talk between channels.

2. A fit is performed to the ADC spectrum formed from samples corresponding to the 5 ns time interval around the peak signal to background separation using equation 4.8 with 7 free parameters. Physically, all parameters except c_{eff} are independent of time.

3. All parameters are fixed except c_{eff}; the value of which is extracted from fits to ADC spectra which have been formed from samples corresponding to the same 5 ns time interval. Each value of c_{eff} corresponds to a point on the MaPMT/BeetleMA pulse shape at a point in time given by the midpoint of the time-interval.

In step 1, significant asymmetric cross-talk is observed between channels. Figure 4.5 shows the correlation between the ADC value of a typical pixel (number 286) and the neighbouring pixels. For the purposes of measuring the BeetleMA pulse shape the effects are removed by excluding those events where there is a significant ADC count in the cross-talk partner of the pixel being studied; a significant ADC count being defined as a value greater than $p_0 + 5\sigma_0$.

The ADC spectrum fits are performed with the MINUIT tool for function minimisation [97]. Since the free parameters c and c_{eff} are correlated, it is found that the fit converges faster if c_{eff} is defined as,

$$c_{eff}(t) = a_{eff}(t) \times c \tag{4.10}$$

with the time dependent effective amplitude, a_{eff}, becoming the free parameter in place of c_{eff}. The result of the 7 parameter fit to the ADC spectrum formed from samples taken in a 5 ns time interval at the time of peak signal to background separation is shown in Figure 4.6(a). The corresponding parameter values extracted are given in Table 4.2. After the 7 parameter fit has converged, all parameters are fixed except for a_{eff} and a fit is made to each ADC spectrum formed from 5 ns time intervals. Examples fits are shown in Figure 4.6 for time intervals corresponding to the time period before the signal

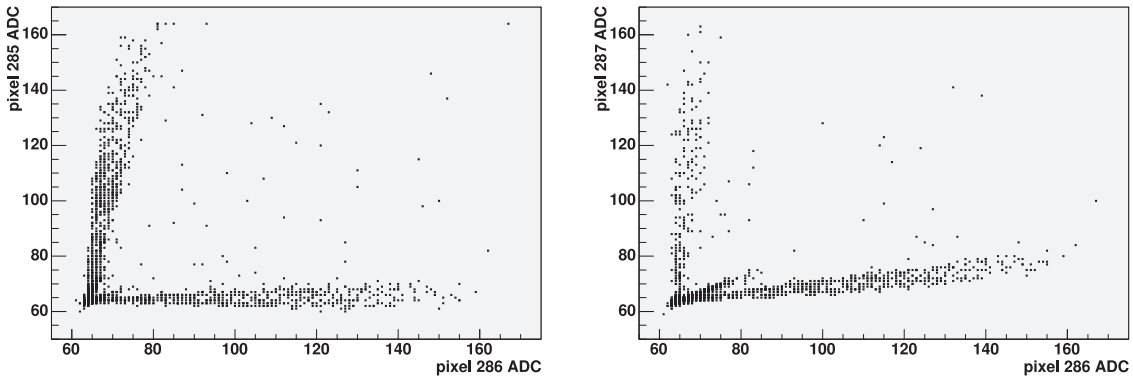

(a) (b)

Figure 4.5: Asymmetric cross-talk between MaPMT channels for a typical pixel (number 286) and the two adjacent pixels; (a) number 285 and (b) number 287.

Parameter	Fit Value
λ_1	$(5.688 \pm 0.004) \times 10^{-2}$ photoelectrons / event
g_1	5.68 ± 0.08
p_0	63.786 ± 0.007 ADC counts
σ_0	0.379 ± 0.005 ADC counts
c	$(1.0 \pm 0.3) \times 10^{-5}$
a_{eff}	7 ± 1
γ_1	$(1.4 \pm 0.2) \times 10^{-2}$ photoelectrons / event
χ^2/dof	46/93

Table 4.2: Results of the 7 parameter fit to the ADC spectrum of the peak signal-to-background separation.

(4.6(b)), at the signal peak (Figure 4.6(d)) and to the period corresponding to signal undershoot (Figure 4.6(c)).

The MaPMT / BeetleMA pulse shape is inferred by plotting the fitted value of a_{eff} at the midpoint of the 5 ns time-interval from which the ADC spectra was formed. The result is shown in Figure 4.7.

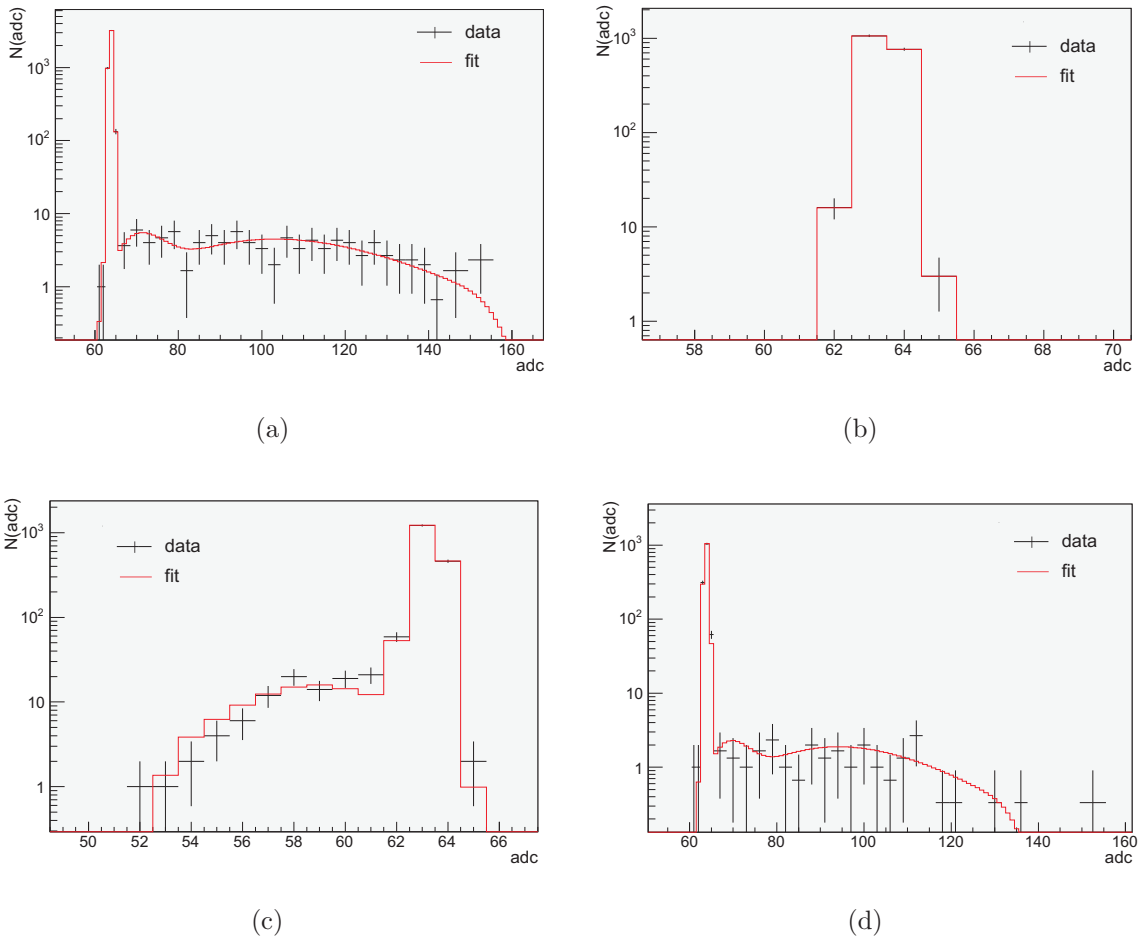

Figure 4.6: (a) The 7 parameter fit to the ADC spectra formed from samples taken in a 5ns time interval around the time of peak signal-to-background. The other 3 plots correspond to fits with a_{eff} as the only free parameter, to the ADC spectra formed from samples taken at (a) times before the signal ($t <$ 0 ns, $a_{eff} = 0$), (c) the period corresponding to signal undershoot ($t > 50$ ns, $a_{eff} < 0$) and (d) the period of peak signal-to-background (15 ns $< t <$ 20 ns, $a_{eff} = 7 - 8$).

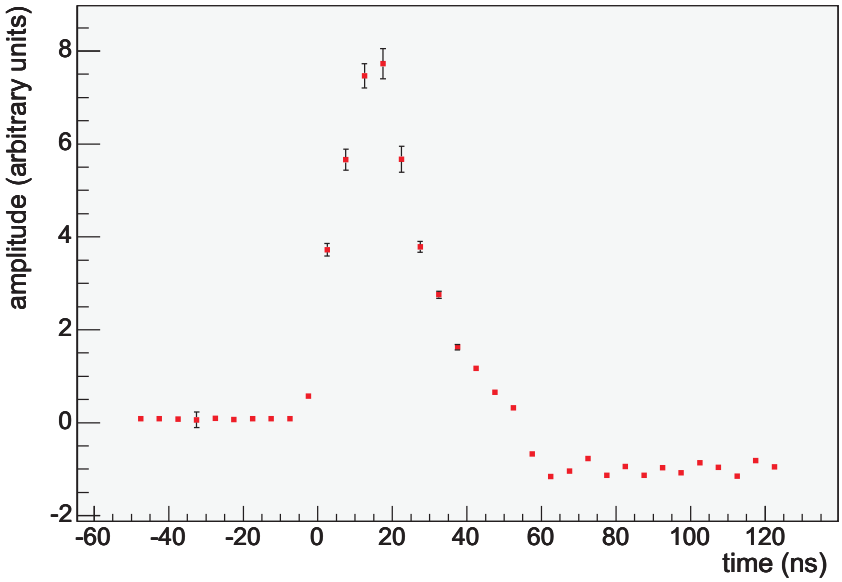

Figure 4.7: MaPMT / BeetleMA pulse shape as measured from fits to ADC spectra with equation 4.8. The amplitude corresponds to the a_{eff} fit value to 5ns wide ADC spectra.

4.4 Conclusion

The LHCb readout architecture specifies that the readout electronics must be able to trigger on consecutive bunch crossings. Therefore the pulse shape must return to zero within 25ns of the trigger. From Figure 4.7 it is evident that this is not the case for the pulse from the BeetleMA; the signal peaks at 20ns and has not returned to zero by the time of the last measurement point at 125ns. The effect of these features are twofold;

- The signal overshoot will lead to ghost hits.
- The signal undershoot will lead to the loss of genuine hits.

Furthermore, if the occupancy is such that the signal never returns zero before another hit arrives in the pixel, the pedestal may drift outside the dynamic range of the amplifier. The effect of the overshoot could be overcome by not triggering on consecutive events, but this would compromise the LHCb readout specification. The undershoot could be compensated for by lowering the threshold at which an ADC count is considered a hit; but this would be at the cost of increased background counts.

4.5 Choice of Photon Detector

Throughout the development of the RICH photodetectors the MaPMT solution has been developed as a backup option in case serious problems were encountered with the HPD development and production. The MaPMT was chosen as a backup option since, as a commercial product, the MaPMT itself required little development and it has been proven to be a successful photon detector for the HERA-B RICH detector [98].

In 2002 significant problems were encountered in the development of the procedure to solder each of the HPD sensor pixels to the readout chip. The number of pixels that were insensitive or noisy after the so-called bump-bonding procedure was unacceptably high, a problem caused by the solder joints between the pixel and readout chip breaking during the tube's vacuum bake-out cycle. The decision was therefore taken in 2003 to switch to the backup MaPMT option. This lead to intensive development of the MaPMT readout electronics and subsequent tests in a prototpye RICH detector. Significant problems were, however, encountered with the readout electronics during these tests; this included channel-to-channel cross talk and signal overshoot and undershoot.

Whilst the readout for the MaPMTs was being tested, the solution was found to many of the HPD production problems, in particular, the bump-bonding problem was solved by the use of a new high lead content solder. Given the problem encountered with the MaPMT readout it was decided to revert back to the HPD as the photon detector for the RICH system. By December 2006, all 484 HPDs required for the RICH1 and RICH2 detectors had been produced and successfully tested [99].

Chapter 5

Flavour Tagging with Baryons

This chapter presents a study of flavour tagging with protons and Λ baryons. It is shown that protons and Λ's have the potential to be useful for flavour tagging, but the implementation is challenging. However, a Λ produced in the same fragmentation process as a B_s^0 meson is found to have useful and implementable tagging power.

5.1 Flavour Tagging at LHCb

This section motivates the requirement for flavour tagging and presents the standard methods employed in LHCb. The aim is to familiarise the reader with the typical methods, figures of merit and performances that will serve as a basis for the later discussion of baryon flavour tagging.

5.1.1 Flavour tagging of neutral B mesons

$\mathcal{CP}$ violation studies typically require a measurement of an asymmetry, $\mathcal{A}_{\text{phys}}$, between the decays of B^0 and $\overline{B}^0$ mesons to some final state, f,[1]

$$\mathcal{A}_{\text{phys}} = \frac{\Gamma(B^0 \to f) - \Gamma(\overline{B}^0 \to f)}{\Gamma(B^0 \to f) + \Gamma(\overline{B}^0 \to f)} \tag{5.1}$$

In order to measure such an asymmetry the flavour of the signal B-meson at creation

[1] For simplicity the time dependences of the decay rates are suppressed.

needs to be known. This information can not be inferred from the B-meson decay products, as the neutral B-meson may have oscillated to the conjugate state before decay, and must be determined by information from the rest of the event.

A common technique, known as "opposite-side tagging", is to infer the flavour of the reconstructed B-meson from the other B-hadron in the event, commonly referred to as the *companion* B-hadron. The b-quark pair is assumed to be produced by a flavour conserving reaction, such as $\mathrm{g}+\mathrm{g} \to \mathrm{b}\ \overline{\mathrm{b}}$, whereby the flavour of the companion B-hadron must be opposite to that of the signal B-meson. Another common technique is called "same-side tagging", which exploits correlations in the fragmentation decay chain of the reconstructed B-hadron to infer the b-quark flavour at production.

The flavour tagging performance has a direct effect on the statistical uncertainty of a $\mathcal{CP}$ asymmetry measurement. To demonstate this, consider the number of observed events for a neutral B-meson decay, $\mathrm{N}_{\mathrm{obs}}$, and the corresponding charge conjugate decay $\overline{\mathrm{N}}_{\mathrm{obs}}$. The observed number of events can be expressed in terms of the true number of events, N and $\overline{\mathrm{N}}$, and the fraction of flavour tags that are incorrect, ω_{tag},

$$\begin{aligned} \mathrm{N}_{\mathrm{obs}} &= (1-\omega_{tag})\mathrm{N} + \omega_{tag}\overline{\mathrm{N}} \\ \overline{\mathrm{N}}_{\mathrm{obs}} &= (1-\omega_{tag})\overline{\mathrm{N}} + \omega_{tag}\mathrm{N}. \end{aligned} \tag{5.2}$$

The observed asymmetry, $\mathcal{A}_{\mathrm{obs}}$, is therefore diluted by a factor, $\mathcal{D}$, which is directly related to the wrong tag fraction:

$$\mathcal{A}_{\mathrm{obs}} = \frac{\mathrm{N}_{\mathrm{obs}} - \overline{\mathrm{N}}_{\mathrm{obs}}}{\mathrm{N}_{\mathrm{obs}} + \overline{\mathrm{N}}_{\mathrm{obs}}} = \mathcal{D}\mathcal{A}_{\mathrm{phys}} \qquad \text{where } \mathcal{D} = (1 - 2\cdot\omega_{tag}). \tag{5.3}$$

It follows from a quadratic propagation of the binomial uncertainties of the number of observed events, $\mathrm{N}_{\mathrm{obs}}$ and $\overline{\mathrm{N}}_{\mathrm{obs}}$, that the statistical uncertainty on the observed asymmetry, $\sigma_{\mathcal{A}_{\mathrm{obs}}}$, is given by

$$\sigma^2_{\mathcal{A}_{\mathrm{obs}}} = \frac{4\mathrm{N}_{\mathrm{obs}}\overline{\mathrm{N}}_{\mathrm{obs}}}{\left(\mathrm{N}_{\mathrm{obs}} + \overline{\mathrm{N}}_{\mathrm{obs}}\right)^3} = \frac{1 - \mathcal{A}^2_{\mathrm{obs}}}{\mathrm{N}_{\mathrm{obs}} + \overline{\mathrm{N}}_{\mathrm{obs}}}. \tag{5.4}$$

As the observed asymmetry is diluted by wrong flavour tags, an event is not considered if the flavour can not be deduced from the tagging methods. The tagging efficiency, ε_{tag}, is defined as the fraction of offline selected events that are assigned a tag decision

$$\mathrm{N}_{\mathrm{obs}} + \overline{\mathrm{N}}_{\mathrm{obs}} = \mathrm{N}_{\mathrm{tag}} = \varepsilon_{tag}\mathrm{N}_{\mathrm{sel}}, \tag{5.5}$$

where N_{tag} is the number of tagged events and N_{sel} is the number of events that are reconstructed, triggered and passed by the offline selection algorithms. Combining equations 5.4 and 5.5:

$$\sigma^2_{\mathcal{A}_{\mathrm{obs}}} = \frac{1 - \mathcal{A}^2_{\mathrm{obs}}}{\varepsilon_{tag}\mathrm{N}_{sel}}. \tag{5.6}$$

The statistical uncertainty on the physical asymmetry, $\sigma_{\mathcal{A}_{\mathrm{phys}}}$ is thus,

$$\begin{aligned}\sigma_{\mathcal{A}_{\mathrm{phys}}} &= \frac{\sigma_{\mathcal{A}_{\mathrm{obs}}}}{1 - 2\omega_{tag}} = \frac{\sqrt{1 - \mathcal{A}_{\mathrm{obs}}}}{\sqrt{N_{sel}\varepsilon_{tag}}(1 - 2\omega_{tag})} \\ &= \frac{\sqrt{1 - \mathcal{A}_{\mathrm{obs}}}}{\sqrt{N_{sel}\ \varepsilon^{eff}_{tag}}}\end{aligned} \tag{5.7}$$

where the effective tagging efficiency, ε^{eff}_{tag}, is defined as :

$$\varepsilon^{eff}_{tag} = \varepsilon_{tag}(1 - 2\omega_{tag})^2. \tag{5.8}$$

The statistical uncertainty of the physical asymmetry is directly related to the effective tagging efficiency. The aim of the flavour tagging algorithms is therefore to maximise equation 5.8. The methods employed at LHCb to achieve this are the subject of the next section.

5.1.2 Flavour tag signatures

The opposite and same-side tagging techniques used at LHCb are depicted schematically in Figure 5.1 [100]. For opposite-side tagging one would ideally reconstruct all possible decay modes of the companion B-hadron. However, reconstructing such a large number of decay modes would be highly impractical to implement and maintain, and subject to low reconstruction and selection efficiencies on account of the high multiplicity of some decay modes. The solution is to use generic signatures, called *tags*, the charge of which is correlated with the flavour of the companion B hadron. At LHCb this is principally achieved by measuring either the charge of a lepton from a semileptonic B decay, called a "lepton tag", or by measuring the charge of a kaon from a $\mathrm{b} \to \mathrm{c} \to \mathrm{s}$ transition, referred to as a "kaon tag". Also, by inclusive reconstruction of the companion B decay vertex, the companion B flavour may be inferred from the vertex charge, a method called "vertex-charge" tagging.

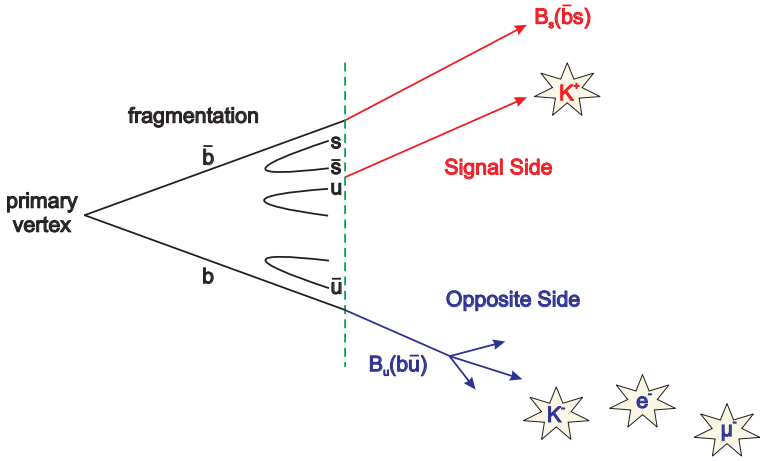

Figure 5.1: Topology of opposite-side flavour tagging with kaon, electron and muon tags and same-side tagging with a kaon produced in the fragmentation chain of the signal B-meson.

Same-side tags measure the production flavour of the signal B-hadron directly from particles produced adjacent to the signal B in the fragmentation process. For example, if a $B_s^0(\overline{b}s)$ is produced in the fragmentation of a $\overline{b}$ quark, an extra $\overline{s}$ quark is available. This may hadronise into a $K^+(\overline{s}u)$, the charge of which implies a B_s^0 at production. This is called a same-side kaon tag. Similarly, if the signal is a $B_d^0(\overline{b}d)$ then an extra $\overline{d}$ is available to hadronise into a $\pi^+(\overline{d}u)$, which is called a same-side pion tag.

The opposite-side tagging performance is subject to a number of intrinsic limitations that sets on upper limit on the potential effective tagging efficiency:

- If the companion B is neutral it may oscillate to the conjugate flavour state before decay, resulting in an incorrect assumption for the signal B flavour at production and subsequent enhancement of the wrong tag fraction.
- The tagging efficiency is limited by the branching fraction of each B-hadron species into kaons or leptons, combined with the production fraction of each B-hadron species.

The same-side tag is limited by the probability of producing a kaon/pion in the fragmentation chain of the signal B-meson. In addition, both the opposite and same-side tagging efficiencies will be limited by the track reconstruction efficiency and the efficiency of the algorithm to select the tag particle.

5.1.3 Tag selection

In order to select tag particles there are two principal categories of background to overcome: particles from the underlying fragmentation products of the pp collision and B-hadron decay modes that have the wrong tag particle charge, e.g. leptons from charm decays and kaons direct from the decay of a B_s^0 meson. Fortunately, for the reduction of the underlying event background, tag particles have certain characteristics that aids selection:

- Owing to the large B-hadron masses ($\sim$5 GeV), the lepton and kaon have a hard momentum spectrum. Also, the B-hadron decay products are distributed isotropically in the B rest frame, such that the tag particles have a large transverse momentum.
- The lepton and kaons are formed from weak interactions and are thus spatially displaced from the primary vertex. The impact parameter significance with respect to the reconstructed primary vertex is therefore a particularly powerful discriminant.

Reduction of the wrong charge background is more challenging, as the decay modes are typically both kinematically and topologically similar to the correct charge tag particles. Ultimately, parameters are tuned to maximise the effective tagging efficiency. For the lepton tag, cuts are made on the momentum and transverse momentum:

$$p > 5 \text{ GeV/c} \qquad p_t > 1.2 \text{ GeV/c} \tag{5.9}$$

Similarly, for opposite-side kaon tag selection, cuts are typically made on the kaon momentum, transverse momentum and impact parameter significance:

$$p > 3 \text{ GeV/c} \qquad p_t > 0.4 \text{ GeV/c} \qquad (\text{IP}/\sigma_{\text{IP}})_{\text{PV}} > 3.7 \tag{5.10}$$

The vertex-charge tag requires the reconstruction of the companion B-hadron vertex. However, given the detector acceptance and tracking limitations, a full reconstruction is not practical. Rather, a partial reconstruction of the companion B vertex is made, which, if the companion B is charged, will be biased toward this charge. Given that charged mesons do not oscillate, this has the advantage of no intrinsic dilution from flavour oscillations.

Same-side kaon tags are characterised by a phase space correlation with the signal B_s^0 meson. Thus, kaons are selected that have an impact parameter significance $(IP/\sigma_{IP})_{PV} < 2.5$, and relative to the reconstructed B_s^0, a minimum difference in pseudo-rapidity $|\Delta\eta| < 1$ and azimuthal angle $|\Delta\phi| < 1.1$. In addition, a cut is made on the mass difference between the B_s^0 K combination and the B_s^0 mass $\Delta m < 1.5$ GeV/c^2. Physically, this can be thought of as the combination of a kaon transverse momentum cut relative to the B-hadron, which should be small for a kaon produced in the B-hadron fragmentation chain, and a kaon momentum cut, which one would expect to be small compared to kaons from the decay of a B-hadron.

The same selection methods also apply to same-side pion tagging for reconstructed B_d^0 mesons. However, the high abundance of pions in the detector inhibits the performance of this tag.

5.1.4 Tagging performance

The search for each tag particle is done independently, thus it is possible for more than one tag to be found. In order to obtain the optimal tagging performance, the results of the opposite-side and same-side tags are combined. Studies are ongoing as to the optimal method of combining the tag decisions. At present, two methods are employed. The first is based on a neural network approach, which seeks to exploit high order correlations between tagging variables [101]. The second is a simple majority based decision and is described in detail below [102].

If more than one lepton is identified, the one with the greater transverse momentum is taken as it more likely to have come from a heavy B decay, rather than fragmentation. If the reconstructed signal is a B_s^0-meson then the same-side pion tag is ignored; similarly, the same-side kaon tag is neglected if the signal is a B_d^0-meson. If only two tags remain and they disagree, equation 5.8 implies that the overal tagging power benefits from not applying a tag decision in such cases. Finally, for the case of three tags, the final decision is taken as the majority decision of the three tags. This is the standard procedure for combining tag decisions and is for historical reasons referred to as the "combined TDR" decision [100].

The flavour tagging performance for 90k *selected* $B_s^0 \to J/\psi\,\phi$ events[2] is shown in

[2] an event is defined as selected if it passes the L0 trigger and the appropriate signal selection

Tag method	ε_{tag}^{eff} (%)	ε_{tag} (%)	ω_{tag} (%)
Muons	0.85 ± 0.06	5.80 ± 0.08	30.9 ± 0.6
Electrons	0.37 ± 0.04	4.21 ± 0.07	35.3 ± 0.8
OS kaons	1.55 ± 0.08	28.62 ± 0.15	38.3 ± 0.3
SS pi/k	2.64 ± 0.11	27.61 ± 0.15	34.5 ± 0.3
VertexCh	1.00 ± 0.07	21.25 ± 0.14	39.2 ± 0.4
Combined TDR	5.30 ± 0.22	54.72 ± 0.17	34.44 ± 0.22
Combined NN	6.73 ± 0.23	58.06 ± 0.17	32.98 ± 0.21

Table 5.1: Tagging performance for 90k selected $B_s^0 \to J/\psi\,\phi$ events. Uncertainties are statistical.

Tag method	ε_{tag}^{eff} (%)	ε_{tag} (%)	ω_{tag} (%)
Muons	1.15 ± 0.08	7.97 ± 0.11	31.0 ± 0.6
Electrons	0.41 ± 0.05	4.23 ± 0.08	34.4 ± 0.9
OS kaons	1.87 ± 0.10	26.01 ± 0.17	36.6 ± 0.4
SS pi/k	0.74 ± 0.07	39.81 ± 0.19	43.2 ± 0.3
VertexCh	0.96 ± 0.08	18.90 ± 0.15	38.7 ± 0.4
Combined TDR	4.08 ± 0.23	63.93 ± 0.19	37.36 ± 0.24
Combined NN	5.02 ± 0.24	63.74 ± 0.19	35.97 ± 0.24

Table 5.2: Tagginging performance for 65k selected $B_d^0 \to K\,\pi$ events. Uncertainties are statistical.

Table 5.1 and for 65K selected $B^0_d \to K\pi$ events in Table 5.2. The difference in tagging efficiency and wrong tag fraction between the decay channels can be understood in terms of the systematic effects caused by the trigger and kinematical correlations between the two B-hadrons [103]. This is the subject of the next section.

5.1.5 Interplay between the trigger and tagging

The LHCb L0 and L1 triggers are based on generic characteristics of B-hadron decays and so it is possible for the trigger decision to be made on either the signal or companion B-hadron. This has the effect of causing variation in tagging performance between the decay modes of interest [76]. For example, consider a trigger strategy that selects a muon with large impact parameter applied to the decay modes $B^0_s \to J/\psi(\mu^-\mu^-)\ \phi(KK)$ and $B^0_d \to D\pi$. It is assumed for simplicity that in both cases the B-meson flavour is inferred from an opposite-side kaon tag. For the B^0_s decay mode, the trigger will predominately select the muon from the decay of the J/ψ, while the B^0_d will be triggered by the companion B-hadron. Consequently, the B^0_d decay mode is biased towards events with a long lived, high impact parameter, companion B-hadron. The probability that the companion B-meson oscillates before decay, and thus implies the wrong flavour tag, is therefore greater for the B^0_d mode.

Wrong tag fraction variations are also seen between decay modes that trigger on the signal. The L0 lepton and hadron triggers have different transverse momentum requirements, thus biasing the kinematics of the signal B-hadron. As the kinematics of the two B-hadrons in an event are correlated, this results in differences in the transverse momentum of the companion B. Given the strong influence of the transverse momentum cut on the tag selections, this results in varying tagging performances.

The interplay between the trigger and tagging also has consequences for measuring the wrong tag fraction in data. As discussed in section 5.1.1, an asymmetry measurement requires a measurement of the wrong tag fraction. For signal decay modes with a flavour neutral final state this is achieved using a *control* channel that has a flavour specific final state. The systematic effects of the trigger requires that control channel samples must only be used if they bias the companion B in the same manner as the signal decay mode. One method to achieve this is to require that both the signal and control samples are triggered by the companion B-hadron. To correct for kinematic correlations between

algorithm.

	Proton decay mode (% of decays to protons)			
B-hadron	p	$\overline{\text{p}}$	p and $\overline{\text{p}}$	other (p p, $\overline{\text{p}}$ $\overline{\text{p}}$, etc.)
Λ_b (b u d)	$96.2 \pm 1.0\%$	$1.5 \pm 0.1\%$	$1.5 \pm 0.1\%$	$0.71 \pm 0.08\%$
B^- (b $\overline{\text{u}}$)	$10.1 \pm 0.4\%$	$43.3 \pm 0.8\%$	$46.4 \pm 0.8\%$	$0.24 \pm 0.06\%$
$\overline{B}{}^0_d$ (b $\overline{\text{d}}$)	$31.8 \pm 0.7\%$	$30.7 \pm 0.7\%$	$37.2 \pm 0.8\%$	$0.27 \pm 0.07\%$
$\overline{B}{}^0_s$ (b $\overline{\text{s}}$)	$31.2 \pm 1.5\%$	$32.8 \pm 1.6\%$	$35.4 \pm 1.6\%$	$0.6 \pm 0.2\%$

Table 5.3: Distribution of B-hadron decay modes that comprise decays either directly or indirectly to protons. The corresponding charge conjugate modes are implicitly included. Uncertainties are statistical.

the two B-hadrons, the wrong tag fraction is measured in the control channel in bins of the signal B phase space and then re-weighted to correct for phase space differences between the control and signal decay modes [104].

5.2 Flavour Tagging with opposite-side Protons

The flavour tagging methods outlined in section 5.1 make use of electrons, muons, pions and kaons. These particles are ideal for flavour tagging, as in addition to the intrinsic correlation between particle charge and the B-hadron flavour from which it originates, they are reconstructed and identified with high purity and efficiency. Protons are also well reconstructed and identified at LHCb over the momentum range 2-100 GeV/c [49]. The question therefore arises as to whether protons can be used for flavour tagging. In this section we present the potential performance of a proton flavour tag and discuss the possible implementation of such a tag.

5.2.1 Potential flavour tagging performance

The distribution of B-hadron decay modes to protons and anti-protons is shown in Table 5.3 for the decay of 100k inclusive $b\overline{b}$ events. The study is made at the generator level and as such does not include any reconstruction and selection effects, but does include a 400 mrad detector acceptance cut, which is applied at the generator level. A

	kaon decay mode (% of decays to kaons)			
B-hadron	K^+	K^-	K^+ and K^-	other
Λ_b (b u d)	22.4 ± 0.7	50.7 ± 1.1	19.3 ± 0.7	7.6 ± 0.4
B^- (b $\overline{u}$)	4.7 ± 0.1	70.1 ± 0.4	11.9 ± 0.2	13.3 ± 0.2
$\overline{B}{}^0_d$ (b $\overline{d}$)	18.5 ± 0.2	54.7 ± 0.4	14.1 ± 0.2	12.6 ± 0.2
$\overline{B}{}^0_s$ (b $\overline{s}$)	25.6 ± 0.5	26.1 ± 0.5	35.3 ± 0.6	13.0 ± 0.4

Table 5.4: Distribution of B-hadron decay modes that comprise decays either directly or indirectly to kaons. The corresponding charge conjugate modes are implicitly included. Uncertainties are statistical.

B-hadron	f_B (%)	$\mathcal{B}_{\text{incl}} \to \ldots \text{p}$ (%)	ε_{tag}^{pot} (%)
Λ_b	8.02 ± 0.06	63.1 ± 0.8 (29.2 ± 0.5)	5.06 ± 0.05 (2.34 ± 0.03)
B^+	41.0 ± 0.1	8.5 ± 0.1 (59.7 ± 0.3)	3.49 ± 0.04 (24.5 ± 0.1)
B^0_d	40.9 ± 0.1	7.4 ± 0.1 (55.1 ± 0.3)	3.02 ± 0.04 (22.6 ± 0.1)
B^0_s	10.05 ± 0.07	6.7 ± 0.2 (52.4 ± 0.6)	0.68 ± 0.02 (5.27 ± 0.05)

Table 5.5: Percentage of events with a proton either directly or indirectly from the decay of a B-hadron (ε_{tag}^{pot}). Calculated from the product of the inclusive branching ratio to protons ($\mathcal{B}_{\text{incl}} \to \ldots \text{p}$) and the b quark hadronisation fractions (f_B). For comparison, the corresponding kaon values are shown in parenthesis. Uncertainties are statistical.

Λ_b (b u d) decays to a proton and the $\overline{\Lambda}_b$ ($\overline{b}$ $\overline{u}$ $\overline{d}$) decays to an anti-proton in $96.2 \pm 1.0\%$ of cases. In contrast, the B^- (b $\overline{u}$) decays to an anti-proton and the B^+ ($\overline{b}$ u) to a proton approximately four times more frequently than the conjugate case. For the case of B^0_d and B^0_s mesons there is no correlation between b-quark flavour and proton decay mode. The correlation between the flavour and proton charge in the case of Λ_b baryons and B^+ mesons suggests the possibility of an opposite-side proton flavour tag. However, the Λ_b and B^- proton decay modes have the opposite correlation between b-quark flavour and proton charge. Compare this with the distribution of B-hadron decays to kaons shown in Table 5.4, for which the B-hadron flavour correlation with kaon charge is the same for all B-hadron flavours (except B^0_s-mesons, for which there is no correlation on account of the higher frequency of flavour oscillations).

B-hadron flavour	ε_{tag}^{eff} (%)	ω_{tag} (%)	ε_{tag} (%)
Λ_b	4.35 ± 0.06	1.9 ± 0.2	4.71 ± 0.06
B^+	0.70 ± 0.04	19.0 ± 0.8	1.82 ± 0.04
B_d^0	0.001 ± 0.001	51 ± 1	1.87 ± 0.04
B_s^0	0.001 ± 0.002	47 ± 2	0.50 ± 0.02

Table 5.6: Maximum potential proton tagging performance for each B-hadron species, *before reconstruction and offline tag selection*. From the analysis of 120k $B_s^0 \to J/\psi\,\phi$ decays that have passed the L0 trigger and decay selection algorithm. Uncertainties are statistical.

The potential tagging efficiency, before reconstruction and offline selection, ε_{tag}^{pot}, is a product of the B-hadron inclusive branching fraction, either directly or indirectly, to protons, $\mathcal{B}_{\text{incl}} \to \ldots \text{p}$, and the production fraction, f_B, of the B-hadron itself. These factors are listed for each B-hadron species in Table 5.5 from the analysis of 100k inclusive $b\overline{b}$ events. The majority of Λ_b's decay to a final state which includes a proton, while the inclusive branching ratio of B-mesons to protons is an order of magnitude smaller. However, Λ_b's account for only 8% of all B-hadrons. Consequently, the percentage of events containing a proton from a B-meson decay is not too dissimilar to the percentage of events with a proton from a Λ_b decay. By comparison, the inclusive branching ratio of B-mesons to kaons is of a similar magnitude to that of Λ_b's to protons, $\mathcal{B}_{\text{incl}} \to \ldots \text{K} = 59.7\%$ for B^+ compared with $\mathcal{B}_{\text{incl}} \to \ldots \text{p} = 63.1\%$ for Λ_b, but the overall tagging efficiency is much higher on account of the larger production fraction of B-mesons compared to Λ_b's.

The potential tagging efficiency, wrong tag fraction and effective tagging efficiency are listed in Table 5.6 for each B-hadron species. The study is performed on 120k $B_s^0 \to J/\psi\,\phi$ events that pass both the L0 trigger and decay selection cuts. Perfect proton reconstruction and selection efficiency and purity is assumed and as such represents the upper limit of flavour tagging performance that could be achieved.

A proton from a Λ_b identifies the decay from a b-flavoured hadron, and, vice-versa, an anti-proton tags a $\overline{b}$ flavour. However, as $B^\pm$ mesons have the opposite b-quark flavour correlation with proton charge, it follows that a proton tags a decay from a $\overline{b}$ flavour meson and an anti-proton a b flavour meson. Experimentally, however, this requires the distinction to be made between protons from Λ_b decays and those from $B^\pm$ decays. For

the purposes of establishing a limit on the potential flavour tagging performance, three possible experimental scenarios are envisaged:

1. It is experimentally possible to identify a proton as deriving from the decay of either a Λ_b, a $B^{\pm}$ or a B^0_d/ B^0_s.

2. A proton can be identified as deriving from either a Λ_b or a B-meson, but no distinction can be made as to the B-meson type.

3. It is not possible experimentally to identify which type of B-hadron the proton originates from. As more tag protons originate from a Λ_b decay than a B^+ decay and with a much lower wrong tag fraction, it is assumed that all protons are from a Λ_b decay.

Assuming perfect reconstruction and selection efficiency, the following limit can be estimated for the maximum possible flavour tagging performance with protons:

$$1.3\% < \max(\varepsilon_{tag}^{eff}) < 4.9\% \tag{5.11}$$

The upper bound corresponds to scenario 1), while the lower bound is set by scenario 3). In addition to the tagging performance from Λ_b's, the upper bound includes the potential tagging performance from $B^{\pm}$'s. For the the intermediate scenerio 2), a greater ε_{tag}^{eff} is achieved by not tagging an event if the proton is from a B-meson. This follows from equation 5.8, whereby the potential gain in ε_{tag}^{eff} from the increase in ε_{tag} by including proton tags from B^+ decays, is outweighed by the overall increase in wrong-tag fraction. In the latter scenerio, strong dilution due to protons from B-mesons has the effect of raising the intrinsic wrong tag fraction to $30.8 \pm 0.4\%$, which leads to a significant drop in the potential tagging performance.

5.2.2 Proton reconstruction and identification

The potential tagging performance of *reconstructed* protons from Λ_b baryons and B^+ mesons is listed in Table 5.7 for various track combinations. Perfect particle identification and selection efficiency is assumed. The reduction in potential tagging performance compared to Table 5.6 is due to the geometric acceptance of the tag B-hadron and the reconstruction efficiency. Long tracks traverse all the tracking stations, while upstream

B-hadron	Track Types	ε_{tag}^{eff} (%)	ω_{tag} (%)	ε_{tag} (%)
Λ_b	Long	1.33 ± 0.04	2.5 ± 0.3	1.48 ± 0.03
	Long + Downstream	1.82 ± 0.04	2.3 ± 0.3	2.00 ± 0.04
	Long + Downstream + Upstream	1.94 ± 0.04	2.3 ± 0.3	2.13 ± 0.04
B^+	Long	0.47 ± 0.03	20 ± 1	1.28 ± 0.03
	Long + Downstream	0.34 ± 0.03	24 ± 1	1.30 ± 0.03
	Long + Downstream + Upstream	0.42 ± 0.03	22 ± 1	1.36 ± 0.03

Table 5.7: Potential proton tagging performance *after reconstruction, assuming perfect tag selection efficiency and purity.* From the reconstruction of 120k $B_s^0 \to J/\psi\,\phi$ events that pass the L0 trigger and decay selection. Uncertainties are statistical.

	Maximum potential ε_{tag}^{eff}		
Channel	Scenario 1)	Scenario 2)	Scenario 3)
$B_s^0 \to J/\psi\,\phi$	2.23 ± 0.06	1.94 ± 0.04	0.29 ± 0.03
$B_d^0 \to K\,\pi$	2.33 ± 0.09	2.15 ± 0.07	0.41 ± 0.05

Table 5.8: Potential proton tagging performance *after reconstruction, assuming perfect tag selection efficiency and purity*, as a function of the selection scenarios described in section 5.2.1. Uncertainties are statistical.

and downstream tracks only have hits in a subset of the tracking system (see section 2.4.2). Downstream tracks have a poorer resolution with respect to the primary vertex, as there are only hits downstream of the magnet. However, as is shown in Table 5.7, there is a potential gain in the Λ_b tagging performance from including both downstream and upstream tracks. This can be understood from the fact that a significant proportion of protons from a Λ_b decay via the relatively long lived Λ and are therefore reconstructed as downstream tracks.

At the generator level it is found that $46.4 \pm 0.8\%$ of B^+ decays to protons consist of a p and $\overline{p}$ state (see Table 5.3), which provides no tagging information and are thus ignored. However, in 31% of cases only one of the two protons is reconstructed, which leads to an increase in the wrong tag fraction of protons from B^+ mesons after reconstruction compared with the generator level.

The potential proton tagging performance is shown in Table 5.8 for each of the various selection scenarios described in section 5.2.1 for a B_s^0 and B_d^0 signal decay channel. All three track types are included and perfect particle identification and selection are assumed. The potential tagging performance is substantially reduced if it is not possible to distinguish protons from a Λ_b from those of B-mesons. However, the inability to distinguish protons from neutral and charged B-mesons does not lead to a significant performance reduction. There is some variation in potential tagging performance between the two signal decay channels. The difference is most likely caused by the kinematic correlation between the signal and tag B, whereby the signal B selection cuts will influence the kinematics of the tag B.

Protons are identified using the global particle identification (PID) as discussed in section 3.5. The delta-log likelihoods for the proton hypothesis versus the pion or kaon hypothesis are shown in Figure 5.2 for true hadrons and ghost tracks, the latter being reconstructed tracks that are not associated with a true particle. The peak at zero DLL for the proton / kaon DLL plot is caused by tracks for which neither RICH1 nor RICH2 PID information is available. In the case of RICH1 this will occur if the track momentum is less than the momentum threshold at which kaons radiate Cherenkov light in aerogel and in RICH2 if the momentum is less than the threshold for radiation in the CF_4 radiator. Similarly, the peak at zero DLL for the proton / pion DLL plot is caused by tracks that are below the momentum threshold at which pions radiate.

For any potential proton flavour tag it is particularly important to ensure that kaons are not misidentified as protons. From Table 5.4 it is evident that positively charged kaons are correlated with a b-quark flavour and, vice-versa, a negatively charged kaon with a $\overline{b}$ flavour. This is the same charge correlation with b-quark flavour as for protons from $B^{\pm}$ mesons. However, as discussed in section 5.2.1, a proton from Λ_b has the opposite charge correlation with b-quark flavour. Hence, if a kaon is mis-identified as a proton and is assumed to derive from a Λ_b, then the incorrect b-quark flavour will be assigned.[3]

As a starting point for proton tag selection, a loose set of DLL cuts is used to remove most of the non-proton tracks; $\Delta\ln\mathcal{L}_{p\pi} > 3$ and $\Delta\ln\mathcal{L}_{pK} > 2$. The effect of these cuts upon the ratio of background tracks to protons for various background categories are listed in Table 5.9. The final DLL selection criteria are chosen to optimise the effective proton tagging efficiency.

[3]The conjugate argument applies to flavour tagging with kaons, whereby protons mis-identified as kaons that originate from Λ_b will dilute the tagging performance.

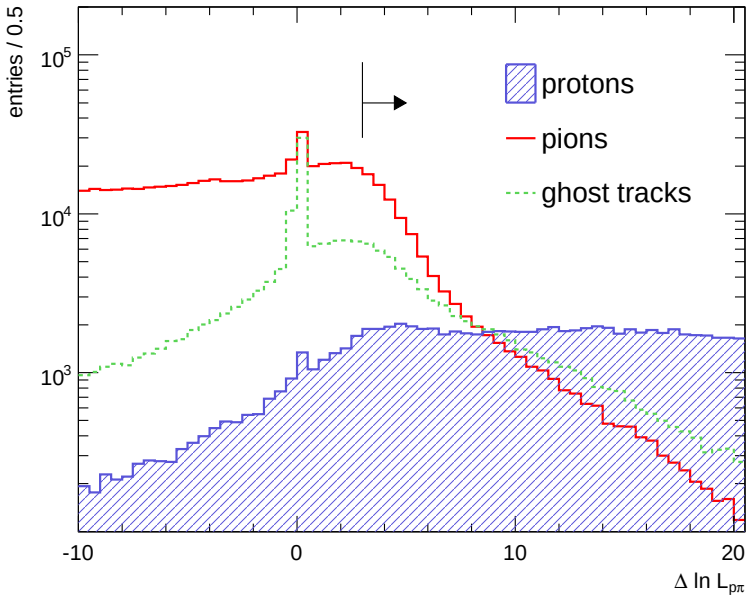

(a) Difference in log-likelihood between the proton and pion hypothesis.

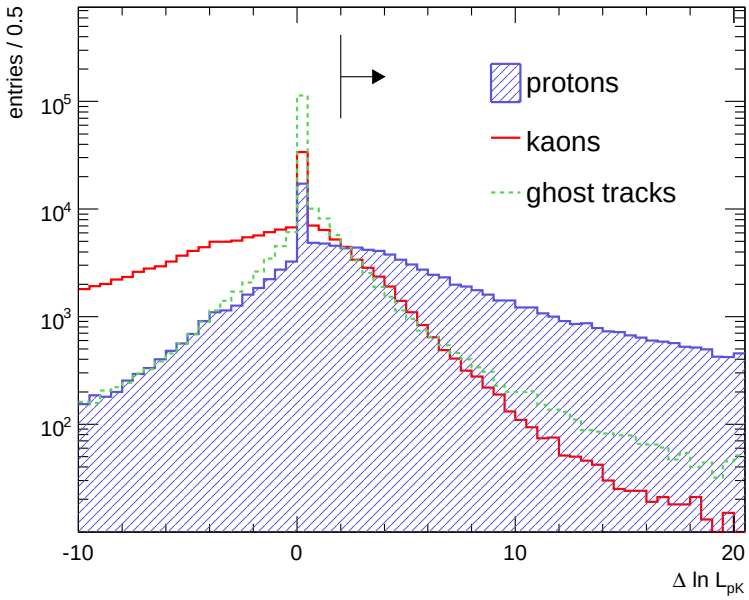

(b) Difference in log-likelihood between the proton and kaon hypothesis.

Figure 5.2: Proton identification with difference in log-likelihood (DLL) cuts in a sample of 60k $B_s^0 \rightarrow J/\psi\ \phi$ events. The arrows indicate the respective loose DLL cut positions. The shaded areas corresponds to true protons, the solid line the incorrect PID hypothesis and the dashed line ghost tracks.

	background / protons	
background	before PID cuts	after PID cuts
kaons	1.6	0.3
pions	6.1	0.3
others	2.1	0.2

Table 5.9: Ratio of background particles to protons before and after loose DLL selection criteria.

5.2.3 Proton tag signatures

The selection of an opposite-side tag particle typically exploits two key features of a B-hadron decay. Firstly, the large B-hadron mass leads to a hard momentum and transverse spectrum and, secondly, the relatively long lifetime results in a large impact parameter with respect to the origin vertex. The momentum and transverse momentum spectrum are shown in Figures 5.3(a) and 5.3(b), for true protons from a Λ_b, true protons from a B-meson[4] and the underlying fragmentation protons. Tracks mis-identified as protons are included in the latter class. As expected, the protons from a B-hadron have a harder momentum than the underlying protons, but the distinction is less effective than for leptons owing to the larger proton mass. However, there is no significant difference between the momentum spectrums of protons from a Λ_b compared to those from a B-meson.

The impact parameter (IP) is defined as the magnitude of the vector that is perpedicular to the track and in the direction of the primary vertex (or any other vertex of interest). The impact parameter significance, $\mathrm{IP}/\sigma_{\mathrm{IP}}$ (IPS), is defined as the ratio of the impact parameter to the measurement error of the impact parameter vector σ_{IP}. A signed impact parameter includes a sign that is determined by projecting the impact parameter vector on to the beam axis; the sign is defined as positive if the projection is directed downstream and negative if the direction is upstream.

The signed impact parameter significance with respect to the reconstructed primary vertex is shown in Figure 5.3(c) for protons reconstructed as long tracks. This provides a powerful separation between underlying protons and those from a B-hadron decay.

[4]For resons of simplicity the distinction between neutral and charged B-mesons is neglected as there is only a small potential performance gain from separating these two cases.

However, there is no distinction between the B-hadron origin types. The IPS is shown in Figures 5.4(a) and 5.4(b) for reconstructed downstream and upstream tracks respectively. As previously discussed in Section 5.2.2, the downstream and upstream tracks have a poor track resolution. This is reflected in the IPS plots for these track types, for which there is no distinction between the various proton origins. For this reason the remainder of this study will only use reconstructed long tracks.

A secondary vertex reconstruction algorithm has been developed for the inclusive vertex charge flavour tag [100]. The signed impact parameter significance with respect to this reconstructed secondary vertex is shown in Figure 5.3(d). Protons from the underlying event are skewed towards negative values as they originate mainly upstream of the secondary vertex. Although there is a clear distinction between underlying protons and those from a B-hadron decay, the variable is limited by the $\sim 50\%$ efficiency of the secondary vertex reconstruction algorithm.

5.2.4 Optimising the proton flavour tagging performance

From the studies of the previous section, it is evident that protons from a Λ_b can not be distinguished from those of a B-meson decay with the simple kinematic and geometric cuts considered. However, as was discussed in scenerio 3) of 5.2.1, a useful tagging performance is still potentially possible by assuming that all tag protons originate from a Λ_b. In which case, a *right tag* proton originates from a hadron with a b quark or, in the conjugate decay, an anti-proton from a $\overline{b}$ quark, and a *wrong tag* proton derives from the decay of $\overline{b}$ quark or an anti-proton from a b quark.

The aim is to optimise the effective tagging efficiency by tuning the selection criteria listed in Table 5.10. Cut positions are optimised on a dataset of 60k $B_s^0 \to J/\psi\,\phi$ events that pass the L0 filter and the Technical Design Report (TDR) selection algorithms. To avoid over tuning the cuts on the data, the cuts are evaluated on a second independent 60k event dataset.

The impact parameter significance of protons with respect to the reconstructed vertex is shown in Figure 5.5(a) for right tag, wrong tag and background proton categories. The background category includes all protons that do not derive from B-hadron decays, including ghost tracks and mis-identified protons. Two significant problems for a potential flavour tag are apparent :

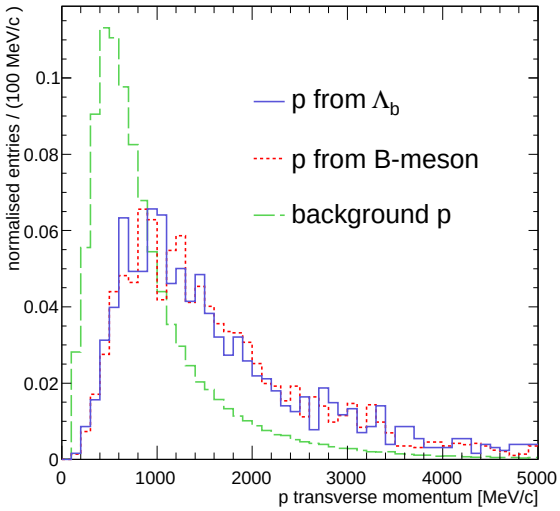

(a) Proton transverse momentum distribution.

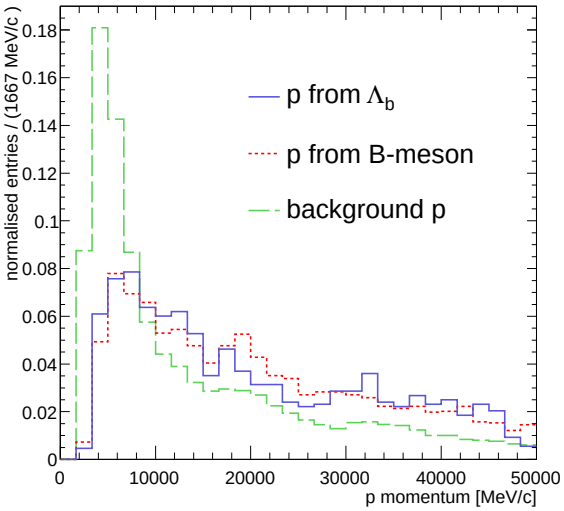

(b) Proton momentum distribution.

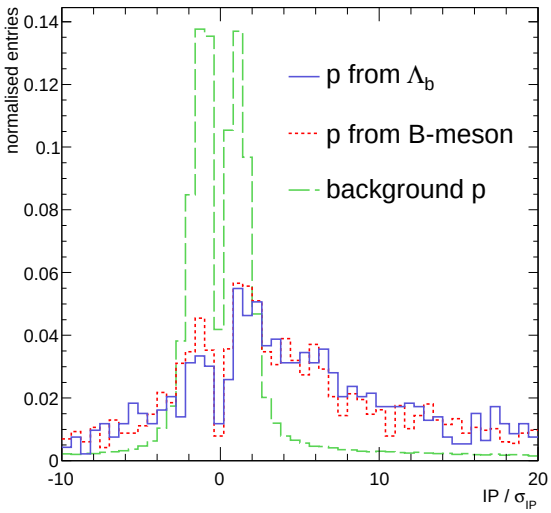

(c) Proton impact parameter significance w.r.t. the reconstructed primary vertex.

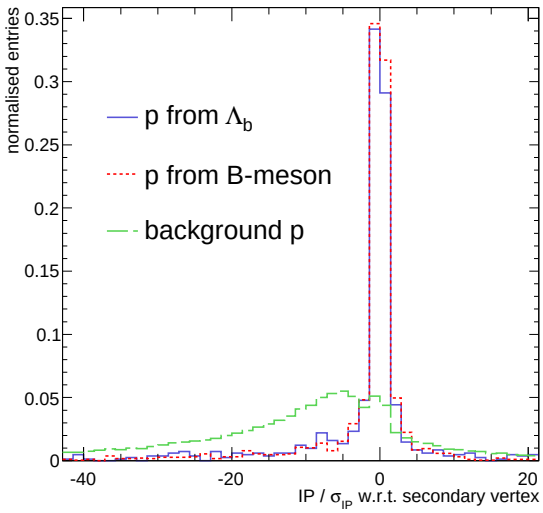

(d) Proton impact parameter significance w.r.t. the reconstructed secondary vertex.

Figure 5.3: Kinematic and topological variables to identify reconstructed protons from various sources. Long tracks only. Distributions taken from 120k $B_s^0 \to J/\psi\ \phi$ events that have passed the L0 trigger and TDR selection. Distributions are normalised to unity.

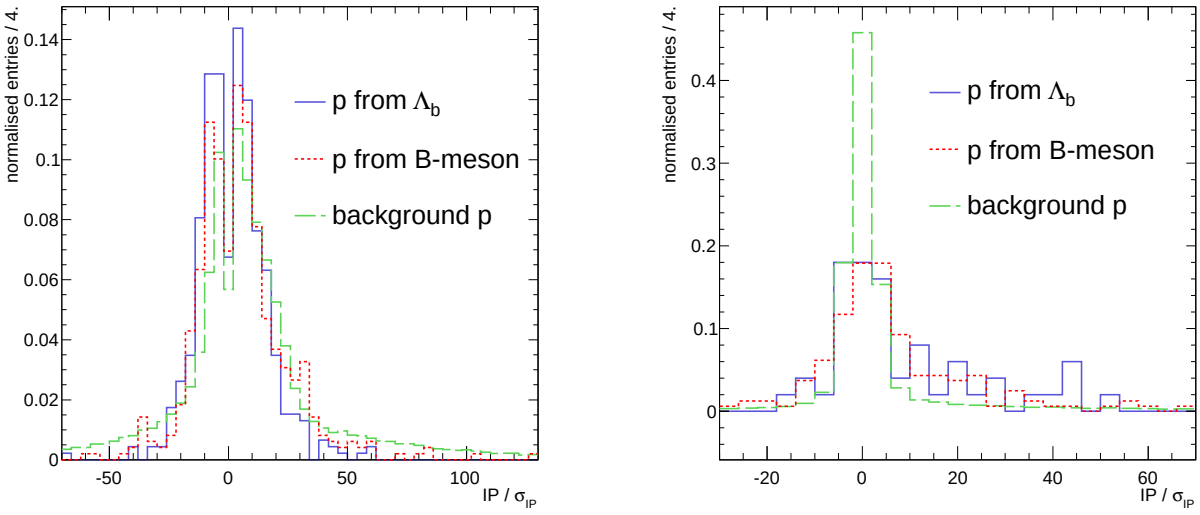

(a) Downstream tracks.

(b) Upstream tracks.

Figure 5.4: Proton impact parameter significance w.r.t. the reconstructed primary vertex.

Cut variable	Description
$(\mathrm{IP}/\sigma_{\mathrm{IP}})_{\mathrm{PV}}$	p impact parameter significance w.r.t primary vertex
$(\mathrm{IP}/\sigma_{\mathrm{IP}})_{\mathrm{SV}}$	p impact parameter significance w.r.t secondary vertex
$(\mathrm{IP}/\sigma_{\mathrm{IP}})_{\mathrm{pile}}$	p minimum impact parameter significance w.r.t. pileup vertices
p	p momentum
p_{T}	p transverse momentum w.r.t. detector z-axis
$\Delta\ln\mathcal{L}_{\mathrm{p}\pi}$	difference in log-likelihood between p and π hypothesis
$\Delta\ln\mathcal{L}_{\mathrm{pK}}$	difference in log-likelihood between p and K^+ hypothesis

Table 5.10: Criteria for the selection of proton flavour tags.

1. There are approximately three order of magnitude more fragmentation protons than tag protons.

2. The number of wrong tags is of the same order of magnitude as the number of right tags.

The first problem can be addressed by kinematic and geometrical cuts. For example,

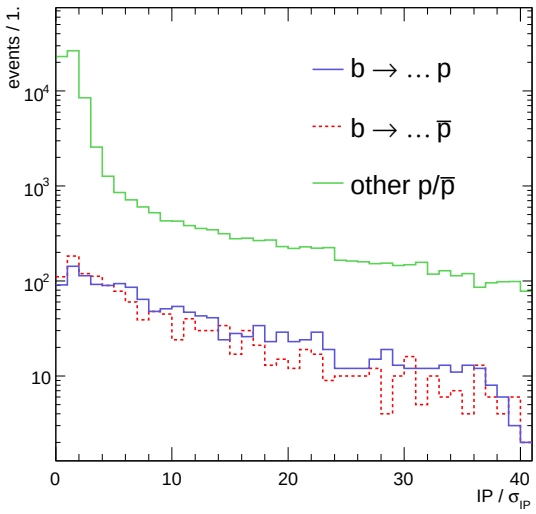

(a) $(\mathrm{IP}/\sigma_{\mathrm{IP}})_{\mathrm{PV}}$ distribution for right tag (solid blue line), wrong tag (dashed red line) and background protons (solid green line).

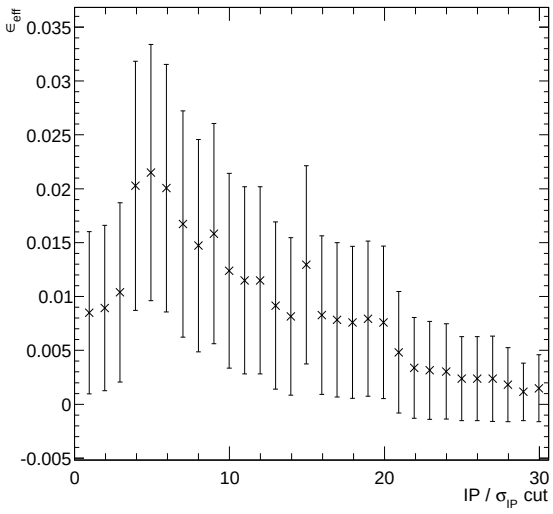

(b) Effective efficiency of opposite-side proton tag as a function of the $(\mathrm{IP}/\sigma_{\mathrm{IP}})_{\mathrm{PV}}$ cut.

Figure 5.5: Opposite-side proton tag selection with an impact parameter significance cut with respect to the reconstructed primary vertex.

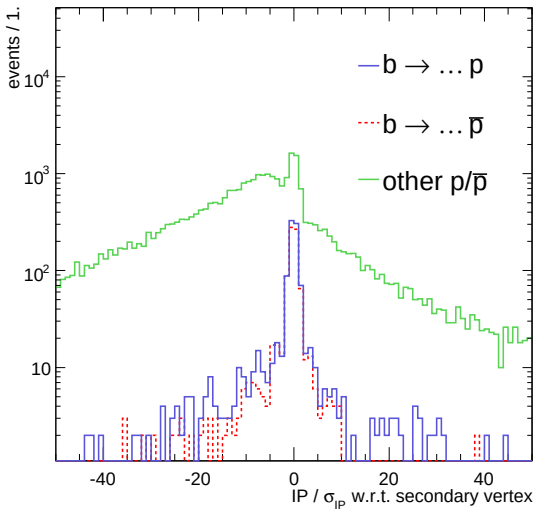

(a) $(\mathrm{IP}/\sigma_{\mathrm{IP}})_{\mathrm{SV}}$ distribution for right tag (solid blue line), wrong tag (dashed red line) and background protons (solid green line).

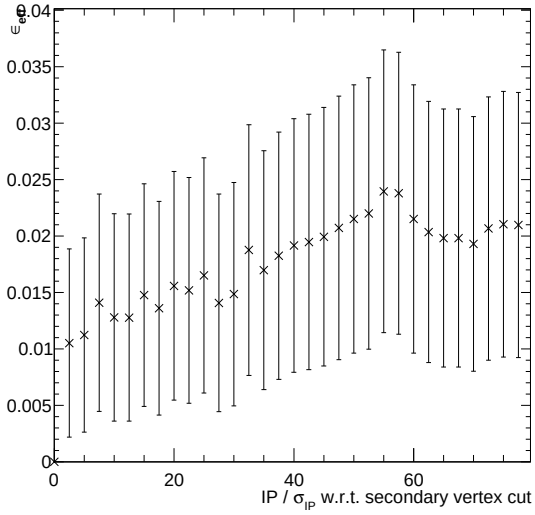

(b) Effective efficiency of opposite-side proton tag as a function of the $(\mathrm{IP}/\sigma_{\mathrm{IP}})_{\mathrm{SV}}$ cut.

Figure 5.6: Opposite-side proton tag selection with an impact parameter significance cut with respect to the reconstructed secondary vertex.

Figure 5.5(b) shows how the effective tagging efficiency evolves as the impact parameter cut is increased, with the other cut variables fixed at the retained value. The effective tagging efficiency increases after the removal of the significant background peak at low impact parameter signifances.

The second problem is caused by protons from B-mesons, which are difficult to separate from the Λ_b protons, as demonstrated in the previous section. However, it is informative to establish what perfomance is possible with simple kinematic and geometric criteria, whereby setting a benchmark for later studies.

The effect of an impact parameter cut with respect to the reconstructed secondary vertex is shown in Figure 5.6. Although a cut on this variable helps to remove fragmentation protons, there is no distinction between the right and wrong tags. Furthermore, the secondary vertex is only reconstructed with a 54% efficiency.

The momentum and transverse momentum distributions of right tag, wrong tag and background category protons are shown in Figures 5.7(a) and 5.7(b) respectively. Figure 5.7(c) shows the evolution of effective efficiency with cuts on both momentum and transverse momentum with the retained $(\mathrm{IP}/\sigma_{\mathrm{IP}})_{\mathrm{PV}}$ cut value applied. The tagging performance has some dependency upon the transverse momentum cut, but the effect of the momentum cut is weaker.

Particle identification performance is a function of the particle momentum, hence the absolute efficiency performance varies depending upon the chosen momentum cuts. However, the peak in tagging efficiency for a large $\Delta\ln\mathcal{L}_{\mathrm{pK}}$ cut is a feature common to all reasonable momentum cut values. This is reasonable since, as was discussed in section 5.2.2, kaons mis-identified as protons will dilute the tagging performance.

The final cut values are listed in Table 5.11. Applying these cuts to a second dataset of 60k $\mathrm{B}^0_{\mathrm{s}} \to \mathrm{J}/\psi\,\phi$ events, the following proton flavour tagging performance is achieved:

$$\varepsilon^{eff}_{tag} = (0.014 \pm 0.009)\% \qquad \omega_{tag} = (45.1 \pm 1.7)\% \qquad \varepsilon_{tag} = (1.42 \pm 0.009)\% \qquad (5.12)$$

Therefore, with the present kinematic and topological cuts, no statistically significant flavour tagging performance is achieved. Since, from equation 5.3, the tagging power decreases as the square of the wrong tag fraction, the performance is severely limited by the very large 45% wrong tag fraction. Typically, for opposite-side kaon and lepton tags a wrong tag fraction of order 30-40 % is achieved. To explain the origin of the large

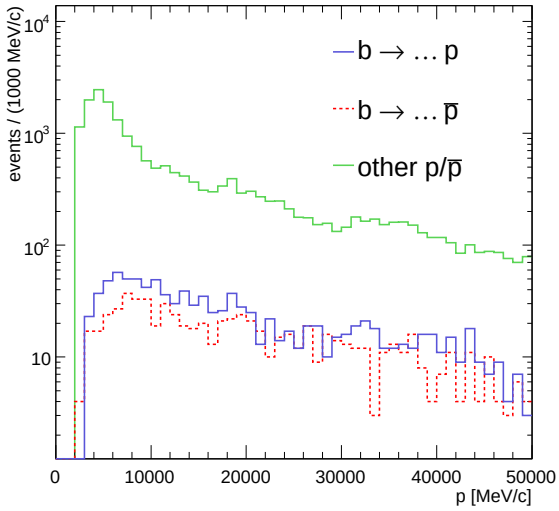

(a) Momentum distribution for right tag (solid blue), wrong tag (dashed red line) and background protons (sold green line).

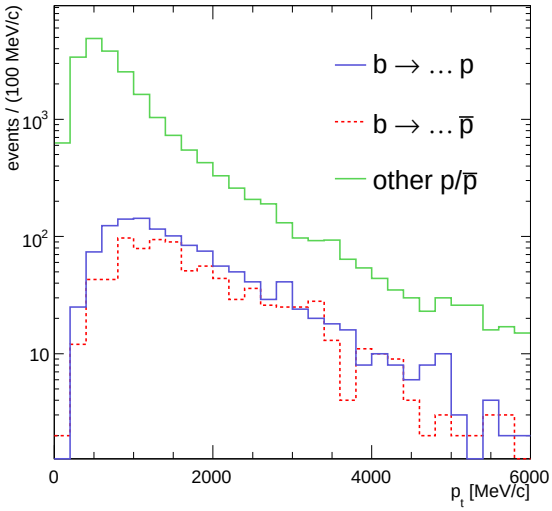

(b) Transverse momentum distribution for right tag (solid blue), wrong tag (dashed red line) and background protons (sold green line).

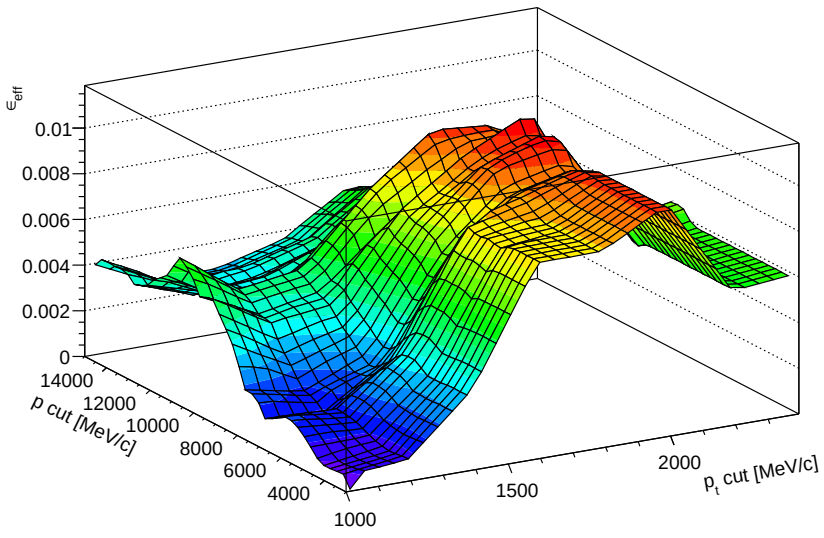

(c) Effective efficiency as a function of momentum and transverse momentum cut

Figure 5.7: Opposite-side proton tag selection with momentum cuts.

Cut variable	Cut
$(\mathrm{IP}/\sigma_{\mathrm{IP}})_{\mathrm{PV}}$ (p)	> 5
$(\mathrm{IP}/\sigma_{\mathrm{IP}})_{\mathrm{pile}}$ (p)	> 5
p (p)	> 8000 MeV/c
p_{T}(p)	> 1800 MeV/c
$\Delta\ln\mathcal{L}_{\mathrm{p}\pi}$	> 5
$\Delta\ln\mathcal{L}_{\mathrm{pK}}$	> 17

Table 5.11: Proton flavour tagging cut variables.

wrong tag fraction it is useful to define the following signal and background categories:

- Signal (S), true protons that originate from a Λ_{b}.
- Charged B-meson background ($\mathrm{B}_{\mathrm{B}^\pm}$), true protons that originate from a $\mathrm{B}^\pm$.
- Neutral B-meson background ($\mathrm{B}_{\mathrm{B}^0}$), true protons that originate from a $\mathrm{B}^0_{\mathrm{d}}$ or $\mathrm{B}^0_{\mathrm{s}}$.
- Fragmentation background ($\mathrm{B}_{\mathrm{frag\ p}}$), all other protons, mis-identified protons and ghost tracks.

and to define:

$$\varepsilon_{sel} = \frac{\text{selected signal protons}}{\text{generated signal protons}}$$

Table 5.12 shows the effect of each reconstruction and selection step on the ratio of selected to generated signal protons and on the charged B-meson, neutral B-meson and fragmentation background to signal proton ratios. As expected from section 5.2.3, the geometric and kinematic cuts are effective at reducing the background from fragmentation protons, but have no effect on removing protons from either $\mathrm{B}^\pm$ or $\mathrm{B}^0_{\mathrm{d}}/\mathrm{B}^0_{\mathrm{s}}$ mesons. In fact, the effect of using only long tracks is to raise the ratio of $\mathrm{B}_{\mathrm{B}^\pm}$ and $\mathrm{B}_{\mathrm{B}^0}$ to signal protons, due to the greater proportion of protons from a Λ_{b} that are reconstructed as downstream tracks.

After selection the wrong tag fraction of the $\mathrm{B}_{\mathrm{B}^\pm}$ background is $(72 \pm 4)\%$, while the $\mathrm{B}_{\mathrm{B}^0}$ and $\mathrm{B}_{\mathrm{frag\ p}}$ backgrounds are $(56 \pm 5)\%$ and $(46 \pm 2)\%$ respectively. However, there

Cut variable	ε_{sel}	$B_{B^\pm}$ / S	B_{B^0} / S	$B_{\text{frag p}}$ / S
Reconstruction - All tracks	42.2	1.08 ± 0.04	0.99 ± 0.04	1240 ± 30
Long tracks	29.0	1.25 ± 0.06	1.06 ± 0.05	1100 ± 40
Loose DLL ($\Delta\ln\mathcal{L}_{\text{p}\pi} > 3$, $\Delta\ln\mathcal{L}_{\text{pK}} > 2$)	22.3	1.23 ± 0.06	1.03 ± 0.06	130 ± 5
$(\text{IP}/\sigma_{\text{IP}})_{\text{pile}}$	22.1	1.23 ± 0.06	1.01 ± 0.06	114 ± 4
$(\text{IP}/\sigma_{\text{IP}})_{\text{PV}}$	14.6	1.15 ± 0.08	0.89 ± 0.06	34 ± 2
p_{T}, p	5.3	1.2 ± 0.1	0.9 ± 0.1	8.9 ± 0.7
$\Delta\ln\mathcal{L}_{\text{p}\pi}$, $\Delta\ln\mathcal{L}_{\text{pK}}$	3.6	1.2 ± 0.2	1.0 ± 0.1	5.0 ± 0.5
Largest p_{T} proton	3.6	1.1 ± 0.1	0.9 ± 0.1	4.9 ± 0.5

Table 5.12: Effect of the reconstruction and selection steps on the $B_{B^\pm}$, B_{B^0} and $B_{\text{frag p}}$ to signal ratios and on the proton tag selection efficiency ε_{sel}. Each cut variable includes all the preceeding cuts. Uncertainties are statistical.

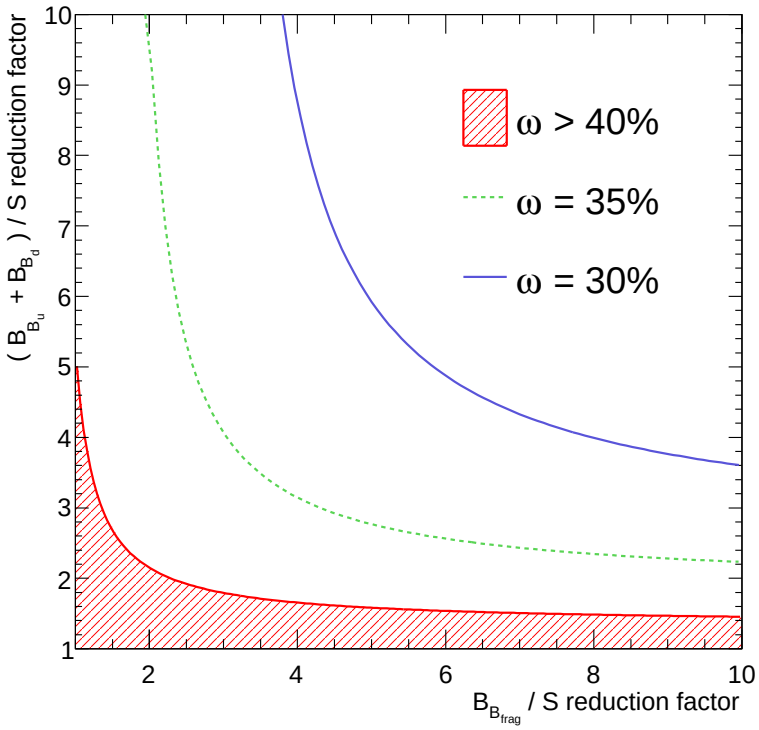

Figure 5.8: Required reduction factors of the $B_{\text{frag p}}$/S ratio and the combined $(B_{B^0} + B_{B^\pm})$/S ratio, to achieve wrong tag fractions of $< 40\%$ (non-shaded area), 35 % (green dashed line) and 30 % (blue solid line).

are approximately five times more remaining fragmentation protons than $B_{B^\pm}$ or B_{B^0} background protons and this is thus the most significant contribution to the tagging dilution.

The question therefore arises as to how much additional background suppression is required to lower the wrong tag fraction to an amount useful for tagging. Figure 5.8 illustrates the required reduction in background to signal ratios to achieve various wrong tag fractions. It is clear that to obtain a wrong tag fraction less than 40% requires at least a factor two reduction in both the fragmentation and B-meson backgrounds. Crucially, it is not possible to achieve such a wrong tag fraction without reducing the background protons from B-mesons. Since the kinematic and topological cuts considered have no effect on removing this background, to achieve a less than 40% wrong tag fraction necessitates the development of selection techniques beyond the simple kinematic and geometric cuts considered. This is the subject of the next section.

5.3 Flavour Tagging with Λ Baryons

Flavour tagging with Λ's is motivated by the observation that protons which derive from a B-hadron decay via a Λ have the same proton charge correlation with b-quark flavour for all B-hadron species. This section begins by investigating the potential performance of an opposite-side Λ tag. The reconstruction and selection of generic Λ decays is presented and the optimisation of selection criteria to select an opposite-side Λ tag is detailed. During this optimisation process it is shown that a class of background arises from Λ's produced during the fragmentation of the signal B-meson, analogous to the same-side kaon tag discussed in section 5.1. Methods to extract useful tagging performance from a same-side Λ tag are presented.

5.3.1 Potential performance

The correlation between Λ flavour and the B-hadron flavour from which it originates is shown in Table 5.13 for each B-hadron species. The study is performed at the generator level, but does include a 400 mrad detector acceptance cut. With the exception of B_s^0 mesons, the B-hadrons with a b quark decay preferentially to an s-flavoured Λ and vice-versa. The correlation derives from the same $b \to c \to s$ weak decay transition that forms the basis of the opposite-side kaon tag, as described in section 5.1. As such, an

	Λ decay mode (% of all decays to Λ s)		
B-hadron	Λ	$\overline{\Lambda}$	Λ and $\overline{\Lambda}$
Λ_b (b u d)	$97 \pm 2\%$	$2.7 \pm 0.3\%$	$0.15 \pm 0.06\%$
B^- (b $\overline{u}$)	$84 \pm 3\%$	$8.9 \pm 0.7\%$	$6.9 \pm 0.6\%$
$\overline{B}{}^0_d$ (b $\overline{d}$)	$66 \pm 2\%$	$25 \pm 1\%$	$8.9 \pm 0.7\%$
$\overline{B}{}^0_s$ (b $\overline{s}$)	$45 \pm 3\%$	$46 \pm 2\%$	$9 \pm 1\%$

Table 5.13: Distribution of B-hadron decay modes that comprise decays either directly or indirectly to Λ's. From a study of 100k inclusive $b\overline{b}$ events at the generator level. The corresponding charge conjugate modes are implicitly included. Uncertainties are statistical only.

opposite-side Λ tag can be considered as being the baryon equivalent of the opposite-side kaon tag.

The two principal branching fractions for Λ decays are [17]:

$$\mathcal{B}[\Lambda \to p\pi^-] = (63.9 \pm 0.5)\%$$
$$\mathcal{B}[\Lambda \to n\pi^0] = (35.8 \pm 0.5)\%$$

The proton charge unambiguously identifies the flavour of the Λ and is thus correlated to the flavour of the opposite-side B^+, B^0_d and Λ_b hadrons. Recall from section 5.2.4 that the proton tagging performance is intrinsically limited by the fact that $B^\pm$ mesons and Λ_b baryons have the opposite correlation between proton charge and b quark flavour. In contrast, the correlation between the charge of the proton from a Λ decay and the flavour of the B-hadron from which the Λ originates is the same for the $B^\pm$, B^0_d and Λ_b hadrons. The weak correlation for the B^0_d meson can be explained by the $(18.8 \pm 0.3)\%$ probability that the B^0_d ($\overline{B}{}^0_d$) oscillates to a $\overline{B}{}^0_d$ (B^0_d) before decaying, whereby diluting the correlation [17]. For B^0_s mesons the probability of decay from the conjugate state is 0.49924 ± 0.00003 [17], which results in the complete dilution of the correlation, as seen in Table 5.13.

The inclusive branching fraction, $\mathcal{B}_{\text{incl}} \to \ldots\Lambda$, to a Λ and corresponding potential tagging efficiency are listed in Table 5.14 for each B-hadron species, from the analysis of 100k inclusive $b\overline{b}$ events. Restricting the study to protons from Λ decays results in an approximately factor 3 reduction in the potential tagging efficiency with respect to

B-hadron	f_B (%)	$\mathcal{B}_{\text{incl}} \to \ldots \Lambda(\%)$	ε_{tag}^{pot} (%)
Λ_b	7.86 ± 0.06	25.6 ± 0.5	2.01 ± 0.03
B^+	40.4 ± 0.1	2.41 ± 0.06	0.97 ± 0.03
B_d^0	40.6 ± 0.1	2.59 ± 0.06	1.05 ± 0.02
B_s^0	10.00 ± 0.07	3.2 ± 0.1	0.32 ± 0.01

Table 5.14: Percentage of events with a Λ either directly or indirectly from the decay of a B-hadron, ε_{tag}^{pot}, and the corresponding inclusive branching fraction to a Λ baryon, $\mathcal{B}_{\text{incl}} \to \ldots \Lambda$, and the b-quark hadronisation fractions (f_B). From the study of 100k inclusive $b\overline{b}$ events at the generator level. Uncertainties are statistical.

Signal channel	ε_{tag}^{eff}	ω_{tag}	ε_{tag}
$B_s^0 \to J/\psi\,\phi$	2.20 ± 0.07	13.8 ± 0.5	4.19 ± 0.06
$B_d^0 \to K\,\pi$	2.15 ± 0.06	13.5 ± 0.5	4.02 ± 0.06

Table 5.15: Maximum potential Λ tagging performance from the analysis of 120k $B_s^0 \to J/\psi\,\phi$ and 125k $B_d^0 \to K\,\pi$ decays that have passed the L0 trigger and decay selection algorithm. Uncertainties are statistical.

the potential proton tagging efficiency listed in Table 5.5.

The maximum potential tagging performance, before the Λ reconstruction and selection, is listed in Table 5.15 for a B_s^0 and B_d^0 signal channel. Although the potential tagging efficiency is lower than for a proton tag, the potential effective tagging efficiency is comparable to that of the potential proton effective tagging efficiency (equation 5.11). Furthermore, for the Λ flavour tag no distinction is required between Λ's from a Λ_b and those from B-mesons. Compared to the lower bound of equation 5.11, which corresponds to the experimental scenerio of not being able to identify the proton B-hadron origin, the potential Λ effective tagging efficiency is some 70% higher.

To reconstruct Λ's from either the direct or indirect decay of a B-hadron, hereafter called tag Λ's, the approach taken is to first reconstruct all $\Lambda \to p\,\pi$ decays, irrespective of the Λ origin, and then to identify the tag Λ's from the background of Λ's from the underlying event.

p track type	π track type	$\varepsilon_{rec}(\%)$	$\varepsilon_{rec}^{norm}(\%)$
downstream	downstream	4.2 ± 0.4	39 ± 3
long	long	3.0 ± 0.3	29 ± 3
long	upstream	2.1 ± 0.3	19 ± 2
other		1.4 ± 0.2	13 ± 2
all tracks		10.6 ± 0.7	100 ± 0

Table 5.16: Percentage of generated flavour tag Λ's for which both the final states are reconstructed, ε_{rec}, as a function of the protons and pion track type. Also listed as a percentage of all reconstructed tracks types (ε_{rec}^{norm}).

Signal channel	ε_{tag}^{eff} (%)	ω_{tag} (%)	ε_{tag} (%)
$B_s^0 \to J/\psi\,\phi$	0.24 ± 0.03	15 ± 2	0.47 ± 0.03
$B_d^0 \to K\,\pi$	0.23 ± 0.03	14 ± 2	0.44 ± 0.03

Table 5.17: Maximum potential Λ tagging performance after Λ reconstruction, assuming perfect selection efficiency and purity. Uncertainties are statistical.

5.3.2 Λ reconstruction and selection

Candidate Λ's are reconstructed by combining pairs of final state protons and pions. The percentages of generator level Λ's for which both the final state proton and pion are reconstructed, ε_{rec}, are listed in Table 5.16. The study is performed in a domain in which a flavour tag is required; in this case a dataset of 60k $B_s^0 \to J/\psi\,\phi$ signal events that have passed the L0 trigger and corresponding signal selection cuts. Only one tenth of the potential tag Λ s can be reconstructed. Furthermore, due to the long Λ lifetime, only 29% of these can be reconstructed from a pair of long, high quality, tracks. The potential tagging performance after reconstruction, listed in Table 5.17, is thus reduced by a tenth. However, the effective tagging efficiency is still potentially a useful flavour tag, but to obtain this performance requires that all three tracks types are used to reconstruct Λ's and the final selection cuts must retain a high proportion of the reconstructed Λ's. The remainder of this section presents the steps required to reconstruct and select *generic* $\Lambda \to p\,\pi$ decays. The selection of flavour tag Λ's from the selected $\Lambda \to p\,\pi$ decays is the subject of sections 5.3.3 and 5.3.4.

Cut variable	long tracks	downstream tracks	upstream tracks
$(\mathrm{IP}/\sigma_{\mathrm{IP}})_{\mathrm{min}}$ (p)	$> 3.$	$> 2.$	$> 3.$
p_{T}(p)	> 150 MeV/c	> 200 MeV/c	> 200 MeV/c
$(\mathrm{IP}/\sigma_{\mathrm{IP}})_{\mathrm{min}}$ (π)	$> 3.$	$> 3.$	$> 3.$

Table 5.18: Cuts used for $\Lambda \to \mathrm{p}\,\pi$ final state selection, given in terms of the condition required to pass the cut.

Reconstructed tracks are identified as protons by applying a loose $\Delta\ln\mathcal{L}_{\mathrm{p}\pi} > -10$ selection cut, while all tracks are considered as being pions. A $\Lambda \to \mathrm{p}\,\pi$ decay is characterised by the long Λ lifetime.

The smallest of the impact parameter significances with respect to the reconstructed primary vertices, $(\mathrm{IP}/\sigma_{\mathrm{IP}})_{\mathrm{min}}$, is illustrated in Figure 5.9 for each of the 3 track types. For protons and pions reconstructed as long and upstream tracks, applying a $(\mathrm{IP}/\sigma_{\mathrm{IP}})_{\mathrm{min}}$ selection cut removes a significant amount of the fragmentation background. However, the cut is less effective for downstream tracks on account of the poor track resolution of downstream tracks. A transverse momentum cut is applied to the final state proton, shown in Figure 5.10, but so as to maintain a high selection efficiency no p_{T} cut is applied to the pion. The final state selection cuts, listed in Table 5.18, are chosen so as to reduce the candidate Λ combinatorics, but to maintain the necessary high Λ selection efficiency.

All final state proton and pions that pass the final state selection criteria are combined in neutral pairs to form candidate Λ's. For simplicity only the track type combinations listed in Table 5.16, which constitute 87% of reconstructed Λ's, are considered.

A significant part of the combinatoric background is removed by requiring that the mass of the candidate Λ is less than ± 100 MeV/c^2 from the true Λ mass of 1115.683 ± 0.006 MeV/c^2 [17]. The selection parameters used to extract the reconstructed candidates associated to a true Λ from the combinatoric background are as follows:

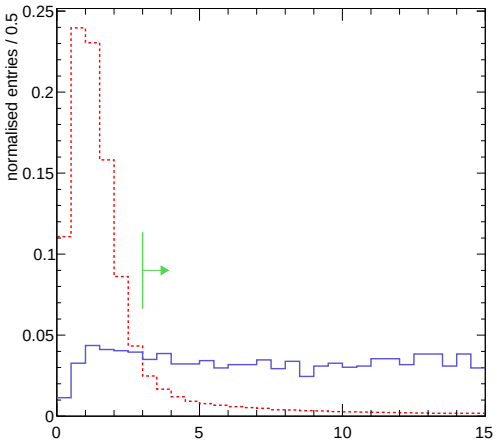

(a) $(\mathrm{IP}/\sigma_{\mathrm{IP}})_{\mathrm{min}}$ of long protons

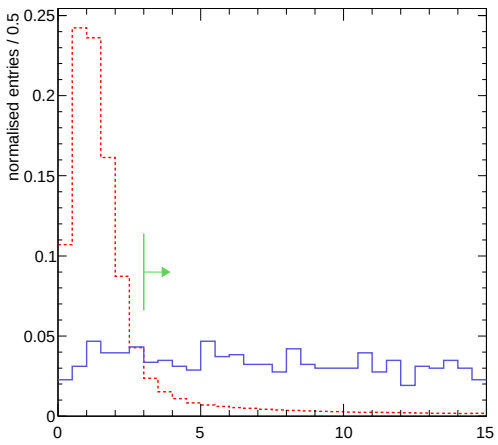

(b) $(\mathrm{IP}/\sigma_{\mathrm{IP}})_{\mathrm{min}}$ of long pions

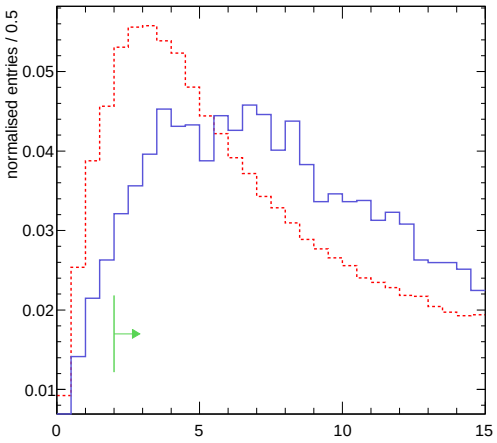

(c) $(\mathrm{IP}/\sigma_{\mathrm{IP}})_{\mathrm{min}}$ of downstream protons

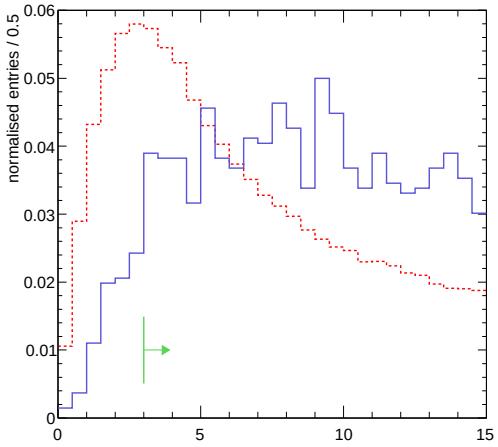

(d) $(\mathrm{IP}/\sigma_{\mathrm{IP}})_{\mathrm{min}}$ of downstream pions

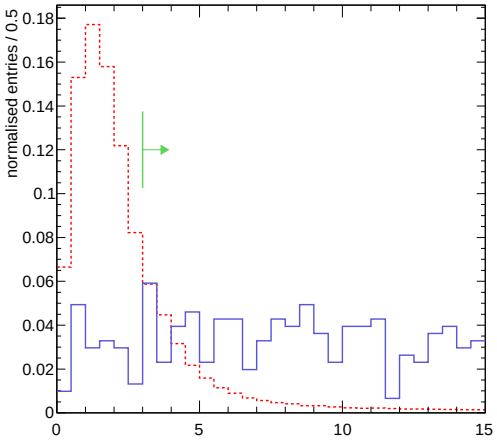

(e) $(\mathrm{IP}/\sigma_{\mathrm{IP}})_{\mathrm{min}}$ of upstream protons

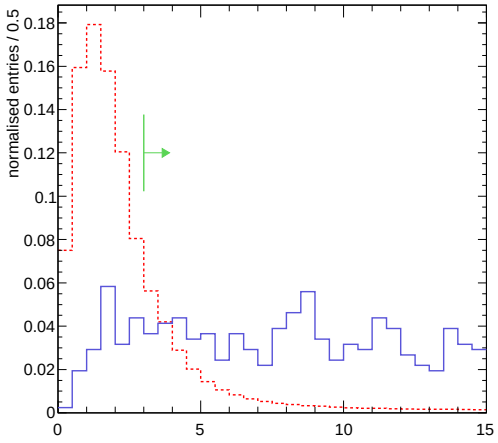

(f) $(\mathrm{IP}/\sigma_{\mathrm{IP}})_{\mathrm{min}}$ of upstream pions

Figure 5.9: Smallest impact parameter significance ($(\mathrm{IP}/\sigma_{\mathrm{IP}})_{\mathrm{min}}$) of protons and pions from a Λ decay (solid blue line) and the fragmentation background (dashed red line), for the three principal track types. Final cut positions are indicated by the green arrows. From the analysis of 60k $\mathrm{B}_{\mathrm{s}}^{0} \to \mathrm{J}/\psi\,\phi$ events that have passed the L0 trigger and corresponding selection channel cuts. Distributions normalised to unity.

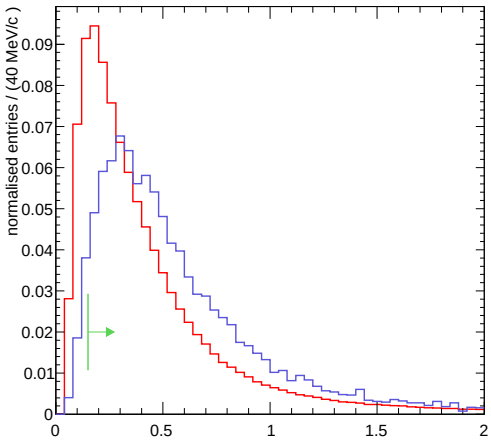

(a) p_{T} of long protons [MeV/c]

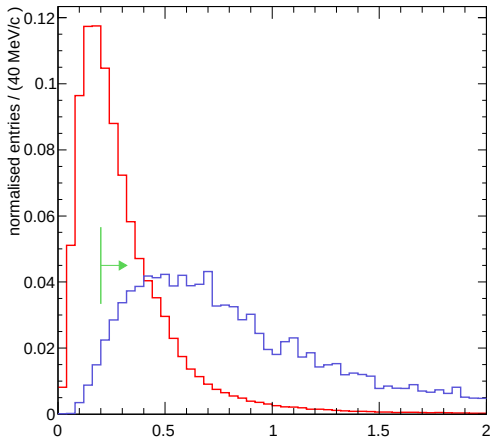

(b) p_{T} of downstream protons [MeV/c]

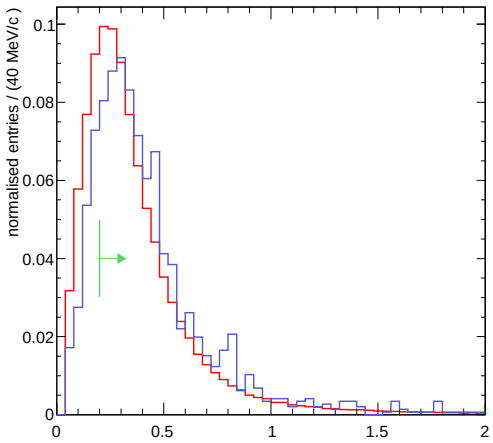

(c) p_{T} of upstream protons [MeV/c]

Figure 5.10: Transverse momentum (p_{T}) distribution of protons from a Λ decay (blue line) and the fragmentation background (red line), for the three principal track types. Final cut positions are indicated by the green arrows. From the analysis of 60k $\mathrm{B}_{\mathrm{s}}^{0} \to \mathrm{J}/\psi\,\phi$ events that have passed the L0 trigger and corresponding selection channel cuts.

Particle identification

- The final state protons require a difference in the log likelihood of the proton and pion hypothesis $> \Delta\ln\mathcal{L}_{\mathrm{p}\pi}(\mathrm{p})$.

Geometric cuts

- The Λ decay vertex is constructed from the final state tracks using an unconstrained fit, the χ^2 of which is an indication of how well the tracks meet to form a vertex and is required to be $< \chi^2_\Lambda$.
- The proton and pion tracks from a true $\Lambda \to \mathrm{p}\,\pi$ will originate from the same point in space. Hence, the closest distance of approach, CDA, between the two tracks is required to be less than CDA_Λ.
- The flight distance, L, is defined as the absolute distance between the reconstructed primary vertex and the candidate Λ vertex. The flight distance significance, $\mathrm{L}/\sigma_\mathrm{L}$, is the ratio of the flight distance to the measurement error in the flight distance σ_L and is required to be $> (\mathrm{L}/\sigma_\mathrm{L})_\Lambda$.
- The cosine of the opening angle between the proton and pion is required to be $< \cos\theta_{\mathrm{p}\pi}$. This cut is useful for identifying candidate Λ's where one of the tracks is incorrectly constructed from hits associated with the other track, resulting in two spatially overlapping tracks.

Kinematic cuts

- The transverse momentum, p_T of the candidate Λ is required to be greater than p_T^Λ.
- The ratio of the proton to the pion momentum is required to be greater than $p(\mathrm{p})/p(\pi)$.
- The invariant mass of the candidate Λ must lie within a range $\pm\,\delta m$ of the nominal Λ mass.

The distributions of the variables listed above are illustrated in Figures 5.11-5.14, from the analysis of 60k $\mathrm{B}^0_\mathrm{s} \to \mathrm{J}/\psi\,\phi$ events that have passed the L0 trigger and the

Cut variable	LL cut	DD cut	LU* cut
$\Delta\ln\mathcal{L}_{\mathrm{p}\pi}(\mathrm{p})$	> 0	> 0	> 4
χ^2_Λ	< 20	< 20	< 10
CDA_Λ	< 1 mm	< 20 mm	< 0.5 mm
$(\mathrm{L}/\sigma_\mathrm{L})_\Lambda$	> 6	> 6	> 8
$\cos\theta_{\mathrm{p}\pi}$	< 0.99998	< 0.99998	< 0.99998
p_T^Λ	> 400 MeV/c	> 800 MeV/c	> 400 MeV/c
$p(\mathrm{p})/p(\pi)$	> 3	> 3	> 3
$\delta m(\Lambda)$	± 4 MeV/c^2	± 9 MeV/c^2	± 20 MeV/c^2

Table 5.19: Selection criteria for the reconstruction of $\Lambda \to \mathrm{p}\,\pi$ decays from i) two long type tracks (LL), ii) two downstream tracks (DD) and iii) a long proton and upstream pion (LU*).

corresponding signal channel offline selection. For all distributions the 100 MeV/c^2 mass window centred on the Λ mass and the final state selection cuts are applied.

The cut values are set initially by visual inspection of the variable distributions and subsequently tuned to further remove the combinatoric background events with the aim of maintaining at least a 50% selection efficiency. The final selection criteria are listed in Table 5.19. Ultimately, the selection criteria are tuned to maximise the effective tagging efficiency. This is the subject of section 5.3.3 and 5.3.4.

The performance of the $\Lambda \to \mathrm{p}\,\pi$ selection cuts are evaluated on a second independent set of 60k $\mathrm{B}^0_\mathrm{s} \to \mathrm{J}/\psi\,\phi$ tagging events[5], in order to avoid effects that may arise from overtuning the selection cuts. The performance is quantified by the selection efficiency, ε_{sel}, and matching efficiency, ε_{match}, which are defined as:

$$\varepsilon_{sel} = \frac{N_\mathrm{sel}}{N_\mathrm{'ted}} \qquad \varepsilon_{match} = \frac{N_\mathrm{sel\&asc}}{N_\mathrm{sel}}, \tag{5.13}$$

where $N_\mathrm{'ted}$ is the number of reconstructed $\Lambda \to \mathrm{p}\,\pi$ decays, N_sel the number of selected Λ candidates and $N_\mathrm{sel\&asc}$ the number of selected candidates that are associated to a true $\Lambda \to \mathrm{p}\,\pi$ decay. The $\Lambda \to \mathrm{p}\,\pi$ selection performance is listed in Table 5.20. A high selection efficiency and a reasonable matching efficiency is achieved.

[5]Events that have passed the L0 trigger and the offline selection cuts.

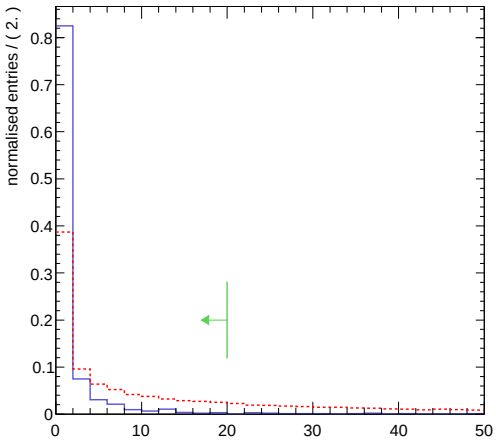

(a) vertex fit-χ^2 for LL Λ

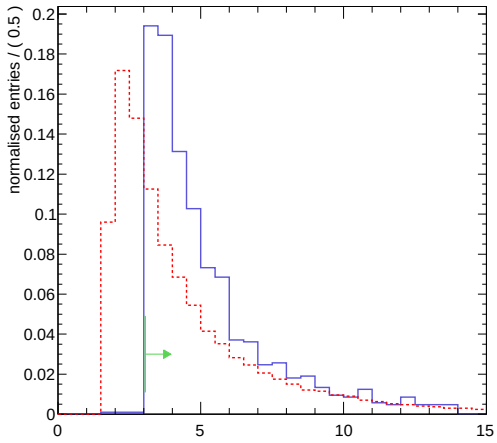

(b) p/π momentum ratio for LL Λ

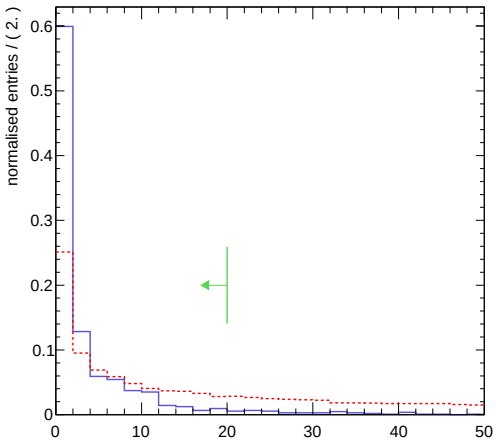

(c) vertex fit-χ^2 for DD Λ

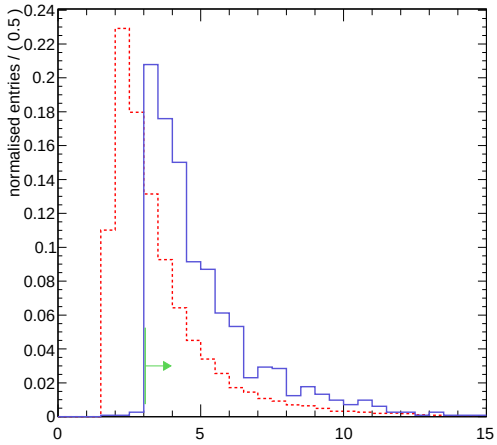

(d) p/π momentum ratio for DD Λ

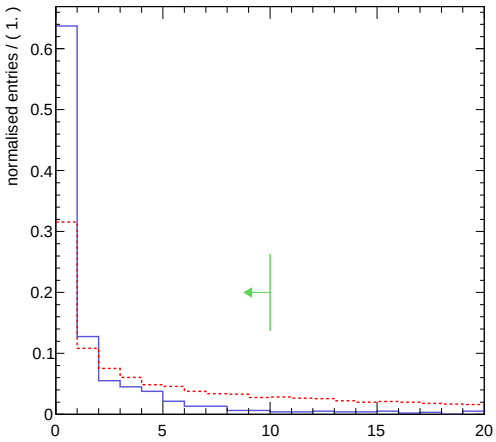

(e) vertex fit-χ^2 for LU Λ

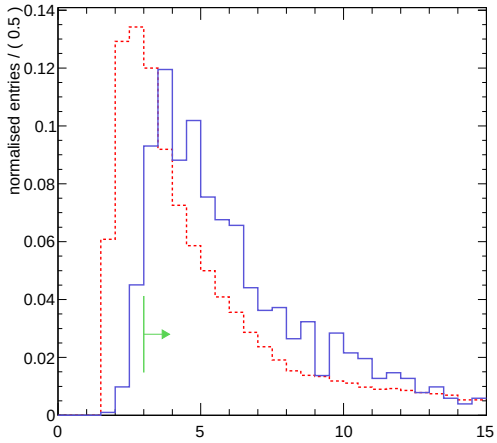

(f) p/π momentum ratio for LU Λ

Figure 5.11: Λ vertex fit χ^2 and p/π momentum ratio distributions for true Λ's (solid blue line) and the combinatoric background (dashed red line). Final cut positions are indicated by the green arrows. Plots normalised to unity.

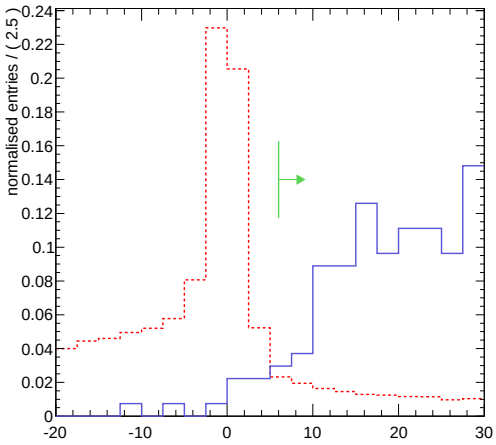

(a) flight significance for LL Λ

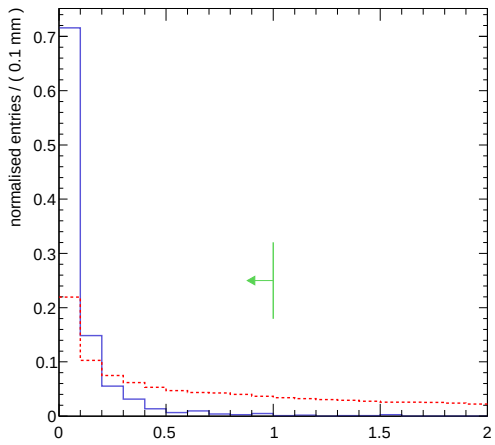

(b) CDA [mm] for LL Λ

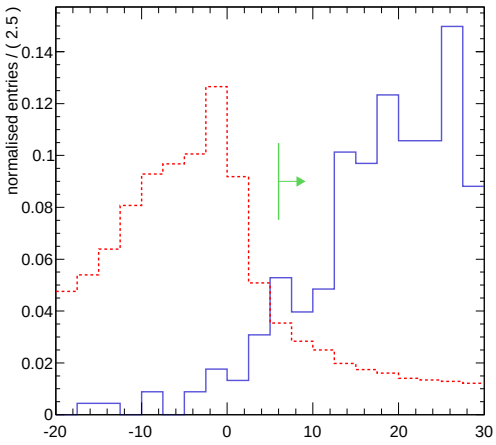

(c) flight significance for DD Λ

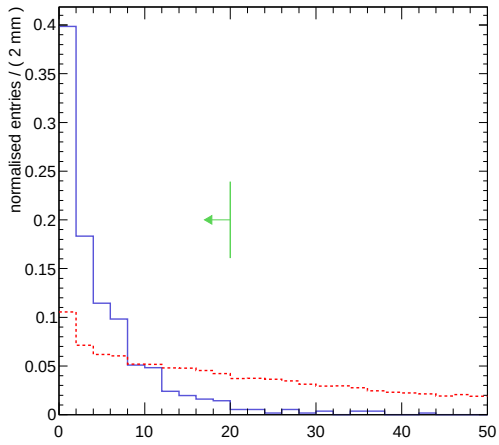

(d) CDA [mm] for DD Λ

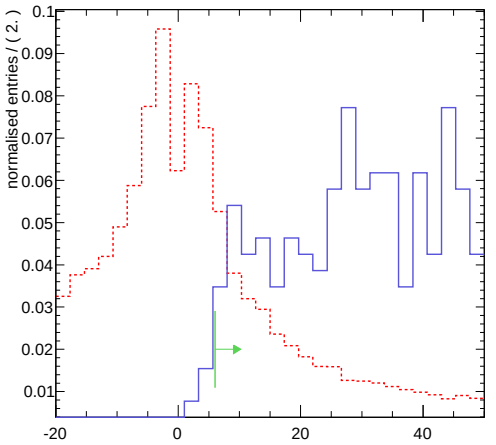

(e) flight significance for LU Λ

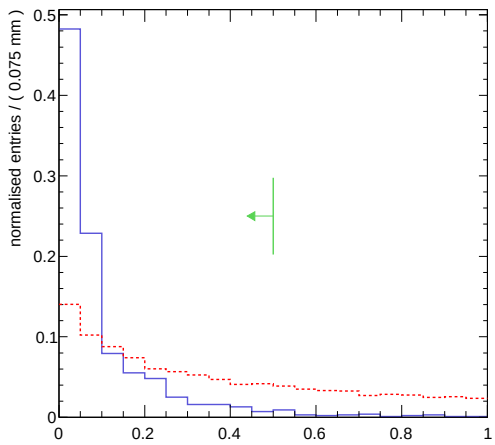

(f) CDA [mm] for LU Λ

Figure 5.12: Λ flight significance and proton/pion track closest distance of approach (CDA) distributions for true Λ's (solid blue line) and the combinatoric background (dashed red line). Final cut positions are indicated by the green arrows. Plots normalised to unity.

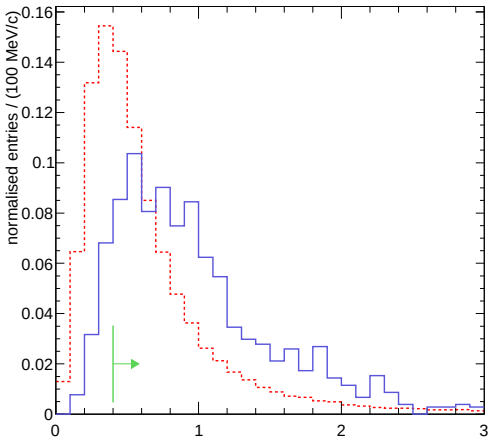

(a) Λ momentum [GeV/c] for LL Λ

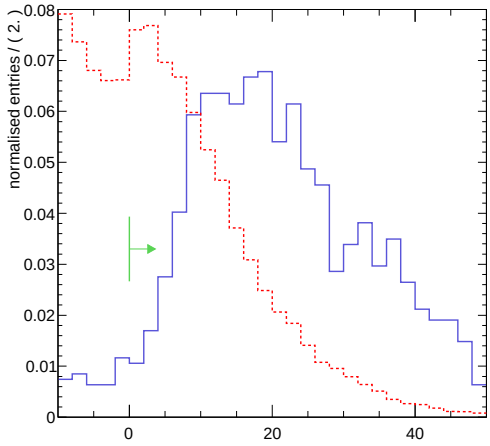

(b) $\Delta\ln\mathcal{L}_{\mathrm{p}\pi}$ for the proton in LL Λ

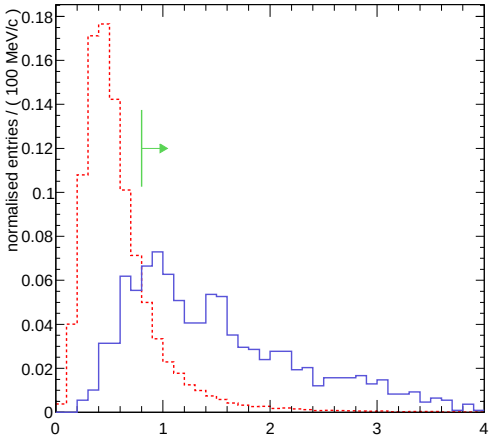

(c) Λ momentum [GeV/c] for DD Λ

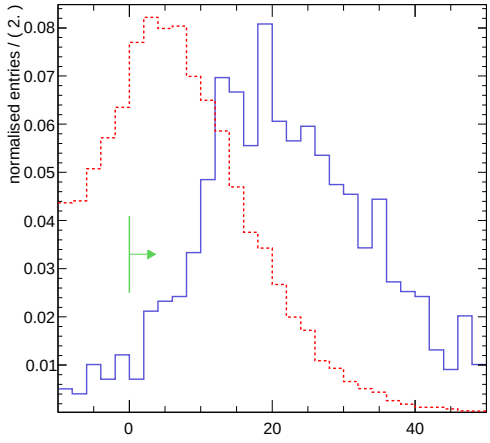

(d) $\Delta\ln\mathcal{L}_{\mathrm{p}\pi}$ for the proton in DD Λ

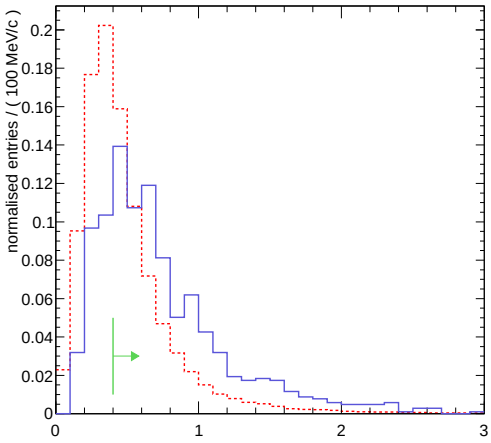

(e) Λ momentum [GeV/c] for LU Λ

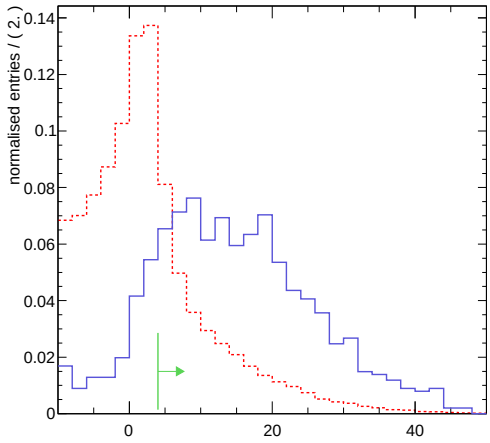

(f) $\Delta\ln\mathcal{L}_{\mathrm{p}\pi}$ for the L proton in LU Λ

Figure 5.13: Λ momentum and the difference in log likelihood of the proton and pion PID hypothesis for the final state proton, shown for true Λ's (solid blue line) and the combinatoric background (dashed red line). Final cut positions are indicated by the green arrows. Plots normalised to unity.

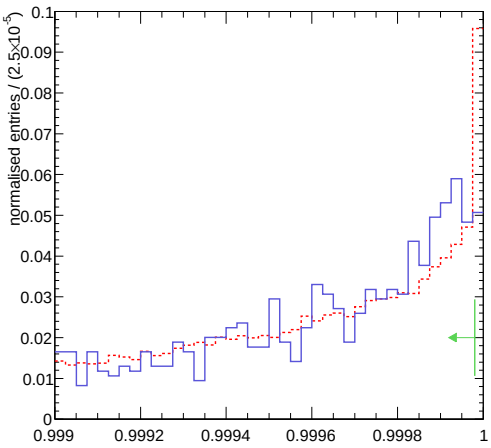

(a) cos $\theta_{p\pi}$ for LL Λ

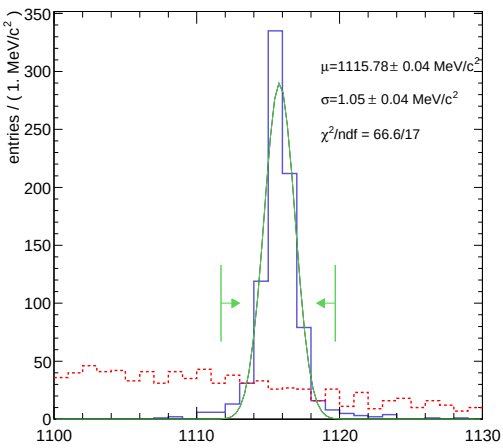

(b) mass [MeV/c^2] for LL Λ

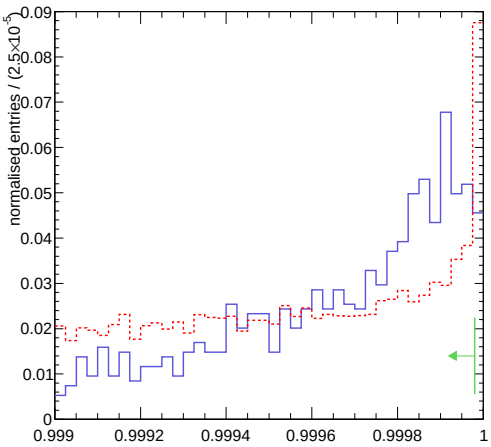

(c) cos $\theta_{p\pi}$ for DD Λ

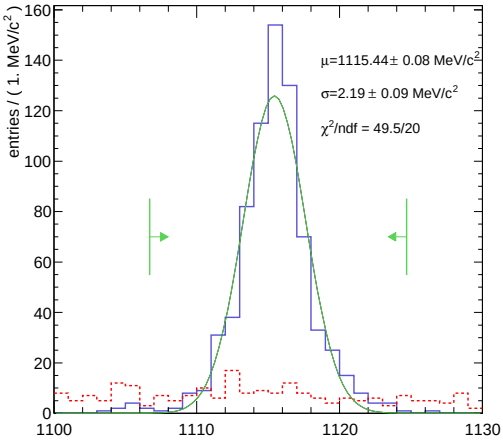

(d) mass [MeV/c^2] for LL Λ

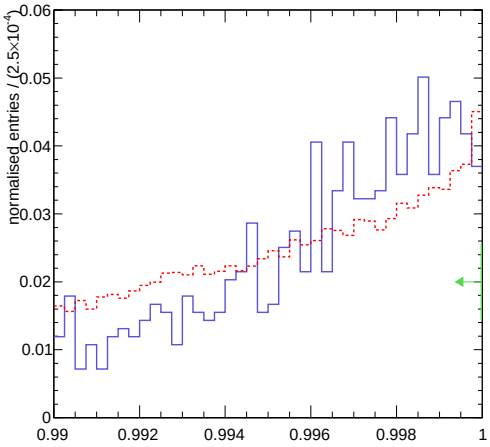

(e) cos $\theta_{p\pi}$ for LU Λ

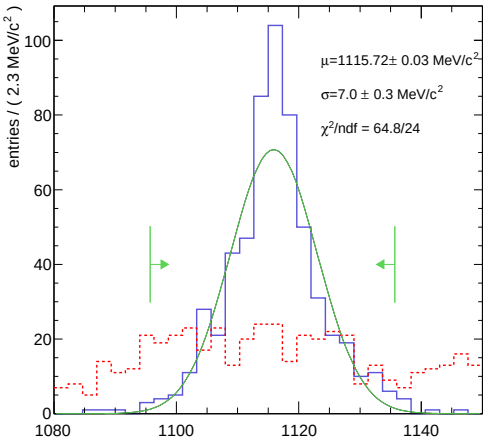

(f) mass [MeV/c^2] for LU Λ

Figure 5.14: Cosine of the angle between the p and π final state tracks and the Λ mass distribution for true $\Lambda \to p\,\pi$ (solid blue line) and the combinatoric background (dashed red line). For the Λ mass distribution the final selection criteria, listed in Table 5.19, are applied and bin contents are left at the absolute values.

Track Types	$\varepsilon_{sel}(\%)$	$\varepsilon_{match}(\%)$
LL	56.0	78.1
DD	50.8	84.8
LU	43.8	64.6
All tracks	43.4	75.8

Table 5.20: Selection efficiency for *all* $\Lambda \to \mathrm{p}\,\pi$ decays, ε_{sel}, and corresponding matching efficiency, ε_{match}.

The selection procedure thus far has aimed to reconstruct and select all $\Lambda \to \mathrm{p}\,\pi$ decays irrespective of the Λ origin. The next section presents the selection of flavour tag Λ's from the background $\Lambda \to \mathrm{p}\,\pi$ decays.

5.3.3 Opposite-side Λ flavour tag

It has been shown in section 5.3.1, that a Λ tags a b quark flavoured companion B-hadron and a $\overline{\Lambda}$ tags a $\overline{\mathrm{b}}$ flavour. However, if a flavour tag is applied on this basis using *all* the Λ's that pass the offline selection, the correlation becomes diluted by Λ's that originate from the underlying event. In order to quantify the dilution it is informative to introduce three categories of selected Λ's:

- Tagging Λ (S) : associated to a true $\Lambda \to \mathrm{p}\,\pi$ decay and originates, either directly or indirectly, from the decay of the companion B-hadron.
- Primary Λ ($\mathrm{B}_{\Lambda_{\mathrm{PV}}}$) : associated to a true $\Lambda \to \mathrm{p}\,\pi$ decay, but does not originate from a B-hadron decay.
- Combinatoric Λ ($\mathrm{B}_{\mathrm{comb}}$) : not associated to a true $\Lambda \to \mathrm{p}\,\pi$ decay.

The background to signal ratios, $\mathrm{B}_{\Lambda_{\mathrm{PV}}}/\mathrm{S}$ and $\mathrm{B}_{\mathrm{comb}}/\mathrm{S}$, and the corresponding tagging performance immediately after selection are listed in Table 5.21 for each of the three track combinations. For all track combinations the principal source of tagging dilution stems from the primary Λ background. It is interesting to note that the wrong tag fraction, ω_{tag}, is biased towards the *opposite* b-quark / Λ flavour correlation and will be discussed later.

Cut variable	$B_{\Lambda_{PV}}/S$	B_{comb}/S	ω_{tag} (%)	ε_{tag} (%)	ε_{tag}^{eff} (%)
LL tracks					
After selection	14 ± 2	4.2 ± 0.6	55 ± 2	1.64 ± 0.05	-0.02 ± 0.01
$(IP/\sigma_{IP})_{pile}$ (Λ)	12 ± 2	4.1 ± 0.6	55 ± 2	1.45 ± 0.05	-0.02 ± 0.01
$\cos(\theta_{PV})$	13 ± 2	0.9 ± 0.2	55 ± 2	1.13 ± 0.04	-0.013 ± 0.009
$\cos(\theta_{SV})$	10 ± 2	0.5 ± 0.1	52 ± 2	0.74 ± 0.03	-0.002 ± 0.003
$(IP/\sigma_{IP})_{PV}$ (Λ)	3.3 ± 0.7	0.4 ± 0.1	47 ± 4	0.20 ± 0.02	0.001 ± 0.002
$(IP/\sigma_{IP})_{SV}$ (Λ)	1.1 ± 0.5	0.	22 ± 9	0.04 ± 0.01	0.012 ± 0.008
DD tracks					
After selection	10 ± 1	2.0 ± 0.3	52 ± 2	1.37 ± 0.05	-0.001 ± 0.003
$(IP/\sigma_{IP})_{pile}$ (Λ)	9 ± 1	1.9 ± 0.3	51 ± 2	1.23 ± 0.04	-0.001 ± 0.002
$(IP/\sigma_{IP})_{SV}$ (Λ)	2.6 ± 0.8	0.13 ± 0.09	32 ± 6	0.10 ± 0.01	0.012 ± 0.008
LU* tracks					
After selection	18 ± 3	11 ± 2	54 ± 2	1.41 ± 0.05	-0.008 ± 0.007
$(IP/\sigma_{IP})_{pile}$ (Λ)	16 ± 3	10 ± 2	54 ± 2	1.27 ± 0.05	-0.007 ± 0.007
$\cos(\theta_{PV})$	17 ± 3	1.2 ± 0.3	51 ± 2	0.79 ± 0.04	-0.001 ± 0.002
$\cos(\theta_{SV})$	12 ± 3	0.9 ± 0.3	53 ± 3	0.47 ± 0.03	-0.001 ± 0.003
$(IP/\sigma_{IP})_{PV}$ (Λ)	2.6 ± 0.9	1.3 ± 0.5	48 ± 7	0.09 ± 0.01	0.0001 ± 0.0008

Table 5.21: Opposite-side Λ tagging performance immediately after the generic Λ selection and the cumulative effect of each of the variables that are applied to select tagging Λ's. The cumulative effect of the selection cuts on the ratio of the primary and combinatoric background Λ's to tagging Λ's, $B_{\Lambda_{PV}}/S$ and B_{comb}/S, are also stated.

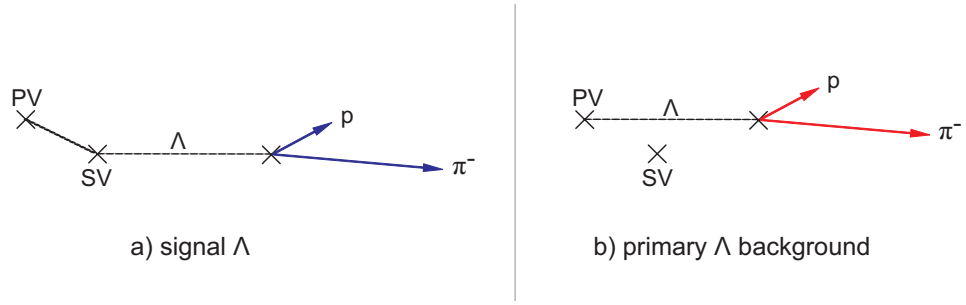

Figure 5.15: Signal and primary Λ topology. PV refers to the primary vertex and SV the secondary vertex.

The expected topology of the tag and primary Λ decays is illustrated schematically in Figure 5.15. A tagging Λ is expected to originate from the secondary vertex that is formed by the decay of the companion B-hadron, whilst the primary Λ is expected to originate from the primary vertex. Therefore, the impact parameter significance with respect to the primary and secondary vertices, $(\mathrm{IP}/\sigma_{\mathrm{IP}})_{\mathrm{PV}}$ and $(\mathrm{IP}/\sigma_{\mathrm{IP}})_{\mathrm{SV}}$, should be able to discriminate between the tag and primary Λ's. Furthermore, the momentum vector of the Λ, **p**, should be biased towards the vertex from which it originates. This motivates the definition of the angles $\cos(\theta_{PV})$ and $\cos(\theta_{SV})$, as follows:

$$\cos(\theta_{PV}) = \frac{\mathbf{p}.\mathbf{u}}{\mid \mathbf{p} \mid\mid \mathbf{u} \mid} \qquad \cos(\theta_{SV}) = \frac{\mathbf{p}.\mathbf{v}}{\mid \mathbf{p} \mid\mid \mathbf{v} \mid}, \tag{5.14}$$

where the vector **u** is directed from the primary to the Λ decay vertex and **v** from the secondary vertex to the Λ decay vertex.

The impact parameter significance distributions for selected Λ's reconstructed from two long tracks are illustrated in Figures 5.16(a) and 5.16(b) for the three Λ categories. Although the expected difference between the tagging and primary Λ distributions is observed, there remains considerable overlap between the two distributions. Similarly, the $\cos(\theta_{PV})$ and $\cos(\theta_{SV})$ distributions, shown in Figures 5.16(c) and 5.16(d) behave as expected, but do not provide a powerful separation between the primary and tag Λ's. However, the $(\mathrm{IP}/\sigma_{\mathrm{IP}})_{\mathrm{PV}}$ and $\cos(\theta_{PV})$ selection variables do facilitate the removal of the combinatoric background.

The $(\mathrm{IP}/\sigma_{\mathrm{IP}})_{\mathrm{PV}}$ distribution of primary and tag Λ's for those Λ's reconstructed from two downstream tracks, illustrated in Figure 5.17(a), shows no evidence for any separation between the two cases. This is not unexpected as the track resolution for down-

stream tracks is worse than that of long tracks. However, the distribution of signed impact parmater significance with respect to the reconstructed secondary vertex, shown in Figure 5.17(b), does show evidence for some discriminating power. The negative bias of the primary Λ distribution is consistent with a track that originates from the primary vertex. For Λ's reconstructed from a long proton and upstream pion, there is some degree of separation between the primary and tag Λ s for both impact parameter significance with respect to the primary and secondary vertices, as is shown in Figures 5.17(c) and 5.17(d).

The $(\mathrm{IP}/\sigma_{\mathrm{IP}})_{\mathrm{PV}}$, $(\mathrm{IP}/\sigma_{\mathrm{IP}})_{\mathrm{SV}}$, $\cos(\theta_{PV})$ and $\cos(\theta_{SV})$ selection cuts are chosen to optimise the effective tagging efficiency. This is achieved by means of a grid scan of the 4-dimension parameter space. The resulting selection cuts are listed in Table 5.22, and include a cut on the impact parameter significance with respect to the pile-up vertices $((\mathrm{IP}/\sigma_{\mathrm{IP}})_{\mathrm{pile}})$.

The optimised selection criteria for the opposite-side proton tag are applied to a second independent set of 60k $\mathrm{B}^0_{\mathrm{s}} \to \mathrm{J}/\psi\,\phi$ events; the resulting tagging performance is;

$$\omega_{tag} = (36.8 \pm 5.5)\% \qquad \varepsilon_{tag} = (0.13 \pm 0.01)\% \qquad \varepsilon^{eff}_{tag} = (0.09 \pm 0.07)\% \qquad (5.15)$$

where ε^{eff}_{tag} is consistent with zero effective tagging power.

To help explain why this is the case, the cumulative effect of each of the selection cuts on the background to signal ratios, $\mathrm{B}_{\Lambda_{\mathrm{PV}}}/\mathrm{S}$ and $\mathrm{B}_{\mathrm{comb}}/\mathrm{S}$, and the corresponding tagging performance, are listed in Table 5.21.

Consider first those Λ's reconstructed from two long tracks. The $\cos(\theta_{PV})$ and $\cos(\theta_{PV})$ cuts remove most of the combinatoric background, at the combined cost of a $\sim 50\%$ tagging efficiency loss. However, the tagging correlation is still completely diluted by the primary Λ background. Cuts on the impact parameter significances with respect to the primary and secondary vertices reduce the number of primary Λ's by an order of magnitude and a wrong tag fraction of $22 \pm 9\%$ is achieved. However, this is at the cost of a significant loss in tagging efficiency, such that no statistically significant tagging performance is achieved. Similarly, for the Λ's reconstructed from two downstream tacks, the tagging efficiency is negligible after a cut is imposed to remove the primary Λ background. Finally, for the Λ's reconstructed from a long proton and upstream pion, despite there remaining a negligible tagging efficiency, the tagging performance is still completely diluted by the remaining background Λ's.

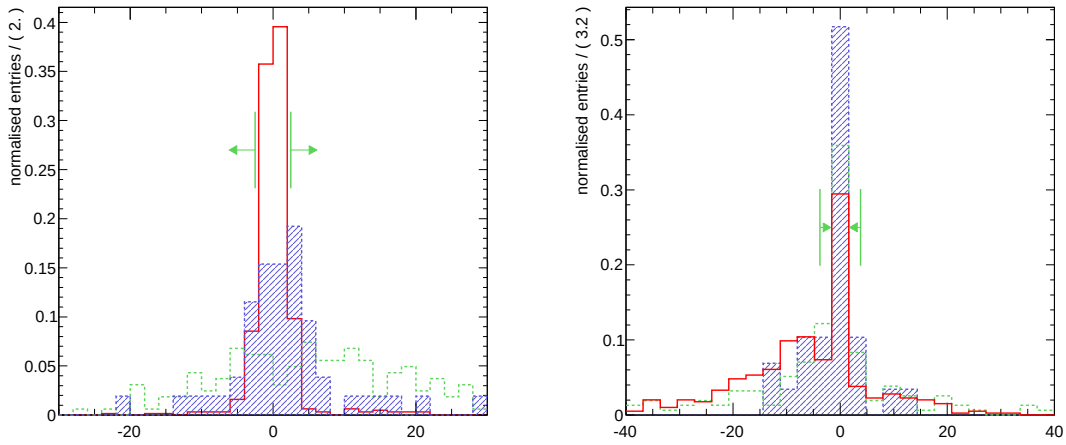

(a) $(\mathrm{IP}/\sigma_{\mathrm{IP}})_{\mathrm{PV}}$ (b) $(\mathrm{IP}/\sigma_{\mathrm{IP}})_{\mathrm{SV}}$

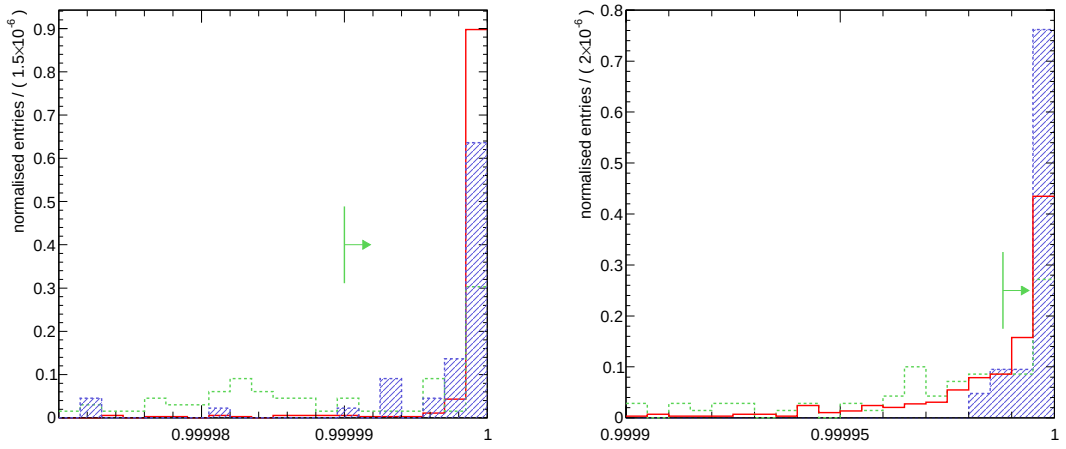

(c) $\cos(\theta_{PV})$ (d) $\cos(\theta_{SV})$

Figure 5.16: Selection of opposite-side tag Λ's (filled blue line) from the primary Λ (solid red line) and combinatoric background (dashed green line) for LL track combinations. Final cut positions are indicated by the green arrow.

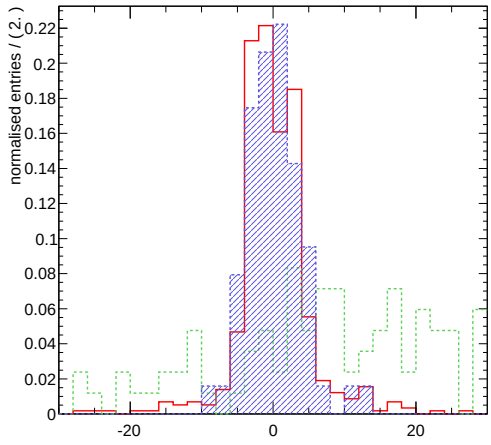

(a) $(\mathrm{IP}/\sigma_{\mathrm{IP}})_{\mathrm{PV}}$ of DD Λ s

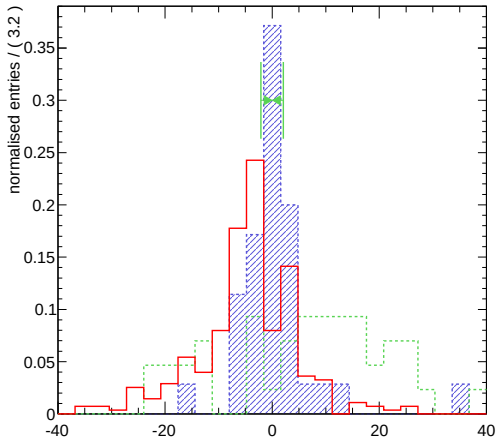

(b) $(\mathrm{IP}/\sigma_{\mathrm{IP}})_{\mathrm{SV}}$ of DD Λ s

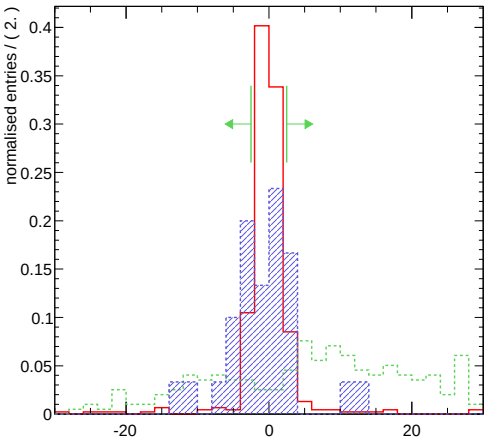

(c) $(\mathrm{IP}/\sigma_{\mathrm{IP}})_{\mathrm{PV}}$ of LU Λ s

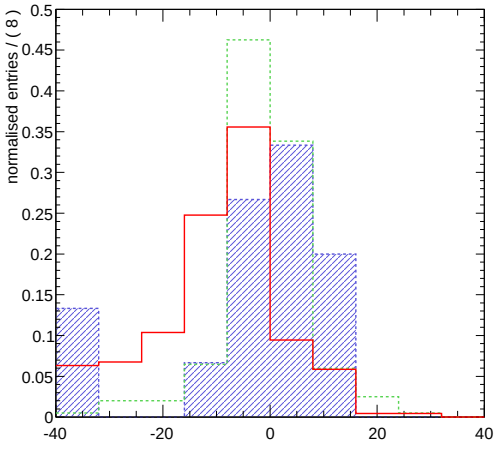

(d) $(\mathrm{IP}/\sigma_{\mathrm{IP}})_{\mathrm{SV}}$ of LU Λ s

Figure 5.17: Selection of opposite-side tag Λ's (solid blue line) from the primary Λ (dashed red line) and combinatoric background (green line) for DD and LU track combinations. Final cut positions are indicated by the green arrow.

Cut variable	LL	DD	LU*
$(\mathrm{IP}/\sigma_{\mathrm{IP}})_{\mathrm{pile}}$	$> 5.$	$> 5.$	$> 5.$
$\cos(\theta_{PV})$	> 0.999990	-	>0.999980
$\cos(\theta_{SV})$	> 0.999988	-	> 0.999985
$(\mathrm{IP}/\sigma_{\mathrm{IP}})_{\mathrm{PV}}$	$> 2.$	-	> 2.5
$(\mathrm{IP}/\sigma_{\mathrm{IP}})_{\mathrm{SV}}$	< 3.8	2.1	-

Table 5.22: Selection variables to select opposite-side tagging Λ's from the background of primary and combinatoric background, given in terms of the condition required to pass the cut.

However, as previously noted, the wrong tag fraction immediately after selection is greater than 50% with a $2-2.5\sigma$ statistical significance. This suggests that, compared to the tagging Λ's, a subset of the selected Λ's must have the opposite correlation between b and Λ flavour. The source of this opposing correlation is the subject of the next section.

5.3.4 Same-side Λ flavour tag

To investigate the source of the opposing correlation it is informative to study the wrong tag fractions if a tag decision is made exclusively with primary Λ's and also with only the combinatoric background. In the latter case the wrong tag fraction is found to be statistically consistent with a 50% wrong tag fraction.

The wrong tag fraction for the primary Λ's at the generator level and after reconstruction is listed in Table 5.23 for both a $\mathrm{B}_{\mathrm{s}}^{0}$ and $\mathrm{B}_{\mathrm{d}}^{0}$ signal channel. For the $\mathrm{B}_{\mathrm{s}}^{0}$ signal channel the wrong tag fraction is greater than 50% at both the generator level and after reconstruction. However, there is no significant correlation evident for the $\mathrm{B}_{\mathrm{d}}^{0}$ signal channel.

A possible explanation for the fact that the correlation is observed for the $\mathrm{B}_{\mathrm{s}}^{0}$ and not the $\mathrm{B}_{\mathrm{d}}^{0}$ signal channel would be if the primary Λ is formed during the fragmentation process of the $\mathrm{B}_{\mathrm{s}}^{0}$ in a manner analogous to a same side kaon tag. Furthermore, the fact that the observed correlation is opposite to that of the opposite-side tag Λ's is entirely consistent with this picture, as is illustrated schematically by Figure 5.18. Opposite-side Λ's are formed from the companion B-hadron $b \to c \to s$ quark transition, which gives

	$B_s^0 \to J/\psi\,\phi$	$B_d^0 \to K\,\pi$
Generator level	51.0 ± 0.1	50.0 ± 0.1
Reconstruction	55.2 ± 0.7	49.5 ± 0.8
LL	56 ± 1	50 ± 1
DD	56 ± 1	49 ± 1
LU*	54 ± 1	50 ± 2

Table 5.23: Primary Λ wrong tag fraction at the generator level and after reconstruction, from the decay of 60k $B_s^0 \to J/\psi\,\phi$ and $B_d^0 \to K\,\pi$. Reconstruction assumes perfect selection efficiency and purity.

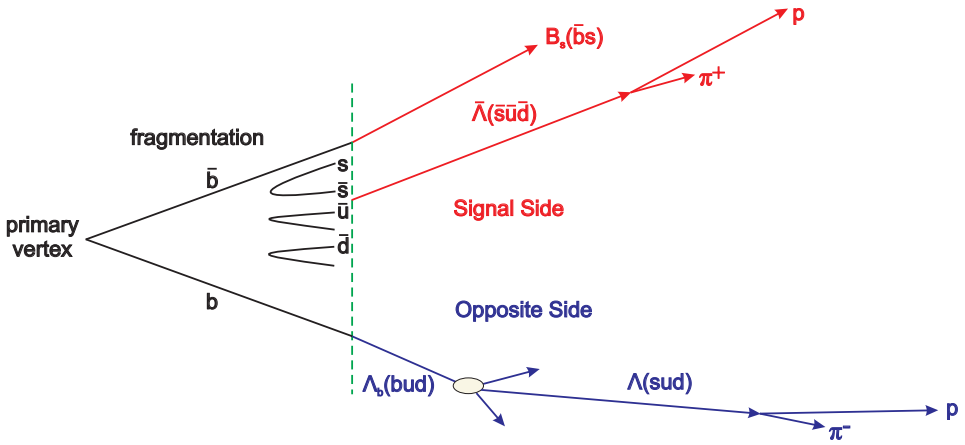

Figure 5.18: Opposite-side and same-side Λ tag topology.

rise to a Λ (s u d) flavour. An $\overline{\mathrm{s}}$ quark is available in the fragmentation chain that forms the signal B_s^0 and could conceivably hadronise to form a $\overline{\Lambda}$ ($\overline{\mathrm{s}}$ $\overline{\mathrm{u}}$ $\overline{\mathrm{d}}$). However, the correlation between B-hadron and Λ flavour would be opposite in the two tagging scenarios: an opposite-side Λ tags a $\overline{\mathrm{b}}$ flavour signal B-hadron, but a same-side Λ tags a b flavour signal B-hadron.

To investigate this effect further the distributions of the following variables are studied, which are also used to select same-side kaons:

- $\Delta\phi$: the difference in azimuthal angle between primary Λ and the reconstructed signal B-hadron.
- ΔQ: the mass difference between the signal B-hadron and the combination of the primary Λ and signal B-hadron mass.

- $p_{\mathrm{T}}^{\mathrm{rel}}$: the momentum of the primary Λ that is transverse to the combined signal B-hadron and primary Λ momentum.

The variables are shown in Figure 5.19 for a $\mathrm{B_s^0}$ and a $\mathrm{B_d^0}$ signal channel as a function of right and wrong tag. The right tag distributions for the $\mathrm{B_s^0}$ channel are consistent with the distributions observed for the same-side kaon tag; the particle is formed in the phase space of the signal $\mathrm{B_s^0}$. Furthermore, no separation between the right and wrong tag distribution are evident for the $\mathrm{B_d^0}$ signal channel, which is consistent with the hypothesis that the correlation observed in the $\mathrm{B_s^0}$ channel arises from the signal string fragmentation.

To investigate the potential flavour tagging performance of a same-side Λ tag, a grid scan of the the parameter space is performed. If more than one Λ passes the selection cuts, the tag is applied using the Λ with the smallest $p_{\mathrm{T}}^{\mathrm{rel}}$. The effective tagging efficiency as a function of each of the cut variables is illustrated in Figure 5.20 and the final selection cuts are listed in Table 5.24. Applying the selection cuts to a second independent data set of 60k $\mathrm{B_s^0} \rightarrow \mathrm{J}/\psi\ \phi$ events yields the following tagging performance:

$$\omega_{tag} = (32 \pm 3)\% \qquad \varepsilon_{tag} = (0.45 \pm 0.03)\% \qquad \varepsilon_{tag}^{eff} = (0.06 \pm 0.02)\%. \tag{5.16}$$

Although a reasonable wrong tag fraction is achieved, the effective tagging efficiency is limited by the relatively small tagging efficiency.

The observation that a small, but non-negligible, tagging performance is possible with Λ's produced in the $\mathrm{B_s^0}$ fragmentation raises the question of whether protons produced in the fragmentation of $\mathrm{B_d^0}$ mesons can be used for flavour tagging. This is the subject of the final section.

5.4 Same-side Proton Tag

The fragmentation diagram that would lead to the observed MC correlation between $\mathrm{B_s^0}$ and Λ's is illustrated in Figure 5.21(a). The analogous correlation that would be expected for protons and $\mathrm{B_d^0}$ mesons is shown in Figure 5.21(b). The idea of a same-side proton tag has been proposed by Gronau et.al [105].

From the correlation diagrams, it follows that a p is expected to tag $\overline{\mathrm{B}}_{\mathrm{d}}^{0}$ and a $\overline{\mathrm{p}}$ will

$B_s^0 \rightarrow J/\psi\ \phi$ $B_d^0 \rightarrow K\ \pi$

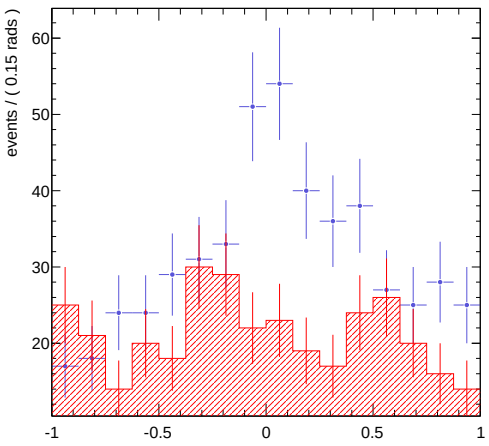

(a) $\Delta\phi$ [*degrees*]

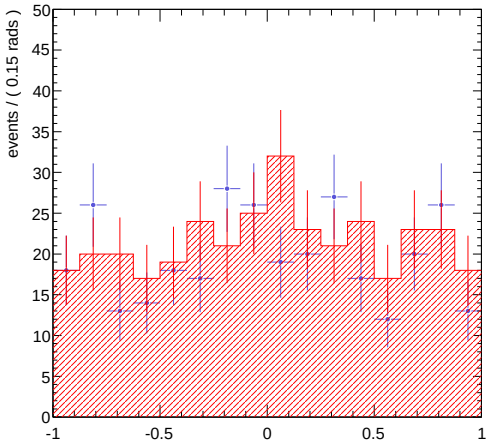

(b) $\Delta\phi$ [*degrees*]

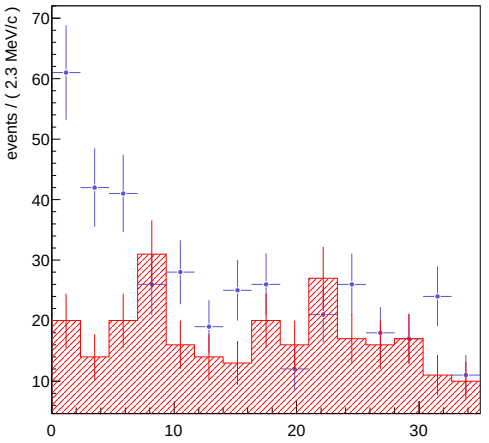

(c) p_T^{rel} [MeV/c]

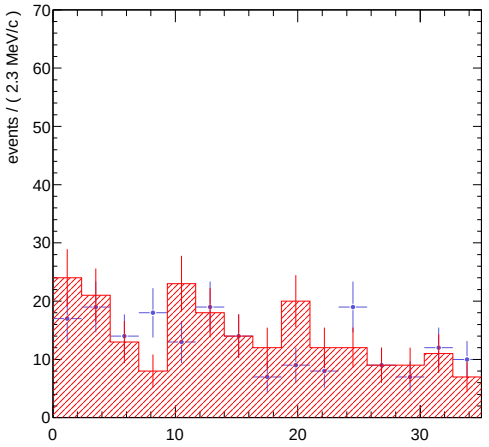

(d) p_T^{rel} [MeV/c]

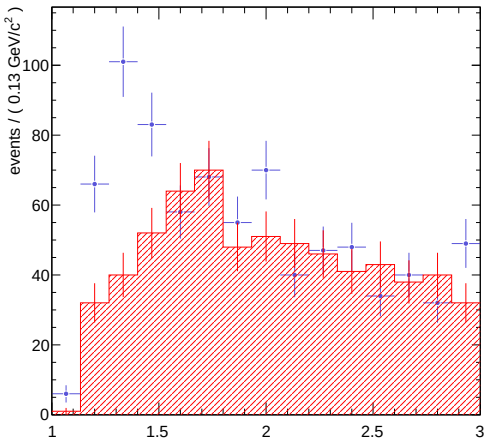

(e) ΔQ [GeV/c^2]

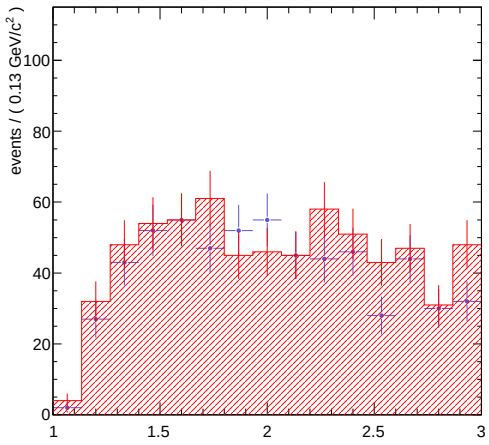

(f) ΔQ [GeV/c^2]

Figure 5.19: Right tag (blue points) and wrong tag (filled red points) Λ distributions for the decay of 60k $B_s^0 \rightarrow J/\psi\,\phi$ (left column) and 60k $B_d^0 \rightarrow K\,\pi$ (right column).

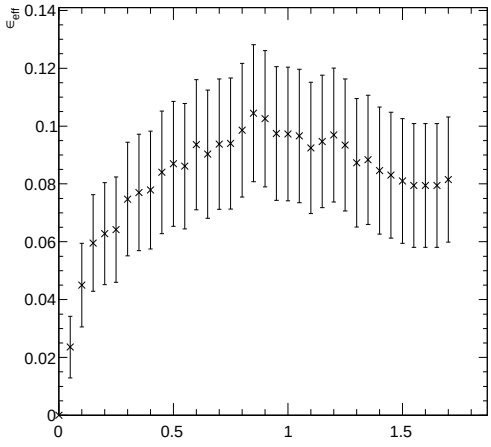

(a) $\Delta\phi$ cut [*degrees*]

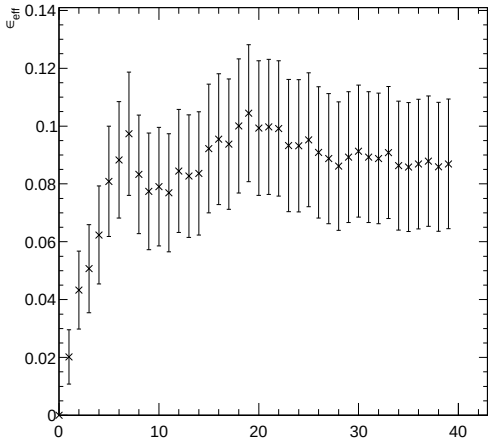

(b) $p_{\mathrm{T}}^{\mathrm{rel}}$ cut [MeV/c]

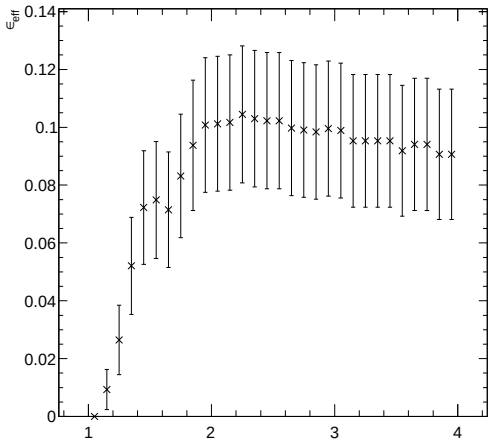

(c) ΔQ cut [GeV/c^2]

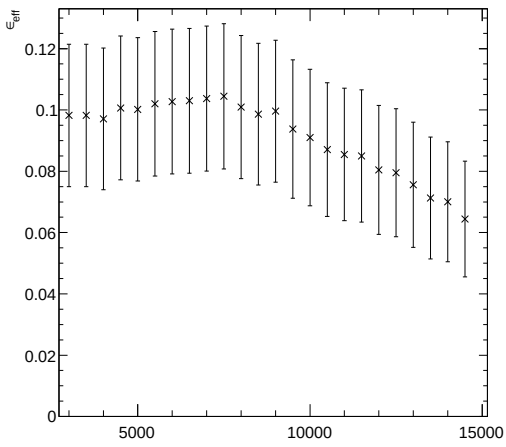

(d) $p(\Lambda)$ cut [MeV/c]

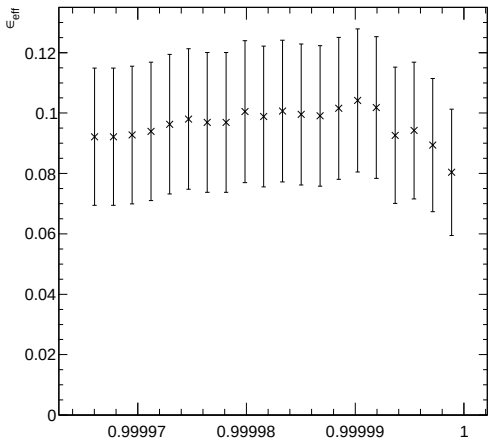

(e) $\cos(\theta_{PV})$ cut

Figure 5.20: Effective tagging efficiency as a function of same-side Λ selection cuts, for 60k reconstructed, triggered and selected $\mathrm{B_s^0} \to \mathrm{J}/\psi\,\phi$ events. For each plot the other selection variables are set to the retained values.

Cut variable	Cut
$\Delta\phi$	< 0.85 rads
ΔQ	< 2.25 MeV/c^2
$p_{\mathrm{T}}^{\mathrm{rel}}$	< 19 MeV/c
$p(\Lambda)$	> 7.5 GeV/c
$\cos(\theta_{PV})$	> 0.99999

Table 5.24: Same-side Λ tag selection cuts, in terms of the condition required to pass the cut.

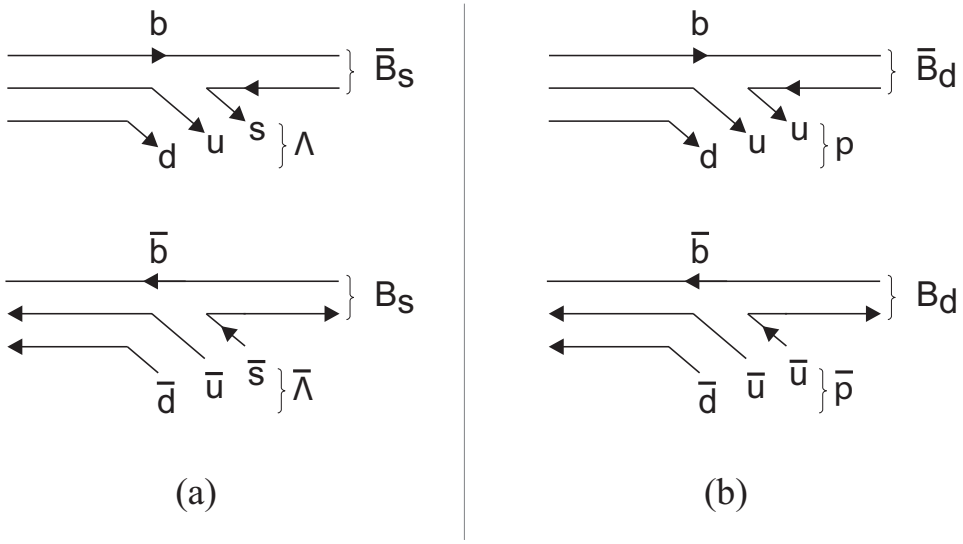

Figure 5.21: Correlations of neutral strange B-mesons with Λ and $\overline{\Lambda}$, and the correlation of neutral non-strange B-mesons with p and $\overline{\mathrm{p}}$. The proton correlation diagram is taken from Gronau et.al [105].

identify a B_d^0. Figure 5.22 illustrates the $\Delta\phi$, p_T^{rel} and ΔQ distributions for both a B_s^0 and B_d^0 channel. To avoid the situation of tagging power arising from kaons mistagged as protons, the MC truth information is used to select only protons associated to a true proton.

Although there is some evidence for separation between the right and wrong tag distributions for the B_d^0 channel, which is not seen in the B_s^0 channel, the correlation is considerably weaker than for the same-side Λ distributions shown in Figure 5.19. Furthermore, a grid scan of the parameter space is unable to extract a useful tagging performance and any potential tagging power is overwhelmed by the large number of background protons.

5.5 Summary and Outlook

The issue of flavour tagging with baryons was motivated by the potential tagging performance of an opposite-side proton tag. Despite a promising potential performance, the performance that can be realised is intrinsically limited by the fact that protons from B-mesons and Λ_b's have the opposite tagging correlation. The difficulty of separating these two cases is further compounded by the background of protons from the underlying event. These difficulties motivated the studies of an opposite-side Λ tag. Such a tag is found to have a number of advantages over the proton tag; both B-mesons and Λ's have the same tagging correlation and the reconstructed Λ's can be well separated from the underlying background. Furthermore, a useful tagging performance is potentially attainable after reconstruction, assuming perfect selection efficiency and purity. However, the performance is diluted by primary Λ's, which could not be removed with simple geometric cuts. Finally, the observation of a tagging correlation in the primary Λ's motivated the search for Λ's produced in the fragmentation of B_s^0 mesons. A small, but non-negligible, performance is achieved with a same-side Λ tag. However, the flavour correlation for the analogous same-side proton tag, after proton reconstruction and selection, is too small for a useful tagging performance.

In conclusion, there is potential for flavour tagging with protons and Λ's, but the implementation is found to be very challenging. However, it should be noted that many of the implementation challenges encountered, such as the balance between protons originating from Λ's and B-mesons, are entirely derived from the Monte Carlo simulation. As such, it would be prudent to revisit many of the issues discussed in this chapter once

$B_s^0 \to J/\psi\,\phi$ $B_d^0 \to K\,\pi$

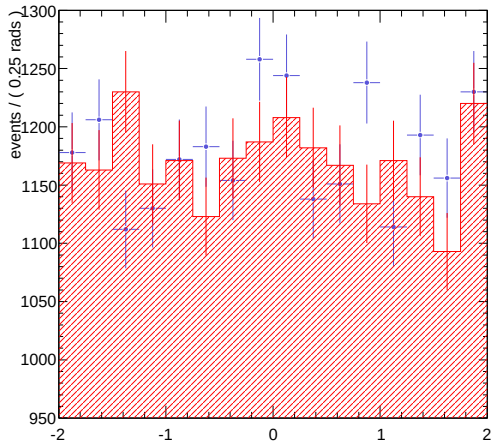

(a) $\Delta\phi$ [*degrees*]

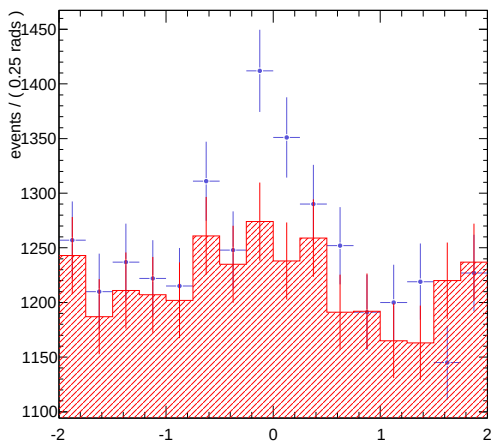

(b) $\Delta\phi$ [*degrees*]

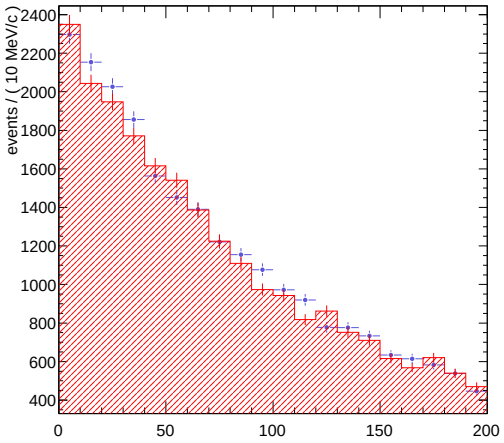

(c) p_T^{rel} [MeV/c]

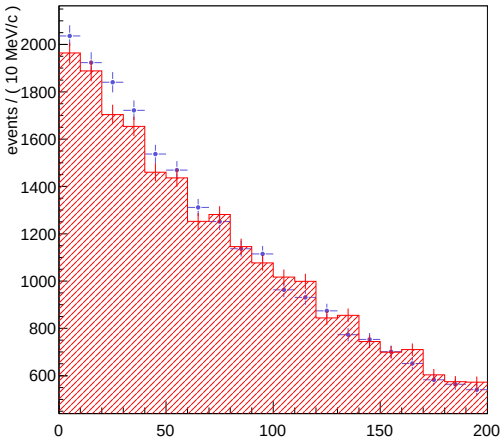

(d) p_T^{rel} [MeV/c]

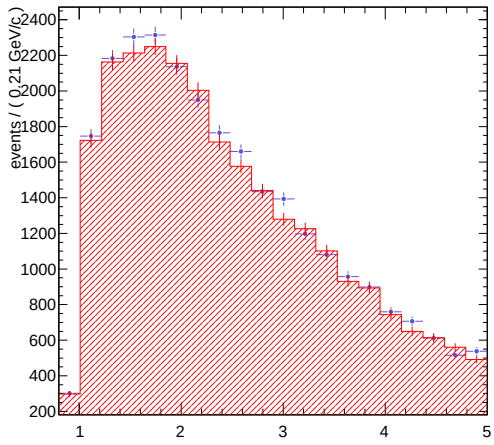

(e) ΔQ [GeV/c^2]

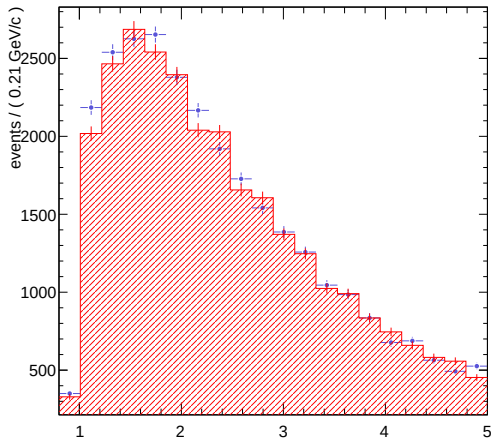

(f) ΔQ [GeV/c^2]

Figure 5.22: Right tag (blue points) and wrong tag (filled red points) p distributions for the decay of 60k $B_s^0 \to J/\psi\,\phi$ (left column) and 60k $B_d^0 \to K\,\pi$ (right column).

real data are available.

Chapter 6

$\Lambda_b \to p\pi/K$ Event Reconstruction and Selection

This chapter presents the procedure for reconstructing $\Lambda_b \to p\pi$ and $\Lambda_b \to pK$ decays with the LHCb apparatus and the selection strategy to extract these rare decays from the underlying background. The aim of this study is to determine the total selection efficiency, ε_{tot} and the background to signal ratio (B/S). Knowledge of ε_{tot}, and B/S enables an estimation of the annual event yield and LHCb's sensitivity to direct $\mathcal{CP}$ asymmetries in these two decay channels. This is the subject of Chapter 7.

6.1 Monte Carlo Data Samples

The studies presented in this thesis use 146k $\Lambda_b \to p\pi$ and 143k $\Lambda_b \to pK$ signal events, the generation and simulation of which is detailed in section 2.4.1. The most significant background source for both channels is expected to be the inclusive decay of $b\bar{b}$ events, of which there will be approximately 10^6 for every signal event. Topologically similar decay modes, such as the charmless two-body decay of B-mesons, are also expected to be an important background. In addition, both signal channels are expected to be a background to each other, as they differ only by the identity of the lighter hadron. The theoretical expectation for the branching ratios for the signal channels and the measured branching ratios for the charmless two body B decay backgrounds are given in Table 6.1. Previous studies have shown the minium bias (pp $\to$ anything) background to be insignificant [49].

Channel	$\mathcal{B}$ ($\times 10^{-6}$)
$\Lambda_b \to p\,\pi$	0.929 [41]
$\Lambda_b \to p\,K$	1.54 [41]
$B_s^0 \to K^+\,\pi^-$	5.00 [106]
$B_s^0 \to K^+\,K^-$	24.4 [106]
$B_d^0 \to K^+\,\pi^-$	18.9 [107]
$B_d^0 \to \pi^+\,\pi^-$	4.90 [107]

Table 6.1: Branching ratios ($\mathcal{B}$) for the decays of interest and the expected background channels.

Channel	N_{gen}	Weight Factor	
	($\times 10^3$ events)	$\Lambda_b \to p\,\pi$	$\Lambda_b \to p\,K$
$\Lambda_b \to p\,\pi$	146	1.0	0.6
$\Lambda_b \to p\,K$	143	1.7	1.0
inclusive $b\bar{b}$	33,000	31,000	18,000
$B_s^0 \to K^+\,\pi^-$	50	17.2	9.9
$B_s^0 \to K^+\,K^-$	70	62.1	35.8
$B_d^0 \to K^+\,\pi^-$	320	42.4	24.5
$B_d^0 \to \pi^+\,\pi^-$	175	19.0	10.9

Table 6.2: Generated Monte Carlo dataset sizes (N_{gen}) and corresponding statistical weight factors

In order to produce an equivalent number of signal and inclusive $b\bar{b}$ events, such that the sample sizes correspond to the same period of intergrated luminosity, would require the production of approximately 10^6 inclusive $b\bar{b}$ events for every signal event produced. For a typical signal sample size of order 10^4 events, this would imply the production of $10^6 \times 10^4 = 10^{10}$ inclusive $b\bar{b}$ events. However, due to the finite computational resources available to produce Monte Carlo data, it is only possible to produce a sample of order 10^7 events. The numbers of signal and background events generated for this study are given in Table 6.2; the implications of the statistical imbalance between the signal and background samples for the selection analysis is addressed here.

The tuning of the event selection is a trade-off between tightening cuts to improve the purity of the selected events and loosening them to retain signal events. The selection purity is typically characterised by the ratio of background to signal events ($B_{\rm sel}/S_{\rm sel}$) that pass the selection criteria. A measurement of the absolute value of $B_{\rm sel}/S_{\rm sel}$ requires that the number of generated signal and background events correspond to the same equivalent period of integrated luminosity, which necessitates the weighting of the background event sample. The number of signal events, $N_{\rm sig}$, generated during a period of luminosity that yields $N_{\rm b\overline{b}}$ $\rm b\overline{b}$ events is,

$$N_{\rm sig} = 2N_{\rm b\overline{b}} f_{\rm sig} \mathcal{B}_{\rm sig} \tag{6.1}$$

where $f_{\rm sig}$ is the hadronisation fraction of the signal B-hadron and $\mathcal{B}_{\rm sig}$ the signal branching fraction. The factor of 2 arises since both the b and $\overline{\rm b}$ quarks can hadronise to the signal B-hadron. The effective, post-weighted, number of background events must correspond to same period of luminosity,

$$\omega_{\rm back} N_{\rm back} = 2N_{\rm b\overline{b}} f_{\rm back} \mathcal{B}_{\rm back}, \tag{6.2}$$

where $N_{\rm back}$ is the number of generated background events, $\omega_{\rm back}$ is the background weight factor, $f_{\rm back}$ is the B-hadron hadronisation fraction and $\mathcal{B}_{\rm back}$ is the branching fraction.

In order to save valuable computational resources only those events which are within the acceptance of the detector are retained after event generation (see section 2.4). The number of signal and backround events which satisfy this criteria, $N^{\rm gen}_{\rm sig}$ and $N^{\rm gen}_{\rm back}$, are given by,

$$N^{\rm gen}_{\rm sig} = \varepsilon^{\rm geom}_{\rm sig} N_{\rm sig} \quad \text{and} \quad N^{\rm gen}_{\rm back} = \varepsilon^{\rm geom}_{\rm back} N_{\rm back}, \tag{6.3}$$

where $\varepsilon^{\rm geom}_{\rm sig}$ and $\varepsilon^{\rm geom}_{\rm back}$ are the fractions of simulated signal and background events within the detector acceptance. Combining equations 6.1, 6.2 and 6.3, yields the following expression for the background weight factor,

$$\omega_{\rm back} = \frac{N^{\rm gen}_{\rm sig}}{N^{\rm gen}_{\rm back}} \times \frac{\varepsilon^{\rm geom}_{\rm back}}{\varepsilon^{\rm geom}_{\rm sig}} \times \frac{f_{\rm back}}{f_{\rm sig}} \times \frac{\mathcal{B}_{\rm back}}{\mathcal{B}_{\rm sig}}. \tag{6.4}$$

For the inclusive $\rm b\overline{b}$ background, $\mathcal{B}_{\rm back} = 1$ and $f_{\rm back} = 1$, and the weight factor, $\omega_{\rm b\overline{b}}$, is

given by

$$\omega_{b\overline{b}} = \frac{N_{sig}^{gen}}{N_{b\overline{b}}^{gen}} \times \frac{\varepsilon_{b\overline{b}}^{geom}}{\varepsilon_{sig}^{geom}} \times \frac{1}{2 \times \mathcal{B}_{sig} \times f_{sig}}. \tag{6.5}$$

The weight factors for the inclusive $b\overline{b}$ and specific background channels are given in Table 6.2. It is evident that whether or not a single $b\overline{b}$ event falls within the selection criteria will shift the number of selected inclusive $b\overline{b}$ background events ($N_{b\overline{b}}^{sel}$) by 31,000 in the case of the $\Lambda_b \to p\,\pi$ signal channel and 18,000 for $\Lambda_b \to p\,K$. The effect of this statistical mismatch is to limit the precision of the background estimate. For example, consider that after the selection procedure 0 inclusive $b\overline{b}$ events pass the selection cuts. Using the procedure described by Feldman and Cousins [108], for a Poisson process with no observed events and a known mean background of 0, the signal mean has a 90% confidence level upper limit of 2.44. Therefore, with respect to the generated signal data samples, the number of selected inclusive $b\overline{b}$ events has an upper limit of:

$$\begin{aligned} N_{b\overline{b}}^{sel} &< 2.44 \times \omega_{b\overline{b}} \\ N_{b\overline{b}}^{sel} &< \begin{cases} 76,440 & \text{if signal} = \Lambda_b \to p\,\pi \\ 44,100 & \text{if signal} = \Lambda_b \to p\,K \end{cases} \end{aligned} \tag{6.6}$$

From equation 6.5 it is evident that to reduce this upper limit one can either increase the inclusive $b\overline{b}$ sample size or use fewer of the available signal statistics, at the cost of decreased statistical precision on the selected signal sample. The procedure adopted in this thesis is to increase the effective number of inclusive $b\overline{b}$ statistics by widening the mass selection window applied to the inclusive $b\overline{b}$ background compared to that applied to the signal data. Assuming that the inclusive $b\overline{b}$ background is uniformly distributed in this mass window, the effective number of inclusive $b\overline{b}$ events is increased by a factor equal to the ratio of the mass window cuts applied to the background and signal samples. This provides a statistically more precise estimate of the background.

6.2 Event Reconstruction

This section details the method of reconstructing candidate $\Lambda_b \to p\,\pi$ and $\Lambda_b \to p\,K$ decays within the framework of the LHCb software environment. Since the signal decays

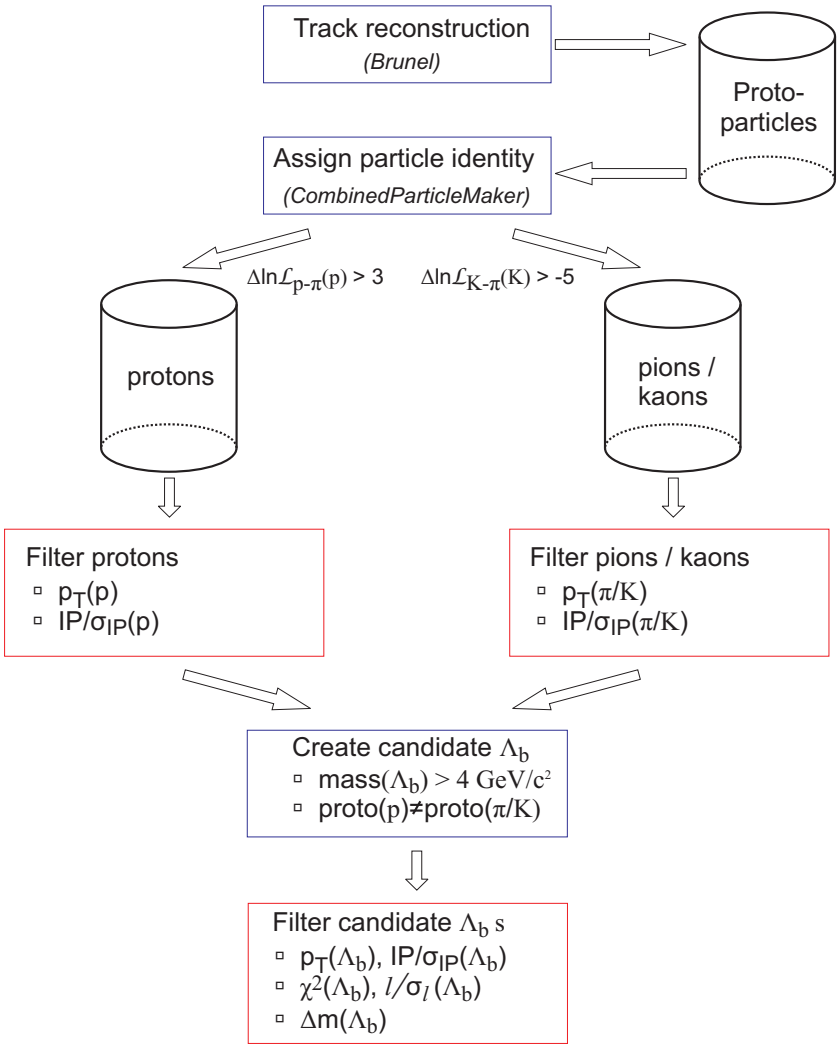

Figure 6.1: Reconstructing and selecting $\Lambda_b \to p\,\pi/K$ decays in the LHCb software framework. All reconstuction and selection algorithms are based on the C++ GAUDI framework [71]. The algorithms for reconstruction are grouped into an application called BRUNEL, which can process either real data or the output of the detector simulation [81]. Algorithms for physics analysis are collected into an application called DAVINCI [83]. All steps in the illustration are DAVINCI algorithms, except for track reconstruction which is part of the BRUNEL application.

differ only in the identify of the lighter hadron, the reconstruction steps that follow apply to both decay channels; any differences in procedure will be explicitly stated.

The sequence of steps to reconstruct and select $\Lambda_b \to p\,\pi/K$ decays in the LHCb software framework are illustrated in Figure 6.1. The reconstruction process begins with track reconstruction, the details of which are given in section 2.4.2. The reconstructed

tracks are not assigned a particular particle identity. The designation of a particle type (γ,e,μ,π,K,p) to each reconstructed track or "protoparticle" is determined by placing cuts on the difference between the likelihoods of the various particle hypotheses, as described in section 3.5. This may result in the track being associated with more than one particle type.

In order to save processing time it is useful to apply an initial set of loose particle identification (PID) selection criteria, which retains a high signal selection efficiency but reduces the background combinatorics. The difference in log likelihood (DLL) between the true[1] proton in $\Lambda_b \to p\,\pi/K$ decays and true pions / kaons in inclusive $b\overline{b}$ events is shown in Figures 6.2(a) and 6.2(b) respectively. Similarly, the DLL between the true kaon in $\Lambda_b \to p\,K$ decays and pions / kaons in inclusive $b\overline{b}$ events is shown in Figures 6.2(c) and 6.2(d). Tracks are assigned a proton identity if,

$$\Delta\ln\mathcal{L}_{p\pi} > 3, \tag{6.7}$$

and a kaon is identified if,

$$\Delta\ln\mathcal{L}_{K\pi} > -5. \tag{6.8}$$

This has the effect of reducing the background combinatorics by an order of magnitude, at the cost of a 10% loss of signal efficiency. The tuning of the PID selection criteria to remove specific backgrounds, such as the charmless two-body decay of B-hadrons, is described in section 6.3.

Candidate $\Lambda_b \to p\,\pi/K$ decays are reconstructed and selected by employing a number of selection criteria that exploit the nature of the decay. The topology of $\Lambda_b \to p\,\pi/K$ decays is illustrated in Figure 6.3. The most distinctive features of the decay are:

- A displaced secondary vertex (SV) : A Λ_b has an average momentum $p \sim 113$ GeV/c in the LHCb acceptance and the relatively long $(1.409 \pm 0.055) \times 10^{-12}$ s Λ_b lifetime [17] results in the Λ_b travelling on average 7.4 mm before decay.
- Two tracks, one positive and one negative, are observed to originate from the displaced secondary vertex.
- Since both final state masses are small compared to the Λ_b rest mass, the final

[1] The track is associated, via the associator algorithms described in section 2.4.2, to the correct particle identity and decay chain position.

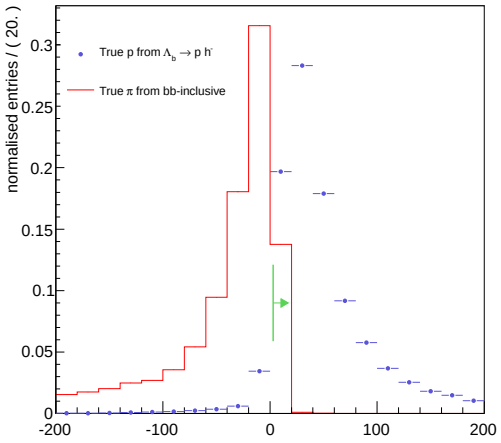

(a) $\Delta\ln\mathcal{L}_{p\pi}$

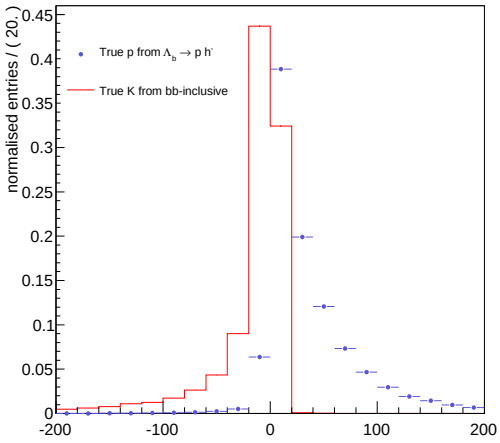

(b) $\Delta\ln\mathcal{L}_{pK}$

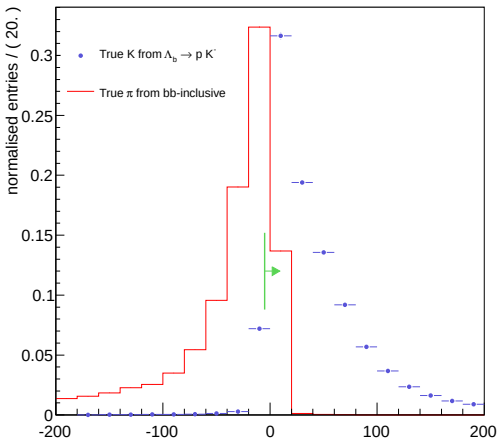

(c) $\Delta\ln\mathcal{L}_{K\pi}$

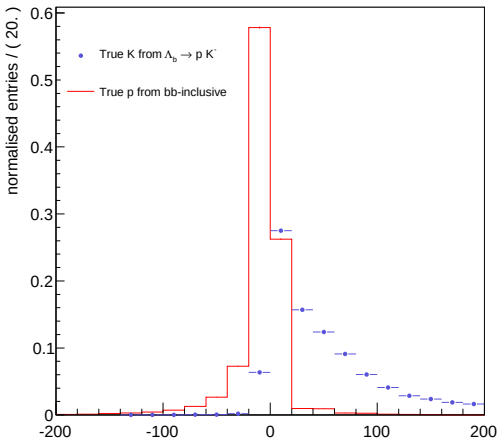

(d) $\Delta\ln\mathcal{L}_{Kp}$

Figure 6.2: Proton and kaon selection with difference in log likelihood (DLL) cuts. The loose PID cuts are indicated by the green arrows. The scale is arbitrary.

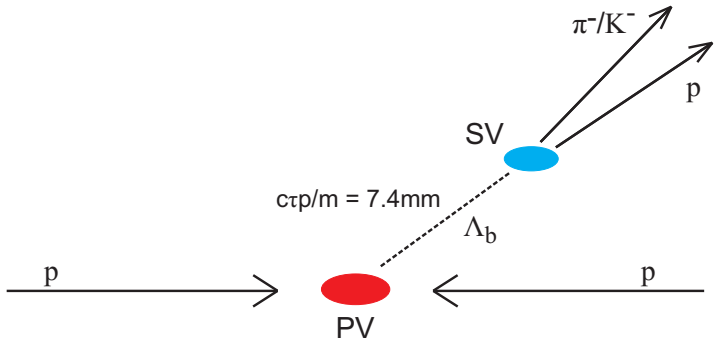

Figure 6.3: Schematic representation of the $\Lambda_b \rightarrow p\,\pi/K$ decay topology. The scale is arbitrary.

states will have a large transverse momentum compared to the inclusive $b\bar{b}$ background.

The protons and pions/kaons selected by the PID crtieria are filtered by imposing selection criteria on the transverse momentum (p_T) and the impact parameter significance with respect to the primary vertex $(IP/\sigma_{IP})_{PV}$. After the final state filtering, all unique combinations of opposite charged tracks are considered. A first check is to ensure that the two particles originate from unique protoparticles, since the latter can be assigned more than one particle type. The two particle tracks are combined to form a secondary vertex by extrapolating the particle tracks through the magnetic field map. A candidate Λ_b is created by combining the 4-momenta of the two particle tracks. The resulting mass distribution for true Λ_b's and the corresponding combinatoric background in 70k signal events is shown in Figure 6.4. A small true Λ_b peak is evident at 5620 MeV/c^2. For computational efficiency, the large combinatoric mass peak is immediately removed by requiring that all Λ_b candidates have a mass greater than 4 GeV/c^2.

Finally, the candidate Λ_b's are filtered by imposing criteria based on the impact parameter significance, $(IP/\sigma_{IP})_{PV}$, transverse momentum, p_T, and invariant mass of the candidate Λ_b, m_{Λ_b}. In addition criteria are imposed on the χ^2 of the secondary vertex fit and the significance of the secondary vertex's displacement from the primary vertex L/σ_L.

The selection criteria at each filter step are developed by means of a ROOT Tree (n-tuple), which is filled with the final state and candidate Λ_b selection variables and the corresponding Monte Carlo truth information (see section 2.4.2) [109]. The result of the L0, L1 and HLT trigger decisions are also recorded in the ROOT Tree, enabling the

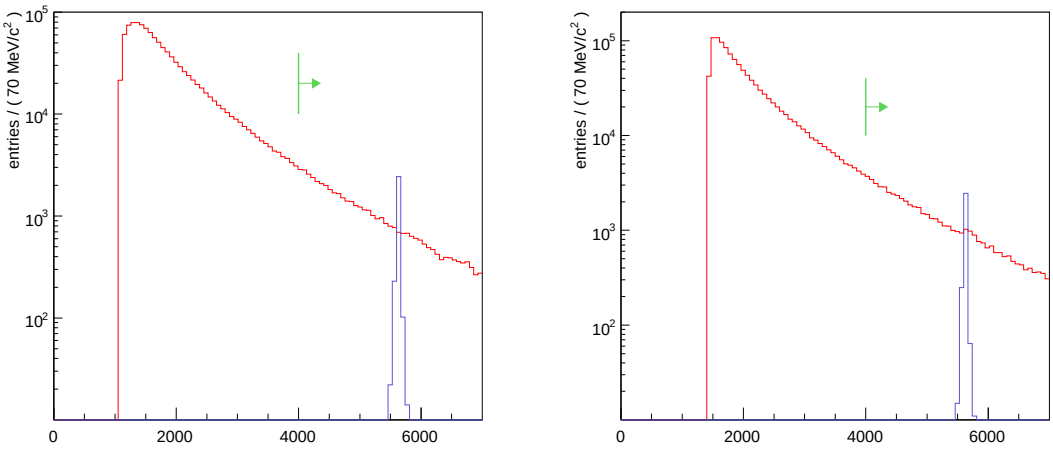

(a) mass(Λ_b) [MeV/c^2] (b) mass(Λ_b) [MeV/c^2]

Figure 6.4: Mass distribution of true candidate Λ_b's (blue line) and the combinatoric background (red line), for (a) $\Lambda_b \to p\,\pi$ and (b) $\Lambda_b \to p\,K$ decays.

effect of the trigger on the selection efficiency to be evaluated.

6.3 Event Selection

This section details the motivation, procedure and performance of methods to extract the signal decays channels from the vast background of reconstructed events. The challenge of this task to well illustrated by Figure 6.5 which shows the mass distribution for reconstructed $\Lambda_b \to p\,\pi$ and $\Lambda_b \to p\,K$ events for which no selection criteria have been applied except for the loose PID criteria. A clear signal peak centred at the nominal Λ_b mass ($5,624 \pm 9$ MeV/c^2 [17]) is evident, but is some 6 orders of magnitude beneath the overwhelming inclusive $b\bar{b}$ background.

The dominant source of background is expected to be inclusive $b\bar{b}$ events, since the production fraction of such events vastly exceeds that of the signal channels. As such, the selection criteria are optimised in the first instance by considering inclusive $b\bar{b}$ events as the only background source. Moreover, in light of the large statistical mismatch between the number of simulated signal decays and inclusive $b\bar{b}$ events (as discussed in section 6.1), the selection criteria are chosen to remove *all* the inclusive $b\bar{b}$ events,

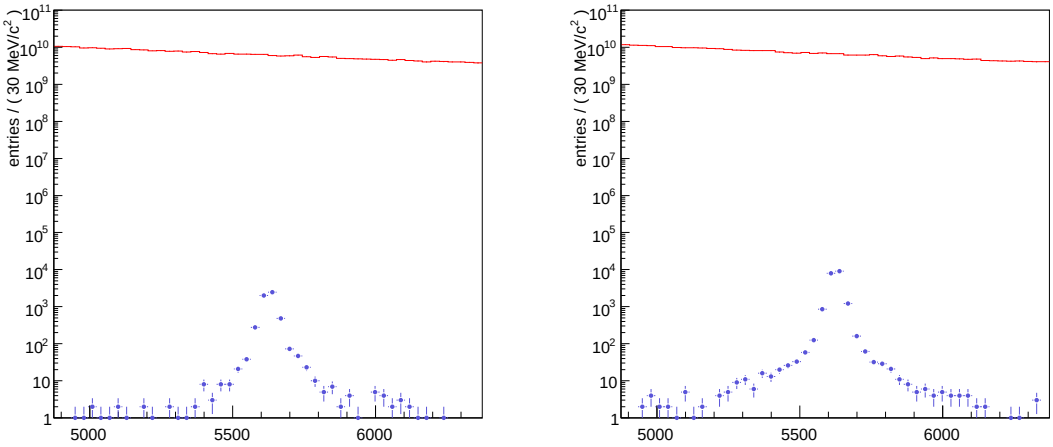

(a) mass(Λ_b) [MeV/c^2] (b) mass(Λ_b) [MeV/c^2]

Figure 6.5: Mass distribution of true candidate Λ_b's (red line) and the inclusive $b\overline{b}$ background (blue line), for (a) $\Lambda_b \rightarrow p\,\pi$ and (b) $\Lambda_b \rightarrow p\,K$ decays. Background weighted to correspond to same equivalent period of luminosity as the signal sample.

while retaining as high as possible selection efficiency. The selection criteria are then further refined by considering specific 2-body backgrounds; the aim at this point being to optimise the selection efficiency and purity with respect to these specific backgrounds.

The selection criteria used to extract the signal decays from the underlying background are as follows:

Track types

- The candidate Λ_b must be reconstructed from two long type tracks (see section 2.4.2 for track definitions.) The 12% of candidate Λ_b decays reconstructed from one or more downstream type tracks are excluded as the mass and impact parameter resolutions of the reconstructed Λ_b is an order of magnitude worse than those Λ_b decays reconstructed from two long type tracks.

Particle identification

- Tracks are identified as protons if the difference between the log likelihoods, $\Delta\ln\mathcal{L}$, of the proton and pion hypothesises, $\Delta\ln\mathcal{L}_{p\pi}(p)$, and the proton and kaon hypothesises, $\Delta\ln\mathcal{L}_{pK}(p)$, exceeds a minimum selection value. Tracks are identified as kaons from the $\Delta\ln\mathcal{L}$ between the kaon and pion hypothesis $\Delta\ln\mathcal{L}_{K\pi}(K)$, while tracks are identified as pions from the $\Delta\ln\mathcal{L}$ between the pion and kaon hypothesis $\Delta\ln\mathcal{L}_{\pi K}(\pi)$.

Kinematic cuts

- Of the two tracks used to reconstruct a candidate Λ_b, the track with the smaller transverse momentum, p_T^{min} , is required to exceed a minimum cut value of transverse momentum (p_T) and the track with the higher transverse momentum, p_T^{max} , must also exceed a minimum of p_T.

- Since B-hadrons are formed from hard interactions (see section 2.4), the candidate Λ_b transverse momentum, $p_T^{\Lambda_b}$, must exceed a certain minimum of p_T.

- The invariant mass of the the candidate Λ_b, m_{Λ_b}, must lie within a range Δm_{Λ_b} of the nominal Λ_b mass.

Geometric cuts

- Since the Λ_b decay vertex is displayed with respect to the primary vertex, minimum impact parameter significance (IPS) conditions are required of the final state with the smaller IPS, S^{min}, and the final state with the larger IPS, S^{max}.

- Considering that a true Λ_b originates from the primary vertex, the impact parameter significance of the candidate Λ_b, $S^{max}_{\Lambda_b}$, is required to be less than a maximum cut value.

- The reconstructed tracks must originate from a common point in space, which is qualified by the $\chi^2_{\Lambda_b}$ of the candidate Λ_b vertex fit.

- The flight distance, L, is defined as the distance between the Λ_b decay vertex and the primary vertex. Since the lifetime of the Λ_b is relatively long, the flight distance significance of a candidate Λ_b, $S^L_{\Lambda_b}$, is required to be greater than a minimum cut value.

6.3.1 Extracting $\Lambda_b \to p\,\pi/K$ decays from the inclusive $b\bar{b}$ background

This section presents the development and performance of selection criteria to extract the signal decay channels from the inclusive $b\bar{b}$ background.

As a first step, loose preselection criteria are applied to reduce the $\mathcal{O}(10^7)$ inclusive $b\bar{b}$ data set to a computationally more manageable size. Figures 6.6-6.8 illustrate the selection variable distributions for a $\sim$158k subset of the inclusive $b\bar{b}$ data sample used for the development of selection cuts, compared to $\sim$75k $\Lambda_b \to p\,\pi$ and $\sim$71k $\Lambda_b \to p\,K$ signal decays. The signal sample sizes correspond to approximately half of the generated Monte Carlo data samples listed in Table 6.2, the remaining data is used for an unbiased evaluation of the selection performance. No selection criteria have been applied except for the combinatoric suppressing loose PID criteria and the $m_{\Lambda_b} > 4$ GeV/c^2 mass cut (see section 6.2). A summary of the preselection cuts for the $\Lambda_b \to p\,\pi/K$ signal channels is given in Table 6.3. The kinematic and geometric preselection criteria are similar to those used in the preselection of generic $B^0 \to h^+h^-$ decays, but with additional PID selection criteria [110]. From an initial $\sim$17.6M inclusive $b\bar{b}$ events, $\sim$3.1k remain after the $\Lambda_b \to p\,\pi$ preselection and only $\sim$1.2k after the $\Lambda_b \to p\,K$ preselection cuts. The approximate factor of 2 difference arises from applying a PID cut on the kaon in the $\Lambda_b \to p\,K$ decay, while no PID cut is applied to the pion in the $\Lambda_b \to p\,\pi$ channel.

Due to the statistical mismatch between the number of available Monte-Carlo signal and inclusive $b\bar{b}$ events, as discussed in section 6.1, the final selection criteria are chosen with the aim of removing *all* the inclusive $b\bar{b}$ background events, while retaining as high as possible signal selection efficiency. The selection variable distributions after the preselection cuts are shown in Figures 6.9-6.12. The final selection criteria, together with the effect of each selection cut on the signal and inclusive $b\bar{b}$ background, are given in Tables 6.4 and 6.5 for the $\Lambda_b \to p\,\pi$ and $\Lambda_b \to p\,K$ signal channels respectively. A mass width selection cut of $\Delta m_{\Lambda_b} = \pm 550$ MeV/c^2 is applied to the inclusive $b\bar{b}$ background, a factor ten greater than the $\Delta m_{\Lambda_b} = \pm 55$ MeV/c^2 cut applied to the signal sample.

The $\Lambda_b \to p\,\pi$ and $\Lambda_b \to p\,K$ selection criteria meet the objective of removing all inclusive $b\bar{b}$ events from the narrow, ± 55 MeV/c^2, mass window. However, a number of background events pass the selection criteria in the the wider, ± 550 MeV/c^2, mass

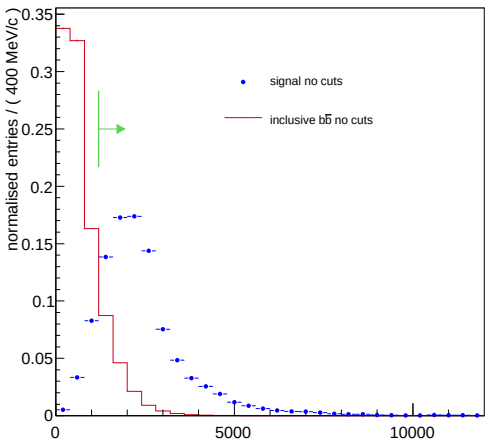

(a) p_T^{min} [MeV/c^2]

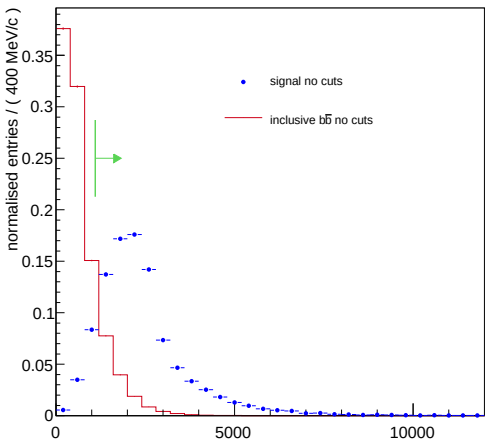

(b) p_T^{min} [MeV/c^2]

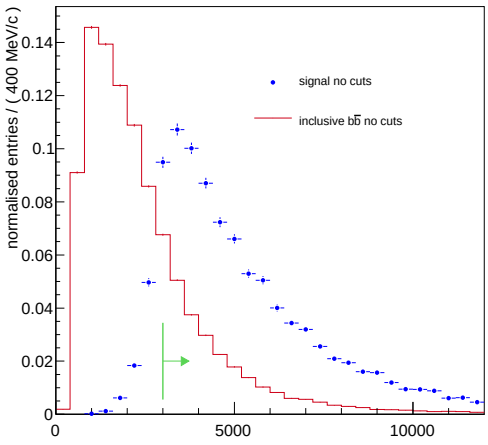

(c) p_T^{max} [MeV/c^2]

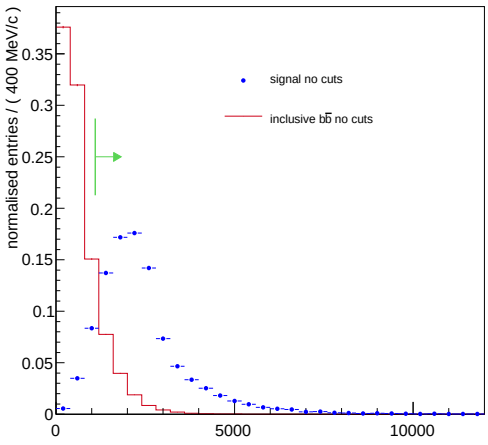

(d) p_T^{max} [MeV/c^2]

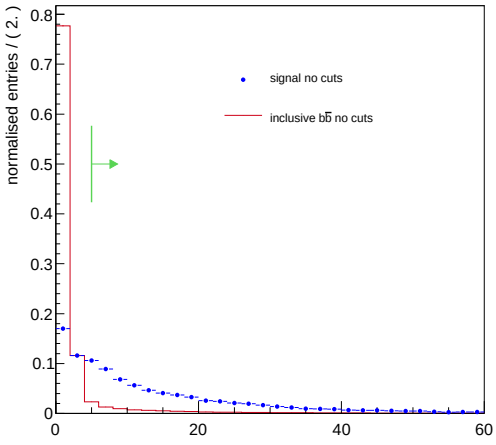

(e) S^{min}

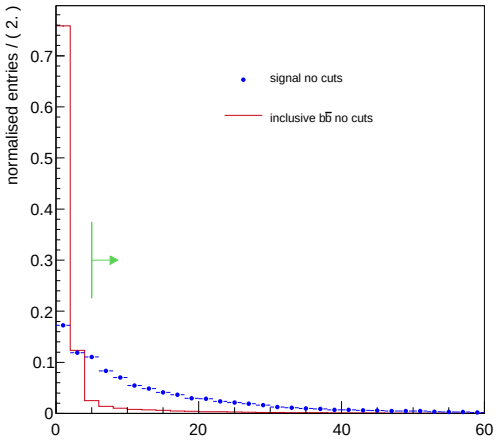

(f) S^{min}

Figure 6.6: p_T^{min} (top row), p_T^{max} (middle row) and S^{min} (bottom row) distributions for the selection of $\Lambda_b \to p\,\pi$ (left column) and $\Lambda_b \to p\,K$ (right column) decays. The blue points represent the signal and the red lines represent the inclusive $b\bar{b}$ background. *No pre-selection cuts applied.* Green lines indicate the position of the *final selection cuts*.

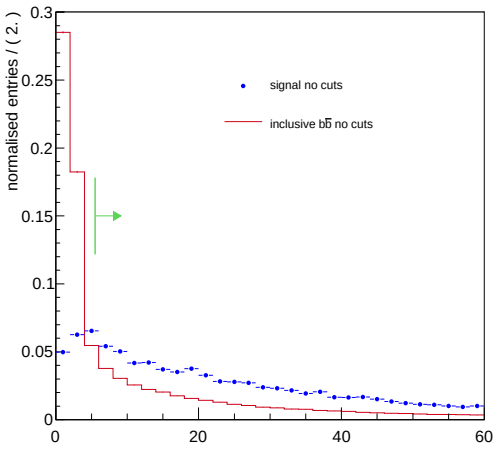

(a) S^{max}

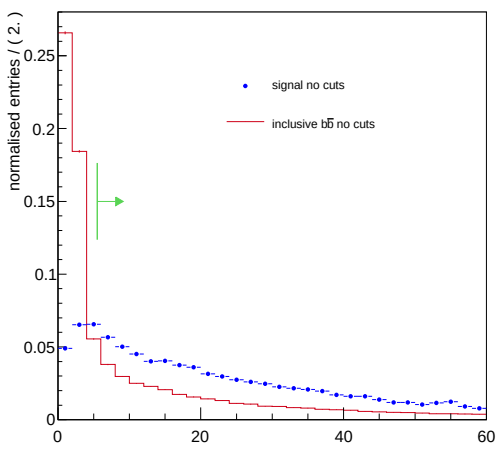

(b) S^{max}

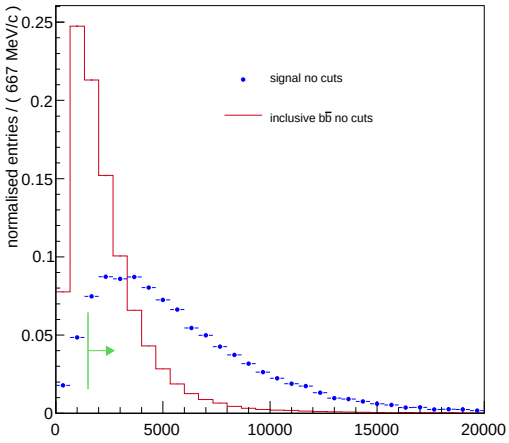

(c) $p_T^{\Lambda_b}$ [MeV/c^2]

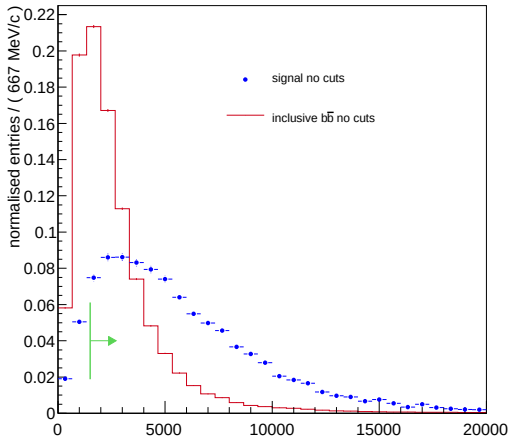

(d) $p_T^{\Lambda_b}$ [MeV/c^2]

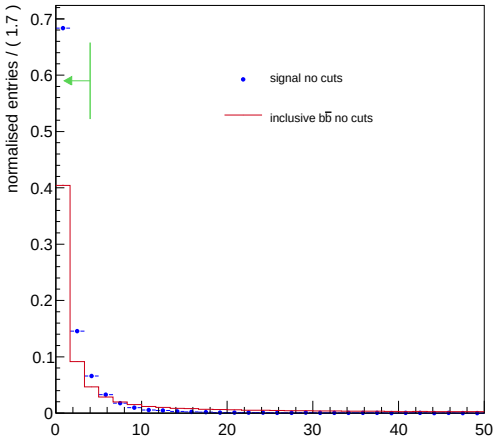

(e) $\chi^2_{\Lambda_b}$

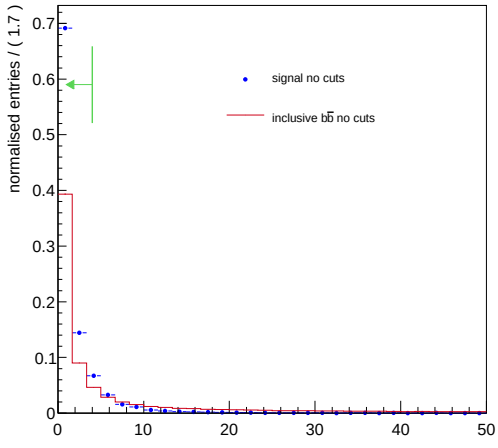

(f) $\chi^2_{\Lambda_b}$

Figure 6.7: S^{max} (top row), $p_T^{\Lambda_b}$ (middle row), $\chi^2_{\Lambda_b}$ (bottom row) distributions for the selection of $\Lambda_b \to p\,\pi$ (left column) and $\Lambda_b \to p\,K$ (right column) decays. The blue points represent the signal and the red lines represent the inclusive $b\bar{b}$ background. *No pre-selection cuts applied.* Green lines indicate the position of the *final selection cuts*.

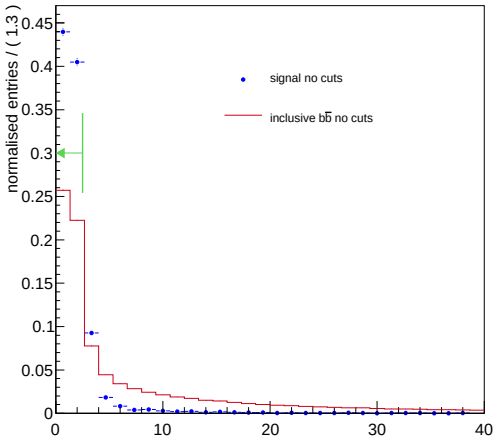

(a) $S^{max}_{\Lambda_b}$

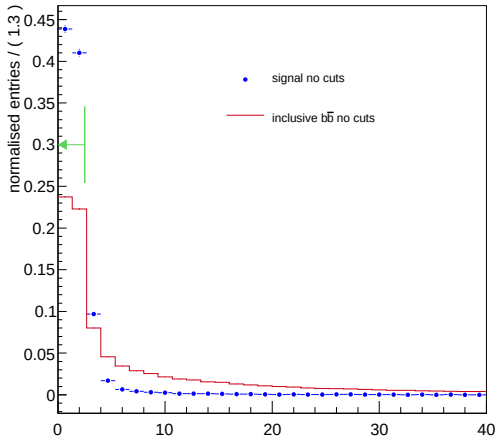

(b) $S^{max}_{\Lambda_b}$

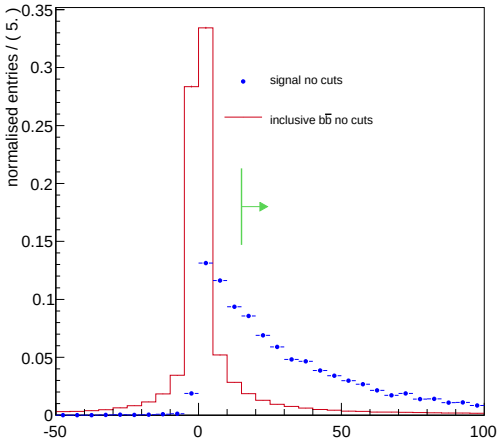

(c) $S^{L}_{\Lambda_b}$

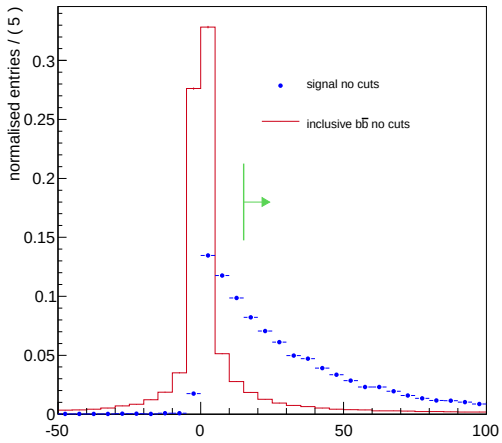

(d) $S^{L}_{\Lambda_b}$

Figure 6.8: $S^{max}_{\Lambda_b}$ (top row), $S^{L}_{\Lambda_b}$ (bottom row) distributions for the selection of $\Lambda_b \to p\,\pi$ (left column) and $\Lambda_b \to p\,K$ (right column) decays. The blue points represent the signal and the red lines represent the inclusive $b\overline{b}$ background. *No pre-selection cuts applied.* Green lines indicate the position of the *final selection cuts*.

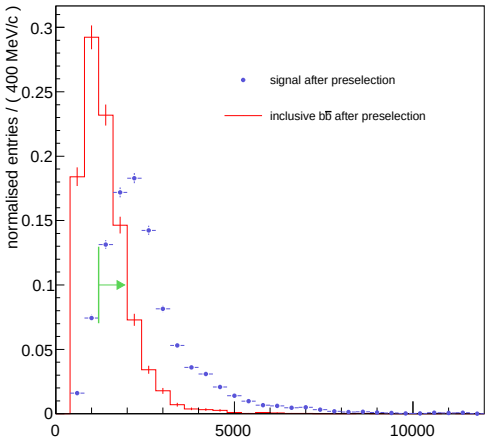

(a) p_T^{min} [MeV/c^2]

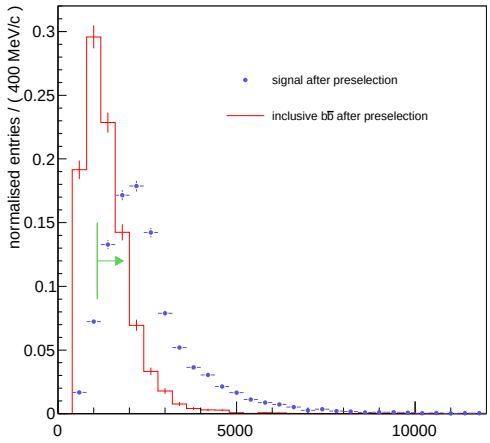

(b) p_T^{min} [MeV/c^2]

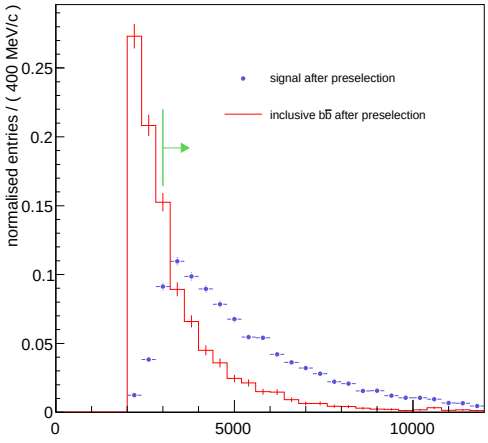

(c) p_T^{max} [MeV/c^2]

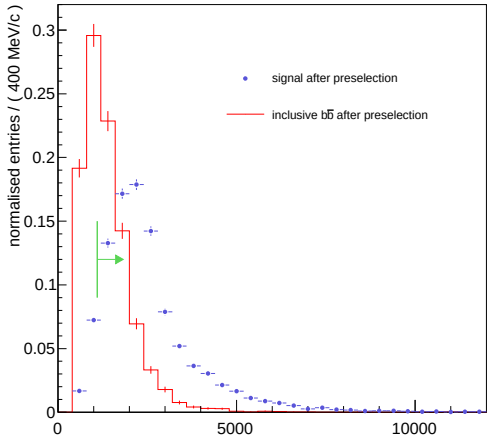

(d) p_T^{max} [MeV/c^2]

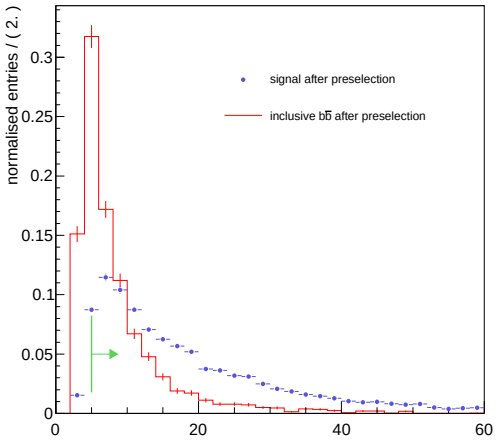

(e) S^{min}

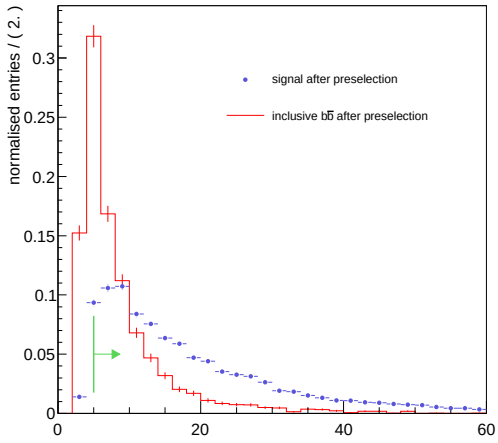

(f) S^{min}

Figure 6.9: Final state cut variable distributions for $\Lambda_b \to p\,\pi$ (left column) and $\Lambda_b \to p\,K$ (right column) decays, *after preselection cuts*. The blue points represent the signal and the red lines represent the inclusive $b\overline{b}$ background. Vertical green lines indicates the *final selection cuts*.

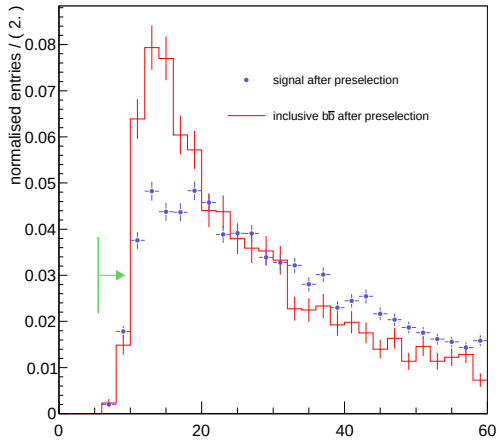

(a) S^{max}

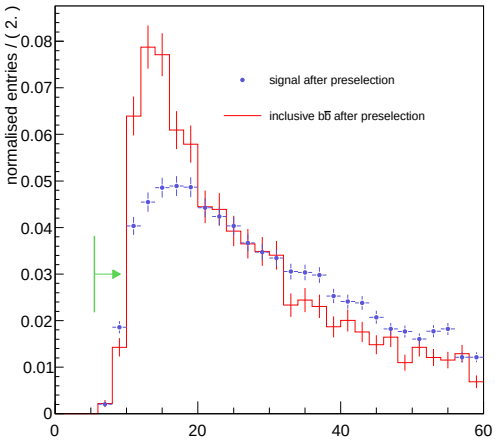

(b) S^{max}

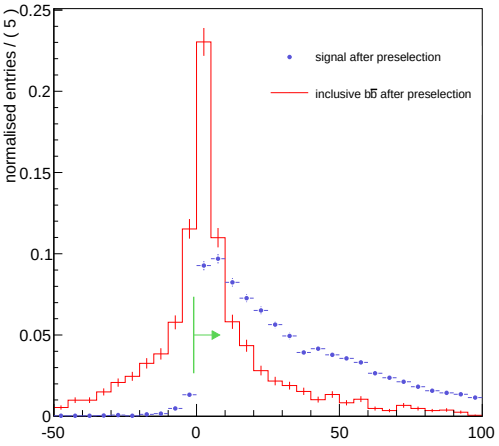

(c) $\Delta\ln\mathcal{L}_{pK}(p)$

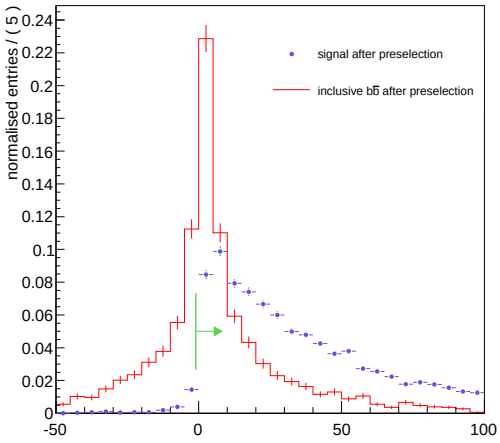

(d) $\Delta\ln\mathcal{L}_{pK}(p)$

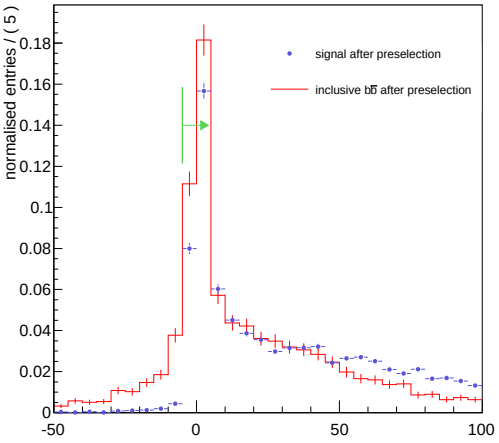

(e) $\Delta\ln\mathcal{L}_{\pi K}(\pi)$

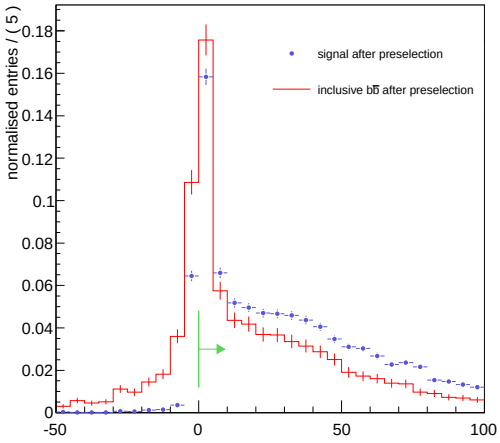

(f) $\Delta\ln\mathcal{L}_{K\pi}(K)$

Figure 6.10: Final state cut variable distributions for $\Lambda_b \to p\,\pi$ (left column) and $\Lambda_b \to p\,K$ (right column) decays, *after preselection cuts*. The blue points represent the signal and the red lines represent the inclusive $b\overline{b}$ background. Vertical green lines indicates the *final selection cuts*.

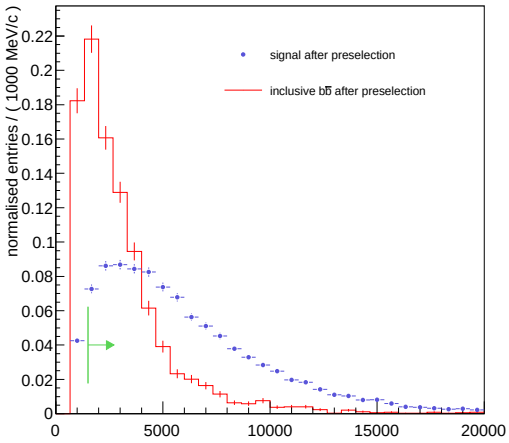

(a) $p_T^{\Lambda_b}$ [MeV/c^2]

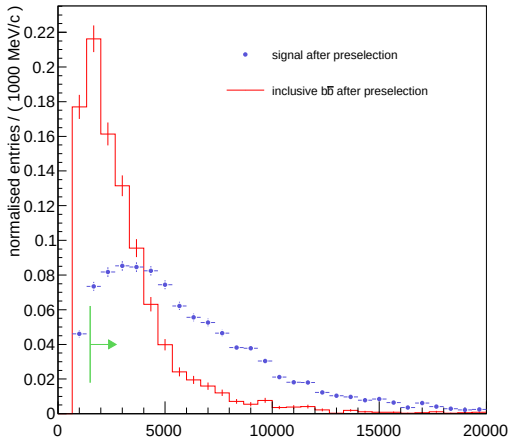

(b) $p_T^{\Lambda_b}$ [MeV/c^2]

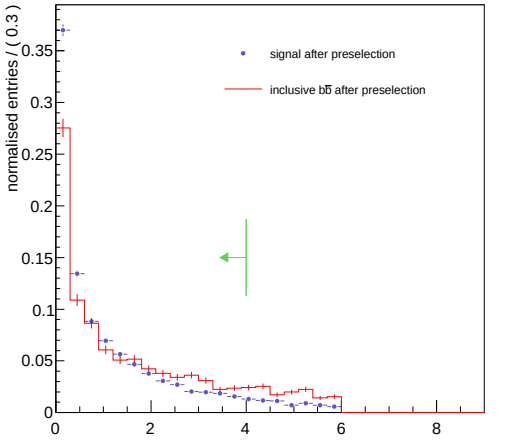

(c) $\chi^2_{\Lambda_b}$

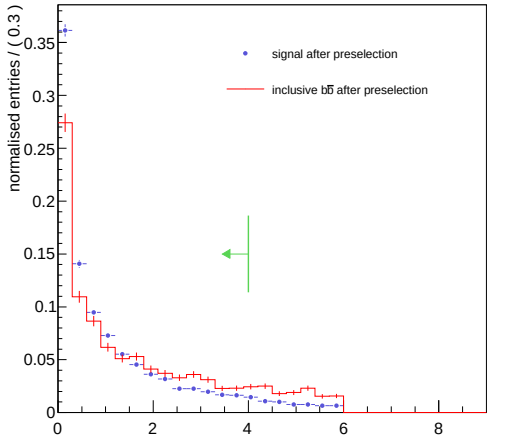

(d) $\chi^2_{\Lambda_b}$

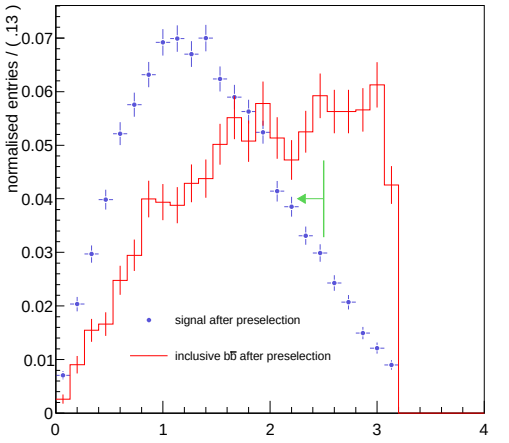

(e) $S^{max}_{\Lambda_b}$

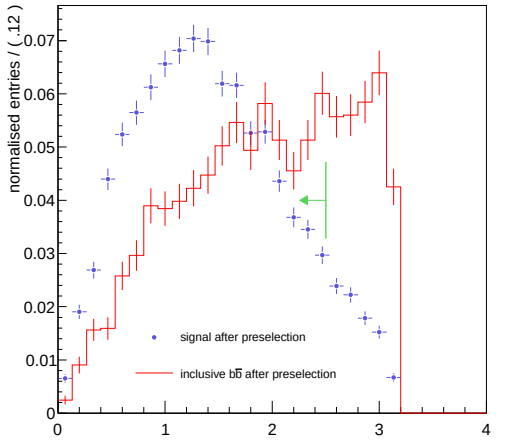

(f) $S^{max}_{\Lambda_b}$

Figure 6.11: Candidate Λ_b cut variable distributions for $\Lambda_b \to p\,\pi$ (left column) and $\Lambda_b \to p\,K$ (right column) decays, *after preselection cuts*. The blue points represent the signal and the red lines represent the inclusive $b\overline{b}$ background. Vertical green lines indicates the *final selection cuts*.

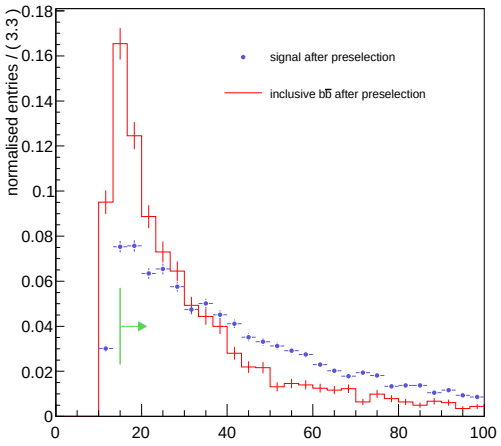

(a) $S^L_{\Lambda_b}$

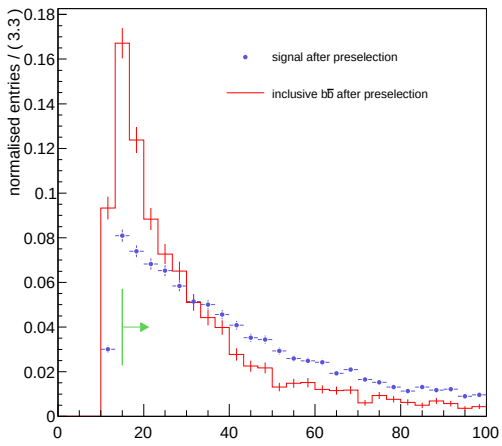

(b) $S^L_{\Lambda_b}$

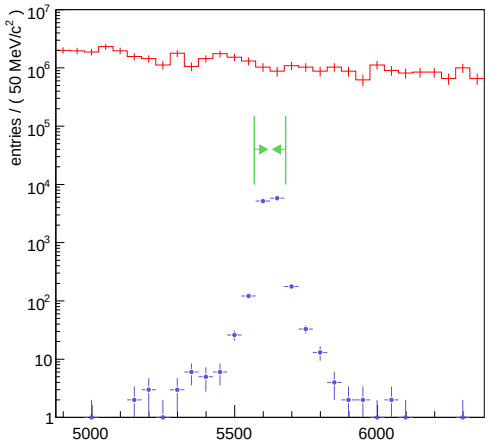

(c) m_{Λ_b} [MeV/c^2]

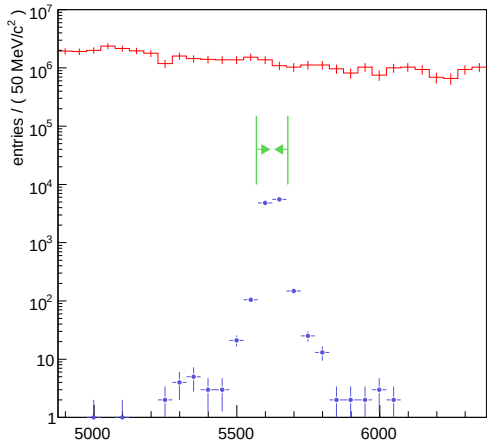

(d) m_{Λ_b} [MeV/c^2]

Figure 6.12: $S^L_{\Lambda_b}$ and m_{Λ_b} distributions for $\Lambda_b \to p\,\pi$ (left column) and $\Lambda_b \to p\,K$ (right column) decays, *after preselection cuts*. The blue points represent the signal and the red lines represent the inclusive $b\overline{b}$ background. The vertical green line indicates the *final selection cut*. The inclusive $b\overline{b}$ distribution of the mass distribution is weighted to correspond to the same period of simulated luminosity as the signal sample.

Cut variable	Preselection cut value	
	$\Lambda_b \to p\,\pi$	$\Lambda_b \to p\,K$
$\Delta\ln\mathcal{L}_{p\pi}(p)$	> 3	> 3
$\Delta\ln\mathcal{L}_{K\pi}(K)$	n/a	> -5
p_T^{max}	> 2000 MeV/c	> 2000 MeV/c
p_T^{min}	> 600 MeV/c	> 600 MeV/c
S^{max}	> 5.5	> 5.5
S^{min}	> 3.5	> 3.5
$p_T^{\Lambda_b}$	> 700 MeV/c	> 700 MeV/c
$S^L_{\Lambda_b}$	> 12	> 12
$S^{max}_{\Lambda_b}$	< 3.15	< 3.15
$\chi^2_{\Lambda_b}$	< 6	< 6
Δm_{Λ_b}	± 1700 MeV/c^2	± 1700 MeV/c^2

Table 6.3: Preselection cut variables for $\Lambda_b \to p\,\pi$ and $\Lambda_b \to p\,K$ signal channels, given in terms of the condition required to pass the selection cut.

window. For the purposes of understanding the source of these events, it is informative to introduce the following background categories:

- *Combinatorial* $b\overline{b}$: both tracks are from different B-hadrons and each is associated to a true MC particle.
- *Partially reconstructed decay* : both tracks are from the same B-hadron and each is associated to a true MC particle.
- *Ghost* : one or more of the tracks is not associated to a MC particle and arises from incorrectly reconstructed tracks.

In addition, there are a few signal events in the inclusive $b\overline{b}$ sample, but these events are removed from the studies of the inclusive $b\overline{b}$ background. Of the 23 inclusive $b\overline{b}$ events passing the $\Lambda_b \to p\,\pi$ selection, 11 are combinatorial $b\overline{b}$ events and 12 are partially reconstructed B-hadrons. Furthermore, of the latter 12 events, 10 derive from selecting the proton and charged pion from the decay $\Lambda_b \to p\,\rho(770) \to p\,\pi^-\,\pi^0$. This decay has yet to be observed [17] and is not included explicitly in the list of Λ_b decay channels used by EvtGen [77], therefore it must arise from Pythia hadronisation processes [48].

Cut variable	Cut value	Signal		Inclusive $b\bar{b}$ Background	
		Only this cut	All except this cut	Only this cut	All except this cut
Preselection		11,631		3,128	
p_T^{max}	> 3 GeV/c	10,594	7,073	1,376	39
p_T^{min}	> 1.2 GeV/c	10,565	7,308	1,649	47
S^{min}	> 5	10,980	6,873	2,078	31
$p_T^{\Lambda_b}$	> 1.5 GeV/c	10,931	6,881	2,379	27
$S^L_{\Lambda_b}$	> 15	10,836	7,041	2,565	29
$S^{max}_{\Lambda_b}$	< 2.5	10,563	7,319	2,231	35
$\chi^2_{\Lambda_b}$	< 4	10,923	7,119	2,738	28
$\Delta\ln\mathcal{L}_{pK}(p)$	> -1	11,390	6,765	2,092	51
$\Delta\ln\mathcal{L}_{\pi K}(\pi)$	> -5	11,508	6,731	2,754	33
Δm_{Λ_b}	$\pm$ 55 MeV/c^2	11,178	6,884		
All cuts		6,651		23	
... & apply $\pm$ 55 MeV/c^2 mass window to background				0	

Table 6.4: Criteria for the selection of $\Lambda_b \to p\,\pi$ decays. For each cut variable the number of events is given that pass the selection if *only* this cut is applied and the number that pass the selection if all *except* this cut are applied. The numbers of events passing the preselection and final selection cuts are given on the first and last line respectively.

Cut variable	Cut value	Signal		Inclusive $b\bar{b}$ Background	
		Only this cut	All except this cut	Only this cut	All except this cut
Preselection		10,929		1,248	
p_T^{max}	> 3 GeV/c	9,870	6,293	527	15
p_T^{min}	> 1.1 GeV/c	10,193	6,297	675	13
S^{min}	> 5	10,289	6,108	775	16
$p_T^{\Lambda_b}$	> 1.5 GeV/c	10,231	6,116	941	11
$S^L_{\Lambda_b}$	> 15	10,134	6,281	1,056	12
$S^{max}_{\Lambda_b}$	< 2.5	9,906	6,497	884	19
$\chi^2_{\Lambda_b}$	< 4	10,267	6,264	1,057	13
$\Delta\ln\mathcal{L}_{pK}(p)$	> -1	10,559	6,009	835	21
$\Delta\ln\mathcal{L}_{K\pi}(K)$	> 0	10,122	6,349	763	17
Δm_{Λ_b}	$\pm$ 55 MeV/c^2	10,400	6,089		
All cuts		5,901		10	
... & apply $\pm$ 50 MeV/c^2 mass window to background				0	

Table 6.5: Criteria for the selection of $\Lambda_b \to p\,K$ decays. For each cut variable the number of events is given that pass the selection if *only* this cut is applied and the number that pass the selection if all *except* this cut are applied. The numbers of events passing the preselection and final selection cuts are given on the first and last line respectively.

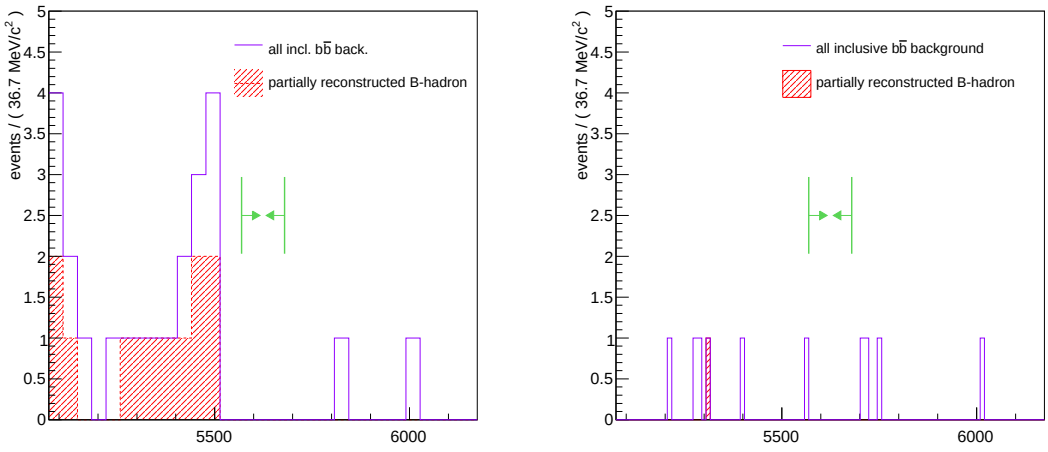

(a) m_{Λ_b} [MeV/c^2] (b) m_{Λ_b} [MeV/c^2]

Figure 6.13: Mass distribution of inclusive $b\bar{b}$ events passing the $\Lambda_b \to p\,\pi$ (left) and $\Lambda_b \to p\,K$ (right) selection cuts. The green arrows indicate the position of the $\Delta m_{\Lambda_b} = \pm 55$ MeV/c^2 selection cuts.

Of the 10 events passing the $\Lambda_b \to p\,K$ selection, 8 are combinatorial, 1 is a partially reconstructed B-hadron and 1 is a ghost background.

The mass distributions of inclusive $b\bar{b}$ events passing the $\Lambda_b \to p\,\pi$ and $\Lambda_b \to p\,K$ selection criteria are shown in Figure 6.13. The combinatoric background in the $\Lambda_b \to p\,\pi$ and $\Lambda_b \to p\,K$ mass distribution is approximately linearly distributed across the mass window. Those background events that are partially reconstructed B-hadrons, have a mass distribution biased towards the mass of the parent B-hadron. Such events can be neglected as counting towards the total inclusive $b\bar{b}$ background if the mass distribution does not overlap the tight 55 MeV/c^2 mass window.

In order to investigate the background due to $\Lambda_b \to p\,\rho(770) \to p\,\pi^-\,\pi^0$ events a dedicated MC sample of 8.5k were simulated using the same software as the signal and other background samples. Figure 6.14 illustrates the mass distribution of $\Lambda_b \to p\,\rho(770) \to p\,\pi^-\,\pi^0$ events that pass the $\Lambda_b \to p\,\pi$ selection criteria. The mass distribution is centred outside of the tight mass window and thus the background from such events will be negligible. The effect of the trigger and specific background selection cuts on the remaining combinatoric background events is the subject of section 6.4.

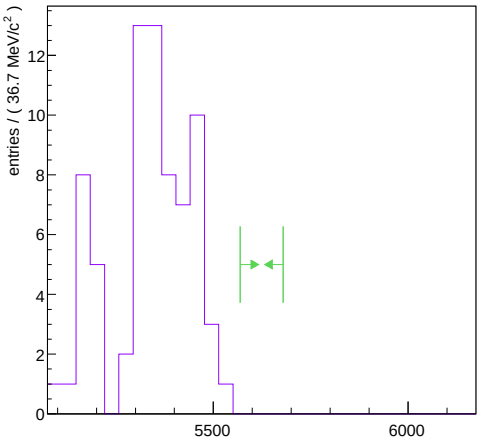

(a) mass(Λ_b) [MeV/c^2]

Figure 6.14: Mass distribution of 8.5k $\Lambda_b \to p\,\rho(770) \to p\,\pi^-\,\pi^0$ after the $\Lambda_b \to p\,\pi$ selection cuts. The green arrows indicate the position of the $\Delta m_{\Lambda_b} = \pm 55$ MeV/c^2 selection cuts.

6.3.2 Exclusive two body B-hadron backgrounds

The decay of B-hadrons into two charged particles are a specific source of background for both Λ_b signal decay channels. Figure 6.15 illustrates the mass distribution of the various specific background channels after the inclusive $b\overline{b}$ rejection cuts, but without applying the Δm_{Λ_b}cut. The signal and background distributions are weighted by the factors given in Table 6.2 such that, for each dataset, the number of events before selection corresponds to the same luminosity.

To gauge the potential effect on the selection purity caused by the selection of the specific background events, an estimate of the background to signal ratio is calculated,

$$B_{spec.}/S = \omega_{back} \times \frac{N^{sel}_{back}}{N^{sel}_{sig}}, \tag{6.9}$$

where N^{sel}_{back} is the number of selected background events, N^{sel}_{sig} the number of selected signal events and ω_{back} is given by equation 6.4. Table 6.6 gives an estimate of the specific background to signal ratio expected for each background channel after all selection criteria have been applied, including the $\Delta m_{\Lambda_b} = \pm 55$ MeV/c^2 cut. When the number

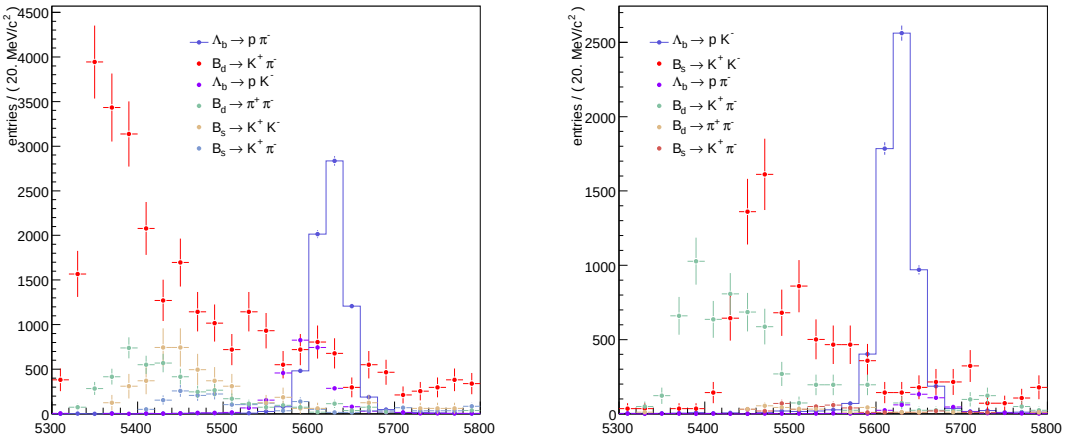

(a) m_{Λ_b} [MeV/c^2] (b) m_{Λ_b} [MeV/c^2]

Figure 6.15: Mass distributions for signal (sold blue line) and specific backgrounds for the $\Lambda_b \to p\,\pi$ (left) and $\Lambda_b \to p\,K$ (right) decay channels. Uncertainties are statistical. Scale is arbitrary.

of selected background events, N^{sel}_{back}, is small (less than 10), the number of background events passing the selection is quoted as a 90% confidence level interval for the mean of a Poisson distribution given N^{sel}_{back} observed events. The method of Feldman and Cousins is used to construct the confidence level intervals [108].

The overall background to signal ratio of the $\Lambda_b \to p\,\pi$ channel is approximately three times that of the $\Lambda_b \to p\,K$ channel. This is due in part to the lower $\Lambda_b \to p\,\pi$ branching ratio and the fact that the principal background source stems from misidentifying a kaon as a proton. This results, in the case of the $\Lambda_b \to p\,\pi$ channel, in the selection of $B^0_d \to K\,\pi$ decays and in the selection of $B^0_s \to K^+K^-$ decays in the $\Lambda_b \to p\,K$ case. Given the greater B^0_d compared to B^0_s hadronisation fraction, this has a more significant impact on the $\Lambda_b \to p\,\pi$ selection purity.

Removing the B-meson backgrounds

The B-meson backgrounds can be removed by either tightening the PID criteria applied to select the proton, or by further exploiting the mass difference between the Λ_b and B-meson background by recalculating the Λ_b mass on the assumption that the proton

Background channel	$B_{spec.}/S$	
	$\Lambda_b \to p\,\pi$	$\Lambda_b \to p\,K$
$\Lambda_b \to p\,\pi$	n/a	0.054 ± 0.002
$\Lambda_b \to p\,K$	0.34 ± 0.01	n/a
$B_d^0 \to K^+\,\pi^-$	0.50 ± 0.06	0.054 ± 0.001
$B_d^0 \to \pi^+\,\pi^-$	0.05 ± 0.01	0.013 ± 0.005
$B_s^0 \to K^+\,\pi^-$	0.04 ± 0.01	0.013 ± 0.005
$B_s^0 \to K^+\,K^-$	[0.02,0.09]	0.22 ± 0.04
Total	0.98 ± 0.06	0.35 ± 0.04

Table 6.6: Background to signal ratios for specific background channels after applying the inclusive $b\overline{b}$ selection criteria. If the number of selected background events is small (< 10), $B_{spec.}/S$ is quoted as a 90% confidence interval.

is actually a misidentified kaon.

Figure 6.16(a) shows the mass distribution of $\Lambda_b \to p\,\pi$ decays for two different proton PID assignments: one in which the proton is assumed to be a true proton, the other in which the proton is assumed to be a kaon. In both cases the full inclusive $b\overline{b}$ selection criteria are applied, including the $\Delta m_{\Lambda_b} = \pm 55$ MeV/c^2 mass window cut. With respect to the proton hypothesis, the kaon hypothesis skews the Λ_b mass distribution to lower masses, as is expected given that the kaon mass is some 445 MeV/c^2 less than the proton mass. Figure 6.16(c) illustrates the same two PID assignments applied to $B_d^0 \to K\,\pi$ decays, the most significant of the $\Lambda_b \to p\,\pi$ specific backgrounds. For the proton assignment the distribution is approximately uniform across the 110MeV/c^2 mass window centred on the Λ_b mass. However, if the proton is assigned the kaon mass, the mass distribution is transformed to an approximately Gaussian distribution centred on the B_d^0 mass. Hence, the following selection criteria can be defined:

$$|\,m(B_d^0) - m(\Lambda_b{}^{p\,\to K})| > \Delta m_{B_d^0}(\Lambda_b{}^{p\,\to K}) \tag{6.10}$$

where $m(\Lambda_b{}^{p\,\to K})$ is the Λ_b mass assuming that that proton is actually a kaon and $\Delta m_{B_d^0}(\Lambda_b{}^{p\,\to K})$ is a mass window cut centred on the B_d^0 mass that is applied to the recalculated $\Lambda_b{}^{p\,\to K}$ mass. Requiring that $\Delta m_{B_d^0}(\Lambda_b{}^{p\,\to K}) = 50$ MeV/c^2, reduces the specific $B_d^0 \to K\,\pi$ background to signal ratio from 0.50 ± 0.06 to <0.08, at the cost of a small 0.30% reduction in selection efficiency. To achieve the same improvement by

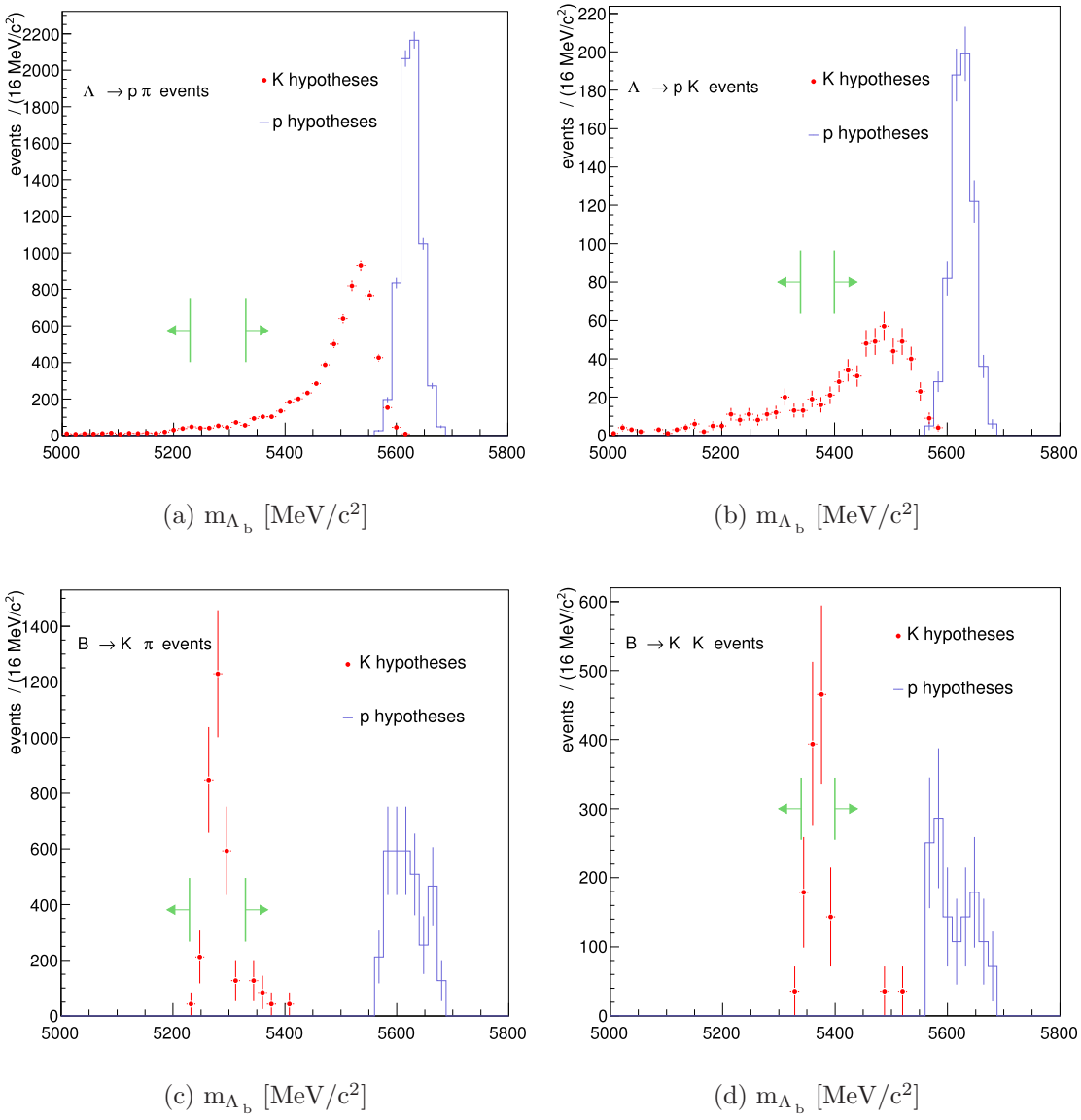

(a) m_{Λ_b} [MeV/c^2] (b) m_{Λ_b} [MeV/c^2]

(c) m_{Λ_b} [MeV/c^2] (d) m_{Λ_b} [MeV/c^2]

Figure 6.16: Λ_b mass distributions, after the inclusive $b\bar{b}$ selection cuts, for two different proton PID hypotheses : one in which the proton is assumed to be a true proton (blue line), in the other the proton is assigned the kaon mass (red points). The left column corresponds to the $\Lambda_b \to p\,\pi$ selection applied to signal (top) and $B_d^0 \to K\,\pi$ background events (bottom). The right column corresponds to the $\Lambda_b \to p\,K$ selection applied to signal (top) and $B_s^0 \to K^+\,K^-$ background events (bottom). The green arrows indicate the selection cuts applied to the Λ_b mass for which the proton is assumed to be a kaon (red points).

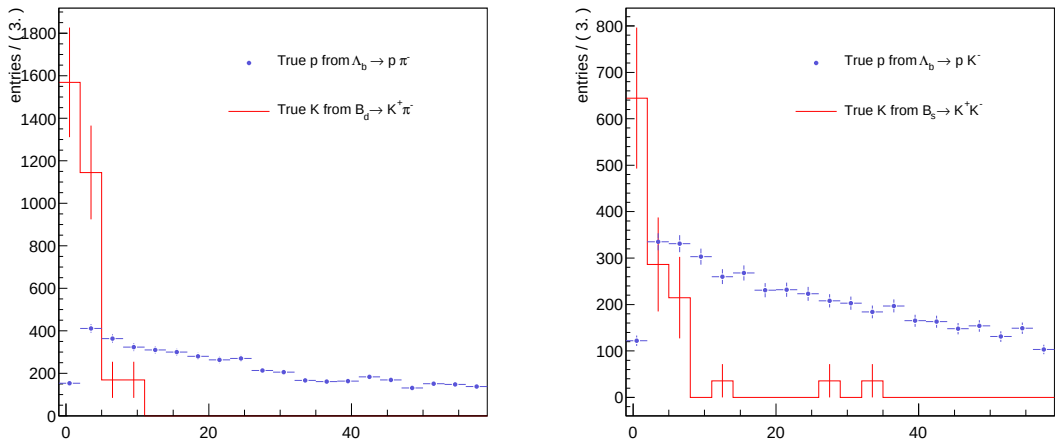

(a) $\Delta\ln\mathcal{L}_{pK}(p)$ (b) $\Delta\ln\mathcal{L}_{pK}(p)$

Figure 6.17: $\Delta\ln\mathcal{L}_{pK}(p)$ distributions for the signal and most significant B-meson background events that pass the $\Lambda_b \to p\,\pi$ (left) and $\Lambda_b \to p\,K$ (right) inclusive $b\overline{b}$ selection cuts. The background events are weighted by the factors given in Table 6.2.

means of the $\Delta\ln\mathcal{L}_{pK}(p)$ PID cut, shown in Figure 6.17(a), results in a higher 1.1% selection efficiency loss.

In the same manner, the $B_s^0 \to K^+K^-$ background can be removed from the $\Lambda_b \to p\,K$ selection by assigning the kaon mass to the proton and removing those events that lie within a mass window centred on the B_s^0 mass. This is illustrated in Figures 6.16(b) and 6.16(d). Background $B_s^0 \to K^+K^-$events are removed by requiring that:

$$|\,m(B_s^0) - m(\Lambda_b{}^{p\to K})| > \Delta m_{B_s^0}(\Lambda_b{}^{p\to K}) \tag{6.11}$$

where $\Delta m_{B_s^0}(\Lambda_b{}^{p\to K})$ is the mass window cut centred on the B_s^0 mass. Setting $\Delta m_{B_s^0}(\Lambda_b{}^{p\to K})$ =30 MeV/c^2 reduces the $B_s^0 \to K^+K^-$ background to signal ratio from 0.22 ± 0.04 to <0.06 with an efficiency loss of 0.45%. To gain the same improvement from increasing the $\Delta\ln\mathcal{L}_{pK}(p)$ cut, the distribution of which is shown in Figure 6.17(b), leads to a larger 0.97% selection efficiency loss.

This study suggests that recalculating the Λ_b mass under the assumption that the proton is a kaon is a useful method of removing background events where the proton

has been mis-identified and where the background decay has a different parent mass to the signal channel. In the cases considered, this method enables the same background suppression as can be gained from PID selection cuts, but with a smaller loss in selection efficiency.

The method can be extended to remove the smaller $B_d^0 \to \pi^+\pi^-$ background. In this case, the proton is assigned a pion mass and the recalculated Λ_b is required to satisfy:

$$|\, m(B_d^0) - m({\Lambda_b}^{p\,\to\pi})| > \Delta m_{B_d^0}({\Lambda_b}^{p\,\to\pi}) \tag{6.12}$$

where ${\Lambda_b}^{p\,\to\pi}$ is the recalculated Λ_b mass assuming that the proton is in fact a pion and $\Delta m_{B_d^0}({\Lambda_b}^{p\,\to\pi})$ is the mass window cut entered on the B_d^0 mass applied to the recalculated Λ_b mass.

Separating $\Lambda_b \to p\,\pi$ and $\Lambda_b \to p\,K$ signal events

The Λ_b signal channels are a specific background to the other channel; in the $\Lambda_b \to p\,\pi$ selection the pion can be misidentified as a kaon and vice-versa for the $\Lambda_b \to p\,K$ selection. The background to signal ratio is approximately a factor 6 worse in the $\Lambda_b \to p\,\pi$ case compared to the $\Lambda_b \to p\,K$ selection, partly because of the lower branching ratio of the former decay and also due to the tighter PID cuts applied to select a kaon.

The PID selection variables provide one possible means of separating the two decay modes. Figure 6.18(a) illustrates the $\Delta\ln\mathcal{L}_{\pi K}(\pi)$ distribution for signal $\Lambda_b \to p\,\pi$ and background $\Lambda_b \to p\,K$ events that pass the inclusive $b\overline{b}$ selection criteria. Although a high purity is achievable by increasing the $\Delta\ln\mathcal{L}_{\pi K}(\pi)$ cut, it is at the cost of significant efficiency loss, as the peak distribution of both the signal and background peaks are coincident. The same feature is evident in the $\Delta\ln\mathcal{L}_{K\pi}(K)$ distribution for signal $\Lambda_b \to p\,K$ and background $\Lambda_b \to p\,\pi$ events shown in Figure 6.18(b).

An alternative means of separating the two decays modes is to consider the Λ_b mass distribution for two cases: one in which the hadron is assigned the pion mass, the other in which the hadron is assigned the kaon mass. The two cases are shown, after the inclusive $b\overline{b}$ $\Lambda_b \to p\,\pi$ selection, in Figures 6.19(a) and 6.19(c) for $\Lambda_b \to p\,\pi$ and $\Lambda_b \to p\,K$ events respectively. For the $\Lambda_b \to p\,\pi$ events, the mass distribution is centred on the Λ_b mass for the pion hypotheses and skewed to higher masses for the kaon hypotheses, as expected given the additional kaon mass. In contrast, for the $\Lambda_b \to p\,K$ events, the distribution is centred on the Λ_b mass for the kaon hypotheses and skewed to lower masses if the pion

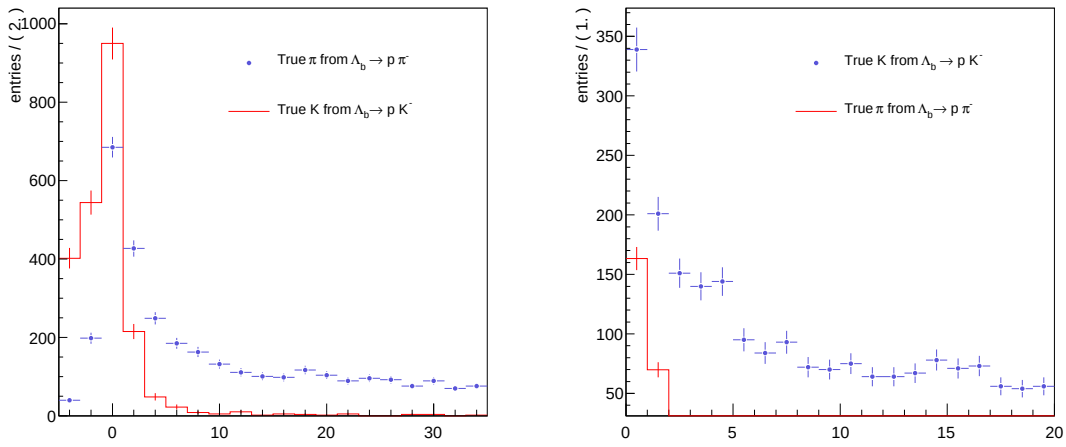

(a) $\Delta\ln\mathcal{L}_{\pi K}(\pi)$ (b) $\Delta\ln\mathcal{L}_{K\pi}(K)$

Figure 6.18: Separating the two signal channels with PID selection variables. Distributions shown for signal (blue points) and background (red line) events that pass the $\Lambda_b \to p\,\pi$ (left) and $\Lambda_b \to p\,K$ (right) inclusive $b\bar{b}$ selection criteria. Background statistics weighted by the factors given in Table 6.2.

identity is assumed. The behaviour of the $\Lambda_b \to p\,\pi$ and $\Lambda_b \to p\,K$ mass distributions under different hadron PID assumptions can be encapsulated into the following selection variable,

$$K_{veto} = (\Lambda_b{}^{h\,\to\pi} - \Lambda_b{}^{true}) + (\Lambda_b{}^{h\,\to K} - \Lambda_b{}^{true}), \tag{6.13}$$

where $\Lambda_b{}^{h\,\to\pi}$ and $\Lambda_b{}^{h\,\to K}$ are the Λ_b mass for the pion and kaon PID cases respectively, and $\Lambda_b{}^{true}$ is the nominal Λ_b mass. Figure 6.20(a) shows the distribution of equation 6.13 for $\Lambda_b \to p\,\pi$ and $\Lambda_b \to p\,K$ decays that pass the $\Lambda_b \to p\,\pi$ selection. A degree of signal and background separation is evident, but to remove all the background events leads to a significant signal efficiency loss. Therefore, the approach taken is to apply a loose $K_{veto} > -30$ cut and study the effect of increasing the $\Delta\ln\mathcal{L}_{\pi K}(\pi)$ selection criteria on the specific background to signal ratio ($B_{spec.}/S$) and on the efficiency of selecting the generated signal events ($\varepsilon_{sel/gen}$), the latter being defined as,

$$\varepsilon_{sel/gen} = \frac{N_{sel}}{N_{gen}}, \tag{6.14}$$

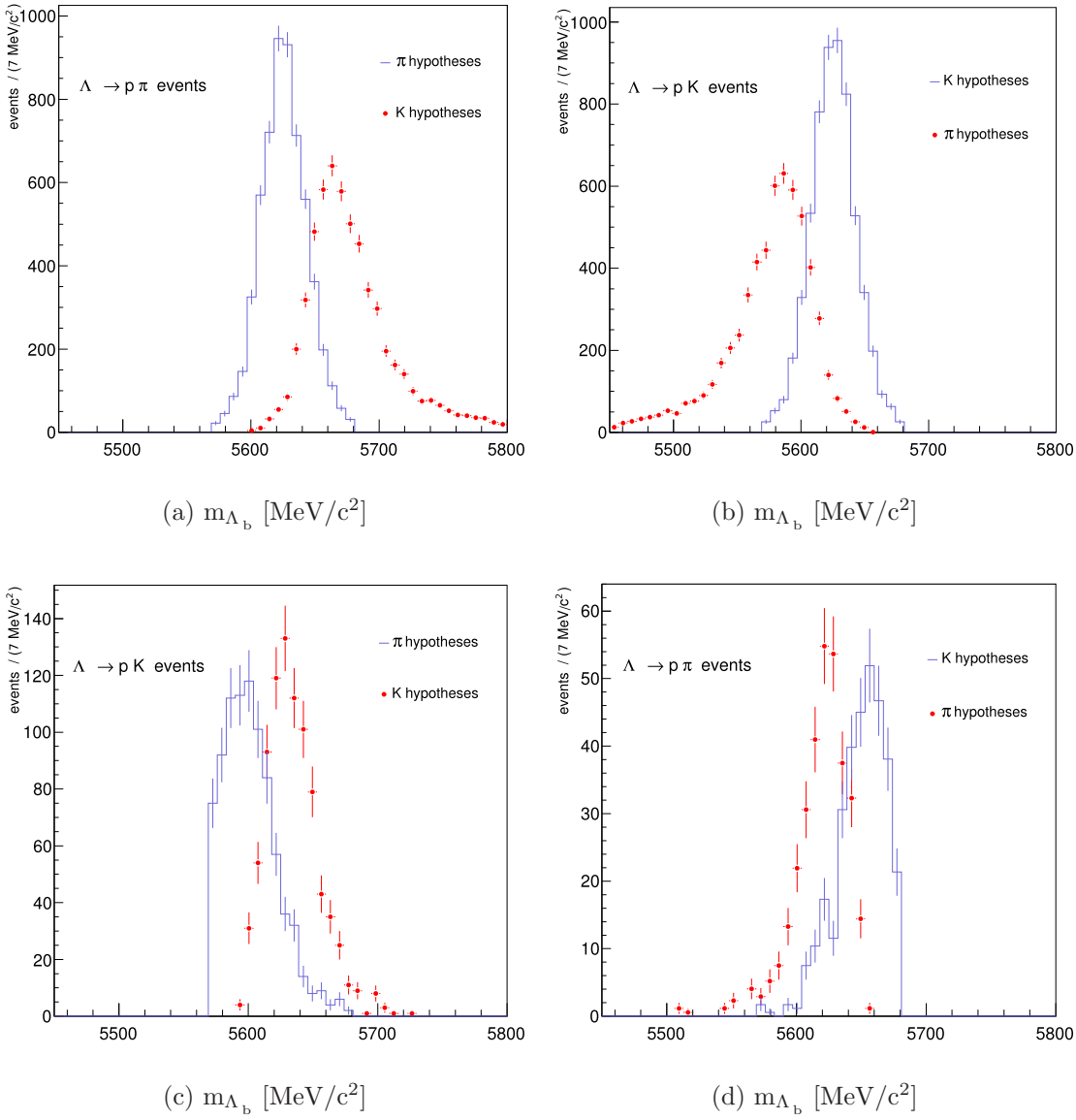

(a) m_{Λ_b} [MeV/c^2] (b) m_{Λ_b} [MeV/c^2]

(c) m_{Λ_b} [MeV/c^2] (d) m_{Λ_b} [MeV/c^2]

Figure 6.19: Λ_b mass distributions, after the inclusive $b\overline{b}$ selection cuts, assuming that the hadron is a pion in one case and a kaon in the other. The left column corresponds to the $\Lambda_b \to p\,\pi$ selection applied to signal (top) and the $\Lambda_b \to p\,K$ background (bottom). The right column corresponds to the $\Lambda_b \to p\,K$ selection applied to signal (top) and the $\Lambda_b \to p\,\pi$ background (bottom). The correct hadron particle identity is coloured blue for the signal events and red for the background events.

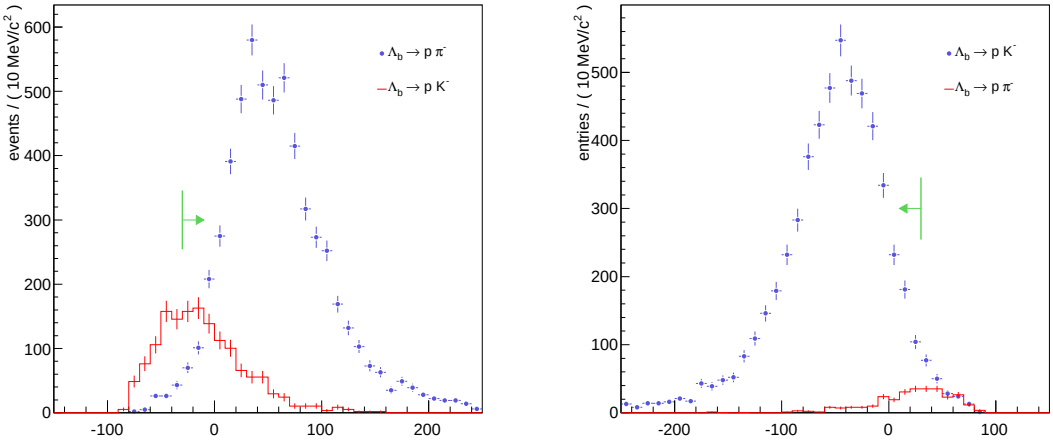

(a) K_{veto} [MeV/c^2] (b) K_{veto} [MeV/c^2]

Figure 6.20: Separating the two signal channels with the K_{veto} selection variable, for events pass the $\Lambda_b \to p\,\pi$ (left) and $\Lambda_b \to p\,K$ (right) inclusive $b\bar{b}$ selection criteria. Signal channels are illustrated as blue points and the corresponding background as a red line. Background events are weighted by the factors given in Table 6.2.

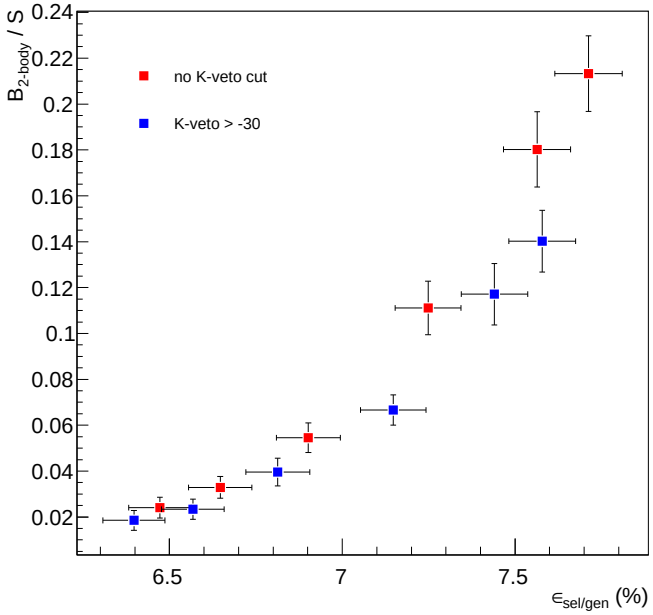

Figure 6.21: Specific background to signal ratio and selection efficiency topology for integer increases of the $\Delta\ln\mathcal{L}_{\pi K}(\pi)$ cut from $\Delta\ln\mathcal{L}_{\pi K}(\pi)$ >-2 (top right) to $\Delta\ln\mathcal{L}_{\pi K}(\pi)$ >4 (bottom left), with and without a K_{veto} selection cut. Other specific background selection cuts at the retained value. Uncertainties are statistical.

where N_{sel} is the the number of selected events and N_{gen} is the number of generated Monte Carlo signal events. The study is illustrated in Figure 6.21 for integer increases in the $\Delta\ln\mathcal{L}_{\pi K}(\pi)$ selection cut. It is evident that the application of the K_{veto} cut for a particular $\Delta\ln\mathcal{L}_{\pi K}(\pi)$ cut results in a lower background to signal ratio and only a small efficiency loss.

The $\Delta\ln\mathcal{L}_{K\pi}(K)$ and K_{veto} distributions for the $\Lambda_b \to p\,K$ selection are shown in Figures 6.18(b) and 6.20(b) respectively. Given that the $\Lambda_b \to p\,\pi$ decays are a relatively small background to the $\Lambda_b \to p\,K$ selection, there is no benefit from increasing the $\Delta\ln\mathcal{L}_{K\pi}(K)$ cut as the background and the peak of the signal distribution are coincident. However, for the K_{veto} distribution the background is coincident with the tail of the signal distribution, and a loose cut on this variable is found to be beneficial.

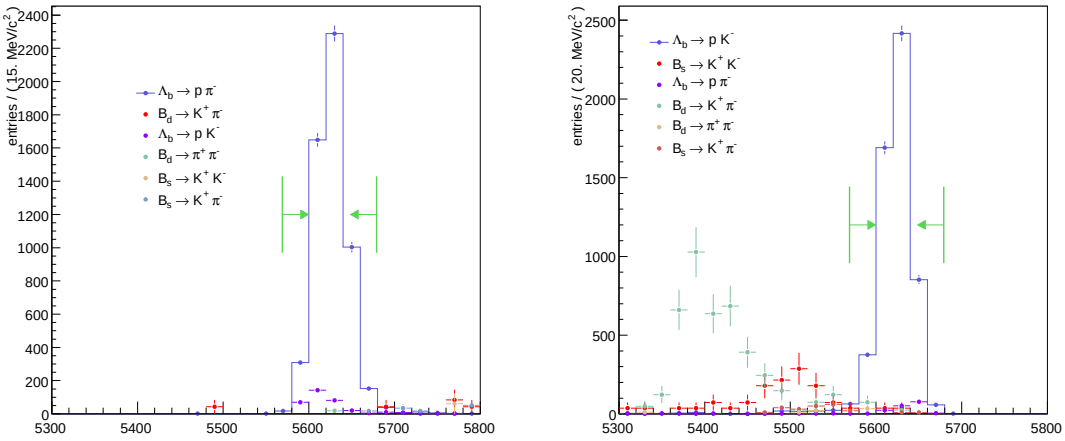

(a) m_{Λ_b} [MeV/c^2] (b) m_{Λ_b} [MeV/c^2]

Figure 6.22: Signal and specific background mass distributions after final selection criteria for the $\Lambda_b \to p\pi$ (left) and $\Lambda_b \to pK$ (right) selection. Backgrounds are weighted by the factors given in Table 6.2. Uncertainties are statistical.

Specific background selection cuts

Tables 6.7 and 6.8 list the final criteria to extract $\Lambda_b \to p\pi$ and $\Lambda_b \to pK$ decays from the expected specific backgrounds. The specific background to signal ratio for the $\Lambda_b \to p\pi$ selection is reduced from 0.98 ± 0.06 to 0.067 ± 0.007, with a corresponding reduction in selection efficiency from $(8.9 \pm 0.1)\%$ to $(7.15 \pm 0.10)\%$. Less stringent criteria are required for the $\Lambda_b \to pK$ selection, such that the addition of a K_{veto} and loose $\Delta m_{B_s^0}(\Lambda_b{}^{p \to K})$ cut are sufficient to reduce the expected $\Lambda_b \to pK$ specific background form 0.35 ± 0.04 to 0.08 ± 0.02, with a corresponding reduction in selection efficiency from $(8.4 \pm 0.1)\%$ to $(7.6 \pm 0.1)\%$.

The mass distributions of the expected specific backgrounds that pass the final selection criteria are illustrated in Figures 6.22(a) and 6.22(b). It is a noticeable feature that a significant number of B-meson events pass the $\Lambda_b \to pK$ selection, while most are removed by the $\Lambda_b \to p\pi$ selection. The vast majority of the retained B-mesons lie outside of the Δm_{Λ_b}mass window cut and therefore are expected to have a negligible effect on the selection purity. However, as a check that the selection variables behave as

Cut variable	Background	$B_{spec.}/S$		$\varepsilon_{sel/gen}$	
		Only this cut	All except this cut	Only this cut	All except this cut
Inclusive $b\bar{b}$	$B_d^0 \to K^+\pi^-$	0.50 ± 0.06		8.9 ± 0.10	
cuts only	$\Lambda_b \to p\,K$	0.34 ± 0.01			
	$B_d^0 \to \pi^+\pi^-$	0.05 ± 0.01			
	All channels	0.98 ± 0.06			
$\Delta m_{B_s^0}(\Lambda_b{}^{p\to K})$	$B_d^0 \to K^+\pi^-$	[0.02,0.08]	0.39 ± 0.05	8.5 ± 0.1	7.5 ± 0.1
> 50 MeV/c^2	$\Lambda_b \to p\,K$	0.31 ± 0.01	0.070 ± 0.004		
	$B_d^0 \to \pi^+\pi^-$	0.05 ± 0.01	[0.00,0.02]		
	All channels	0.50 ± 0.03	0.47 ± 0.06		
$\Delta\ln\mathcal{L}_{\pi K}(\pi) > 0$	$B_d^0 \to K^+\pi^-$	0.38 ± 0.05	[0.00,0.03]	8.0 ± 0.1	7.8 ± 0.1
& $K_{veto} > -30.$	$\Lambda_b \to p\,K$	0.081 ± 0.005	0.255 ± 0.009		
	$B_d^0 \to \pi^+\pi^-$	0.04 ± 0.01	[0.00,0.02]		
	All channels	0.54 ± 0.06	0.29 ± 0.02		
$\Delta m_{B_d^0}(\Lambda_b{}^{p\to\pi})$	$B_d^0 \to K^+\pi^-$	0.50 ± 0.06	[0.00,0.04]	8.2 ± 0.1	7.7 ± 0.1
> 50 MeV/c^2	$\Lambda_b \to p\,K$	0.29 ± 0.01	0.073 ± 0.005		
	$B_d^0 \to \pi^+\pi^-$	[0.00,0.02]	0.04 ± 0.01		
	All channels	0.81 ± 0.06	0.17 ± 0.02		
All cuts	$B_d^0 \to K^+\pi^-$	[0.00,0.02]		7.15 ± 0.10	
	$\Lambda_b \to p\,K$	0.060 ± 0.004			
	$B_d^0 \to \pi^+\pi^-$	[0.00,0.02]			
	All channels	0.067 ± 0.007			

Table 6.7: Effect of the $\Lambda_b \to p\,\pi$ selection cuts on the expected specific background to signal ratio ($B_{spec.}/S$) and the selection efficiency ($\varepsilon_{sel/gen}$). For each cut variable the $B_{spec.}/S$ and $\varepsilon_{sel/gen}$ are given for the case that *only* this cut variable is applied and for the case that all *except* this cut are applied. The first and last sections give the $B_{spec.}/S$ and $\varepsilon_{sel/gen}$ before and after the specific selection criteria are applied. Backgrounds weighted by the factors given in Table 6.2. For small backgrounds (<10), $B_{spec.}/S$ given as a 90% confidence interval.

Cut variable	Background	$B_{spec.}/S$	$\varepsilon_{sel/gen}$
		Only this cut	Only this cut
Inclusive $b\bar{b}$	$B_s^0 \to K^+ K^-$	0.22 ± 0.04	8.4 ± 0.1
cuts only	$\Lambda_b \to p\,\pi$	0.054 ± 0.002	
	$B_d^0 \to K^+ \pi^-$	0.054 ± 0.001	
	All channels	0.35 ± 0.04	
$\Delta m_{B_s^0}(\Lambda_b{}^{p \to K})$	$B_s^0 \to K^+ K^-$	[0.01,0.06]	7.8 ± 0.1
$> 30.\text{MeV}/c^2$	$\Lambda_b \to p\,\pi$	0.051 ± 0.002	
	$B_d^0 \to K^+ \pi^-$	[0.01,0.04]	
	All channels	0.11 ± 0.02	
$K_{veto} < 30.$	$B_s^0 \to K^+ K^-$	0.18 ± 0.03	8.0 ± 0.1
	$\Lambda_b \to p\,\pi$	0.031 ± 0.002	
	$B_d^0 \to K^+ \pi^-$	0.05 ± 0.01	
	All channels	0.28 ± 0.04	
All cuts	$B_s^0 \to K^+ K^-$	[0.01,0.05]	7.6 ± 0.1
	$\Lambda_b \to p\,\pi$	0.029 ± 0.002	
	$B_d^0 \to K^+ \pi^-$	[0.01,0.04]	
	All channels	0.08 ± 0.02	

Table 6.8: Criteria to remove specific backgrounds from the $\Lambda_b \to p\,K$ selection. Specific background to signal ratio ($B_{spec.}/S$) and selection efficiency ($\varepsilon_{sel/gen}$) given for the case that *only* the selection criteria is applied and finally for the case that both criteria are applied. The $B_{spec.}/S$ and $\varepsilon_{sel/gen}$ before before the specific selection criteria are given in the first section.Backgrounds weighted by the factors given in Table 6.2. For small backgrounds (<10), $B_{spec.}/S$ given as a 90% confidence interval.

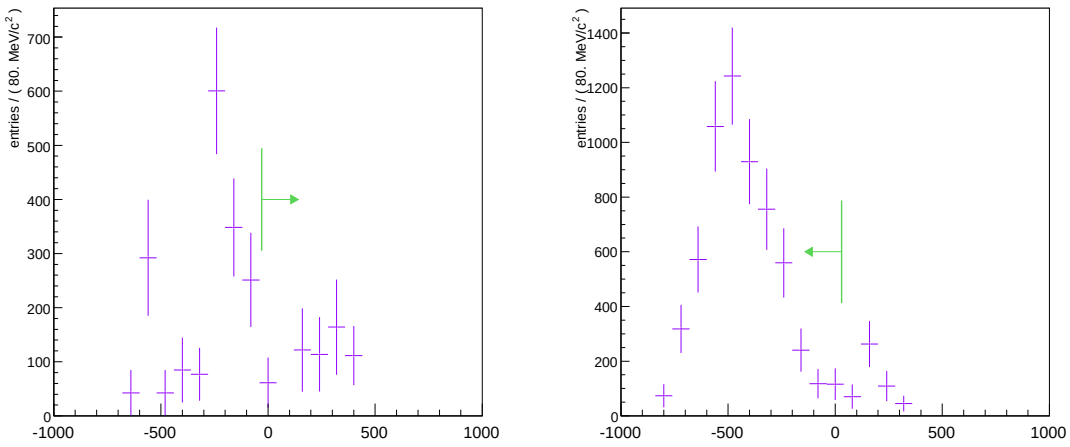

(a) K_{veto} [MeV/c^2] (b) K_{veto} [MeV/c^2]

Figure 6.23: K_{veto} distributions for the expected specific B-meson backgrounds that pass the $\Lambda_b \to p\,\pi$ (left) and $\Lambda_b \to p\,K$ (right) final selection variables, but with a reconstructed mass that lies in the mass range of Figures 6.22(a) and 6.22(b). The green arrows indicate the position and direction of the retained K_{veto} cuts.

expected, it is informative to consider how this feature may arise.

The difference between the mass distributions is partly explained by the more stringent criteria required for the $\Lambda_b \to p\,\pi$ selection. However, the principal cause is the K_{veto} selection variable. Figures 6.23(a) and 6.23(b) illustrate the K_{veto} distribution for B-meson backgrounds that pass the $\Lambda_b \to p\,\pi$ and $\Lambda_b \to p\,K$ selection criteria, but with the Λ_b mass window cut extended to the range covered by Figures 6.22(a) and 6.22(b). The mean of both distributions are negative, as is expected from equation 6.13 given the lighter B-meson masses compared to the Λ_b. For the $\Lambda_b \to p\,\pi$ selection, K_{veto} is required to be > -30, whereby removing the majority of the B-mesons. However, for the $\Lambda_b \to p\,K$ selection, K_{veto} is required to be < 30, such that the B-meson distribution is retained.

Cut variable	$\Lambda_b \to p\,\pi$	$\Lambda_b \to p\,K$
p_T^{max}	> 3000 MeV/c	> 3000 MeV/c
p_T^{min}	> 1200 MeV/c	> 1100 MeV/c
S^{max}	> 5.5	> 5.5
S^{min}	> 5	> 5
$p_T^{\Lambda_b}$	> 1500 MeV/c	> 1500 MeV/c
$S^L_{\Lambda_b}$	> 15	> 15
$S^{max}_{\Lambda_b}$	< 2.5	< 2.5
$\chi^2_{\Lambda_b}$	< 4	< 4
Δm_{Λ_b}	$\pm$ 55MeV/c^2	$\pm$ 55MeV/c^2
$\Delta\ln\mathcal{L}_{p\pi}(p)$	> 3	> 3
$\Delta\ln\mathcal{L}_{pK}(p)$	$>$ -1	-
$\Delta\ln\mathcal{L}_{\pi K}(\pi)$	> 0	-
$\Delta\ln\mathcal{L}_{K\pi}(K)$	-	> 0
K_{veto}	$>$ -30 MeV/c^2	$<$ 30 MeV/c^2
$\Delta m_{B^0_d}(\Lambda_b{}^{p\to K})$	$>$ 50 MeV/c^2	-
$\Delta m_{B^0_d}(\Lambda_b{}^{p\to \pi})$	$>$ 50 MeV/c^2	-
$\Delta m_{B^0_s}(\Lambda_b{}^{p\to K})$	-	$>$ 30 MeV/c^2

Table 6.9: Final criteria for the selection of $\Lambda_b \to p\,\pi$ and $\Lambda_b \to p\,K$ events, given in terms of the condition required to pass the cut.

6.4 Selection Performance

The final criteria for the selection of $\Lambda_b \to p\,\pi$ and $\Lambda_b \to p\,K$ decays are given in Table 6.9. In order to determine the selection efficiency loss at each step in the reconstruction and selection process, the following definitions are introduced:

- N_{gen}: total number of generated Monte Carlo events used in the analysis.
- $N_{\text{'ble}}$: number of reconstructible[2] events, where both final states are reconstructible as long tracks.
- $N_{\text{'ted}}$: number of reconstructed events, where both final states are reconstructed as long tracks.
- $N_{\text{rec'\&}}$: number of reconstructed events, where both final states are both reconstructed *and* reconstructible.
- N_{sel}: number of selected events after the final selection criteria.
- N_{trg}: number of selected events that pass the L0, L1 and HLT triggers.

The numbers of events for the above definitions are given in Table 6.10. In order to obtain an unbiased value for the background to signal ratio and the selection efficiency, the final selection criteria are applied to a set of signal and background data that have not been used to develop the selection cuts.

Channel	N_{gen}	$N_{\text{'ble}}$	$N_{\text{'ted}}$	$N_{\text{rec'\&}}$	N_{sel}	N_{trg}
$\Lambda_b \to p\,\pi$	71,250	23,501	24,510	21,171	5,414	1,892
$\Lambda_b \to p\,K$	72,000	21,899	23,233	20,158	5,524	1,905

Table 6.10: Number of events passing each stage of the $\Lambda_b \to p\,\pi$ and $\Lambda_b \to p\,K$ reconstruction and selection process.

The total selection efficiency, ε_{tot}, is defined as the fraction of generated MC signal events that pass the selection and trigger criteria. The total efficiency can be factorised

[2] A long track is considered reconstructible if the particle has deposited at least 3 hits in both the VELO r and ϕ sensors. Furthermore, there must be a least 1 x and 1 stereo hit in each of the T1-T3 tracking stations.

in terms of each stage of the reconstruction and selection process,

$$\varepsilon_{\text{tot}} = \varepsilon_{\text{sig}}^{\text{geom}} \times \frac{N_{\text{trg}}}{N_{\text{gen}}} = \varepsilon_{\text{det}} \times \varepsilon_{\text{rec/det}} \times \varepsilon_{\text{sel/rec}} \times \varepsilon_{\text{trg/sel}}, \tag{6.15}$$

where $\varepsilon_{\text{sig}}^{\text{geom}}$ =34.6% is the 400 mrad geometric acceptance criterion applied at the generator level. The efficiency factors after the second equality are:

- $\varepsilon_{\text{det}} = \varepsilon_{\text{sig}}^{\text{geom}} \times \frac{N_{\text{'ted}}}{N_{\text{gen}}} \times \frac{1}{\varepsilon_{\text{rec/det}}}$ is the detection efficiency, which includes the geometrical acceptance in the 4π solid angle and material effects.
- $\varepsilon_{\text{rec/det}} = \frac{N_{\text{rec'\&}}}{N_{\text{'ble}}}$ is the reconstruction efficiency on reconstructible events.
- $\varepsilon_{\text{sel/rec}} = \frac{N_{\text{sel}}}{N_{\text{'ted}}}$ is the efficiency of selecting the reconstructed events.
- $\varepsilon_{\text{trg/sel}} = \frac{N_{\text{trg}}}{N_{\text{sel}}}$ is the combined L0, L1 & HLT trigger efficiencies applied to the selected events.

A summary of the efficiencies is shown in Table 6.11 for both signal channels. The statistical uncertainties are calculated as binomial uncertainties on the number of selected events, whereby the error σ_ε on an efficiency $\varepsilon = \frac{n}{N}$ is given by

$$\sigma_\varepsilon = \sqrt{\frac{\varepsilon(1-\varepsilon)}{N}}. \tag{6.16}$$

A quadratic propagation of errors is used to calculate the statistical error of ε_{det} and the error on ε_{tot} is calculated form the first equality of equation 6.15.

The lower $\Lambda_b \to p\pi$ selection efficiency reflects the fact that tighter cuts are required to remove the specific two-body backgrounds. The reconstruction efficiency is somewhat higher for the $\Lambda_b \to pK$ reconstruction. This is caused by the momentum dependancy of the reconstruction efficiency illustrated in Figure 2.23, where the reconstruction efficiency begins to fall off for tracks with momentum > 40 GeV/c. Variations between the momentum distribution of the two channels leads to the observed difference between reconstruction efficiencies.

6.4.1 Signal purity

The Λ_b candidates that are selected from the signal data sets are not all associated to a true signal decay. For the $\Lambda_b \to p\pi$ channel, 5,419 candidates are selected in 5,414

Channel	ε_{det} (%)	$\varepsilon_{rec/det}$ (%)	$\varepsilon_{sel/rec}$ (%)	$\varepsilon_{trg/sel}$ (%)	ε_{tot} (%)
$\Lambda_b \to p\,\pi$	13.2 ± 0.1	90.1 ± 0.2	22.1 ± 0.3	34.9 ± 0.6	0.92 ± 0.02
$\Lambda_b \to p\,K$	12.1 ± 0.1	92.0 ± 0.2	23.8 ± 0.3	34.5 ± 0.6	0.92 ± 0.02

Table 6.11: Reconstruction and selection efficiencies for $\Lambda_b \to p\,\pi$ and $\Lambda_b \to p\,K$ decays. Uncertainties are statistical.

events. Of the selected candidates :

- 99.6% are associated to a true signal.
- 17 are constructed from a final state that includes a ghost track.
- 3 are reconstructed from the μ^- that originates from the decay $\Lambda_b \to p\,\pi \to p\,\mu^-\,\overline{\nu}_\mu$.
- 2 candidates are reconstructed with the true π misidentified as the p and the true π misidentified as the p.
- 1 candidate is reconstructed after a material interaction.

For the $\Lambda_b \to p\,K$ channel 5,554 candidates are selected in 5,524 events. The breakdown of the selected candidates is as follows :

- 99.1% are associated to a true signal.
- 30 candidates are reconstructed with the true K misidentified as the p and the true p identified as the K. However, for 22 of these 30 candidates a second candidate is reconstructed in the same event which is associated to a true signal decay. The mass of this second candidate is more consistent with the Λ_b mass, thus enabling the combinatoric candidate to be removed from the selection.
- 18 are reconstructed with one final state that is a ghost track.
- 4 are reconstructed from the μ^- that derives from the decay $\Lambda_b \to p\,K \to p\,\mu^-\,\overline{\nu}_\mu$.

6.4.2 Background contamination

To increase the effective number of inclusive $b\overline{b}$ statistics the method of increasing the mass window cut beyond that of the final criteria, as described in section 6.3.1, is employed.

Channel	$B_{b\bar{b}}/S$		$B_{spec.}/S$	
	No trigger	All triggers	No trigger	All triggers
$\Lambda_b \to p\,\pi$	[2.2, 7.8]	[0.0, 4.3]	0.07 ± 0.01	0.09 ± 0.03
$\Lambda_b \to p\,K$	[0.2, 2.2]	[0.0, 2.6]	0.09 ± 0.01	0.05 ± 0.02

Table 6.12: Background to signal ratios for the inclusive $b\bar{b}$ ($B_{b\bar{b}}/S$) and the expected specific background ($B_{spec.}/S$), before and after the combined trigger. If background is small (<10), the 90% confidence interval is quoted, otherwise the central value is quoted. Uncertainties are statistical.

Applying the final $\Lambda_b \to p\,\pi$ selection criteria to a $\sim$18M inclusive $b\bar{b}$ data set, with an enlarged 550 MeV/c^2 mass window, yields 8 events. With reference to the background categories introduced in section 6.3.1, 4 are combinatorial, 3 are caused by one of the final states being a ghost track and 1 is a partially reconstructed B-meson. For the $\Lambda_b \to p\,K$ selection, 5 inclusive $b\bar{b}$ events pass the final selection cuts. Of the 5 events, 3 are partially reconstructed B-mesons, 1 is reconstructed from a ghost track and 1 is a combinatoric background.

The inclusive $b\bar{b}$ background to signal ratio is given by

$$B_{b\bar{b}}/S = \frac{N^{sel}_{b\bar{b}} \times \omega_{b\bar{b}}}{N_{sel} \times M_{scale}}, \tag{6.17}$$

where $\omega_{b\bar{b}} = 33{,}831$ for $\Lambda_b \to p\,\pi$ and $\omega_{b\bar{b}} = 20{,}623$ for $\Lambda_b \to p\,K$, are the statistical weight factors given by equation 6.5. $M_{scale} = 550/55 = 10$ is the factor to scale the tight to the large mass widow.

Table 6.12 lists the inclusive background to signal ratios for the $\Lambda_b \to p\,\pi$ and $\Lambda_b \to p\,K$ selection, both before and after the combined L0, L1 and HLT triggers. As the number of background events passing the selection is close to zero, the background is quoted as a 90% confidence interval for the mean of Poisson distribution given $N^{sel}_{b\bar{b}}$ observed events.

Applying the combined L0, L1 and HLT triggers removes *all* inclusive $b\bar{b}$ from both selection channels. In order to reduce further the upper 90% background to signal confidence limit requires the production of additional inclusive $b\bar{b}$ events, as discussed in section 6.1.

The combined background to signal ratio for the expected specific backgrounds are calculated from equation 6.9 and given in Table 6.12. The combined trigger has a negligble effect on the background to signal ratio, as expected considering the similar kinematics and topology of the signal and expected background channels. The statistical uncertainty for the specific background to signal ratio is approximately two orders of magnitude smaller than that on the inclusive $b\overline{b}$ background to signal ratio. This is due to the statistical compatibility between the signal and specific background sample sizes. Consequently, it is not possible to state which, if any, of the backgrounds considered will be dominant.

In summary, a set of selection cuts have been studied to provide the optimal efficiency for the selection of $\Lambda_b \to p\,\pi$ and $\Lambda_b \to p\,K$ events whilst keeping the background to signal ratio to a minimum. The total efficiencies for the selection of the signal events are,

$$\begin{aligned} \varepsilon_{tot} &= (0.92 \pm 0.02)\% : \Lambda_b \to p\,\pi, \\ \varepsilon_{tot} &= (0.92 \pm 0.02)\% : \Lambda_b \to p\,K, \end{aligned}$$

with an inclusive and specific background to signal ratio of,

$$\begin{aligned} B_{b\overline{b}}/S &= [0.0, 4.3] : \Lambda_b \to p\,\pi, \\ B_{b\overline{b}}/S &= [0.0, 2.6] : \Lambda_b \to p\,K, \end{aligned}$$

and

$$\begin{aligned} B_{spec.}/S &= 0.09 \pm 0.03 : \Lambda_b \to p\,\pi, \\ B_{spec.}/S &= 0.05 \pm 0.02 : \Lambda_b \to p\,K. \end{aligned}$$

These results are used in Chapter 7 to extract the annual event yields and physics sensitivities.

Chapter 7

Physics sensitivities with $\Lambda_b \to p\pi/K$ events

This chapter presents a study of the LHCb sensitivity to the $\Lambda_b \to p\pi/K$ branching fractions and rate asymmetries. The expected sensitivities are compared to the present and projected CDF sensitivity [106], the Standard Model [40] and the R-parity violating Minimal Supersymmetric Standard Model [12].

The chapter begins with a calculation of the expected signal yields, using the results of Monte Carlo studies presented in Chapter 6. The resulting signal yields are then used in the subsequent sensitivity studies.

7.1 Signal Yields

The number of $\Lambda_b \to p\pi$ and $\Lambda_b \to pK$ signal events, S^π and S^K, expected to be fully reconstructed, triggered and selected after $\mathcal{L}_{\rm int}$ of integrated luminosity, are given by:

$$S^\pi = 2 \times \sigma_{b\bar{b}} \times \mathcal{L}_{\rm int} \times f_{\Lambda_b} \times \mathcal{B}^\pi \times \varepsilon^\pi_{\rm tot}, \tag{7.1a}$$

$$S^K = 2 \times \sigma_{b\bar{b}} \times \mathcal{L}_{\rm int} \times f_{\Lambda_b} \times \mathcal{B}^K \times \varepsilon^K_{\rm tot}, \tag{7.1b}$$

where $\sigma_{b\bar{b}} = 500\mu b$ is the $b\bar{b}$ production cross section, $\mathcal{B}^{\pi/K}$ is the expected branching ratio (Table 6.1) and $\varepsilon^{\pi/K}_{\rm tot}$ is the selection efficiency (Table 6.11). The π and K superscripts refer to the $\Lambda_b \to p\pi$ and $\Lambda_b \to pK$ signal channels respectively, a nomenclature used throughout this chapter. The probability of a b-quark hadronising to a Λ_b is given

$\mathcal{L}_{\rm int}$ (fb^{-1})	Timescale (yr)	$\Lambda_b \to p\pi$ ($\times 10^3$)	$\Lambda_b \to pK$ ($\times 10^3$)
0.5	2008	0.427 ± 0.009	0.70 ± 0.02
2	2009	1.71 ± 0.04	2.80 ± 0.06
6	2011	5.1 ± 0.1	8.5 ± 0.2
10	2013	8.5 ± 0.2	14.0 ± 0.3
100	~ 2020	85 ± 2	141 ± 3

Table 7.1: Expected $\Lambda_b \to p\pi$ and $\Lambda_b \to pK$ signal event yields, S^π and S^K, for the first 5 years of running at the design luminosity $\mathcal{L} = 2 \times 10^{32}$ cm^{-2}s^{-1}. $\mathcal{L}_{\rm int} = 100$ fb^{-1} corresponds to 5 years data taking at the upgraded luminosity of $\mathcal{L} = 2 \times 10^{33}$ cm^{-2}s^{-1}. Uncertainties are statistical only.

by the hadronisation fraction, f_{Λ_b} =$(9.9 \pm 1.7)\%$ [17], and the factor of 2 accounts for the fact that both the b and $\overline{\rm b}$ can hadronise.

It is anticipated that 0.5 fb^{-1} of physics quality integrated luminosity will be available in 2008. From 2009 onwards, during stable running of the experiment 2 fb^{-1} are expected each year. The anticipated signal yields at various points of integrated luminosity are given in Table 7.1. The statistical uncertainty derives from the binomial uncertainty of the total selection efficiency. The uncertainty in the hadronisation fraction ($\sim 2\%$) and the B production cross section ($\sim 10\%$) are not included [17].

The feasibility of increasing the LHCb luminosity by a factor of 10 from 2×10^{32}cm^{-2}s^{-1} to 2×10^{33}cm^{-2}s^{-1} is currently under study [111]. Since the LHC luminosity is 2×10^{34}, this does not require an LHC upgrade, but would require an upgraded, "Super"-LHCb detector. The expected signal yields derived from the upgraded luminosity are included in Table 7.1.

7.2 Branching Ratio Measurements

The CDF collaboration reported the first observation of the decays $\Lambda_b \to p\pi$ and $\Lambda_b \to pK$, with a significance of 6σ and 11.5σ respectively [106]. The measurement was made from the analysis of 1fb^{-1} of collected data. The relative branching fraction, $R_{\pi/K}$, is measured

to be:

$$R_{\pi/K} = \frac{\mathcal{B}(\Lambda_b \to p\,\pi)}{\mathcal{B}(\Lambda_b \to p\,K)} = 0.66 \pm 0.14(stat.) \pm 0.08(syst.) \tag{7.2}$$

To date, no measurements of the absolute branching ratios have been reported, although a CDF measurement based on a smaller 180 pb^{-1} sample of collected data set a 90% CL limit on both channels of $\mathcal{B}(\Lambda_b \to p\,\pi/K) < 2.3 \times 10^{-5}$ [112]. The relative branching fraction and upper bound measurements are consistent with theoretical expectation [41].

Using the signal yield projections presented in Table 7.1, enables an estimate to be made of the relative and absolute branching fraction statistical uncertainty attainable at LHCb.

The observed number of events, N, is the sum of the signal, S, and background, B, events:

$$N^{\pi} = S^{\pi} + B^{\pi} = S^{\pi}\left(1 + \left(\frac{B}{S}\right)^{\pi}\right), \tag{7.3a}$$

$$N^{K} = S^{K} + B^{K} = S^{K}\left(1 + \left(\frac{B}{S}\right)^{K}\right), \tag{7.3b}$$

where $\left(\frac{B}{S}\right)$ are the background to signal ratios, the study of which was presented in section 6.3. Combining equations 7.1, 7.2 and 7.3 yields an expression for the relative branching fraction in terms of the number of observed events:

$$R_{\pi/K} = \frac{S^{\pi} \times \varepsilon^{K}_{tot}}{S^{K} \times \varepsilon^{\pi}_{tot}} = \frac{N^{\pi} \times \varepsilon^{K}_{tot} \times (1 + \left(\frac{B}{S}\right)^{K})}{N^{K} \times \varepsilon^{\pi}_{tot} \times (1 + \left(\frac{B}{S}\right)^{\pi})}. \tag{7.4a}$$

The uncertainty in the selection efficiency consists of a statistical component, which can be measured from MC studies, and a systematic part which is unknown. However, since $R_{\pi/K}$ is the ratio of two topologically and kinematically similar decay channels, the systematic uncertainties are expected to mostly cancel in the ratio.

The statistical uncertainty of the relative branching fraction is derived from a quadratic propagation of the binomial uncertainty on the number of background subtracted signal events,

$$\sigma_{R_{\pi/K}} = \frac{\varepsilon^{K}_{tot}}{\varepsilon^{\pi}_{tot}} \sqrt{\frac{S^{\pi}\,(S^{\pi} + S^{K})}{(S^{K})^{3}}}. \tag{7.5}$$

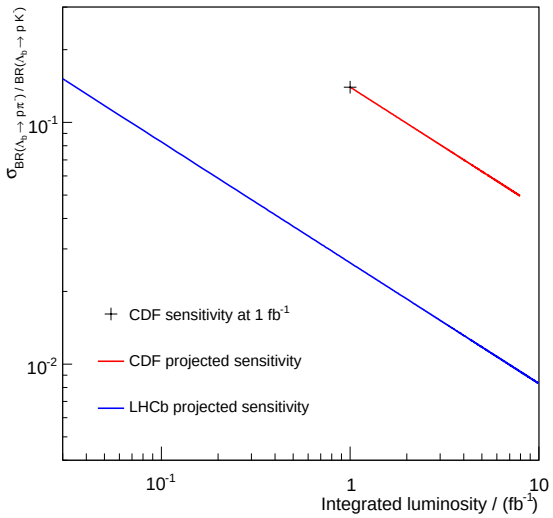

Figure 7.1: Relative branching fraction statistical uncertainty, as attained by CDF with 1fb^{-1} (black mark), and projected resolution for CDF (red line) and LHCb (blue line).

$\mathcal{L}_{\rm int}$ (fb^{-1})	$\sigma_{\rm R_{\pi/K}}$	$\sigma_{\mathcal{B}^\pi}$ ($\times 10^{-8}$)	$\sigma_{\mathcal{B}^{\rm K}}$ ($\times 10^{-8}$)
0.5	0.04	4.5	5.9
2	0.02	3.2	2.9
6	0.01	2.3	1.7
10	0.008	1.0	1.3
100	0.002	0.32	0.41

Table 7.2: Expected statistical precision of the absolute branching fraction and ratio, after $\mathcal{L}_{\rm int}$ of integrated luminosity.

Figure 7.1 illustrates equation 7.5 as a function of integrated luminosity. For comparison, the current CDF resolution is indicated and a projection made to the upper limit of expected integrated luminosity [113]. After 1fb^{-1} LHCb will improve on the present CDF statistical precision by an order of magnitude. The expected precision at various luminosities is summarised in Table 7.2.

To measure the absolute branching fraction, the signal channel is typically measured relative to a control channel of known branching fraction. The benefit of this approach being that the measurement has no dependency on the integrated luminosity and produc-

tion cross section. The chosen control channel should be topologically and kinematically similar to the signal channel, so as to limit the effects of differences between the signal and control channel selection efficiencies and background to signal ratios. The two body charmless B-meson decays, considered in section 6.3.2, meet this criteria. The decay $B^0_d \to K\pi$ is chosen as the fractional uncertainty of the measured branching fraction is the lowest of the charmless two body B-meson decays. The expected yield of $B^0_d \to K\pi$ events, $S^{B^0_d \to K\pi}$, at LHCb is given by:

$$S^{B^0_d \to K\pi} = 2 \times \sigma_{b\bar{b}} \times \mathcal{L}_{int} \times f_{B^0_d} \times \mathcal{B}^{B^0_d \to K\pi} \times \varepsilon^{B^0_d \to K\pi}_{tot}, \tag{7.6}$$

where the total $B^0_d \to K\pi$ efficiency, $\varepsilon^{B^0_d \to K\pi}_{tot}$, is expected to be 0.93% [110] and the measured branching fraction, $\mathcal{B}^{B^0_d \to K\pi}$, is $(1.82 \pm 0.08) \times 10^{-5}$ [17]. Combining equations 7.1 and 7.6, gives the following expression for the signal channel branching fractions relative to $B^0_d \to K\pi$:

$$\mathcal{B}^{\pi} = \frac{S^{\pi} \times \varepsilon^{B^0_d \to K\pi}_{tot} \times f_{B^0_d} \times \mathcal{B}^{B^0_d \to K\pi}}{S^{B^0_d \to K\pi} \times \varepsilon^{\pi}_{tot} \times f_{\Lambda_b}}, \qquad \mathcal{B}^{K} = \frac{S^{K} \times \varepsilon^{B^0_d \to K\pi}_{tot} \times f_{B^0_d} \times \mathcal{B}^{B^0_d \to K\pi}}{S^{B^0_d \to K\pi} \times \varepsilon^{K}_{tot} \times f_{\Lambda_b}}. \tag{7.7}$$

From a quadratic propagation of the statistical uncertainties in equations 7.7 and combining with equations 7.1 and 7.6, it follows that the statistical resolution on the $\mathcal{B}^{\pi}$ and $\mathcal{B}^{K}$ branching fractions, $\sigma_{\mathcal{B}^{\pi}}$ and $\sigma_{\mathcal{B}^{K}}$, are

$$\sigma_{\mathcal{B}^{\pi}/\mathcal{B}^{K}} \propto \frac{1}{\sqrt{\mathcal{L}_{int}}}. \tag{7.8}$$

The projected absolute branching fraction statistical uncertainty as a function of integrated luminosity is illustrated in Figures 7.2(a) and 7.2(b) for the $\Lambda_b \to p\pi$ and $\Lambda_b \to pK$ signal channels respectively. The projection assumes that each channel is measured relative to the $B^0_d \to K\pi$ decay channel and that all other uncertainties are fixed. Both signal channels require only ~ 0.01 fb^{-1} of integrated luminosity to attain a 3σ statistical sensitivity to the predicted Standard Model branching fraction. The anticipated branching fraction resolutions at benchmark integrated luminosities are summarised in Table 7.2.

Although the systematic uncertainty on the efficiency term in equation 7.7 will not be known until data is available, the uncertainties of the hadron production fractions and control channel branching fraction are known. Of the known uncertainties, the fractional uncertainty on the Λ_b production fraction is expected to be dominant, as the

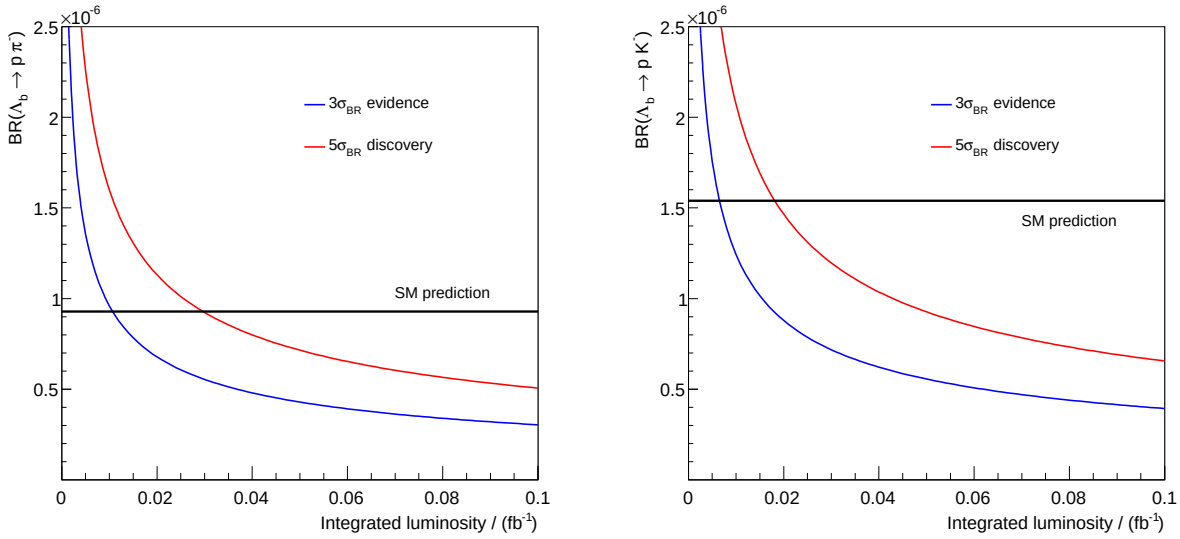

(a) $\Lambda_b \to p\pi$ (b) $\Lambda_b \to pK$

Figure 7.2: The statistical branching fraction resolution as a function of integrated luminosity ($\mathcal{L}_{\text{int}}$) for (a) $\Lambda_b \to p\pi$ and (b) $\Lambda_b \to pK$ decay channels. The blue and red lines indicate the smallest branching fraction that could be measured with 3 and 5 σ resolution respectively. The black line is positioned at the predicted Standard Model value.

measurement is subject to a 20% fractional error.

7.3 Asymmetry Sensitivities

This section presents a study of the potential sensitivity to the $\mathcal{CP}$ asymmetries predicted by the Standard Model and the R-parity violating Minimal Supersymmetric Standard Model (MSSM). The section begins with a derivation of the rate asymmetry statistical precision that is attainable at LHCb. The second part will apply this model to predict the conditions required to provide evidence for the Standard Model and R-parity violating MSSM theoretical predictions.

The *true* $\mathcal{CP}$ asymmetry, $\mathcal{A}_{\mathcal{CP}}$, is defined in terms of the ratio

$$\mathcal{A}_{\mathcal{CP}}(\Lambda_b \to p\pi) = \frac{\Gamma(\Lambda_b \to p\pi^-) - \Gamma(\overline{\Lambda}_b \to \overline{p}\pi^+)}{\Gamma(\Lambda_b \to p\pi^-) + \Gamma(\overline{\Lambda}_b \to \overline{p}\pi^+)} = \frac{S^+ - S^-}{S^+ + S^-}, \tag{7.9}$$

where the superscript $+/-$ denotes the charge of the final state proton, a nomenclature used throughout this section. However, the *observed* asymmetry, $\mathcal{A}_{\rm obs}$, is given by

$$\mathcal{A}_{\rm obs} = \frac{N^+ - N^-}{N^+ + N^-} = \frac{2N^+}{N} - 1, \tag{7.10}$$

where the observed (N), signal (S) and background (B) events are related by

$$N^+ = S^+ + B^+, \qquad N^- = S^- + B^-, \quad \text{and} \quad N = N^+ + N^-. \tag{7.11}$$

Assuming that the background to signal ratio is independent of the charge of the final state π/K, the observed asymmetry (equation 7.10) can be expressed in terms of the true asymmetry and the background to signal ratio,

$$\begin{aligned}\mathcal{A}_{\rm obs} &= \frac{(S^+ + \frac{1}{2}\left(\frac{B}{S}\right)(S^+ + S^-)) - (S^- + \frac{1}{2}\left(\frac{B}{S}\right)(S^+ + S^-))}{(1 + \left(\frac{B}{S}\right))(S^+ + S^-)} = \frac{S^+ - S^-}{(1 + \left(\frac{B}{S}\right))(S^+ + S^-)} \\ &= \frac{\mathcal{A}}{(1 + \left(\frac{B}{S}\right))}.\end{aligned} \tag{7.12}$$

Compared to the true asymmetry, the observed asymmetry is diluted by the background events. The effect of this dilution on the true asymmetry resolution is now presented.

The variance of the observed asymmetry, $\sigma_{\mathcal{A}_{\rm obs}}$, is given by

$$\sigma_{\mathcal{A}_{\rm obs}} = \overline{\mathcal{A}^2_{\rm obs}} - \overline{\mathcal{A}_{\rm obs}}^{\,2} = 4\frac{\overline{N^{+2}} - \overline{N^+}^{\,2}}{N^2}. \tag{7.13}$$

From equation 7.11 it follows that the numerator of equation 7.13 is the variance of a binominal distribution,

$$\sigma_{\mathcal{A}_{\rm obs}} = 2\sqrt{\frac{Nx(1-x)}{N}}, \qquad x = \frac{N^+}{N} = \frac{\mathcal{A}_{\rm obs} + 1}{2}. \tag{7.14}$$

The statistical uncertainty of the true asymmetry, $\sigma_{\mathcal{A}}$, follows from equation 7.12,

$$\begin{aligned}\sigma_{\mathcal{A}} &= \left(1 + \left(\frac{B}{S}\right)\right)\sigma_{\mathcal{A}_{\rm obs}} = \left(1 + \left(\frac{B}{S}\right)\right) 2\sqrt{\frac{Nx(1-x)}{N}} \\ &= \sqrt{\frac{\left(1 + \left(\frac{B}{S}\right)\right)\left(1 - \mathcal{A}^2_{\rm obs}\right)}{S}}\end{aligned} \tag{7.15}$$

Observable	Standard Model	R-parity violating MSSM
Branching fraction ($\mathcal{B}$)	0.9×10^{-6} [41]	$< 1.6 \times 10^{-4}$ [12]
$\mathcal{CP}$ asymmetry ($\mathcal{A}$)	8.3% [41]	0.3% [12]

Table 7.3: Expected theoretical Standard Model and R-parity violating Minimal Supersymmetric Standard Model (MSSM) branching fraction and $\mathcal{CP}$ asymmetry for $\Lambda_b \to p\pi$ decays.

The expected theoretical Standard Model and R-parity violating MSSM branching fractions and $\mathcal{CP}$ asymmetries are listed in Table 7.3 for the $\Lambda_b \to p\pi$ decay channel. Relative to the Standard Model predictions, the R-parity violating MSSM model is expected to suppress the $\mathcal{CP}$ asymmetry, but enhance the branching fraction by up to two orders of magnitude. However, since the upper bound of the $\Lambda_b \to p\pi/K$ decays has been measured by CDF to be $< 2.3 \times 10^{-5}$, the branching fraction enhancement can be no more than an order of magnitude [112].

The $\mathcal{CP}$ asymmetry resolution, calculated from equation 7.15, is illustrated in Figure 7.3(a) for the Standard Model $\mathcal{CP}$ asymmetry prediction and in Figure 7.3(b) for the R-parity violating MSSM. The shaded region corresponds to the 90% confidence range of the expected inclusive $b\bar{b}$ background to signal ratio, the solid line is the interval mid-point. The exclusive background to signal ratio is not included since the absolute value is insignificant compared to the upper bound of the inclusive $b\bar{b}$ background to signal ratio. In the R-parity violating MSSM case, the branching fraction is assumed to be 2.3×10^{-5}, the current upper bound on the $\Lambda_b \to p\pi$ branching fraction. In the Standard Model case the theoretical branching fraction is assumed.

Since the predicted R-parity violating MSSM $\mathcal{CP}$ asymmetry is suppressed relative to the Standard Model asymmetry, significantly more $b\bar{b}$ statistics are required to observe the R-parity violating MSSM $\mathcal{CP}$ asymmetry. This is illustrated by the blue and purple lines in Figures 7.3(a) and 7.3(b) which indicate 3 and 5 standard deviations between the theoretical and zero asymmetry. In the Standard Model case, 3σ evidence for the expected asymmetry is attainable with between 1.5 fb^{-1} and 8.1 fb^{-1} of integrated luminosity, whilst a 5σ discovery requires between 4.2 fb^{-1} and 22.5 fb^{-1}. Therefore, a 3σ evidence for Standard Model $\Lambda_b \to p\pi$ $\mathcal{CP}$-violation should be attainable in the first few years of LHC running. However, observation of R-parity violating MSSM $\mathcal{CP}$-violation requires at least 50 fb^{-1} for 3σ evidence and 130 fb^{-1} for a 5σ discovery, a level of integrated luminosity which will only be attained with the upgraded luminosity

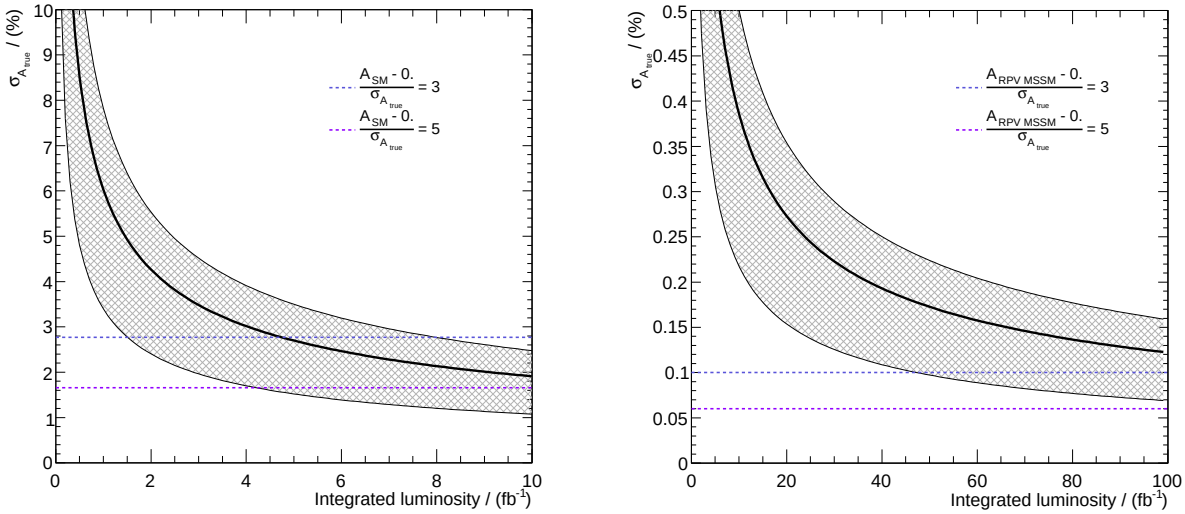

(a) SM (b) $\not{R}$ MSSM

Figure 7.3: Statistical resolution of the true asymmetry as a function of integrated luminosity ($\mathcal{L}_{\text{int}}$) for $\Lambda_b \to p\pi$ decays in the case of (a) Standard Model and (b) R-parity violating MSSM $\mathcal{CP}$-violation. The blue and purple lines correspond to a 3σ and 5σ difference between the theoretical Standard Model / R-parity violating MSSM asymmetry prediction and zero asymmetry.

"Super"-LHCb detector.

The expected statistical precision on the rate asymmetries is listed in Table 7.4 at various integrated luminosity benchmarks for the Standard Model and R-parity violating MSSM cases of $\Lambda_b \to p\pi$ decays and for Standard Model $\Lambda_b \to pK$ decays. In the latter case the optimal possible 66% rate asymmetry is assumed [40] which, combined with the larger expected signal yields, leads to a higher statistical precision on the asymmetry measurement compared to that of Standard Model $\Lambda_b \to p\pi$ decays.

The $\mathcal{CP}$ asymmetry resolution will also be subject to systematic uncertainties. From the expression for CP asymmetry in equation 7.12, it is evident that a systematic uncertainty will arise from the background to signal ratio term. Furthermore, the derivation of equation 7.12 assumes that the number of background events is independent of the final state decay mode. If this is not the case, an additional term, $\left(1 + \frac{B^+ - B^-}{S^+ - S^-}\right)$, is introducted into the numerator of equation 7.12. Systematic uncertainties in the $b\bar{b}$ cross section, Λ_b production fraction, integrated luminosity and branching fraction terms, are

	$\Lambda_b \to p\pi$		$\Lambda_b \to pK$
$\mathcal{L}_{\rm int}$ ($\rm fb^{-1}$)	$\sigma_{\mathcal{A}}^{\rm SM}$ (%)	$\sigma_{\mathcal{A}}^{\rm MSSM}$ (%)	$\sigma_{\mathcal{A}}^{\rm optimal}$ (%)
0.5	4.8-11.1	1.0-2.2	2.8-6.5
2	2.4-5.6	0.5-1.1	1.4-3.3
6	1.4-3.2	0.3-0.6	0.8-1.9
10	1.1-2.5	0.2-0.5	0.6-1.5
100	0.3-0.8	0.1-0.2	0.2-0.5

Table 7.4: Rate asymmetry statistical resolution for the $\Lambda_b \to p\pi$ channel, assuming the predicted values of the standard model, $\sigma_{\mathcal{A}}^{\rm SM}$, and the R-parity violating MSSM model, $\sigma_{\mathcal{A}}^{\rm MSSM}$. The asymmetry resolution for $\Lambda_b \to pK$ decays, $\sigma_{\mathcal{A}}^{\rm optimal}$, assumes the optimal possible asymmetry value.

not expected to effect the resolution as the these terms cancel in equation 7.12. However, systematic uncertainty in the total efficiency will contribute if there is a difference between the $\Lambda_b \to p h^-$ and $\overline{\Lambda}_b \to \overline{p} h^+$ reconstruction, selection and trigger efficiencies.

7.4 Summary of Sensitivities

The unprecedented $b\overline{b}$ statistics available at LHCb will enable measurements of the $\Lambda_b \to p\pi$ and $\Lambda_b \to pK$ branching fractions and Standard Model $\mathcal{CP}$ asymmetries. After 2 $\rm fb^{-1}$ of integrated luminosity, corresponding to approximately one year of LHC running, the statistical precision on the following observables will be attained:

- uncertainty on branching fraction ratio $\sigma_{R_{\pi/K}} = 0.02$,
- absolute $\Lambda_b \to p\pi$ branching fraction uncertainty of $\sigma_{\mathcal{B}^\pi} = 3.2 \times 10^{-8}$ relative to $B_d^0 \to K\pi$,
- absolute $\Lambda_b \to pK$ branching fraction uncertainty of $\sigma_{\mathcal{B}^K} = 2.9 \times 10^{-8}$ relative to $B_d^0 \to K\pi$,
- Standard Model $\mathcal{CP}$ asymmetry in $\Lambda_b \to p\pi$ decays, $\sigma_{\mathcal{A}}^{\rm SM} = 2.4 - 5.6\%$,
- R-parity violating MSSM $\mathcal{CP}$ asymmetry in $\Lambda_b \to p\pi$ decays, $\sigma_{\mathcal{A}}^{\rm MSSM} = 0.5 - 1.1\%$,
- Standard Model $\mathcal{CP}$ asymmetry in $\Lambda_b \to pK$ decays, $\sigma_{\mathcal{A}}^{\rm optimal} = 1.4 - 3.3\%$.

The observation of Standard Model $\mathcal{CP}$-violation in $\Lambda_b \to p\pi$ decays requires a luminosity of $1.5 - 8.1$ fb^{-1} for 3σ evidence, and $4.2 - 22.5$ fb^{-1} for a 5σ discovery. The observation of R-parity violating MSSM $\mathcal{CP}$-violation in $\Lambda_b \to p\pi$ decays requires a luminosity of $50 - 250$ fb^{-1} for 3σ evidence, and $130 - 700$ fb^{-1} for a 5σ discovery.

The statistical precision available at LHCb is sufficient to discover Standard Model $\mathcal{CP}$-violation in $\Lambda_b \to p\pi$ decays, but evidence for the suppression of the $\mathcal{CP}$ asymmetry on account of R-parity violating MSSM will require the luminosity upgraded "Super"-LHCb detector.

Chapter 8

Conclusions

This thesis has presented three aspects of research towards the LHCb detector; the evaluation of the MaPMT readout electronics in a charged particle beam, the development of a flavour tag using proton and Λ baryons, methods to select $\Lambda_b \to p\,\pi/K$ decays and the resulting physics potential.

The MaPMT photodetector was tested in a charged particle beam at CERN. This thesis presents the development of a process to describe the number of expected electrons at the end of the MaPMT dynode chain, including the effect of photoelectric conversion on the first dynode, which has been adapted to model the time-dependency of the BeetleMA output. Using this function the BeetleMA pulse shape has been extracted; the result of which demonstrates that the pulse shape does not return to zero after 125ns. The signal from a previous bunch crossing can therefore spill-over into the current one leading to ghost hits. Evidence is also found for undershoot in the signal, which would lead to a loss in photon detection efficiency. Furthermore, if the occupancy is such that the signal never returns to zero before another hit arrives in a pixel, this could cause the pedestal to drift until eventually it is outside the dynamic range of the the amplifier. The measurement of the BeetleMA output was one consideration in the adoption of HPD photodetector technology for the RICH detectors.

The potential to use protons and Λ baryons for flavour tagging has been investigated. An opposite-side proton flavour tag is found to have a potentially useful tagging power. However, the implementation is found to be challenging on account of the necessity to identify protons from the decay of Λ_b's compared with those of B-meson decays. This difficulty is not present if the tag is restricted to protons from the decay of Λ's,

in which case all B-hadrons have the same correlation between proton and b-quark flavour. However, the selection criteria required to remove Λ's from the underlying events results in a very small tagging efficiency. A correlation between b-quark and Λ flavour is observed for a Λ produced in the same fragmentation process as a B_s^0 meson, analogous to a same-side kaon tag. A non-negligible tagging performance is attained. Preliminary studies of a same-side proton tag indicate that an analogous correlation is present, but extraction of useful tagging power is likely to be challenging on account of the large number of background protons. Since many of the implementation issues encountered are derived from the, as yet, unverified Monte Carlo simulations, it is suggested that the issues raised during this investigation are re-visted once real data is available.

The reconstruction and selection of $\Lambda_\mathrm{b} \to \mathrm{p}\,\pi$ and $\Lambda_\mathrm{b} \to \mathrm{p}\,\mathrm{K}$ decays with the LHCb apparatus has been demonstrated using a full Monte Carlo simulation of the LHCb detector. The chosen selection criteria successfully reject all background from inclusive $\mathrm{b\overline{b}}$ decays, leading to a 90% confidence on the expected background to signal ratio of $\mathrm{B}_{\mathrm{b\overline{b}}}/\mathrm{S} = [0.0, 4.3]$ and $\mathrm{B}_{\mathrm{b\overline{b}}}/\mathrm{S} = [0.0, 2.6]$ for $\Lambda_\mathrm{b} \to \mathrm{p}\,\pi$ and $\Lambda_\mathrm{b} \to \mathrm{p}\,\mathrm{K}$ decays respectively; the upper bound of which is limited by the avaliable sample size of simulated inclusive $\mathrm{b\overline{b}}$ decays. A method for removing the exclusive backgrounds arising from two-body charmless B-meson decays is developed which utilises the excellent detector mass resolution to identify the kaons from B-meson decays which have been mis-identified as protons in $\Lambda_\mathrm{b} \to \mathrm{p}\,\pi/\mathrm{K}$ decays. The background to signal ratio on account of charmless two-body B-meson backgrounds is expected to be $\mathrm{B}_\mathrm{spec.}/\mathrm{S} = 0.09 \pm 0.03$ for $\Lambda_\mathrm{b} \to \mathrm{p}\,\pi$ decays and $\mathrm{B}_\mathrm{spec.}/\mathrm{S} = 0.05 \pm 0.02$ for $\Lambda_\mathrm{b} \to \mathrm{p}\,\mathrm{K}$ decays.

Finally, annual yields of $\sim$2k $\Lambda_\mathrm{b} \to \mathrm{p}\,\pi$ and $\sim$3k $\Lambda_\mathrm{b} \to \mathrm{p}\,\mathrm{K}$ decays are expected after the trigger and offline selections; providing a statistical precision of 3.2×10^{-8} and 2.9×10^{-8} on the $\Lambda_\mathrm{b} \to \mathrm{p}\,\pi$ and $\Lambda_\mathrm{b} \to \mathrm{p}\,\mathrm{K}$ branching fractions respectively. Evidence for Standard Model $\mathcal{CP}$-violation with $\Lambda_\mathrm{b} \to \mathrm{p}\,\pi$ decays is expected to require an integrated luminosity of between 1.5 and 8.1 fb^{-1}, while evidence for $\mathcal{CP}$-violation consistent with R-parity-violation in the Minimal Supersymmetric Standard Model will require an integrated luminosity of between 50 and 250 fb^{-1}. The latter integrated luminosity will only be realised with the construction of the upgraded luminosity "Super"-LHCb detector.

Appendix A

Describing PMT Spectra

A.1 Adapting Function to Include Photon Conversion at First Dynode

Let $P^{t}_{\sim}(k_n)$ be the function that describes the number of photoelectrons (k_n) at the end of a dynode chain, including the effect of photoelectric conversion at the 1st dynode. The function is the convolution of two instances of equation 4.2, corresponding to the probabilities of 1) k_n electrons due to photoelectric conversion at the cathode ,($P^{PC}_{\sim}(k_n)$), and 2) photoelectric conversion at the 1st dynode, $P^{DC}_{\sim}(k_n)$,

$$P^{t}_{\sim}(k_n) = P^{PC}_{\sim}(k_n) * P^{DC}_{\sim}(k_n). \tag{A.1}$$

To evaluate the convolution it is useful to express $P_{\sim}(k_n)$ in the following form,

$$\begin{aligned} P_{\sim}(k_n) =& \sum_{j=0}^{j=\infty} \frac{1}{\sqrt{2\pi}\sqrt{j}\sigma_0} e^{-\frac{(jg_{\text{left}}-k_n)^2}{(\sqrt{2j}\sigma_0)^2}} P(j) \\ =& \lim j \to 0^{+} \frac{1}{\sqrt{2\pi}\sqrt{j}\sigma_0} e^{-\frac{(jg_{\text{left}}-k_n)^2}{(\sqrt{2j}\sigma_0)^2}} P(j) + \sum_{j=1}^{j=\infty} \frac{1}{\sqrt{2\pi}\sqrt{j}\sigma_0} e^{-\frac{(jg_{\text{left}}-k_n)^2}{(\sqrt{2j}\sigma_0)^2}} P(j) \\ =& \delta(k_n)P(0) + \sum_{j=1}^{j=\infty} \frac{1}{\sqrt{2\pi}\sqrt{j}\sigma_0} e^{-\frac{(jg_{\text{left}}-k_n)^2}{(\sqrt{2j}\sigma_0)^2}} P(j), \end{aligned}$$

where the last step uses the identity $\delta(x) = \lim \epsilon \to 0^{+} \frac{1}{2\sqrt{\pi\epsilon}} e^{-\frac{x^2}{4\epsilon}}$. Evaluating the convolution in equation A.1,

$$
\begin{aligned}
P^{t}_{\sim}(k_n) = &\left[\delta(k_n)P(0) + \sum_{j=1}^{j=\infty} \frac{1}{\sqrt{2\pi}\sqrt{j}\sigma_0^{PC}} e^{-\frac{(jg_{\text{left}}-k_n)^2}{\left(\sqrt{2j}\sigma_0^{PC}\right)^2}} P(j)\right] * \\
&\left[\delta(k_n)P(0) + \sum_{h=1}^{h=\infty} \frac{1}{\sqrt{2\pi}\sqrt{h}\sigma_0^{DC}} e^{-\frac{(hg_{\text{left}}-k_n)^2}{\left(\sqrt{2h}\sigma_0^{DC}\right)^2}} P(h)\right] \\
= &\sum_{j=1}^{j=\infty} \frac{P^{DC}(0)}{\sqrt{2\pi}\sqrt{j}\sigma_0^{PC}} e^{-\frac{\left(jg_{\text{left}}^{PC}-k_n\right)^2}{2\left(\sqrt{j}\sigma_0^{PC}\right)^2}} P^{PC}(j) + \sum_{h=1}^{h=\infty} \frac{P^{PC}(0)}{\sqrt{2\pi}\sqrt{h}\sigma_0^{DC}} e^{-\frac{\left(hg_{\text{left}}^{DC}-k_n\right)^2}{2\left(\sqrt{h}\sigma_0^{DC}\right)^2}} P^{DC}(h) \\
&+ P^{PC}(0)P^{DC}(0) + \sum_{j=1}^{j=\infty}\sum_{h=1}^{h=\infty} \frac{P^{PC}(j)P^{DC}(h)}{\sqrt{2\pi}\left(j\sigma_0^{PC^2} + h\sigma_0^{DC^2}\right)} e^{-\frac{\left(k_n-\left(jg_{\text{left}}^{PC}+hg_{\text{left}}^{DC}\right)\right)^2}{2\left(j\sigma_0^{PC^2}+h\sigma_0^{DC^2}\right)^2}},
\end{aligned}
\tag{A.2}
$$

where the following convolution identities have been used

- $f(t) = \frac{1}{\sqrt{2\pi}\sigma_1} e^{-\frac{(t-\mu_1)^2}{2\sigma_1^2}}$, $g(t) = \frac{1}{\sqrt{2\pi}\sigma_2} e^{-\frac{(t-\mu_2)^2}{2\sigma_2^2}}$,
  $f(t) * g(t) = \frac{1}{\sqrt{2\pi\left(\sigma_1^2+\sigma_2^2\right)}} e^{-\frac{(t-\mu_1-\mu_2)^2}{2\left(\sigma_1^2+\sigma_2^2\right)}}$,
- $F(k) * \delta(k) = F(k)$,
- $f * (g + h) = (f * g) + (f * h)$.

A.2 Adapting Function to Include Electonic Noise Effects

Electronic noise effects are accounted for by convolving $P^{t}_{\sim}(k_n)$ (equation A.2) with a Gaussian, $N(k_n)$, of width σ_n. Hence, the probability density $F(k_n)$ for k_n electrons at

the end of the dynode chain is given by

$$
\begin{aligned}
F(k_n) &= N(k_n) * P^t_{\sim}(k_n) \\
&= \frac{P^{PC}(0)P^{DC}(0)}{\sqrt{2\pi}\sigma + n} e^{-\frac{k_n^2}{2\sigma_n^2}} + \sum_{j=1}^{j=\infty} \frac{P^{DC}(0)}{\sqrt{2\pi}\left(\sigma_n^2 + \sqrt{j}\sigma_0^{PC^2}\right)} e^{-\frac{\left(jg_{\text{left}}^{PC} - k_n\right)^2}{2\left(\sigma_n^2 + \sqrt{j}\sigma_0^{PC^2}\right)^2}} P^{PC}(j) \\
&+ \sum_{h=1}^{h=\infty} \frac{P^{PC}(0)}{\sqrt{2\pi}\left(\sigma_n^2 + \sqrt{h}\sigma_0^{DC^2}\right)} e^{-\frac{\left(hg_{\text{left}}^{DC} - k_n\right)^2}{2\left(\sigma_n^2 + \sqrt{h}\sigma_0^{DC^2}\right)^2}} P^{DC}(h) \\
&+ \sum_{j=1}^{j=\infty} \sum_{h=1}^{h=\infty} \frac{P^{PC}(j)P^{DC}(h)}{\sqrt{2\pi}\left(\sigma_n^2 + j\sigma_0^{PC^2} + h\sigma_0^{DC^2}\right)} e^{-\frac{\left(k_n - \left(jg_{\text{left}}^{PC} + hg_{\text{left}}^{DC}\right)\right)^2}{2\left(\sigma_n^2 j\sigma_0^{PC^2} + h\sigma_0^{DC^2}\right)^2}}.
\end{aligned}
\tag{A.3}
$$

$F(k_n)$ satisfies the normalisation condition $\int_{-\infty}^{\infty} F(k_n), dk_n = 1$. The first term of equation A.3 corresponds to the pedestal contribution (defined as $F^P(k_n)$), the remaining terms to the signal contribution (defined as $F^S(k_n)$).

Bibliography

[1] Steven Weinberg. A model of leptons. *Phys. Rev. Lett.*, 19:1264–1266, 1967.

[2] S. L. Glashow, J. Iliopoulos, and L. Maiani. Weak interactions with lepton-hadron symmetry. *Phys. Rev.*, D2:1285–1292, 1970.

[3] Jeffrey Goldstone, Abdus Salam, and Steven Weinberg. Broken symmetries. *Phys. Rev.*, 127:965–970, 1962.

[4] C. S. Wu, E. Ambler, R. W. Hayward, D. D. Hoppes, and R. P. Hudson. Experimental Test of Parity Conservation in Beta Decay. *Phys. Rev.*, 105:1413–1414, 1957.

[5] J. H. Christenson, J. W. Cronin, V. L. Fitch, and R. Turlay. Evidence for the 2 π Decay of the K_2^0 Meson. *Phys. Rev. Lett.*, 13:138–140, 1964.

[6] B. Aubert et al. Observation of CP violation in the B^0 meson system. *Phys. Rev. Lett.*, 87:091801, 2001.

[7] K. Abe et al. Observation of large CP violation in the neutral B meson system. *Phys. Rev. Lett.*, 87:091802, 2001.

[8] Makoto Kobayashi and Toshihide Maskawa. CP Violation in the Renormalizable Theory of Weak Interaction. *Prog. Theor. Phys.*, 49:652–657, 1973.

[9] A. D. Sakharov. Violation of CP invariance, C asymmetry, and baryon asymmetry of the universe. *Pisma Zh. Eksp. Teor. Fiz.*, 5:32–35, 1967.

[10] V. A. Rubakov and M. E. Shaposhnikov. Electroweak baryon number non-conservation in the early universe and in high-energy collisions. *Usp. Fiz. Nauk*, 166:493–537, 1996.

[11] R. Barbier et al. R-parity violating supersymmetry. *Phys. Rept.*, 420:1–202, 2005.

[12] Rukmani Mohanta. Effects of R-parity violation on CP asymmetries in the $\Lambda_b \to p\ \pi$ decay. *Phys. Rev.*, D63:056006, 2001.

[13] Gustavo C. Branco, Luis Lavoura, and Joao P. Silva. CP violation. Oxford, UK: Clarendon (1999) 511 p.

[14] V. Weisskopf and Eugene P. Wigner. Calculation of the natural brightness of spectral lines on the basis of dirac's theory. *Z. Phys.*, 63:54–73, 1930.

[15] Luis Fernandez. Exclusive Trigger Selections and Sensitivity to the $B_s - \bar{B}_s$ Mixing Phase at LHCb. 2006. PhD thesis, EPFL Lausanne.

[16] E. Leader and E. Predazzi. An introduction to gauge theories and modern particle physics. Vol. 2: CP violation, QCD and hard processes. *Camb. Monogr. Part. Phys. Nucl. Phys. Cosmol.*, 4:1–431, 1996.

[17] W. M. Yao et al. Review of particle physics. *J. Phys.*, G33:1–1232, 2006. Available from: http://pdg.lbl.gov.

[18] Zoltan Ligeti. The CKM matrix and CP violation. *Int. J. Mod. Phys.*, A20:5105–5118, 2005.

[19] Yosef Nir. CP violation in and beyond the Standard Model. 1999. hep-ph/9911321.

[20] V. Gibson. B physics. Prepared for 57th Scottish Universties Summer School in Physics: LHC Phenomenology (SUSSP 2003), St. Andrews, Scotland, United Kingdom, 17-29 Aug 2003.

[21] B. Aubert et al. Observation of direct CP violation in $B^0 \to K^+\pi^-$ decays. *Phys. Rev. Lett.*, 93:131801, 2004.

[22] Y. Chao et al. Evidence for direct CP violation in $B^0 \to K^+\pi^-$ decays. *Phys. Rev. Lett.*, 93:191802, 2004.

[23] T. Nakada. CP violation: Current status and future prospects. *Surveys High Energ. Phys.*, 17:3–36, 2002.

[24] B. Aubert et al. Measurement of CP violating asymmetries in B^0 decays to CP eigenstates. *Phys. Rev. Lett.*, 86:2515–2522, 2001.

[25] A. Abashian et al. Measurement of the CP violation parameter $sin(2\phi(1))$ in B^0 meson decays. *Phys. Rev. Lett.*, 86:2509–2514, 2001.

[26] ed. Harrison, P. F. and ed. Quinn, Helen R. The BaBar physics book: Physics at an asymmetric B factory. Papers from Workshop on Physics at an Asymmetric B Factory (BaBar Collaboration Meeting), Rome, Italy, 11-14 Nov 1996, Princeton, NJ, 17-20 Mar 1997, Orsay, France, 16-19 Jun 1997 and Pasadena, CA, 22-24 Sep 1997.

[27] C. Jarlskog. Commutator of the Quark Mass Matrices in the Standard Electroweak Model and a Measure of Maximal CP Violation. *Phys. Rev. Lett.*, 55:1039, 1985.

[28] Lincoln Wolfenstein. Parametrization of the Kobayashi-Maskawa Matrix. *Phys. Rev. Lett.*, 51:1945, 1983.

[29] Robert Fleischer. Flavour physics and CP violation. 2004. hep-ph/0405091.

[30] Heavy Flavor Averaging Group (HFAG). Averages of b-hadron properties at the end of 2006. arXiv:0704.3575 [hep-ex].

[31] A. Abulencia et al. Observation of B_s^0 - $\overline{B_s^0}$ oscillations. *Phys. Rev. Lett.*, 97:242003, 2006.

[32] J. Charles et al. CP violation and the CKM matrix: Assessing the impact of the asymmetric B factories. *Eur. Phys. J.*, C41:1–131, 2005.

[33] M. Bona et al. The unitarity triangle fit in the standard model and hadronic parameters from lattice QCD. *JHEP*, 10:081, 2006.

[34] P Vankov. Sensitivity to the B_s mixing phase at LHCb. Technical Report LHCb-2007-065, CERN, Geneva, Apr 2007.

[35] S Cohen, M Merk, and E Rodrigues. $\gamma + \phi_s$ sensitivity studies from combined $B_s^0 \pi^0$ and $B_s^0 \to D_s^{\mp}\ K^{\pm}$ samples at LHCb. Technical Report LHCb-2007-041, CERN, Geneva, Jul 2007.

[36] K Akiba and M Gandelman. Estimate of LHCb's sensitivity to the CKM angle γ using $B^0 \to D^0\ K^{*0}$ Decays. Technical Report LHCb-2007-050, CERN, Geneva, Jun 2007.

[37] M Patel. Measuring γ at LHCb with an Atwood-Dunietz-Soni Method. Technical Report LHCb-2006-066, CERN, Geneva, Dec 2006.

[38] V Gibson. The LHCb experiment. Technical Report LHCb-2007-100, CERN, Geneva, Jul 2007.

[39] A Carbone, J Nardulli, S Pennazzi, A Sarti, and V Vagnoni. Charmless charged two-body B decays at LHCb. Technical Report LHCb-2007-059, CERN, Geneva, Sep 2007.

[40] Isard Dunietz. CP violation with beautiful baryons. *Z. Phys.*, C56:129–144, 1992.

[41] R. Mohanta, A. K. Giri, and M. P. Khanna. Charmless two body hadronic decays of Λ_b baryon. *Phys. Rev.*, D63:074001, 2001.

[42] LHC web pages. http://lhc.web.cern.ch/lhc.

[43] LHC Design Report Volume 1. http://ab-div.web.cern.ch/ab-div/Publications/LHC-DesignReport.html.

[44] Tevatron luminosity web pages. http://www.fnal.gov/pub/now/tevlum.html.

[45] LHCb Collaboration. LHCb Technical Proposal. 1998. CERN/LHCC/98/4.

[46] P. Nason et al. Bottom production. *In 1999 CERN Workshop on Standard Model Physics (and more) at the LHC, CERN, Geneva, Switzerland, 25 - 26 May 1999: Proceedings, edited by G. G. Altarelli and M. L. Mangano*, 2000. CERN-2000-004.

[47] Michelangelo L. Mangano. Heavy-quark production in hadronic collisions. 1997. CERN-TH/97-328.

[48] Torbjorn Sjostrand, Stephen Mrenna, and Peter Skands. PYTHIA 6.4 physics and manual. *JHEP*, 05:026, 2006.

[49] LHCb Collaboration. LHCb Reoptimised Detector Design and Performance Technical Design Report. 2003. CERN/LHCC/2003/030.

[50] LHCb web pages. http://www.cern.ch/lhcb.

[51] B.Epp for the ATLAS Collaboration. Physics at the LHC, Prague. *Proc. Advanced Studies Institute*, 2003.

[52] LHCb Collaboration. LHCb Vertex Locator Technical Design Report. 2001. CERN/LHCC/2001/011.

[53] S Lochner and M Schmelling. The Beetle Reference Manual. Technical Report LHCb-2005-105. CERN-LHCb-2005-105, CERN, Geneva, Nov 2006.

[54] T.Bowcock et. al. Performance of an irradiated p-on-n Micron prototype VELO detector. Technical report, May 2001. LHCb-2001-040.

[55] T.Bowcock et. al. Performance of an irradiated n-on-n Hamamatsu prototype VELO detector. Technical report, May 2001. LHCb-2001-039.

[56] J.F.J. van den Brand et. al. Conceptual design of the LHCb VELO vacuum system. Technical report, June 2001. LHCb-2001-080.

[57] Marcello Losasso. LHCb Dipole Test and Field Mapping. *IEEE Transaction on Applied Superconductivity June 2006, Vol 16, Number 2, pg.1700.*

[58] R. L. Gluckstern. Uncertainties in track momentum and direction, due to multiple scattering and measurement errors. *Nucl. Instrum. Meth.*, 24:381–389, 1963.

[59] LHCb Collaboration. LHCb Inner Tracker Technical Design Report. 2002. CERN/LHCC/2002/029.

[60] LHCb Collaboration. LHCb Outer Tracker Technical Design Report. 2001. CERN/LHCC/2001/024.

[61] LHCb Collaboration. LHCb Calorimeters Technical Design Report. 2000. CERN/LHCC/2000/0036.

[62] Andrey Golutvin. Calorimeters for Collider Experiments. 2007. Presented at the 11th Vienna Conference on Instrumentation.

[63] LHCb Collaboration. LHCb Muon System Technical Design Report. 2001. CERN/LHCC/2001/0010.

[64] LHCb Collaboration. LHCb addendum 1 to the LHCb Muon System Technical Design Report. 2003. CERN/LHCC/2003/0002.

[65] LHCb Collaboration. LHCb addendum 2 to the LHCb Muon System Technical Design Report. 2005. CERN/LHCC/2005/0012.

[66] F. Sauli. Gem: A new concept for electron amplification in gas detectors. *Nucl. Instrum. Meth.*, A386:531–534, 1997.

[67] LHCb Collaboration. LHCb Trigger System Technical Design Report. 2003. CERN/LHCC/2003/0031.

[68] LHCb Collaboration. LHCb Online System Technical Design Report. 2001. CERN/LHCC/2001/0040.

[69] LHCb, T. Schietinger. High-level trigger strategy at 1 MHz. Presentation to LHCb collaboration, November 2005. http://lhcb-trig.web.cern.ch/lhcb-trig/HLT/HltDocumentation.htm.

[70] J.A.Hernando. The LHCb Trigger. Physics at LHC. Proceedings, 3rd Conference, Cracow, Poland, July 3-8, 2006.

[71] G. Barrand et al. GAUDI - a software architecture and framework for building HEP data processing applications. *Comput. Phys. Commun.*, 140:45–55, 2001.

[72] Torbjorn Sjostrand et al. High-energy-physics event generation with PYTHIA 6.1. *Comput. Phys. Commun.*, 135:238–259, 2001.

[73] Torbjorn Sjostrand. Theory of Hadronic Collisions. Presented at the 1st CERN-Fermilab Collider School, 9-18th August 2006.

[74] Jeroen Van Tilburg. Track simulation and reconstruction in LHCb. 2005. PhD thesis, NIKHEF Amsterdam.

[75] E. Norrbin and T. Sjostrand. Production and hadronization of heavy quarks. *Eur. Phys. J.*, C17:137–161, 2000.

[76] N.Tuning H.Dijkstra and N.Brook. Some remarks on systematic effects of the trigger and event generator studies. Technical report, December 2003. LHCb-2003-157.

[77] D. J. Lange. The EVTGEN particle decay simulation package. *Nucl. Instrum. Meth.*, A462:152–155, 2001.

[78] S. Agostinelli et al. GEANT 4: A simulation toolkit. *Nucl. Instrum. Meth.*, A506:250–303, 2003.

[79] LHCb. LHCb Gauss simulation framework. http://lhcb-release-area.web.cern.ch/LHCb-release-area/DOC/gauss/.

[80] LHCb. LHCb Boole digitisation framework. http://lhcb-release-area.web.cern.ch/LHCb-release-area/DOC/boole/.

[81] LHCb. LHCb Brunel reconstruction framework. http://lhcb-release-area.web.cern.ch/LHCb-release-area/DOC/brunel/.

[82] O. Callot. A new implementation of the relations: The linker objects. CERN-LHCb/2004-007, 2004.

[83] LHCb. LHCb DaVinci analysis framework. http://lhcb-release-area.web.cern.ch/LHCb-release-area/DOC/davinci/.

[84] LHCb Collaboration. LHCb RICH Technical Design Report. 2000. CERN/LHCC/2000/037.

[85] D. Green. The physics of particle detectors. *Camb. Monogr. Part. Phys. Nucl. Phys. Cosmol.*, 12:1–361, 2000.

[86] T. Ypsilantis and J. Seguinot. Theory of ring imaging Cherenkov counters. *Nucl. Instrum. Meth.*, A343:30–51, 1994.

[87] J Rademacker. Evaluation of the LHCb RICH detectors and a measurement of the CKM angle γ. 2001. PhD thesis, Oxford Univ.

[88] C D'Ambrosio, B J Franek, C Gaspar, M Laub, R Lindner, F Muheim, A Papanestis, and FJP Soler. Monitoring, alignment and control of the RICH detectors. Technical Report LHCb-2000-080, CERN, Geneva, Apr 2001.

[89] F Muheim. Proposal for multi-anode photo multiplier tubes as photo detectors for the LHCb RICH. Technical Report LHCb-2000-065, CERN, Geneva, Apr 2001.

[90] M Campbell, F Formenti, Thierry Gys, W Snoeys, and Ken H Wyllie. Development of pixel hybrid photon detectors for the RICH counters of LHCb. Technical Report LHCb-98-035, CERN, Geneva, Jan 1998.

[91] N Smale. Multi-anode Photon-Multiplier Readout Electronics for the LHCb Ring Imaging Cherenkov Detectors. 2004. PhD thesis, Oxford Univ.

[92] E Albrecht et al. Performance of a cluster of Multi-anode Photomultipliers equipped with lenses for use in a prototype RICH detector. *Nucl. Instrum. Methods Phys. Res., A*, 488, Jul 2001.

[93] M Schmelling. Specifications of the Front End Chip for the LHCb Vertex Detector. Technical Report LHCb-2001-048, CERN, Geneva, Apr 2001.

[94] K. Wyllie. The front-end electronics of the LHCb ring-imaging- Cherenkov system. *Nucl. Instrum. Meth.*, A567:184–187, 2006.

[95] Jonas Rademacker. An Exact Formula to Describe the Amplification Process in a Photomultiplier Tube. *Nucl. Instrum. Methods Phys. Res., A*, 484:432, 2002.

[96] I. Chirikov-Zorin et al. Method for precise analysis of the metal package photomultiplier single photoelectron spectra. *Nucl. Instrum. Meth.*, A456:310–324, 2001.

[97] F. James and M. Roos. Minuit: A System for Function Minimization and Analysis of the Parameter Errors and Correlations. *Comput. Phys. Commun.*, 10:343–367, 1975.

[98] I. Arino et al. The HERA-B ring imaging Cerenkov counter. *Nucl. Instrum. Meth.*, A516:445–461, 2004.

[99] T. Gys. Production of 500 pixel hybrid photon detectors for the RICH counters of LHCb. *Nucl. Instrum. Meth.*, A567:176–179, 2006.

[100] M.Musy M.Calvi, O.Dormond. LHCb flavour tagging performance. Technical report, September 2003. LHCb-2003-115.

[101] M Calvi, O Leroy, and M Musy. Flavour tagging algorithms and performances in LHCb. Technical Report LHCb-2007-058, CERN, Geneva, May 2007.

[102] O Dormond. Determination of the Flavour of Beauty Mesons in LHCb and Contribution to the Development of the LHCb Vertex Locator. 2004. PhD thesis, Lausanne Univ.

[103] G.Wilkinson. Strategies for combating systematics at LHCb. Technical report, October 2005. LHCb-2005-078.

[104] Miriam Calvo Gomez. Backsplash Effects on SPD and Flavour Tagging at LHCb. 2006. PhD thesis, Universitat de Barcelona.

[105] Michael Gronau and Jonathan L. Rosner. Identification of neutral B mesons using correlated hadrons. *Phys. Rev.*, D49:254–264, 1994.

[106] The CDF Collaboration. Measurment of branching fractions and direct CP assymetries of $B_s \to h^+h^-$ decays in 1 fb^{-1}. 2006. CDF/8579.

[107] E. Barberio et al. Averages of b-hadron properties at the end of 2005. *hep-ex/0603003*, 2006.

[108] Gary J. Feldman and Robert D. Cousins. A unified approach to the classical statistical analysis of small signals. *Phys. Rev.*, D57:3873–3889, 1998.

[109] R. Brun and F. Rademakers. Root: An object oriented data analysis framework. *Nucl. Instrum. Meth.*, A389:81–86, 1997.

[110] V.Vagnoni et al. Selection of $B^0 \to h^+h^-$ decays at LHCb. Technical report, 2003. LHCb-2003-123.

[111] 1st LHCb collaboration upgrade workshop. January 2007. http://indico.cern.ch/conferenceDisplay.py?confId=8351.

[112] D. Acosta et al. Search for $\Lambda_b \to p\pi$ and $\Lambda_b \to pK$ decays in $p\bar{p}$ collisions at $\sqrt{s} = 1.96$ TeV. *Phys. Rev.*, D72:051104, 2005.

[113] The CDF and D0 Collaborations. The case for run II : Submission to the particle physics project prioritization panel the CDF and D0 experiments. 2005.